Topology and Excitations in Low-Dimensional Quantum Matter

Dissertation
zur Erlangung des akademischen Grades
Doctor rerum naturalium
(Dr. rer. nat.)

vorgelegt von
Ruben Verresen
geboren am 11.02.1991 in Leuven
Max-Planck-Institut für Physik komplexer Systeme, Dresden

Wissenschaftliche Betreuer:
Prof. Dr. Roderich Moessner und Prof. Dr. Frank Pollmann

Fakultät Physik
Bereich Mathematik und Naturwissenschaften
Technische Universität Dresden
2019

Eingereicht am 4. Juli 2019

1. Gutachter: Prof. Dr. Frank Pollmann
2. Gutachter: Prof. Dr. Roderich Moessner
3. Gutachter: Prof. Dr. Matthias Vojta

Verteidigt am 27. August 2019

Abstract

The Schrödinger equation is nearly a century old, yet we are still in the midst of uncovering the remarkable phenomena emerging in many-body quantum systems. From superconductivity to anyonic quasiparticles, nature consistently surprises with its rich self-organization. To elucidate and grasp this variety, it is paramount to understand the phases of matter that can occur in many-body ground states, as well as their emergent collective excitations.

Of particular interest are topological phases of matter, characterized by exotic excitations or edge phenomena. There exist by now several universal frameworks for gapped systems, i.e., those with an energy gap above the ground state. However, in the last decade, a multitude of gapless quantum wires—effectively one-dimensional systems—have been reported to be topologically non-trivial. A framework for their understanding and classification is missing. In addition to ground state order—topological or otherwise—a more complete picture involves the properties of excitations above the ground state. Alas, little is known about excitations beyond the universal low-energy regime. In part, this is due to a lack of analytical and numerical methods able to describe excitations at finite energies, especially in strongly-interacting systems beyond one dimension.

In this thesis, we address these issues: firstly, we build a general understanding of topological phases in one dimension, including both gapped and gapless cases. In particular, we unify previously studied examples into a single framework. Secondly, we develop a novel numerical method for obtaining spectral functions in two dimensions—these give direct insight into the properties of excitations and are moreover experimentally measurable. Using this numerical method, we uncover a variety of robust properties of excitations at finite energies.

Part I of this thesis concerns gapped and gapless topological phases in one dimension. In Chapter 2, we first treat the case of non-interacting fermions. Therein, we review the known classification of gapped phases before extending it to the gapless case, showing that exponentially-localized Majorana zero modes can still emerge at the edge when the bulk is gapless. Interacting gapped phases are discussed in Chapter 3, with a focus on symmetry-protected topological order. These have already been classified; our contribution is to provide a non-technical review of this classification as well as showing that many paradigmatic model Hamiltonians can be related to one another. Finally, Chapter 4 introduces the notion of symmetry-enriched quantum criticality, which we propose as a framework for classifying gapless phases. The key message is that in the presence of symmetries, a universality class can divide into distinct phases, characterized by the symmetry action on the low-energy scaling operators. This includes gapless topological phases, with examples hiding in plain sight; we clarify their stability and reinterpret previously studied examples.

Part II studies the excitations above the ground states of two-dimensional quantum spin models. The main object of our study is the dynamic spin structure factor; this type of spectral function is reviewed in the first part of Chapter 5. The second part of this chapter introduces a novel matrix-product-state-based algorithm to efficiently compute it, opening a new window on the dynamics of two-dimensional quantum systems. We benchmark this numerical method in Chapter 6 on the exactly-solvable Kitaev model—a paradigmatic topological model realizing a quantum spin liquid. By adding non-integrable Heisenberg perturbations, we identify the first unequivocal theoretical realization of a proximate spin liquid: the ground state becomes conventionally ordered, yet the high-energy spectral properties are structurally similar to those of the nearby Kitaev spin liquid. The lat-

ter agrees with aspects of recent inelastic neutron scattering experiments on α-$RuCl_3$. In Chapter 7, we turn to one of the oldest models in many-body quantum physics: the spin-1/2 Heisenberg antiferromagnet on the square lattice. Despite its venerable history, there is still disagreement about the physical origin of high-energy spectral features which low-order spin wave theory cannot account for. We provide a simple picture for this strongly-interacting-magnon feature by connecting it to a simple Ising limit. Lastly, Chapter 8 discusses the stability of quasiparticles—collective excitations behaving like a single emergent entity, of which magnons are a prime example. These are often known to be stable at the lowest energies and are presumed to decay whenever this is seemingly allowed by energy and momentum conservation. However, we show that strong interactions can prevent this from happening. We numerically confirm this principle of avoided decay in the (slightly-detuned) Heisenberg antiferromagnet on the triangular lattice. Moreover, we can even identify its fingerprints in existing experimental data on $Ba_3CoSb_2O_9$ and superfluid helium.

In this thesis, we thus enlarge our understanding of quantum phases and their excitations. The identification of the key principles of gapless topological phases in one dimension calls for direct analogues in higher dimensions, waiting to be uncovered. With regard to the robust properties of the excitations identified in this thesis, we are hopeful that these can be extended into a theory of quasiparticle properties away from the universal low-energy regime.

Zusammenfassung

Die Schrödingergleichung ist fast ein Jahrhundert alt, aber wir sind immer noch dabei, die bemerkenswerten Phänomene aufzudecken, die in Vielkörperquantensystemen auftreten. Von der Supraleitung bis zu anyonischen Quasiteilchen überrascht die Natur immer wieder mit ihrer reichen Selbstorganisation. Um diese Vielfalt zu erfassen, ist es von größter Bedeutung, die Phasen der Materie zu verstehen, die in Grundzuständen von Vielkörpersystemen auftreten können, sowie ihre Anregungen zu studieren.

Von besonderem Interesse sind topologische Phasen der Materie, die durch exotische Anregungen oder Randphänomene gekennzeichnet sind. Mittlerweile existieren mehrere universelle Beschreibungen für Systeme mit Energielücke über dem Grundzustand. Im letzten Jahrzehnt wurde jedoch über eine Vielzahl eindimensionaler masseloser Systeme berichtet, die topologisch nicht trivial zu sein scheinen. Ein allgemeines Modell für ihr Verständnis und ihre Klassifizierung ist noch nicht vorhanden. Zusätzlich zur Ordnung des Grundzustandes—topologisch oder anderweitig—sollte eine vollständige Charakterisierung die Eigenschaften von Anregungen über dem Grundzustand beinhalten. Über Anregungen jenseits des universellen Niedrigenergieregimes ist leider wenig bekannt. Dies ist zum Teil auf den Mangel an analytischen und numerischen Methoden zurückzuführen, mit denen Anregungen bei endlichen Energien beschrieben werden können, insbesondere in stark wechselwirkenden Systemen jenseits einer Dimension.

In dieser Arbeit werden diese Fragen behandelt: Zunächst wird ein allgemeines Verständnis der topologischen Phasen in einer Dimension einschließlich Systemen mit und ohne Energielücke erarbeitet. Insbesondere vereinen wir zuvor untersuchte Beispiele in einem einheitlichen konzeptionellen Rahmen. Zweitens entwickeln wir eine neuartige numerische Methode, um Spektralfunktionen in zwei Dimensionen zu erhalten—diese geben einen direkten Einblick in die Eigenschaften von Anregungen und sind darüber hinaus experimentell messbar. Mit dieser numerischen Methode decken wir eine Vielzahl robuster Eigenschaften von Anregungen bei endlichen Energien auf.

Teil I dieser Arbeit befasst sich mit topologisch geordneten Phasen in einer Dimension mit und ohne Energielücke. In Kapitel 2 behandeln wir zunächst den Fall nicht wechselwirkender Fermionen. Darin überprüfen wir die bekannte Klassifizierung von Phasen mit Energielücke, bevor wir sie auf den masselosen Fall übertragen. Dabei zeigen wir, dass immer noch exponentiell lokalisierte Majorana-Nullmoden am Rand auftreten können, selbst ohne Energielücke. Wechselwirkende Phasen mit Energielücken werden in Kapitel 3 diskutiert, wobei der Schwerpunkt auf symmetriegeschützten topologischen Phasen liegt. Diese wurden bereits klassifiziert; Unser Beitrag besteht darin, eine nicht-technische Übersicht über diese Klassifikation zu geben und zu zeigen, dass viele paradigmatische Modell-Hamiltonians miteinander verwandt sein können. Schließlich wird Kapitel 4 der Begriff der mit Symmetrie angereicherten Quantenkritikalität eingeführt, den wir als Rahmen für die Klassifizierung lückenloser Phasen vorschlagen. Die Kernaussage ist, dass bei Vorhandensein von Symmetrien eine Universalitätsklasse in verschiedene Phasen unterteilt werden kann, die durch die Symmetriewirkung auf die Niedrigenergie-Skalierungsoperatoren gekennzeichnet sind. Dies schließt lückenlose topologische Phasen ein; Wir demonstrieren ihre Stabilität und interpretieren zuvor untersuchte Beispiele neu.

Teil II untersucht die Anregungen über den Grundzuständen zweidimensionaler Quantenspinmodelle. Das Hauptziel unserer Studie ist der dynamische Spinstrukturfaktor; Diese Art der Spektralfunktion wird im ersten Teil von Kapitel 5 besprochen. Im zweiten

Teil dieses Kapitels wird ein neuartiger Algorithmus vorgestellt, der auf Matrix-Produkt-Zuständen basiert, um die Spektralfunktion effizient zu berechnen. Dadurch wird ein neues Fenster zur Dynamik zweidimensionaler Quantensysteme geöffnet. Wir vergleichen diese numerische Methode in Kapitel 6 mit dem exakt lösbaren Kitaev-Modell—einem paradigmatischen topologischen Modell, das ein Quanten Spin Liquid darstellt. Indem wir nichtintegrierbare Heisenberg-Störungen hinzufügen, identifizieren wir die erste eindeutige theoretische Realisierung eines Proximate Spin Liquid: Der Grundzustand wird konventionell geordnet, die hochenergetischen spektralen Eigenschaften sind jedoch strukturell denen des nahen Kitaev Spin Liquid ähnlich. Letzteres stimmt mit Aspekten kürzlich durchgeführter inelastischer Neutronenstreuungsexperimente an α-$RuCl_3$ überein. In Kapitel 7 wenden wir uns einem der ältesten Modelle der Vielkörperquantenphysik zu: dem Spin-Heisenberg-Antiferromagneten auf dem Quadratgitter. Trotz seiner langen Geschichte gibt es immer noch Uneinigkeit über die physikalische Herkunft von hochenergetischen Spektralmerkmalen, die die Spinwellentheorie niedriger Ordnung nicht erklären kann. Wir liefern ein einfaches Bild für diese stark wechselwirkende Magnonen, indem wir sie mit einem einfachen Ising-Modell verbinden. Schließlich wird in Kapitel 8 die Stabilität von Quasiteilchen erörtert—kollektive Erregungen, die sich wie eine einzelne emergente Einheit verhalten, wofür Magnonen ein Paradebeispiel sind. Es ist oft bekannt, dass diese bei den niedrigsten Energien stabil sind, und es wird angenommen, dass sie zerfallen, wenn dies durch Energie- und Impulserhaltung möglich ist. Wir zeigen jedoch, dass starke Wechselwirkungen dies verhindern können. Wir bestätigen numerisch dieses Prinzip des vermiedenen Zerfalls im (leicht gestörten) Heisenberg-Antiferromagneten auf dem Dreiecksgitter. Darüber hinaus identifizieren wir Hinweise auf derart vermiedene Zerfallsprozesse in vorhandenen experimentellen Daten über $Ba_3CoSb_2O_9$ und superfluides Helium.

Somit erweitern wir mit dieser Arbeit das Verständnis der Quantenphasen und ihrer Anregungen. Nachdem wir die grundlegenden Prinzipien lückenloser topologischer Phasen in einer Dimension identifiziert haben, bieten es sich an, analoge Phänomene in höheren Dimensionen zu untersuchen. In Bezug auf die robusten Eigenschaften der Anregungen, die in dieser Arbeit identifiziert wurden, hoffen wir, dass diese zu einer Theorie der Quasiteilchen-Eigenschaften erweitert werden können, die auch jenseits vom universellen Niedrigenergie-Regime gültig ist.

opgedragen aan mijn ouders

Contents

1. Introduction

Phases of quantum matter are a fascinating instance of *emergence*—novel collective phenomena arising from the interplay of many smaller constituents. In his seminal piece on how "*more is different*" [1], Anderson illustrated the challenge posed by such quantum phases, noting the 30 years it took to explain superconductivity after all the fundamental laws and experiments were in. It is time well spent, however, since such emergent principles are arguably as fundamental as the Standard Model of particle physics; superconductivity even plays an important role for the latter via the Anderson-Higgs mechanism [2, 3].

Phases of *quantum* matter occur at low or vanishing temperatures. However, this is a relative statement: e.g., for superfluid He-4, the temperature needs to be below that of interstellar space[1], but for a metal, one must simply stay below its melting point[2]. As noted by Nozières and Pines, "*strangely enough, despite the often quite sizable particle interaction and despite the fact that one is dealing with a quantum mechanical many-particle system, quantum liquids at sufficiently low temperatures are better understood than their classical counterparts*" [7]. This is due to another remarkable instance of emergence: because of the wave-particle duality, perturbations in quantum phases often have a corpuscular nature, referred to as *quasiparticles* or *collective excitations*[3]. At low temperatures, a strongly-interacting quantum system can then be described as a gas of quasiparticles.

This thesis sheds new light on both of these aspects—quantum phases of matter and their quasiparticles.

Phases: interplay of symmetry, topology and quantum criticality

Two cornerstones in the characterization of quantum phases of matter are *symmetry* and *topology*[4] [9]. The spontaneous breaking of a symmetry is a standard example, well-known from everyday life. Topological phases of matter are more subtle, characterized by an absence of *local* features—probing their nontriviality requires a more holistic approach[5]. In particular, the order parameter often involves integrating over a whole space, and breaking the continuity of said space can lead to physical consequences, such as localized degeneracies or conducting modes near boundaries of a sample [9–11].

In certain phases of matter, symmetry and topology are inextricably linked. For this, it is instructive to consider quantum systems in one spatial dimension. On the one hand, there are a multitude of emergent quantum phenomena in one dimension—serving as a point of reference for higher-dimensional analogues—whereas on the other hand, a great many *non-perturbative* numerical [12, 13] and analytic [14] techniques are available for their study—which are often absent in higher dimensions. Thanks to such powerful methods, it is now known that in order to have any non-trivial gapped[6] phase of matter in one

[1] At higher pressures, superfluidity is claimed to occur at a toasty billion Kelvin inside neutron stars [4, 5].

[2] The Fermi temperature associated to the electron liquid in metals is typically above the melting point of the underlying atomic lattice [6].

[3] We will use these terms interchangeably, even though some literature uses quasiparticles for dressed versions of microscopic particles, whereas collective excitations represent a macroscopic motion. Note that the example of magnons shows that this distinction is not particulary well-defined.

[4] This list arguably contains Fermi liquid theory, which has been given a topological interpretation [8].

[5] As a more mundane example of what counts as topological: the *hole* in a keyhole is a topological property—it cannot be attributed to any *part* of the lockset.

[6] Being "gapped" means that the many-body energy spectrum has a gap above the (finite-dimensional)

dimension, the Hamiltonian *must* have symmetries [16–19]. If the ground state does not spontaneously break these symmetries, it forms a *symmetry-protected topological* (SPT) phase (barring a few exceptions [20]). SPT phases have topological invariants which are only well-defined in the presence of their protecting symmetries, protecting emergent edge phenomena. A Nobel prize winning [21] example is the Haldane phase realized in the spin-1 Heisenberg chain, $H = \sum_n \boldsymbol{S}_n \cdot \boldsymbol{S}_{n+1}$. This is topologically non-trivial as long as, for example, spin rotation or time-reversal symmetry are preserved [22–24]—with emergent zero-energy spin-1/2 degrees of freedom at its edges [25, 26]. All possible SPT phases for a given symmetry group have been classified in one dimension [16–19] and a variety of solvable models are known to realize such phases [25, 27–32]. However, something is left to be desired in our understanding of any possible interrelationships between such concrete models.

The first goal of Part I of this thesis is to present a unified picture of one-dimensional SPT phases. In particular, we uncover equivalences between the aforementioned models. This allows to import the understanding of one model to another[7], leading, for example, to hitherto-unnoticed topological properties of previously-studied models. This hands-on, example-based review showcases various subtleties of SPT phases which are commonly swept under the rug. For instance, we elucidate how non-local transformations like the Jordan-Wigner transformation [34] change the physics of a phase of matter, and we resolve certain tensions that had previously been raised about the stability of spin SPT phases away from the Mott limit [35, 36].

Gapped phases of matter are thus well-understood in one dimension. This cannot be said for the critical points separating them. Quantum criticality is yet another rich example of emergence: an effective scale invariance develops, which in one dimension is often enhanced to an *infinite-dimensional* symmetry group, such that at low energies it is described by a *conformal field theory* (CFT) [14, 37]. Although phase transitions occur *between* gapped phases, this does not mean that they are of *secondary* importance. Firstly, such quantum critical points tend to dominate a wide region of the finite-temperature phase diagram (the "critical fan") [38–40]. Secondly, critical points can often be stabilized into extended gapless phases by enforcing additional symmetries[8]—for this reason we sometimes use "critical point" and "gapless phase" interchangeably in this thesis.

The second goal of Part I of this thesis is to explore the interplay between *quantum criticality*, *topology* and *symmetry*. A motivating question is whether critical points can be topologically non-trivial, with non-local bulk invariants and localized topological edge modes. More generally, we ask whether a given universality class (such as a CFT) subdivides into distinct phases when additional symmetries are enforced. In the special case of an empty universality class, we recover the question of classifying gapped phases in the presence of symmetries. The question we pose is thus a natural generalization to the gapless case. Remarkably, although concrete examples of such topologically non-trivial critical points have been constructed in the past decade [41–58], no general framework—similar to the gapped case—has been developed. We do this, leading us to the novel notion of *symmetry-enriched quantum criticality*. We define bulk topological invariants for critical systems and we show how these can protect localized edge modes. For example, for the case of the Ising universality class, we classify the distinct symmetry-enriched classes for any symmetry group, in certain cases leading to edge modes which are algebraically localized $\sim 1/L^{14}$. Interestingly, the classification is related to the gapped case: non-trivial critical

space of ground states which moreover remains *nonzero* in the thermodynamic limit. This desirable property bestows correlation functions with a length scale and hence a strict notion of locality [15].

[7] On a less positive note, we may quote McGreevy: "*we thought we could solve* two *systems [...] but since they are really the same system in disguise, it turns out we can only solve one!*" [33]

[8] From a renormalization group (RG) perspective, the symmetries are chosen such that all RG-relevant perturbations can be excluded by symmetry considerations.

points tend to occur when all neighboring gapped phases are themselves non-trivial—the intuition being that some of their non-triviality persists to the critical point.

For clarity, we note that this is different from when the *gaplessness itself* is protected by the interplay of symmetry and topology. Two noteworthy instances of this, are the case of anomalous symmetries [59–63], and topological (e.g., Weyl [64]) semi-metals [65].

Excitations and quasiparticles

Part I of this thesis primarily concerns ground state properties[9], but a lot of interesting information is stored in the excitations above it. Knowledge of the quasiparticles gives information about transport, the effects of heating or quenching, and even the nearby phases obtained by condensing said quasiparticles. Moreover, excitations can be probed through scattering experiments—measuring the so-called dynamic structure factor—and thus form a bridge between theory and experiment [66, 67]. Despite their importance, even the very *existence* of quasiparticles is not a given in strongly-correlated systems, except at the lowest energies, where universal arguments can apply. Goldstone's theorem [68–71] is a famous example: a broken continuous symmetry implies gapless quasiparticles—the first known quasiparticle, the phonon [72, 73], is an example of this.

In Part II of this thesis, we study quasiparticles away from the universal low-energy regime[10]. Rather than finding an unstructured mess, we show that there are still remarkably *general* and *robust* features. More concretely, we discuss: (1) quasiparticle *stability* against decay, (2) certain seemingly-complicated strong quasiparticle interactions having a *simple physical origin*, and (3) the persistence of certain spectral properties across a ground state phase transition, encapsulated in the notion of a *proximate spin liquid*. Each of these features is showcased in a nearest-neighbor quantum magnet on the triangular, square and honeycomb lattice, respectively. We briefly comment on each:

1. The most general of these results is the surprising *stability* of quasiparticles. It was commonly expected that they would decay whenever allowed by conservation laws [74–76]. On the contrary, we find that if interactions are strong enough, this is avoided—which we explain by generalizing the well-known notion of level repulsion. In addition to numerically verifying this in the paradigmatic spin-1/2 Heisenberg antiferromagnet on the triangular lattice, we identify this mechanism in existing experimental data on $Ba_3CoSb_2O_9$ [77] and even superfluid He-4 [78–83]. The roton—one of the first instances a quasiparticle [84]—still has surprises in store.

2. Unlike for the *triangular* lattice, spin wave theory (SWT) does not predict magnon decay for the Heisenberg antiferromagnet on the *square* lattice. Nevertheless, previous studies on this lattice indicate that to various orders in $1/S$, SWT fails to capture the high-energy magnons [85–94]. We confirm that this is due to strong magnon interactions and elucidate this by connecting these features to an Ising limit—revealing that the interaction is based on a simple counting of Ising domain walls.

3. Despite the quantitative mismach, SWT still *qualitatively* describes magnons for the above square lattice model. This is a priori not a given; we show that this indeed breaks down for magnets which are sufficiently close to a topological (spin liquid) phase. We identify this in the Heisenberg model on the honeycomb lattice with strong Kitaev couplings [95]. Similar to measurements on α-$RuCl_3$ [96, 97], we observe high-energy features in the dynamic structure factor resembling those of the Kitaev spin liquid [98]. This establishes the notion of a *proximate spin liquid*.

[9] Quantum criticality also concerns states above the ground state, but due to the emergent Lorentz symmetry, most universal properties are already encoded in the ground state correlation functions.

[10] More precisely, we study excitations at finite energies, but we do not consider the effects of temperature.

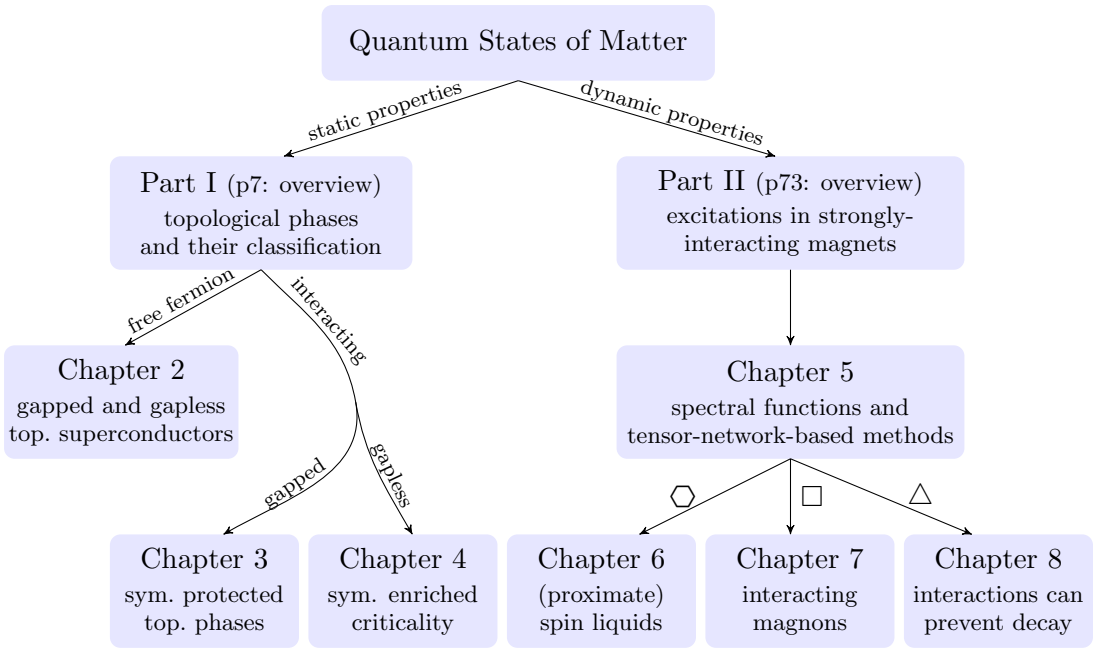

Figure 1.1.: **A thematic guide to this thesis.** The abbreviations symm. and top. stand for symmetry and topological, respectively. The symbols on the arrows to Chapters 6, 7 and 8 denote that these chapters focus on models on the honeycomb, square and triangular lattices, respectively.

These type of discoveries are made possible by a recent revolution in our understanding of *quantum entanglement*—arguably the most non-classical of all quantum phenomena [99]. It had been argued that the wavefunction of a many-body system is unphysical or even ill-defined due to the exponential blow-up necessary to encode all its entanglement [100, 101]. However, it has recently been discovered that the entanglement of ground states of local Hamiltonians has a particular structure [102]. This led to the development of *tensor network states* [25, 103–105]—a powerful analytic *and* numerical tool. Using these developments—in particular the density matrix renormalization group (DMRG) [12, 106, 107] and related time-evolution methods [13, 108]—we introduce a method to numerically calculate dynamic structure factors of strongly-interacting quantum systems in two dimensions, allowing us to identify the above features.

A bird's-eye view of this thesis

The chapters of this thesis—and their interconnection—are shown in Fig. 1.1. These naturally split up into two parts, which have overviews on pages 7 and 73, respectively.

Part I concerns symmetry-protected topological phases in one dimension. Chapter 2 discusses this in the simplest possible setting, i.e., the non-interacting case; we first review the known gapped case before extending this to critical systems. Chapter 3 reviews the gapped interacting case, elucidating connections between models. The notion of *symmetry-enriched quantum criticality* in Chapter 4 generalizes this to the interacting gapless case.

Part II studies quasiparticles in two-dimensional magnets. To this end, in Chapter 5, we first review the notion of the dynamic structure factor and introduce a tensor-network-based algorithm to numerically compute this for two-dimensional lattice models. We benchmark and use this in Chapter 6 to study the Kitaev-Heisenberg model, therein observing a proximate spin liquid. In Chapter 7, we demystify the strongly-interacting magnons of the square lattice Heisenberg model with an interpolation to the Ising model. Lastly, Chapter 8 explains how strong interactions can prevent quasiparticle decay.

Part I.

Gapped and gapless topological phases in one dimension

Overview of Part I

As mentioned in the introduction, Part I of this thesis focuses on the interplay between symmetry, topology and quantum criticality in one-dimensional quantum phases of matter.

Chapter 2: Non-interacting fermions: gapped and gapless topological phases

Chapter 2 explores this interplay in the simplest possible setting, namely non-interacting fermions. In that case, gapped phases of matter have been classified in all dimensions [109–111]. These are called topological insulators or topological superconductors [10] (depending on whether or not particle number is conserved), which are the non-interacting analogues of the symmetry-protected topological (SPT) phases mentioned in the introduction. In the first part of Chapter 2, we review this gapped classification for a particular symmetry class in one dimension (called the BDI class). This naturally leads us to introduce a (generalized) Kitaev chain with coupling of range $\alpha \in \mathbb{Z}$, which we refer to as the α-chain—this will be a key player in Chapter 3. As a new contribution to our understanding of the topological phases in the BDI class, we point out that the Hamiltonians can be naturally encoded into certain polynomials $f(z)$ on the complex plane; in Section 2.3, we show that many physical properties of interest—topological invariants, edge modes, correlation lengths, et cetera—are directly obtained by finding the roots of $f(z)$.

Curiously, much less is known about *gapless* non-interacting models. There has been a classification of topological semi-metals [65], but this studies what type of gaplessness one can have (e.g., Dirac points, Fermi surfaces, et cetera) and which symmetries and topological invariants can protect this gaplessness. What has *not* been studied is how many distinct phases one can have with a *given* universality class, e.g., how many distinct phases[11] of one-dimensional non-interacting lattice models there are which are described by a gapless Dirac fermion. In the last part of Chapter 2, we answer this for the illustrative case of the BDI class. For this, we use the above $f(z)$ to define a topological invariant ω *at criticality*. Rather than just being a way of labeling phases, we prove that ω counts *exponentially localized* zero-energy Majorana edge modes, despite the bulk having only gapless degrees of freedom. We show that this labeling is complete: the gapless phases are classified by ω and the (half-integer) central charge c of the low-energy conformal field theory (CFT), giving a $\mathbb{Z} \times \left(\frac{1}{2}\mathbb{N}\right)$ labeling. In addition, we prove that the central charge at the critical point between two gapped phases satisfies a topological lower bound.

Chapter 3: Interacting gapped symmetry-protected topological (SPT) phases

Upon including interactions, there are two types of gapped phases of matter in one dimension: symmetry-breaking and symmetry-protected topological (SPT) phases. Chapter 3 considers these two phases, with a focus on the latter. After briefly reviewing the known classification for fermionic and bosonic chains [16–19] using an example-based approach, we present a unified perspective on SPT phases in one dimension. In particular, we use symmetry as a guide to map various well-known fermionic and spin SPT models to the (generalized) Kitaev chain introduced in Chapter 2, i.e., the α-chain. This unified picture uncovers new properties of old models—such as how the cluster state [31] is the fixed

[11] We can define two critical systems to be in distinct phases if there is no local path of Hamiltonians connecting them that preserves the low-energy universality class.

point limit of the Affleck-Kennedy-Lieb-Tasaki state [25] in disguise—and elucidates the connection between fermionic and bosonic phases—with the Hubbard chain interpolating between four Kitaev chains and a spin chain in the Haldane phase.

Chapter 4: Interacting gapless topological phases: symmetry-enriched criticality

In the last chapter of Part I, we show that interacting critical chains can also be topologically non-trivial. This can be seen as the interacting analogue of Section 2.4, but Chapter 4 (with the exception of Section 4.5) is self-contained and can thus be read independently of the previous chapters. We focus on critical bosonic and fermionic chains which are described by an emergent conformal field theory (CFT) at low energies. We show that the symmetry properties of operators in this low-energy CFT provide discrete invariants, establishing the notion of *symmetry-enriched quantum criticality*. If the operators with non-trivial symmetry properties are moreover *nonlocal* (i.e., string operators), then their charge can function as a *topological invariant*. Using a boundary renormalization group analysis, we show that such a topological invariant implies the presence of localized edge modes. Depending on the symmetry, the finite-size splitting of this topological degeneracy can be exponential or algebraic in system size. An example of the former is given by the spin-1 Heisenberg chain with an easy-axis anisotropy. An example of the latter arises between the gapped Ising and cluster phases: this symmetry-enriched Ising CFT has an edge mode with finite-size splitting $\sim 1/L^{14}$.

This novel concept of *symmetry-enriched quantum criticality* unifies various examples of topologically non-trivial critical chains previously studied in the literature [41–48, 50–52, 54–58]. We explicitly show this for a selection of works, which we reinterpret in terms of symmetry-enrichment. Similar to the gapped SPT phases encountered in Chapter 3, a given CFT can split into several distinct symmetry-enriched CFTs. This raises the question of classification, to which we give a partial answer—including a complete characterization of symmetry-enriched Ising CFTs. To illustrate this with a concrete example: similar to the known result that there are *six* distinct gapped one-dimensional phases of matter with $\mathbb{Z}_2 \times \mathbb{Z}_2$ symmetry (see subsection 4.4.1), we derive that there are *nine*[12] distinct $\mathbb{Z}_2 \times \mathbb{Z}_2$-enriched critical Ising chains (see subsection 4.4.2).

[12] More precisely, these are for critical points which only require tuning one parameter (in the presence of $\mathbb{Z}_2 \times \mathbb{Z}_2$ symmetry). If we allow for higher fine-tuning, there are $9 + 6 = 15$ distinct $\mathbb{Z}_2 \times \mathbb{Z}_2$-enriched Ising CFTs (see subsection 4.4.2).

2. Non-interacting fermions: gapped and gapless topological phases

Gapped topological phases of matter occurring in systems of non-interacting fermions, i.e., topological insulators and topological superconductors, are well-understood and were classified over a decade ago[1] [109–111, 114, 115]. In one dimension, such phases are characterized by topological winding numbers, which can be related to exponentially-localized zero-energy edge modes with open boundaries. This chapter is devoted to showing that the same concepts—topological winding numbers and localized edge modes—can apply to critical systems.

Rather than working in complete generality, it is instructive to consider a particular symmetry class. One class that illustrates the essential idea of topological insulators and superconductors is that of spinless fermions with time-reversal symmetry, called the BDI class[2] [110]. This contains the well-known Kitaev chain [30] as a special case, as well as longer-range generalizations [116]; these gapped phases are distinguished by an integer winding number and display exponentially-localized Majorana edge modes [11, 110]. Although this class is well-studied, we introduce a novel and particularly useful parametrization, revealing that each Hamiltonian is equivalent to specifying a complex polynomial $f(z)$. As already mentioned in the overview, a lot of physical information is readily obtainable from knowing the roots of $f(z)$, without having to go through standard-but-tedious free-fermion calculations. Hence, even if one is *not* interested in topological critical phases, the formulation of $f(z)$ can be very useful, both for qualitative as well as quantitative purposes.

The key to generalizing the topological winding number to the critical case is that $f(z)$ allows us to re-express it as a *counting* problem[3]. It is commonly said that the formula for the winding number breaks down when then system is critical; this is true, but the latter counting problem remains well-defined! We thus have a topological invariant for gapless systems, which we illustrate for simple models occurring as phase transitions between topologically-distinct gapped phases. In addition to discussing such concrete examples, we prove three general theorems: Theorem 1 shows that this topological invariant implies *exponentially-localized* Majorana edge modes; Theorem 2 shows that this invariant provides a complete classification; and Theorem 3 shows how the central charge of a critical point satisfies a topological lower bound.

This chapter is structured as follows. In Section 2.1, we review the BDI class in one dimension; along the way, we introduce the α-chain, which is a generalized Kitaev chain. We recap its well-known topological invariant in Section 2.2. In Section 2.3, we introduce the new perspective that a BDI Hamiltonian is equivalent to a polynomial $f(z)$ and show how a multitude of physical quantities are encoded in its roots. Using this novel formulation, we discuss topologically non-trivial critical phases in Section 2.4; in addition to discussing illustrative examples and general theorems, we numerically show the stability against disorder and interactions. (The interacting critical case is studied in much more detail in Chapter 4; in particular, see Section 4.5.)

[1] At least for internal symmetries; the extension to spatial symmetries followed [112, 113].

[2] The AIII class—containing the Su-Schrieffer-Heeger model [28]—can be embedded into it; see Chapter 3.

[3] Interestingly, a similar observation had been made before [116–119], but it was not used to define a topological invariant at criticality.

2.1. The BDI Hamiltonian: time-reversal-symmetric spinless fermions

The most general quadratic superconducting Hamiltonian for spinless fermions in one dimension is of the form

$$H = -\sum_{m,n=1}^{L} \left(\tilde{t}_{m,n} c_m^\dagger c_n + \frac{\Delta_{m,n}}{2} c_m^\dagger c_n^\dagger + \frac{\Delta_{n,m}^*}{2} c_m c_n \right). \tag{2.1}$$

Note that $\tilde{t}_{m,n}^* = \tilde{t}_{n,m}$ (due to Hermiticity) and we can take $\Delta_{m,n} = -\Delta_{n,m}$ (due to anti-commutativity of fermions). In the rest of this chapter, we enforce time-reversal symmetry T, defined as complex conjugation in the on-site basis: $T c_n^{(\dagger)} T^{-1} = c_n^{(\dagger)}$. This requires $t_{n,m}$ and $\Delta_{n,m}$ to be real. The resulting set of models is sometimes called the *BDI class*. As we will discuss in Section 2.2, this class is known to have infinitely many topologically-distinct gapped phases, labeled by the integers $\mathbb{Z}$ [109–111].

2.1.1. An interlude: connection to the Tenfold Way

In this thesis, we always work with *many-body* Hamiltonians, as in Eq. (2.1). However, in the literature on topological phases of free-fermion Hamiltonians, it is customary to consider the *single-particle* Hamiltonian and its symmetries [109–111, 114, 115, 120]. To allow for an easy comparison to that literature, we briefly comment on that perspective. The single-particle Hamiltonian $\mathcal{H}$ is defined by writing $H = \frac{1}{2}\boldsymbol{c}^\dagger \mathcal{H} \boldsymbol{c}$ where $\boldsymbol{c}^\dagger \equiv (c_1^\dagger, c_2^\dagger, \cdots c_N^\dagger, c_1, \cdots, c_N)$, following the Bogoliubov-de Gennes formalism [121]. For Eq. (2.1), we thus obtain $\mathcal{H} = \begin{pmatrix} \tilde{t} & \Delta \\ -\Delta^* & -\tilde{t}^* \end{pmatrix}$, where $\tilde{t}$ and Δ are the $L \times L$ matrices with components $\tilde{t}_{m,n}$ and $\Delta_{m,n}$.

The Tenfold Way [109–111, 114] is a topological classification of such single-particle Hamiltonians, taking into account three types of symmetries: an anti-unitary symmetry $\mathcal{T}$ that commutes with $\mathcal{H}$ ('time-reversal symmetry'), an anti-unitary symmetry $\mathcal{C}$ that anti-commutes with $\mathcal{H}$ ('particle-hole symmetry'), and a unitary symmetry that anti-commutes with $\mathcal{H}$ ('chiral or sublattice symmetry'). The BDI class[4] is then defined as the class that has *all three* symmetries, moreover satisfying $\mathcal{T}^2 = \mathcal{C}^2 = \mathcal{S}^2 = +1$. Indeed, if we define $\mathcal{T}$ as complex conjugation, then the time-reversal symmetry of the many-body Hamiltonian (2.1) implies that $\mathcal{T}\mathcal{H}\mathcal{T}^{-1} = \mathcal{H}$. This is the only *physical* symmetry of Eq. (2.1). Due to the Bogoliubov-de Gennes Hamiltonian *artificially* doubling the Hilbert space dimension (by including both *particle* and *hole* bands), we can define the particle-hole symmetry $\mathcal{C} = (\sigma^x \otimes \mathbb{I}_L)\mathcal{T}$, for which $\mathcal{C}\mathcal{H}\mathcal{C}^{-1} = -\mathcal{H}$. Lastly, the chiral symmetry is then $\mathcal{S} = \mathcal{C}\mathcal{T}$.

2.1.2. Majoranas and α-chains: the generalized Kitaev chain

We now return to the many-body Hamiltonian in Eq. (2.1). We introduce two simplifications. The first is notational: in superconducting systems with T symmetry, it is convenient to use the Majorana representation defined by $\gamma_n = c_n^\dagger + c_n$ and $\tilde{\gamma}_n = i(c_n^\dagger - c_n)$. These operators are Hermitian and satisfy the Majorana algebra: $\{\gamma_n, \gamma_m\} = 2\delta_{n,m}$, $\{\tilde{\gamma}_n, \tilde{\gamma}_m\} = 2\delta_{n,m}$ and $\{\gamma_n, \tilde{\gamma}_m\} = 0$. The second simplification is to assume translation invariance: $\tilde{t}_{m,n} = \tilde{t}_{n-m}$ and $\Delta_{m,n} = \Delta_{n-m}$. This is not necessary for what follows, but it drastically simplifies the treatment. Later, we comment on the more general case (with a unit cell or even disorder). To get rid of the redundancies in $\tilde{t}_\alpha$ and Δ_α (i.e.,

[4] There are ten classes. Nine are characterized by $\mathcal{T}^2 = -1, 0, 1$ and $\mathcal{C}^2 = -1, 0, 1$. If $\mathcal{T}$ and $\mathcal{C}$ are both absent (i.e., $\mathcal{T}^2 = \mathcal{C}^2 = 0$), one has to specify whether $\mathcal{S}$ is absent or not, i.e., $\mathcal{S}^2 = 0, 1$.

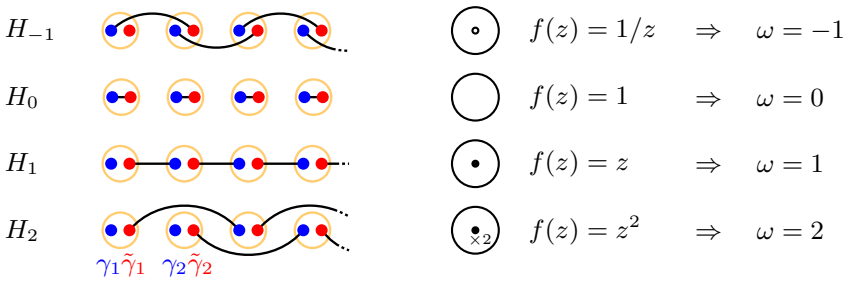

Figure 2.1.: **Generalized Kitaev chains in the BDI class.** The α-chains H_α ($\alpha \in \mathbb{Z}$) are a complete basis for translation-invariant Hamiltonians in the BDI class. We pictorially represent H_α for certain values of α, showcasing the edge modes near their left boundary. (Each fermionic site is decomposed into Majorana modes: γ (blue) and $\tilde{\gamma}$ (red), a bond signifies a term in the Hamiltonian.) Note that $\alpha = 1$ is the Kitaev chain [30]; $\alpha = -1$ is the spatially-inverted Kitaev chain; $\alpha = 2$ is a stack of two Kitaev chains. We also show the zeros (filled dots) and poles (hollow dots) of their associated polynomials $f(z)$ (the solid line indicates the unit circle), and the corresponding winding number $\omega = N_z - N_p$; see subsection 2.3.

$\tilde{t}_{-\alpha} = \tilde{t}_\alpha$ and $\Delta_{-\alpha} = -\Delta_\alpha$), we can parametrize the model with $t_\alpha \equiv \tilde{t}_\alpha + \Delta_\alpha$. Altogether, Eq. (2.1) becomes:

$$H = -\frac{1}{2}\sum_{n,\alpha} t_\alpha \left(c_n^\dagger c_{n+\alpha} + c_n^\dagger c_{n+\alpha}^\dagger + h.c.\right) = \frac{i}{2}\sum_{n,\alpha} t_\alpha \tilde{\gamma}_n \gamma_{n+\alpha} \qquad (t_\alpha \in \mathbb{R}). \tag{2.2}$$

This is the most general translation-invariant Hamiltonian in the BDI class. To understand why terms of the type $i\gamma_n\gamma_{n+\alpha}$ and $i\tilde{\gamma}_n\tilde{\gamma}_{n+\alpha}$ (where the factor i is necessary for Hermiticity) cannot appear, note that $T\gamma_n T^{-1} = \gamma_n$ and $T\tilde{\gamma}_n T^{-1} = -\tilde{\gamma}_n$.

The above Hamiltonian, which is determined by a single list of numbers $\{t_\alpha\}_{\alpha\in\mathbb{Z}}$, is a sum of Hamiltonians: $H = \sum_\alpha t_\alpha H_\alpha$, where we define $H_\alpha = \frac{i}{2}\sum_n \tilde{\gamma}_n\gamma_{n+\alpha}$. Hence, the list of Hamiltonians $\{H_\alpha\}_{\alpha\in\mathbb{Z}}$ is a *complete basis* for translation-invariant BDI models. For a fixed value of α, we sometimes refer to H_α as the α-chain [122]. These α-chains are *frustration-free*. In fact, H_α is a sum of commuting terms, each squaring to $\left(\frac{i}{2}\tilde{\gamma}_n\gamma_{n+\alpha}\right)^2 = \frac{1}{4}$ (Hamiltonians with these properties are called *stablizer codes* [123]).

The special case $\alpha = 1$ is the celebrated Kitaev chain [30]: as shown in Fig. 2.1, each Majorana in the bulk is part of exactly *one* bond in H_1, but at the left edge, γ_1 is free. More precisely, with open boundaries, $[\gamma_1, H] = 0$ on the left end and $[\tilde{\gamma}_L, H] = 0$ on the right end. We thus have two anti-commuting symmetries, γ_1 and $\tilde{\gamma}_L$, giving us a twofold ground state degeneracy, labeled by the nonlocal boundary occupation $i\gamma_1\tilde{\gamma}_L = \pm 1$. These are the famous (zero-energy) Majorana edge modes, whose stability we will soon discuss. Similarly, H_2 has *two* Majorana edge modes per edge. More generally, we see that H_α has $|\alpha|$ edge modes per edge, with the sign of α determining whether the left edge has *real* or *imaginary* Majorana modes (e.g., H_1 has γ_1, whereas H_{-1} has $\tilde{\gamma}_1$, as shown in Fig. 2.1).

2.1.3. Diagonalization

For periodic boundary conditions, the Hamiltonian in Eq. (2.2) can be diagonalized by Fourier transforming and subsequently rotating particles and holes into one another over a so-called *Bogoliubov angle*. A quantity that naturally appears upon Fourier transforming the Hamiltonian is $f_k \equiv \sum_\alpha t_\alpha e^{ik\alpha}$. Its *complex phase* $f_k/|f_k|$ gives us the momentum-dependent Bogoliubov angle, and its *modulus* $|f_k|$ gives us the spectrum. More precisely,

write $f_k = \varepsilon_k e^{i\varphi_k}$ (with ε_k and φ_k real-valued) and define

$$d_k \equiv \cos(\varphi_k/2)c_k + i\sin(\varphi_k/2)c_{-k}^\dagger = \frac{1}{2\sqrt{L}}\sum_n e^{-ikn}\left(e^{i\varphi_k/2}\gamma_n + ie^{-i\varphi_k/2}\tilde{\gamma}_n\right), \tag{2.3}$$

which satisfies $\{d_k, d_q^\dagger\} = \delta_{k,q}$ and $\{d_k, d_q\} = 0$. One can show that $H = -\sum_k \varepsilon_k d_k^\dagger d_k$ up to a constant (see Appendix A.1 for details). If we chose ε_k to be positive, then the ground state is characterized by $\langle d_k^\dagger d_k\rangle = 1$.

2.2. Gapped topological superconductors: the winding number

We saw that the single-particle spectrum of the Hamiltonian H in Eq. (2.2) is given by the amplitude of $f_k = \sum_\alpha t_\alpha e^{ik\alpha}$. Hence, if the system is gapped, then $f_k/|f_k| = e^{i\varphi_k}$ is well-defined. In one dimension, momentum lives on a circle S^1, such that we can interpret this as a function $e^{i\varphi_k} : S^1 \to U(1) \cong S^1$. Moreover, if H is local, then this function is continuous[5]. Continuous functions from the circle to itself come with a *topological invariant*, which counts the number of times it winds around the circle. This winding cannot change *as long as* the system is gapped (i.e., $|f_k| \neq 0$ for all k) and local (i.e., f_k, is continuous). This topological winding number can be expressed as $\omega = \frac{1}{2\pi i}\int \frac{f_k'}{f_k}\mathrm{d}k = \frac{1}{2\pi}\int \mathrm{d}\varphi_k \in \mathbb{Z}$. It labels the $\mathbb{Z}$ classification for the one-dimensional BDI class in the Tenfold Way [109–111].

In the special case of an α-chain, $H = H_\alpha$, we have $f_k = e^{ik\alpha}$. The α-chain thus has a topological winding number $\omega = \alpha$ (and its spectrum is completely flat, $\varepsilon_k = 1$). This exactly corresponds to the number of edge modes. This is of course no coincidence and is an instance of a *bulk-boundary correspondence*: a topological bulk quantity (in this case, ω) is related to a topological edge phenomena (in this case, Majorana zero modes). There are various ways of arguing this correspondence (see Ref. [117] for one of the earliest works treating the BDI case, using a transfer matrix approach; more recently, see Ref. [116]). We will take a different but related route, pointing out that ω and the edge modes are simply two ways of counting zeros of a given polynomial.

2.3. The BDI Hamiltonian is equivalent to a polynomial $f(z)$

From now on, we start to deviate from the established literature. We point out how every BDI Hamiltonian is equivalent to a particular polynomial. This will directly give us many physical properties of interest *and* it will be the key to have topological invariants and edge modes at criticality in Section 2.4. At the end of this subsection, we will comment on the relationship with previous works (employing a transfer-matrix approach) [116, 117].

We already saw that the Hamiltonian in Eq. (2.2) is completely determined by $f_k = \sum_\alpha t_\alpha e^{ik\alpha}$. Let us now interpret this as a complex function evaluated on the unit circle, $z = e^{ik}$. This motivates us to associate a complex function $f(z)$ (essentially a Laurent series around the origin) to every translation-invariant Hamiltonian in the BDI class:

$$\boxed{H = \sum_{\alpha\in\mathbb{Z}} t_\alpha H_\alpha \qquad \Rightarrow \qquad f(z) = \sum_{\alpha\in\mathbb{Z}} t_\alpha z^\alpha}\,. \tag{2.4}$$

Note that $f_k = f(e^{ik})$, i.e., the single-particle spectrum and Bogoliubov angle are determined by the function on the unit circle. However, it is much more powerful to work with

[5] One only needs the weak condition $\sum_\alpha |t_\alpha| < \infty$ (this is guaranteed if $t_\alpha = O\left(1/|\alpha|^\beta\right)$ for some $\beta > 1$). Then its Fourier transform f_k is continuous, and by extension, is $f_k/|f_k|$ as well. See also Refs. [124, 125].

$f(z)$ instead of f_k. Firstly, note that if the Hamiltonian has finite range, then $f(z)$ is a polynomial *after* we separate out the possible pole at the origin, $f(z) = \frac{1}{z^{N_p}} f_{\text{poly}}(z)$. We can now invoke the fundamental theorem of algebra to conclude that $f_{\text{poly}}(z)$ is completely determined by its set of zeros $\{z_i\}_i$ (up to a global prefactor), i.e.,

$$\boxed{f(z) = \frac{a}{z^{N_p}} \prod_i (z - z_i)}. \tag{2.5}$$

Since $t_\alpha \in \mathbb{R}$, we have that $f(z)^* = f(z^*)$, or, equivalently, that a is real and that the zeros are either real or come in complex-conjugate pairs. Conversely, any set of zeros satisfying these properties defines a unique model according to Eq. (2.4) (up to a global prefactor). For the particular case of the α-chains, we have that $f(z) = z^\alpha$, as shown in Fig. 2.1.

2.3.1. Physical properties are encoded in the zeros of $f(z)$

Knowing the zeros of $f(z)$ makes a lot of physical information readily apparent:

1. **The topological invariant.** In Section 2.2, we saw that if the system is gapped, then we have a topological invariant $\omega = \frac{1}{2\pi i} \int \frac{f_k'}{f_k} \mathrm{d}k = \frac{1}{2\pi i} \oint \frac{f'(z)}{f(z)} \mathrm{d}z$. The latter is a contour integral in the complex plane, which can be deformed. In particular, by Cauchy's argument principle, we have that $\omega = N_z - N_p$, where N_z is the number of zeros within the unit circle and N_p is the order of the pole at the origin. Instead of having to integrate, we can thus obtain ω by counting zeros and poles. This is illustrated in Fig. 2.1.

   While this connection between the winding number and zeros was presumably known (even if not spelled out in the literature), what was apparently not appreciated is that one can take $\omega = N_z - N_p$ as the *definition* of the topological invariant. The advantage is that—unlike the integral of $\frac{f_k'}{f_k}$ on the unit circle—this formula is well-defined even if the system is critical. We explore this in Section 2.4.

2. **The edge modes and their localization lengths.** Not only the *total* number of zeros inside the unit circle is of interest: each individual zero can be linked to a Majorana edge mode with localization length $\xi_{\text{loc}} = 1/|\ln|z_i||$, at least if there is no pole at the origin ($N_p = 0$). More precisely, let z_i be a zero of $f(z)$ such that $|z_i| < 1$ and define[6] $\gamma_{\text{left}}^{(i)} = \sum_{n=1}^{\infty} z_i^{n-1} \gamma_n$ for a half-infinite chain. This is indeed a zero-energy Majorana mode:

$$\left[H, \gamma_{\text{left}}^{(i)}\right] = \frac{i}{2} \sum_{m,n,\alpha} t_\alpha z_i^{m-1} \tilde{\gamma}_n \underbrace{\{\gamma_{n+\alpha}, \gamma_m\}}_{=2\delta_{n+\alpha,m}} = i \Bigg(\underbrace{\sum_{\alpha=0}^{\infty} t_\alpha z_i^\alpha}_{=f(z_i)=0} \Bigg) \Bigg(\sum_{n=1}^{\infty} z_i^{n-1} \tilde{\gamma}_n \Bigg) = 0. \tag{2.6}$$

   Since $|z_i| < 1$, we see that $\gamma_{\text{left}}^{(i)}$ is exponentially localized near the left edge, with localization length $\xi_{\text{loc}} = -1/\ln|z_i|$. If we have a finite chain of length L, this will give a finite-size energy-splitting $\sim e^{-L/\xi_{\text{loc}}}$.

   In the above, we used that $N_p = 0$, or, equivalently, that $t_\alpha = 0$ for $\alpha < 0$, to identify $f(z_i)$ in Eq. (2.6). Nevertheless, one can show that if $N_p \neq 0$ and $\omega = N_z - N_p > 0$, one can still construct edge modes for each of the $N_z - N_p$ zeros inside the unit circle which are closest to the unit circle. Similarly, if $\omega < 0$ and the system is gapped, one can construct $|\omega|$ exponentially-localized, T-odd Majorana edge modes at the left

[6] For convenience, let us presume that z_i is real, such that $\gamma_{\text{left}}^{(i)}$ is T-even. Otherwise, one must take linear combinations corresponding to the complex-conjugate pair of zeros.

edge, with their localization length being determined by the zeros *outside* the unit circle: $\xi_{\text{loc}} = 1/\ln|z_i|$. See Appendix A.2 for details. Much of the above applies to the case when the system is critical, as we discuss in Section 2.4 (see Theorem 1).

3. **Correlation functions.** For example, the bulk correlation length is determined by the zero closest to the unit circle, i.e., $\xi = \max_i\{1/|\ln|z_i||\}$. Due to Wick's theorem, it is enough to prove this for the two-point function $\langle\tilde{\gamma}_n\gamma_{n+N}\rangle$ (note that, e.g., $\langle\gamma_n\gamma_{n+N}\rangle = 0$ due to T-symmetry[7]). By inverting[8] Eq. (2.3), we have

$$\langle\tilde{\gamma}_n\gamma_{n+N}\rangle = \frac{i}{L}\sum_{k,q} e^{iqN}e^{-i(\varphi_k+\varphi_q)/2}\underbrace{\langle d_k^\dagger d_q\rangle}_{=\delta_{k,q}} = \frac{i}{L}\sum_k e^{ikN}e^{-i\varphi_k}. \tag{2.7}$$

Moreover, by the change of variables $k \to -k$ and taking the continuum limit, we have $\langle\tilde{\gamma}_n\gamma_{n+N}\rangle = \frac{i}{2\pi}\int e^{i\varphi_k}e^{-ikN}\mathrm{d}k$. Finally, we can express this as a contour integral[9]:

$$\langle\tilde{\gamma}_n\gamma_{n+N}\rangle = \frac{1}{2\pi}\oint\sqrt{\frac{f(z)}{f(1/z)}}\,z^{-N-1}\mathrm{d}z. \tag{2.8}$$

The contour is along the unit circle, but we can freely deform this until we encounter a singularity of $\sqrt{f(z)/f(1/z)}$. This occurs exactly at the zeros of $f(z)$ (and their inverses), which will hence dominate the integral. In particular, in Appendix A.3 we show that if the closest zero z_i to the unit circle is *inside* (*outside*) the unit circle, then Eq. (2.8) is asymptotically dominated by $\sim z_i^N$ ($\sim z_i^{-N}$). This thus proves that $\xi = \max_i\{1/|\ln|z_i||\}$. (Note that not all correlation functions have to decay with this correlation length; it serves as an upper bound, which is saturated for the two-point function.)

In a work [126] with Nick Jones—which we do not further discuss in this thesis—we also studied the correlation functions of nonlocal string order parameters using $f(z)$. Some results include an expression for the long-distance value of order parameters in terms of the zeros of $f(z)$ and the observation that the ratio of correlation lengths of different string order parameters is *universal* to each phase of matter. The latter allows us to extract the topological invariant ω from such a single ratio.

4. **A visual way of representing models.** Since much of the physical information of interest is readily available in the zeros and poles of $f(z)$, it is convenient to represent models purely in terms of the latter; see Fig. 2.1 for examples. A model is then characterized by first drawing a circle (representing the unit circle) and the location of its zeros. The model being critical is then equivalent to it having a zero *on* the unit circle. Such a picture also easily tells us how close we are to a phase transition and what phases are nearby, which are related to dragging zeros through the unit circle (thereby thus also changing $\omega = N_z - N_p$). Indeed, one can argue that a continuous change of t_α implies that the zeros move continuously across the complex plane [126]. Zero-pole pairs can be created at the origin or at infinity—corresponding to changing the range of the Hamiltonian.

5. **An easy way to construct models with desired properties.** For instance, we have already seen that if $\omega > 0$, then the (largest) edge mode localization length is determined by the zero z_i *closest* to the unit circle with $|z_i| < 1$. The *bulk* correlation

[7] I.e., $\langle\gamma_n\gamma_{n+N}\rangle = \langle\gamma_n\gamma_{n+N}\rangle^* = \langle(\gamma_n\gamma_{n+N})^\dagger\rangle = -\langle\gamma_n\gamma_{n+N}\rangle$.

[8] This gives us $\gamma_n = \frac{1}{\sqrt{L}}\sum_k\left(e^{-i(kn-i\varphi_k/2)}d_k^\dagger + h.c.\right)$ and $\tilde{\gamma}_n = \frac{i}{\sqrt{L}}\sum_k\left(e^{-i(kn+i\varphi_k/2)}d_k^\dagger - h.c.\right)$.

[9] We use that $e^{i\varphi_k} = \frac{f(e^{ik})}{|f(e^{ik})|} = \frac{f(e^{ik})}{\sqrt{f(e^{ik})f(e^{ik})^*}} = \sqrt{\frac{f(e^{ik})}{f(e^{-ik})}}$ and $i\mathrm{d}k = \frac{\mathrm{d}z}{z}$ if $z = e^{ik}$.

length, however, is determined by the zero closest to the unit circle, which might be inside or outside the unit circle. This tells us that in a wide (and stable) range of circumstances, $\xi \neq \xi_{\mathrm{loc}}$. Using $f(z)$, we can easily construct models with this property. Suppose we place one zero at $z_1 = 0$ (corresponding to an edge mode with $\xi_{\mathrm{loc}} = 0$) and another zero $z_2 = \lambda$ which lies outside the unit circle for $\lambda > 1$. We see that $0 = \xi_{\mathrm{loc}} < \xi = 1/\ln\lambda$. The corresponding Hamiltonian is determined by $f(z) = z(z-\lambda) = z^2 - \lambda z$, i.e., $H = H_2 - \lambda H_1$. An interesting limit is $\lambda \to 1$, where $\xi \to \infty$ yet ξ_{loc} remains finite! This occurs at $H = H_2 - H_1$, a phase transition between the 2-chain and the Kitaev chain.

More generally, we can choose $z_1 = e^{-1/\xi_{\mathrm{loc}}}$ and $z_2 = e^{1/\xi}$ with $\xi > \xi_{\mathrm{loc}}$. Then $f(z) = (z-z_1)(z-z_2) = z^2 - \left(e^{-1/\xi_{\mathrm{loc}}} + e^{-1/\xi}\right) z + e^{-1/\xi_{\mathrm{loc}}+1/\xi}$. The Hamiltonian with this property is thus $H = H_2 - \left(e^{-1/\xi_{\mathrm{loc}}} + e^{1/\xi}\right) H_1 + e^{-1/\xi_{\mathrm{loc}}+1/\xi} H_0$.

6. **The bulk universality class.** The zeros also tell us whether the bulk is critical and what its central charge is; this is explained in more detail in the next section. In Ref. [126], we also determined scaling dimensions and critical exponents for various critical points in the BDI class.

The case with a unit cell

So far we have presumed translation invariance for convenience. Let us briefly comment on the more general case where the system is translation invariant with respect to an N-site unit cell. Then the Hamiltonian is of the form $H = \frac{i}{2}\sum_n \tilde{\boldsymbol{\gamma}}_n^T T_\alpha \boldsymbol{\gamma}_{n+\alpha}$, where $T_\alpha \in \mathbb{R}^N \times \mathbb{R}^N$. We generalize our above definition for $f(z)$ to

$$f(z) \equiv \det F(z), \qquad \text{with } F(z) \equiv \sum_\alpha T_\alpha z^\alpha. \tag{2.9}$$

Similar to above, the zeros of this function contain physical information. In particular, the topological invariant is $\omega = N_z - N_p$, where N_z denotes the number of zeros of $f(z)$ within the unit disk, and N_p is the order of the pole at $z = 0$. Moreover, the zeros of $f(z)$ encode localization and correlation lengths, as above, although they are now measured relative to the size of the unit cell. See Appendix A.4 for details.

2.3.2. Relation to the literature

Our above formalism has a similarity to transfer matrices [127–129]. These were first applied to BDI systems by Motrunich et al. [117] in 2001 and later by DeGottardi et al. [116], where the eigenvalues of the transfer matrix can be related to topological edge mode properties of the system. Let us first clarify the *connection* between $f(z)$ and transfer matrices; afterwards, we discuss the *differences* between the two approaches.

If we write $H = \frac{i}{2}\sum_n \tilde{\gamma}_n \left(\sum_\alpha t_\alpha \gamma_{n+\alpha}\right)$, then we see that the equation of motion is $\partial_t \tilde{\gamma}_n = i[H, \tilde{\gamma}_n] = \sum_\alpha t_\alpha \gamma_{n+\alpha}$. There are various ways of setting up a transfer matrix; one way of obtaining it is by starting from the equation of motion at zero energy, i.e., $\sum_\alpha t_\alpha \gamma_{n+\alpha} = 0$. Let $\alpha_{\min}$ ($\alpha_{\max}$) be the smallest (largest) α for which $t_\alpha \neq 0$. Define $d = \alpha_{\max} - \alpha_{\min}$ (we exclude the special case $d = 0$, for which H is an α-chain). The

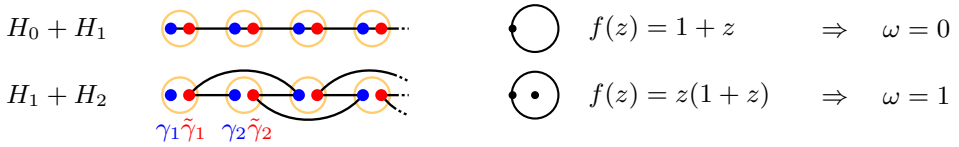

Figure 2.2.: **Two topologically distinct critical Majorana chains (central charge $c = 1/2$).** Representation of the critical Hamiltonians $H_0 + H_1$ and $H_1 + H_2$, i.e., critical points between α-chains H_α shown in Fig. 2.1. (Each fermionic site is decomposed into Majorana modes: γ (blue) and $\tilde{\gamma}$ (red), a bond signifies a term in the Hamiltonian.) The latter model, $H_1 + H_2$, has an edge mode. The associated complex function $f(z)$ and its zeros in the complex plane are shown, as well as the topological invariant $\omega = N_z - N_p$.

transfer matrix is then the $d \times d$-dimensional matrix A defined by

$$\begin{pmatrix} \gamma_{n+d} \\ \gamma_{n+d-1} \\ \gamma_{n+d-2} \\ \vdots \\ \gamma_{n+1} \end{pmatrix} = \underbrace{\begin{pmatrix} -\frac{t_{\alpha_{\max}-1}}{t_{\alpha_{\max}}} & -\frac{t_{\alpha_{\max}-2}}{t_{\alpha_{\max}}} & -\frac{t_{\alpha_{\max}-3}}{t_{\alpha_{\max}}} & \cdots & -\frac{t_{\alpha_{\min}}}{t_{\alpha_{\max}}} \\ 1 & 0 & 0 & \cdots & 0 \\ 0 & 1 & 0 & \cdots & 0 \\ \vdots & \vdots & \vdots & \ddots & \vdots \\ 0 & 0 & 0 & \cdots & 0 \end{pmatrix}}_{\equiv A} \begin{pmatrix} \gamma_{n+d-1} \\ \gamma_{n+d-2} \\ \gamma_{n+d-3} \\ \vdots \\ \gamma_n \end{pmatrix}. \tag{2.10}$$

The characteristic polynomial of A is $p(z) = \det(z\mathbb{I} - A)$. It is easy to see that $f(z) = z^{\alpha_{\min}} t_{\alpha_{\max}} p(z)$. This establishes a very direct relationship between $f(z)$ and the characteristic polynomial of the transfer matrix. As a direct consequence, we observe that

$$\omega = \#\{\text{negative Lyapunov exponents of } A\} + \alpha_{\min} \tag{2.11}$$

where the Lyapunov exponents $\{\lambda_i\}_i$ of A are defined by $\lambda_i \equiv \ln|a_i|$ for each eigenvalue a_i of A. This corrects the formula in Ref. [116], where it was claimed that $\omega = \#\{\text{negative Lyapunov exponents}\} - d/2$; that is only true for the special case where $\alpha_{\max} = -\alpha_{\min}$, i.e., $d = -2\alpha_{\min}$.

Hence, the transfer matrix—supplemented by the range of the Hamiltonian—carries the same information as the polynomial $f(z)$. The formalism with $f(z)$ is arguably easier, as it is more straightforwardly obtained from the Hamiltonian, as shown in Eq. (2.4); on the other hand, we have only defined $f(z)$ for systems with a unit cell, whereas transfer matrices are more generally applicable (indeed, they are a staple of disordered systems [127, 128]). We note two meaningful contributions given by our $f(z)$ formalism. First, as discussed and illustrated in subsection 2.3.1, it allows us to easily *construct* Hamiltonians with specific physical properties; it is less straightforward to go from transfer matrices to Hamiltonians. The second is the contribution to our understanding of critical systems with edge modes, which is the topic we turn to now.

2.4. Gapless topological superconductors

Above, we have reviewed the well-known physics of Majorana edge modes in gapped topological superconductors, albeit from a novel perspective—using that physical properties are naturally encoded in the zeros of a polynomial $f(z)$. Here, we use the latter perspective to investigate *gapless* topological superconductors.

The intuitive idea is that if one tunes from a gapped phase with, e.g., *two* edge modes toward the gapped phase with *one* edge mode, then at the critical point *one* mode can

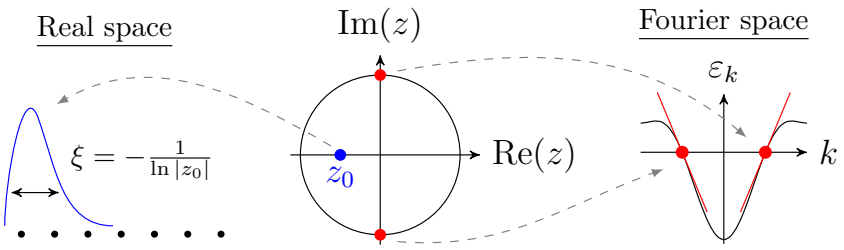

Figure 2.3.: **Edge modes and criticality from the zeros of $f(z)$.** The middle figure shows the zeros of $f(z)$. The zero z_0 within the disk (blue) corresponds to an edge mode (for each edge) with localization length $\xi = \frac{1}{|\ln|z_0||}$. Each zero on the unit circle (red) implies a massless Majorana field in the low-energy limit (contributing a central charge $c = \frac{1}{2}$).

remain localized. This happens for $H_1 + H_2$, as shown in Fig. 2.2. Remarkably, this edge mode moreover remains exponentially localized upon adding arbitrary (T-preserving and non-interacting) perturbations, even though there are no additional gapped degrees of freedom present! More precisely, there is no local operator $\mathcal{O}$ with $\langle \mathcal{O}_n \mathcal{O}_m \rangle \sim e^{-|n-m|/\xi}$ [10]. Indeed, for periodic boundary conditions, shifting $\gamma_n \to \gamma_{n-1}$ (which one *cannot* smoothly implement in a local and T-preserving way) maps $H_1 + H_2$ to $H_0 + H_1$, the well-studied critical Majorana chain described by a CFT with central charge $c = \frac{1}{2}$ [37].

To make precise that a critical system can be topologically non-trivial, we first show how $f(z)$ allows us to read off the universality class and the topological invariant of the bulk. We then relate this invariant to exponentially localized edge modes (Theorem 1). Intriguingly, the potential presence of edge modes at criticality was already implicit in the work by Motrunich et al. [117] in 2001—a work which was perhaps before its time. This phenomenon and its consequences have not been explored since. Lastly, we also show how $f(z)$ allows us to classify topologically distinct critical points (Theorem 2) and predict the universality class separating two arbitrary gapped phases (Theorem 3).

2.4.1. Topological invariant and central charge at criticality

Motivated by subsection 2.3.1, we define the topological invariant $\omega = N_z - N_p$ where N_z is the number of zeros of $f(z)$ *strictly* within the unit circle, and N_p the order of the pole of $f(z)$ at $z = 0$. In case that the system is gapped, this agrees with the winding number as usually defined. If the system is critical, i.e., at least one zero lies on the unit circle, then the aforementioned winding number breaks down. The quantity $N_z - N_p$, however, remains well-defined. This is moreover an *invariant* of the critical phase, since ω can only change by dragging a zero through the unit circle. However, this would change the bulk physics: every non-degenerate zero e^{ik_0} of $f(z)$ implies that $\varepsilon_k \sim k - k_0$, contributing a massless Majorana fermion (with central charge $c = \frac{1}{2}$) to the CFT (see Fig. 2.3).

In summary, $\omega = N_z - N_p$ defines a topological invariant—both for gapped and gapless chains—and the central charge c of the bulk CFT is given by

$$c = \frac{1}{2} \times \#\{\text{zeros of } f(z) \text{ on the unit circle}\}. \tag{2.12}$$

More precisely, the above definition of c coincides with the central charge when the bulk is indeed a CFT, i.e., when the zeros on the unit circle are all non-degenerate. The special case of degenerate zeros implies that ε_k is not locally linear near its gapless point, leading to a dynamical critical exponent larger than one.

[10] One can also imagine a box function, corresponding to $\xi = 0$.

2.4.2. Exponentially localized edge modes at criticality

In Section 2.3.1, we saw that ω counts edge modes, with the localization lengths being given by the zeros of $f(z)$; see Fig. 2.3 for the conceptual picture. In this section, we present the complete and precise statement about the relationship between zeros and edge modes, which also applies to critical systems:

Theorem 1 *If the topological invariant $\omega > 0$, then*

1. *each boundary has ω Majorana zero modes,*
2. *the modes have localization length $\xi_i = -\frac{1}{\ln|z_i|}$ where $\{z_i\}$ are the ω largest zeros of $f(z)$ within the unit disk,*
3. *the modes on the left (right) are real (imaginary).*

If $\omega < -2c$ (where c = half the number of zeros on the unit circle), the left (right) boundary has $|\omega + 2c|$ imaginary (real) Majorana modes with localization length $\xi_i = \frac{1}{\ln|z_i|}$, with $\{z_i\}$ the $|\omega + 2c|$ smallest zeros outside the unit disk.

For any other value of ω, no localized edge modes exist.

Before we outline the proof, note that in the gapped case c is zero, with $|\omega|$ correctly counting edge modes. At criticality, $2c$ counts the zeros on the unit circle, and if these are non-degenerate, the bulk is a CFT with central charge c. However, if $f(z)$ has a zero e^{ik_0} with multiplicity m, then $\varepsilon_k \sim (k - k_0)^m$, implying a dynamical critical exponent $z_{\text{dyn}} = m$.

The above theorem is proven in Appendix A.2. We briefly sketch the steps here. If $\omega > 0$, we construct for each z_i (defined above) a real edge mode $\gamma^{(i)}_{\text{left}} = \sum_{n\geq 1} b^{(i)}_n \gamma_n$ by requiring $[\gamma^{(i)}_{\text{left}}, H] = 0$. This gives constraints $\sum_{a\geq 1} b^{(i)}_a \; t_{a-n} = 0$ for $n \geq 1$, leading to standard solvable recurrence relations, with the function $f(z)$ appearing as the characteristic polynomial. If $N_p = 0$, the solution is simply $b^{(i)}_n \propto z_i^n$ (hence $\left|b^{(i)}_n\right| \sim e^{-n/\xi_i}$; see Section 2.3), while $N_p > 0$ modifies $b^{(i)}_n$ without affecting its asymptotic form. Details are treated in Appendix A.2. The case $\omega < -2c$ follows by noting that inverting left and right effectively implements $f(z) \leftrightarrow f\left(\frac{1}{z}\right)$ and one can show that this changes the topological invariant $\omega \leftrightarrow -\omega - 2c$. This completes the proof. Note that the exponential localization implies that the commutator—and hence the energy gap of the edge mode—is exponentially small for finite systems.

2.4.3. Classifying topologically distinct critical points

Similar to gapped phases, we can classify topologically-distinct critical phases. We define two Hamiltonians to be in the same phase if and only if they are connected by a path of local Hamiltonians (within the symmetry class) along which the low-energy description of the bulk changes smoothly. (This is different from the notion of Furuya and Oshikawa [62] where CFTs are in the same phase if a renormalization group flow connects them.) Hamiltonians described by CFTs with different central charges are automatically in distinct phases by the c-theorem [130]. If, on the other hand, both Hamiltonians have the same CFT description, one might expect them to be in the same phase. However, we have shown that $H_1 + H_2$ and $H_0 + H_1$ have different topological invariants (respectively, $\omega = 1$ and $\omega = 0$), despite having the same CFT description. Hence, they cannot be connected within the BDI class, which we illustrate in Fig. 2.4: linearly interpolating from $H_0 + H_1$ to $H_1 + H_2$ indeed keeps the system in the Ising universality class throughout, *except* at the midway point, where the dynamical critical exponent $z_{\text{dyn}} = 2$. Visually, this corresponds to a zero crossing the unit circle, coinciding with the zero which was already there.

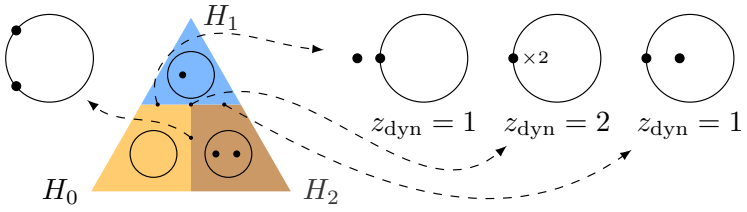

Figure 2.4.: **Topologically-distinct CFTs must be separated by a phase transition.** Phase diagram illustrating how critical points with the same CFT description but different topological invariants cannot be connected: interpolating $H_0 + H_1$ and $H_1 + H_2$ induces a point where the dynamical critical exponent z_{dyn} changes discontinuously. From the perspective of $H_1 + H_2$, this corresponds to a gradual delocalization of its edge mode.

This is illustrative of the general case. We have seen that any translation invariant Hamiltonian H_{BDI} can be identified with a complex function $f(z)$, with its set of zeros and poles, as in Fig. 2.3. Conversely, the zeros and poles uniquely identify $f(z)$ and hence the Hamiltonian, a discussed in Section 2.3. This correspondence between a BDI Hamiltonian and a picture of zeros and poles reduces the classification to an exercise in geometric insight.

Let us focus on the physically interesting case where the bulk is described by a CFT, i.e., the zeros on the unit circle have multiplicity one. There is only one rule restricting the movement of the zeros on the unit circle: since t_α is real, the zeros of $f(z)$ are real or come in complex-conjugate pairs. This means we *cannot* move a zero off the real axis. However, we *can* bring $f(z)$ to a *canonical form* where the zeros are equidistantly distributed on the unit circle with mirror symmetry about the real axis. There are only two such patterns, given by the solutions of $z^{2c} = \pm 1$. Thus, we can always tune to the canonical form $f(z) = \pm\left(z^{2c} \pm 1\right) z^{\omega}$. Hence, for a given nonzero $c \in \frac{1}{2}\mathbb{N}$ and $\omega \in \mathbb{Z}$, there are $\mathbb{Z}_2 \times \mathbb{Z}_2$ translation invariant phases, labeled by the two signs. These signs are protected by translation symmetry: the first encodes the spatially modulating sign of correlations, the second whether $\varepsilon_k = |f\left(e^{ik}\right)|$ vanishes at time-reversal invariant momenta.

Hence, allowing for paths with unit cells, two systems can be smoothly connected *if* they have identical c and ω (see Appendix A.4 for details). To confirm that this is a *necessary* condition, recall from Section 2.3 that we can extend ω to systems with an N-site unit cell, $H = \frac{i}{2}\sum \tilde{\boldsymbol{\gamma}}_n^T T_\alpha \boldsymbol{\gamma}_{n+\alpha}$ where $T_\alpha \in \mathbb{R}^{N\times N}$. Defining $f(z) = \det\left(\sum_\alpha T_\alpha z^\alpha\right)$, then analogous to before, one can show that $|f\left(e^{ik}\right)|$ is the *product* of the energy bands $\varepsilon_k^{n=1,\cdots,N}$; this is extensively discussed in Appendix A.4. Thus, $\omega = N_z - N_p$ cannot change without a bulk transition.

For gapped phases, ω is known to be additive under stacking [11]. Our extension to critical systems still satisfies this property (as does the central charge c [37]). Moreover, the classification straightforwardly generalizes to stackings, with a small caveat. E.g., a Kitaev chain stacked onto $H_0 + H_1$ has the same invariants as $H_1 + H_2$ ($c = \frac{1}{2}$ and $\omega = 1$). One might expect these to be in the same phase, but the latter has no gapped degrees of freedom. This is resolved by adding a decoupled trivial chain—after which one can indeed connect them. Details are given in Appendix A.4.

We thus obtain a *semigroup* classification ('*semi*' because c cannot decrease under stacking, i.e., critical systems do not have inverses under stacking, unlike gapped topological superconductors):

Theorem 2 *The phases in the BDI class described in the bulk by a CFT and obtained by deforming a translation invariant Hamiltonian (or a stacking thereof) with an arbitrary unit cell, are classified by the semigroup* $\mathbb{N} \times \mathbb{Z}$*: they are labeled by the central charge*

$c \in \frac{1}{2}\mathbb{N}$ *and the topological invariant* $\omega \in \mathbb{Z}$.

Translation invariance gives an extra $\mathbb{Z}_2$ *invariant when* $c = 0$ *and an extra* $\mathbb{Z}_2 \times \mathbb{Z}_2$ *invariant when* $c \neq 0$.

2.4.4. A topological lower bound on the central charge

Related to the above topic of classifying critical phases, is the question: "*Given two gapped phases, can we predict the universality class of the phase transition that separates them?*" This can indeed be straightforwardly answered using the $f(z)$ formalism. By continuity, the difference in winding number between two gapped phases is the number of zeros that must cross the unit circle at the transition, i.e.:

Theorem 3 *A phase transition between two gapped phases with winding numbers* ω_1 *and* ω_2 *obeys* $c \geq \frac{|\omega_1 - \omega_2|}{2}$.

As before, c should be understood as counting half the number of zeros on the unit circle. If these zeros are non-degenerate, the bulk is a CFT with central charge c. Note that for a free-fermion CFT, knowing the central charge specifies the full CFT. Generically, c *equals* $\frac{|\omega_1 - \omega_2|}{2}$, but one can fine-tune the transition with zeros bouncing off the unit circle[11]. Note that this theorem gives us a *topological lower bound* on the central charge. In Ref. [122], we explored a possible generalization of this bound to the interacting case.

2.4.5. Stability against disorder and interactions

In the remainder of this chapter, we numerically demonstrate that the topological edge modes—in the presence of bulk criticality—can survive disorder and interactions.

Disorder

Let us consider $H = \frac{i}{2}\sum_{\alpha=0}^{3}\sum_n t_\alpha^{(n)}\,\tilde{\gamma}_n\gamma_{n+\alpha}$. The disorder-free case $t_1^{(n)} = t_2^{(n)} = 1$ and $t_0^{(n)} = t_3^{(n)} = a$ is critical with $c = \frac{1}{2}$ and $\omega = 1$ if $-1 < a < \frac{1}{3}$. In paticular, if we set $a = 0$, it reduces to $H_1 + H_2$. We now introduce strong disorder, drawing $t_1^{(n)}, t_2^{(n)}$ independently from the flat distribution on $[0, 1]$ and $t_0^{(n)}, t_3^{(n)}$ from $[-0.5, 0]$.

First, we confirm the system flows to the infinite randomness fixed point with effective central charge $c_{\text{eff}} = \ln\sqrt{2}$ [117, 131, 132]. To this end, we diagonalize systems of size L (with periodic boundary conditions) and calculate the entanglement entropy $S(L, L_{\text{block}})$ of a region of length L_{block}. The average is predicted to obey the asymptotic scaling $S \sim \frac{c_{\text{eff}}}{3}\ln L_{\text{block}}$ (for $1 \ll L_{\text{block}} \ll \frac{L}{2}$), as shown in Fig. 2.5(a).

Second, in the presence of open boundary conditions, we observe one Majorana edge mode per boundary. These are exponentially localized, with Fig. 2.5(b) showing the distribution of localization lengths over different disorder realizations. The inset gives a generic example, plotting $|b_n|$ where the edge mode is $\gamma_{\text{left}} = \sum_{n=1}^{L} b_n\gamma_n$. We note that this can also be diagonalized using the methods of Ref. [117].

Interactions

Introducing interactions can have drastic and interesting effects. A case in point is that the BDI class—which has an infinite number of distinct gapped phases in the non-interacting case as we saw in Section 2.1—has only eight distinct phases in the presence of interactions, labeled by $\mathbb{Z}_8$ [16, 17, 32]; this is explained in Chapter 3. Chapter 4 of this thesis is devoted to studying topologically non-trivial gapless systems in the presence of interactions, using

[11] E.g. $f(z) = (z - b - 1)(z + |b| + 1)$ at $b = 0$ is a CFT with $c = 1$ between the trivial phase and the Kitaev chain phase.

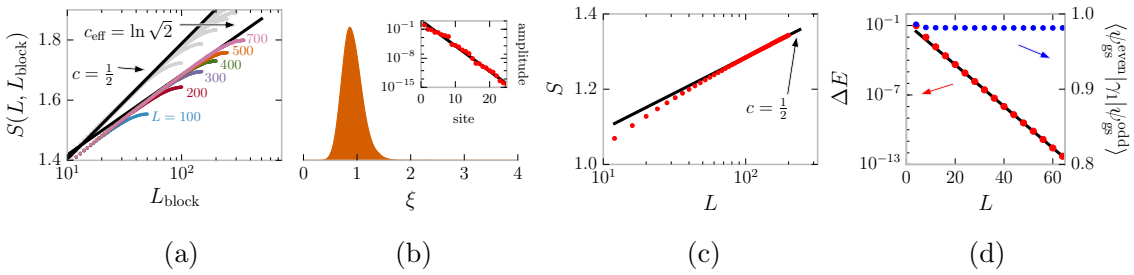

(a) (b) (c) (d)

Figure 2.5.: **The edge mode at criticality is stable against strong disorder (a,b) and interactions (c,d).** (a) Entanglement scaling for the disordered system (averaging 10^5 states) suggests an infinite randomness fixed point with $c_{\text{eff}} = \ln\sqrt{2}$ (black lines guide the eye; gray is the clean case). (b) Distribution of edge mode localization length over disorder realizations (inset: edge mode for one realization). (c) Entanglement scaling for the interacting Hamiltonian (2.13) with open boundaries and $U = 0.3$. The bulk is described by the $c = \frac{1}{2}$ Majorana CFT (black line guides the eye). (d) The finite-size energy splitting (red dots) for (2.13) between different fermionic parity sectors seems to be exponentially small, $\Delta E \sim e^{-L/\xi_{\text{loc}}}$ with $\xi_{\text{loc}} \approx 2.42$. In fact, from analytic arguments we know that there is also an algebraic contribution with a high power $\sim 1/L^{14}$, which is *subdominant* to the observed exponential splitting (for this range of L). The blue dots confirm that the two ground states differ by a localized operator.

both numerical and analytical tools. Here, we numerically show that an interacting critical point between the Kitaev chain and the 2-chain H_2,

$$H = H_1 + H_2 + U \sum_{n=1}^{L} \left(\gamma_n \gamma_{n+1} \gamma_{n+2} \gamma_{n+3} + \tilde{\gamma}_n \tilde{\gamma}_{n+1} \tilde{\gamma}_{n+2} \tilde{\gamma}_{n+3}\right), \tag{2.13}$$

has localized edge modes. The interactions are chosen such that the critical point will not shift when $U \neq 0$ since (2.13) is self-dual under $\gamma_n \to \gamma_{3-n}$ and $\tilde{\gamma}_n \to \tilde{\gamma}_{-n}$.

We use the density matrix renormalization group method [12] to perform finite-size scaling with open boundaries for $U = 0.3$. (Convergence was reached for system sizes shown with bond dimension $\chi = 60$.) In Fig. 2.5(c), we confirm that the system remains critical by using the CFT prediction [133] for the the entanglement entropy of a bipartition into two equal halves of length $\frac{L}{2}$, namely $S \sim \frac{c}{6} \ln L$.

The stability of the edge mode is studied in Fig. 2.5(d). Firstly, we show the finite-size energy splitting between the two lowest energy eigenstates (red dots). We observe that this decays to zero exponentially fast. In fact, from analytic arguments we know that there should also be an algebraic $\sim 1/L^{14}$ contribution, as discussed in Chapter 4. However, although an algebraic decay dominates over an exponential decay for *large enough* systems sizes, for any *reasonable* system size, $1/L^{14}$ is subdominant to the observed exponential decay. To illustrate this point, note that $1/L^{14} < e^{-L/\xi_{\text{loc}}}$ (with $\xi_{\text{loc}} = 2.42$) over the range $2 < L < 174$; by the point that $L = 175$, the algebraic contribution becomes dominant, but $1/175^{14} \approx 4 \times 10^{-32}$. Nevertheless, in Chapter 4 we are able to numerically confirm the $\sim 1/L^{14}$ splitting by fine-tuning the system in order to eliminate the exponentially small term. Lastly, in Fig. 2.5(d) we also confirm that the two ground states only differ an operator whose weight is localized near the boundary: $\langle \psi_{\text{gs}}^{\text{even}} | \gamma_1 | \psi_{\text{gs}}^{\text{odd}} \rangle$ tends to a finite value as $L \to \infty$.

3. Interacting gapped symmetry-protected topological (SPT) phases

Unlike the non-interacting topological superconductors of the previous chapter, interacting SPT phases are not characterized by topological winding numbers. Instead, in one dimension, they are protected by how bulk symmetries act anomalously on the edge [16–19, 24] (in Section 3.1 and Appendix B we present an accessible review of the classification of one-dimensional SPT phases). An archetype is the Haldane phase, realized by the spin-1 Heisenberg chain with its spin-$\frac{1}{2}$ edge modes: the bulk is symmetric with respect to $SO(3)$ whereas the edges transform under $SU(2)$. While that particular model is not analytically tractable, there are a number of exactly soluble fermionic and spin chains that have been uncovered over the decades realizing SPT phases. One might wonder whether there are links between these distinct models. In this chapter, we show that this is the case, unifying various models by relating them to stacks of Kitaev chains [30].

We have already encountered such stacks in the previous chapter, dubbing them the α-chain. The Kitaev chain has a single Majorana zero mode on each edge, but by stacking multiple copies one can have an arbitrary number of such modes. We showed that spinless time-reversal symmetry (TRS) prevents these $|\alpha|$ Majorana modes from gapping out; each value of α defined a different topological superconducting phase of matter. However, in the presence of interactions, there are only eight distinct phases protected by TRS, characterized by how fermionic parity symmetry and TRS are represented on the edge [16, 17]. We will review this fundamental result, after which we relate various other models to this α-chain.

Let us highlight a few of our findings, firstly on how a stack of two Kitaev chains, i.e., the 2-chain, is related to well-known SPT models. This is pictorially represented in Fig. 3.1, with details in the main text below. On the one hand, we find a two-site unitary transforming the superconducting 2-chain into the Su-Schrieffer-Heeger (SSH) model [28], a particle number preserving Hamiltonian with a complex fermionic edge mode protected by sublattice symmetry [111]. This mapping arises naturally when using symmetry as a guide. Such a guiding principle even uncovers new facts in the case of known relationships, such as for the non-local transformation which maps the 2-chain to the cluster model [27, 31], a spin-$\frac{1}{2}$ chain protected by a $\mathbb{Z}_2 \times \mathbb{Z}_2$ symmetry [134]. Despite that mapping being well-known [116, 134–138], we uncover through it a new anti-unitary symmetry

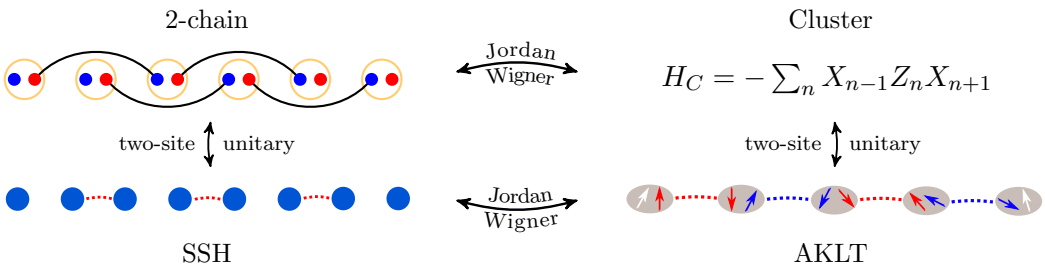

Figure 3.1.: **SPT models related to the α-chain with $\alpha = 2$.** In the case of the AKLT model it is at the level of the ground state, whereas for the other three models it is at the level of the full Hamiltonian.

protecting the cluster model. This means that the cluster model and the Haldane phase are protected by the *same* set of discrete symmetry groups, with a different microscopic action. Writing down a two-site unitary transforming one symmetry into the other, we map the cluster model to a spin chain whose ground state is the fixed point limit of the Affleck-Kennedy-Lieb-Tasaki (AKLT) [25] state. The AKLT model is a well-known perturbed spin-1 Heisenberg chain with an exactly known ground state.

Reconsidering the α-chain also illuminates how the Haldane phase and the stack of four Kitaev chains, i.e., the 4-chain, are two extremes of a single SPT model. The seminal work on the interacting classification of SPT phases showed that the 4-chain has many algebraic similarities to the Haldane phase at the level of symmetries [16]. We show that the interacting 4-chain can locally be rewritten as a spinful Hubbard chain, protected by sublattice symmetry. In the Mott limit, it is a spin chain in the Haldane phase. Interestingly, in this limit the sublattice symmetry protecting the Hubbard chain is indistinguishable from spinful TRS. The latter is known to protect the Haldane phase, but *only* in the Mott limit (even when combined with spin rotation symmetry) [139]. Sublattice symmetry can be seen as a *different* way of extending the same spin symmetry to charge degrees of freedom, in which case our construction shows that the Haldane phase remains stable despite charge fluctuations.

Other new physics arises from mapping the α-chain to the *generalized* spin-$\frac{1}{2}$ cluster models [27]. Such a relationship was observed before [116, 135–138], but we use it to uncover the SPT properties of these spin chains, leading, for example, to spin chains with *both* symmetry breaking and SPT order. It is worth noting that despite these spin chains being mathematically equivalent to the α-chains, their physics is distinct due to the non-locality of the mapping. This makes the set of cluster models useful in its own right (both for didactic and testing purposes), especially since one can add perturbations which break the equivalence to fermions yet leave the SPT properties intact.

An outline of this chapter is as follows: in Section 3.1 we present a brief review of one-dimensional SPTs, focusing on a physical perspective (with a systematic treatment given in Appendix B). Section 3.2 concerns fermionic SPTs where we recap the α-chain and its symmetry fractionalization. In subsection 3.2.2, we illustrate how the 2-chain is the SSH model in disguise, and in subsection 3.2.3, the interacting 4-chain is adiabatically connected to the Haldane phase. We then turn to bosonic SPTs in Section 3.3, where the generalized cluster models emerge as the Jordan-Wigner transform of the α-chain, pointing out how the physics has changed under this non-local mapping. This uncovers new non-trivial symmetries of the cluster model, which in subsection 3.3.2 leads to identifying its ground state as the fixed point limit of the AKLT state. Lastly, subsection 3.3.3 shows how to generalize the Kramers-Wannier dualities to these generalized cluster models, shedding light on their symmetry breaking and SPT properties.

3.1. An example-based introduction to SPT phases and their classification

Here we briefly review the classification of (interacting) SPT phases in 1D using physical pictures [16–19]. First we present the general concept and then illustrate this in the case of the cluster model and Kitaev chain. For more details, we refer to Appendix B or the aforementioned references.

3.1.1. The classification in a nutshell

Consider a gapped one-dimensional system of length N invariant under a global symmetry group G. The classification scheme needs the symmetries to be well-defined even when

having open boundaries[1], which for a unitary symmetry $U \in G$ is guaranteed if $U = \otimes_n U_n$ is a tensor product over sites or unit cells, referred to as an on-site symmetry. (The case of anti-unitaries, where complex conjugation is defined in some on-site/unit cell basis, is discussed in section 3.2.) If we assume that U is not spontaneously broken, then for periodic boundary conditions the ground state must be unique[2] and hence invariant under U. However, if we have open boundary conditions, then the absence of spontaneous symmetry breaking in the bulk still allows for U to act non-trivially near the edges. We write this as $U = U_L U_R$, which is valid in the ground state subspace. These effective operators $U_{L,R}$ are exponentially localized near the boundaries on a length-scale set by the correlation length[3]. In the thermodynamic limit ($N \to \infty$) of a gapped phase, U_L and U_R thus have no overlap. Since the Hamiltonian is local, this means that U_L and U_R do not change the energy of a state in the ground state subspace. We refer to this as *symmetry fractionalization*. The same holds for any other unbroken symmetry $V \in G$, so we can write $V = V_L V_R$. Any group relation between U and V then implies a relation between the edge symmetries. In particular, $\{U_L, V_L, \cdots\}$ then obey the same group relations as $\{U, V, \cdots\}$ possibly up to a phase factor. In the bosonic case, where U_L and U_R commute, both edges completely decouple and the physical symmetry is then *projectively represented* on each edge. Such a projective representation has discrete labels that cannot change smoothly. Since any *non-trivial* projective representation has a minimal dimension > 1, it protects degenerate modes on the edge (which will be clear from the example of the cluster model). Fermions can have extra structures related to U_L and U_R not necessarily commuting, as will be clarified in the discussion of the Kitaev chain below.

3.1.2. Bosonic example: the cluster model

The cluster model is a spin chain with three-spin interactions:

$$H_C = -\sum_n X_{n-1} Z_n X_{n+1} \tag{3.1}$$

where we denote the Pauli spin operators $\sigma_{x,y,z}$ as X, Y, Z. Its earliest appearance in the literature is in Suzuki's work on quantum systems that are dual to two-dimensional classical dimer models [27] but it was rediscovered by Raussendorf and Briegel in the context of measurement-based quantum computation [31]. Keating and Mezzadri independently arrived at it as a spin chain dual to free fermions [135] and Kopp and Chakravarty generated the model through a real space renormalization of the quantum Ising chain [140]. The cluster model was discovered to be an SPT phase protected by $\mathbb{Z}_2 \times \mathbb{Z}_2$ by Son et al. [134], and here we give a simplified treatment of this fact as found in Zeng et al. [141]

If the total number of sites N is even, H_C is symmetric under the $\mathbb{Z}_2 \times \mathbb{Z}_2$ group generated by

$$\begin{cases} P_1 &= Z_1 Z_3 Z_5 \cdots Z_{N-1} \\ P_2 &= Z_2 Z_4 Z_6 \cdots Z_N. \end{cases} \tag{3.2}$$

Let us take open boundary conditions and analyze the edge modes. Note that the terms in Eq. (3.1) square to one, such that the eigenvalues are ± 1. Since all terms in H commute, the ground state subspace will have $X_{n-1} Z_n X_{n+1} = 1$ for all n. Concatenating a list of these, we directly see that this implies $X_1 Z_2 Z_4 Z_6 \cdots Z_{N-2} X_{N-1} = 1$, or equivalently $P_2 = X_1 X_{N-1} Z_N$. So despite P_2 being a global operator, it turns out that in the ground

[1] In case one is interested in spatial inversion symmetry, one has to replace the real-space picture by an entanglement-based approach.

[2] This is clear if we assume our Hamiltonian is translation invariant. However, one does not strictly need translation invariance.

[3] More precisely, the correlation length sets an upper bound. This can be a very bad upper bound, as we will discuss in Chapter 4.

state subspace it merely acts on the left by $P_2^L = X_1$ and on the right by $P_2^R = X_{N-1}Z_N$. Similarly, we obtain $P_1^L = Z_1X_2$ and $P_1^R = X_N$.

We explicitly see that P_1^L and P_2^L are anticommuting symmetries, proving that the cluster model has degenerate edge modes. (Note that symmetry fractionalization generally only holds in the ground state subspace, whereas here $P_{1,2}^{L,R}$ commuting with the Hamiltonian imply so-called *strong* zero modes [142].) Adding terms to Eq.(3.1) that respect the $\mathbb{Z}_2 \times \mathbb{Z}_2$ of P_1 and P_2 will alter the form of P_1^L and P_2^L but cannot change their mutual anticommutation: from $P_1P_2 = P_2P_1$ one can derive that $P_1^LP_2^L = e^{i\alpha}P_2^LP_1^L$, and from $P_1^2 = 1$ one can show that $e^{i\alpha} = \pm 1$, indeed labeling the projective representations of $\mathbb{Z}_2 \times \mathbb{Z}_2$ (see Appendix B for details about symmetry fractionalization). Thus as long as the correlation length is finite, the edges have well-defined degeneracies. Hence the cluster model is an SPT phase protected by $\mathbb{Z}_2 \times \mathbb{Z}_2$. In section 3.3 we will see how it relates to a longer-range Kitaev chain (the 2-chain encountered in Chapter 2) and how that uncovers new topological features and even a hidden $SO(3)$ symmetry in the ground state.

3.1.3. Fermionic example: the Kitaev chain

This is a one-dimensional model of superconducting fermions [30]:

$$H_K = -\frac{1}{2}\sum_n \left(c_n^\dagger c_{n+1} + c_n^\dagger c_{n+1}^\dagger + \text{h.c.}\right). \tag{3.3}$$

Kitaev drew attention to this model in 2001 for the free Majorana modes on its edges. We have encountered the above Hamiltonian in Chapter 2: it is the α-chain for $\alpha = 1$, also denoted by H_1. However, to keep this chapter self-contained, let us briefly repeat how to analyze the above Hamiltonian and, in particular, see its Majorana edge modes. Decompose the fermionic operators into their real and imaginary parts: $\gamma_n = c_n^\dagger + c$ and $\tilde{\gamma}_n = i(c_n^\dagger - c_n)$. These Hermitian operators are Majorana modes, meaning they anticommute and square to unity. One obtains the much simpler $H_K = \frac{i}{2}\sum_n \tilde{\gamma}_n\gamma_{n+1}$. Similar to the reasoning for the cluster model, the ground state subspace will have $i\tilde{\gamma}_n\gamma_{n+1} = -1$.

We now interpret the Kitaev chain as an *interacting* SPT phase protected by fermionic parity symmetry $P = \prod_i(1-2n_i) = \prod(i\tilde{\gamma}_n\gamma_n)$—which is a symmetry for any fermionic system. By the above $i\tilde{\gamma}_n\gamma_{n+1} = -1$, we see that P effectively acts as $P = i\gamma_1\tilde{\gamma}_N$ for open boundaries. So here we see that $P = P_LP_R$ where P_L and P_R anticommute. So now we have a protected twofold degeneracy that is spread out over both edges. In other words there is a Majorana zero mode living on each edge, which can be said to be '$\sqrt{2}$-dimensional'—*by definition* this means that taking two such modes gives a 2-dimensional Hilbert space. Because fermionic parity symmetry cannot be broken[4], this phase is stable against *arbitrary* perturbations.

We see that if we only have P-symmetry, there are exactly two phases, characterized by $P_LP_R = \pm P_RP_L$. In the non-interacting classification this is referred to as the $\mathbb{Z}_2$ invariant of the D class[5]. However, the Kitaev chain is also invariant under spinless time-reversal symmetry $T = K$, where K is the complex conjugation that leaves c and $c^\dagger$ invariant. If we enforce this symmetry, then in the absence of interactions we are put in the BDI class which is known to have $\mathbb{Z}$ distinct phases characterized by a certain topological invariant; see Section 2.1 for details about this. However, in subsection 3.2.1 we review how in the interacting case there are only eight phases [32], labeled by $\mathbb{Z}_8$, where the topological invariants are constructed out of the symmetry fractionalization of

[4]By locality one would require that $\langle c_i^\dagger c_j\rangle \xrightarrow{|i-j|\to\infty} \langle c_i^\dagger\rangle\langle c_j\rangle$. Since the left-hand side is anti-symmetric and the right-hand symmetric, we require $\langle c_i^\dagger\rangle = 0$. Parity symmetry ensures this.

[5]This requires a particle-hole symmetry, but note that *any* fermionic Hamiltonian has a particle-hole symmetry as defined in the Bogoliubov-de Gennes Hamiltonian; this was explained in subsection 2.1.1.

P and T [16, 17, 143]. All the $\mathbb{Z}$ non-interacting phases (and the eight interacting ones) are generated by stacking single Kitaev chains. This uses the so-called group structure of SPT phases, which we explain now.

3.1.4. Group structure of SPT phases

An important and elegant property of these phases is that the set of all SPT phases with respect to a given symmetry group G *itself* has a group structure. The addition of two SPT phases is defined by taking the physical stacking of both chains. This can be applied to both the non-interacting and interacting classification, but here we give the point of view relevant for the interacting classification, i.e., using symmetry fractionalization. For example, let U be some unitary symmetry for a bosonic chain, then if we have $U = U_L^A U_R^A$ for the first chain and $U = U_L^B U_R^B$ for the second, then the combined system has $U_L = U_L^A U_L^B$. This new symmetry fractionalization will then be a realization of a possibly different SPT phase. It is not hard to convince oneself that this operation satisfies all the properties of a group. Mathematically, in the bosonic setting (where the edges fully decouple) this new group is called the second group cohomology group of G with coefficients in $U(1)$, denoted by $H^2(G, U(1))$ [18], although we do not use this language in this paper. For example, for $G = \mathbb{Z}_2 \times \mathbb{Z}_2$, the group of SPT phases is $\mathbb{Z}_2$: this means there is only one non-trivial phase—realized by the above cluster model—which is its own inverse. Indeed, if one has a stack of two cluster models, then one can gap out the edge modes by the symmetry-preserving perturbation $V = \left(P_1^L\right)^A \left(P_1^L\right)^B + \left(P_2^L\right)^A \left(P_2^L\right)^B$.

3.1.5. The subtlety of identifying phases

In the aforementioned, we did not distinguish the symmetry group from its representation. For example, the cluster model H_C in Eq. (3.1) has the abstract symmetry group $\mathbb{Z}_2 \times \mathbb{Z}_2$ which is *represented* by $\{\mathbb{I}, P_1\} \times \{\mathbb{I}, P_2\}$. Indeed: in the classification scheme one usually *fixes* the representation and only allows paths of gapped local Hamiltonians which are symmetric under that particular representation. Along such a path the symmetry fractionalization $\{\mathbb{I}, P_1^L\} \times \{\mathbb{I}, P_2^L\}$ remains well-defined. The downside of this definition is that *any* other model with the same symmetry but in a different physical implementation is automatically in a distinct phase.

For instance, consider the spin-$\frac{1}{2}$ chain of alternating Heisenberg couplings $H = \sum_n \boldsymbol{S}_{2n} \cdot \boldsymbol{S}_{2n+1}$. The leftmost spin $\boldsymbol{S}_1$ is clearly decoupled, and this edge mode is in fact protected by any perturbation that preserves π-spin rotation since the edge transforms as a spin-$\frac{1}{2}$ whereas the bulk is a singlet. Thus it has the same symmetry group $\mathbb{Z}_2 \times \mathbb{Z}_2$ but now it is represented by $\{\mathbb{I}, R_x\} \times \{\mathbb{I}, R_y\} = \{\mathbb{I}, R_x, R_y, R_z\}$, sometimes referred to as the Haldane phase. According to the usual definition, these two models can *not* be connected, despite both having the same properties with respect to $\mathbb{Z}_2 \times \mathbb{Z}_2$.

To resolve this, we can introduce a broader notion of phase equivalence where one allows for paths of gapped local Hamiltonians where the symmetry group is preserved, but its on-site representation can vary smoothly. The symmetry fractionalization and consequent edge modes are then still protected quantities. In this way one can, for example, construct a path between the cluster model and the alternating Heisenberg chain where P_1 and P_2 smoothly transforms into R_x and R_y. In subsection 3.3.2 we naturally arrive at such a path purely from symmetry considerations, which moreover also preserves the other symmetries known to protect the Haldane phase. The condition that the symmetry remains on-site is crucial: if this is dropped, everything becomes trivial [19].

3.2. Topological fermionic chains

3.2.1. Stacking of Kitaev chains: the α-chain

Here we reconsider the phases that arise by stacking multiple Kitaev chains. Instead of literally stacking them on top of one another, it is convenient to rewrite such stacks in a translation invariant manner. This makes it more natural, for example, to interpolate between a different number of chains without keeping systems artificially decoupled from one another. Doing so, we arrive at the α-chains which we introduced in Chapter 2; to wit, these are

$$H_\alpha = \frac{i}{2}\sum_n \tilde{\gamma}_n \gamma_{n+\alpha}. \tag{3.4}$$

These are pictorially represented in Fig. 2.1. We indeed see that for a given α, this can be seen as a stack of $|\alpha|$ copies of $H_{\pm 1}$ (depending on the sign of α). Note that $H_1 = H_K$ and $H_0 = \sum_n \left(1/2 - c_n^\dagger c_n\right)$, the trivial band insulator. This class of long-range Kitaev chains has been considered before in a non-interacting context [116]; in Section 2.2 we discussed their *non-interacting* topological invariant. Their (interacting) SPT properties have been uncovered in the context of stacks of Kitaev chains [16, 17]. Here we first revisit their SPT nature in an equivalent but slightly different language, before illuminating how the α-chain maps to other models by local redefinitions. Non-local transformations to spin chains via a Jordan-Wigner transformation are discussed in Section 3.3. We first discuss the topological nature of the 2-chain before discussing the case for general α.

Symmetry fractionalization of the 2-chain

For $\alpha = 2$, the left (right) has Majorana edge modes γ_1, γ_2 ($\tilde{\gamma}_N, \tilde{\gamma}_{N-1}$). These can be gapped out by the Hermitian perturbation $i\gamma_1\gamma_2$ ($i\tilde{\gamma}_N\tilde{\gamma}_{N-1}$), but this is not invariant under complex conjugation $T = K$. (Note that $T\gamma T = \gamma$ and $T\tilde{\gamma}T = -\tilde{\gamma}$ since we define c and $c^\dagger$ to be invariant.) In fact, T protects a Kramers pair on the right edge, and PT on the left. To see this, let us define the fermionic edge modes

$$\begin{cases} c_L &= \frac{1}{2}\left(\gamma_1 + i\gamma_2\right) \\ c_R &= \frac{1}{2}\left(\tilde{\gamma}_{N-1} + i\tilde{\gamma}_N\right). \end{cases} \tag{3.5}$$

It follows that $Tc_LT = c_L^\dagger$ and $Tc_RT = -c_R^\dagger$ (and oppositely for PT). From this one can derive that

$$\begin{cases} T^2|0\rangle_L &= |0\rangle_L \\ T^2|0\rangle_R &= -|0\rangle_R, \end{cases} \tag{3.6}$$

where we have defined $c_{L,R}|0\rangle_{L,R} = 0$. On first sight, this seems to contradict $T^2 = 1$, however performing the same calculation for *both* edges gives $T^2\left(|0\rangle_L \otimes |0\rangle_R\right) = |0\rangle_L \otimes |0\rangle_R$ (the extra minus sign coming from $c_Lc_R = -c_Rc_L$). These properties are summarized in row '$\alpha = 2$' of Table 3.1.

The fact that any fermionic Hamiltonian has parity symmetry P begs the question whether the statement "T (PT) protects the right (left) edge" has tangible consequences. To confirm it does, consider the Jordan-Wigner transformation which can map the 2-chain to a spin model. This non-local transformation involves string operators which either start at the left or right edge. If the string originates from the right edge then local quantities near this edge will remain local in the new spin variables, hence T protecting a Kramers pair implies a non-trivial spin chain protected by T. Oppositely, starting from the left edge should give a *different* spin chain, now protected by PT. In Section 3.3 we see that this is indeed the case.

α	P	T	PT	total degeneracy
-3	non-local fermion	left, (right)	[left], right	8
-2		fermion on left	right	4
-1	non-local fermion	(left)	[right]	2
0				1
1	non-local fermion	[right]	(left)	2
2		right	left	4
3	non-local fermion	[left], right	left, (right)	8
4		left, right	left, right	4

Table 3.1.: **Symmetry fractionalization and edge degeneracies in the α-chains (3.4).** A 'non-local fermion' means P_L anti-commutes with P_R (as discussed for the Kitaev chain in section 3.1), whereas for example 'T left' means T protects a Kramers pair on the left edge. Round and square brackets correspond to inequivalent choices of fractionalizing complex conjugation in the presence of a non-local mode, i.e. for a given choice one only has one of the two (details in Appendix B). Different choices for distinct α still lead to invariants that distinguish the phases.

As in the cases discussed above, this can be formulated in terms of symmetry fractionalization, which is slightly more subtle for anti-unitary symmetries. If we choose a basis for our low-energy space, then on these basis states T acts as a unitary, with the fractionalization $T = U_L U_R$. Applying it twice, $1 = T^2 = (TU_LT)(TU_RT)U_LU_R$. This means that $TU_LTU_L = \pm 1$, with TU_RTU_R having the same (opposite) sign if $U_{L,R}$ is bosonic (fermionic). These signs correspond to the square of T on the edge modes, as in Eq. (3.6). In particular, in the basis defined by $c_{L,R}$, we obtain $U_L = \gamma_2$ and $U_R = \tilde{\gamma}_{N-1}$ (the derivation and other details are discussed in Appendix B), such that indeed $TU_RTU_R = -1$, agreeing with Eq. (3.6). The approach of previous works [16, 17] was equivalent but different, opting for invariants which for $\alpha = 2$ would have T square to -1 on the *left* edge instead of the right. The above invariants strike us as more natural considering the physics of Eq. (3.6) and the ensuing discussion. Curiously, a recent approach [143] in terms of fermionic matrix product states does not have a spatial asymmetry in the fractionalization of T (which suggest it might be implicitly describing a Jordan-Wigner transformed chain, cf. Section 3.3).

Symmetry fractionalization of the α-chain

Stacks of Kitaev chains have played an important role in elucidating the classification of interacting SPT phases in one dimension [16, 17] and it was realized that upon enforcing P and T symmetry, there are eight possible phases. These correspond to $\alpha = 0, 1, \cdots 7$ forming the group $\mathbb{Z}_8$ under SPT addition. In particular, Kitaev and Fidkowski [32] have shown that a stack of eight non-interacting chains can be smoothly connected to a trivial phase if one allows for interactions (i.e., not just quadratic terms). Subsequently, the eight remaining possibilities have been understood in terms of symmetry fractionalization, proving their stability against symmetry-preserving interactions. We summarize the result (derived in Appendix B) in Table 3.1, using the cyclic nature of $\mathbb{Z}_8$ to instead choose the representatives $\alpha = -3, -2, \cdots, 4$ where the Hamiltonian (3.4) shows that negative α is the same as a left-right inverted $|\alpha|$-chain. For $-3 \leq \alpha \leq 3$, the low-energy subspace of one edge is too small to define interaction terms, hence they have the edge degeneracies we expect from the free fermion picture. For $\alpha = 4$, it was first discussed in Ref. [32] how the perturbation $\gamma_1\gamma_2\gamma_3\gamma_4$ lifts the fourfold degeneracy on the left edge of the 4-chain to

a twofold degeneracy, which cannot be lifted further due to time-reversal symmetry.

Left-right asymmetry

One peculiar feature of Table 3.1 is the spatial asymmetry of the symmetry protection, which is possible due to the explicit inversion symmetry breaking of the model (3.4): swapping left and right does not leave it invariant, but instead changes the sign of α. (We note that it is impossible in bosonic SPT phases for different edges to be protected by different symmetries, however it is possible for them to have different projective representations on each edge [144].) For $\alpha = 4$, however, we see the same symmetries protect each edge, and indeed the fractional symmetries turn out to be bosonic. This means it cannot be represented in a free fermion system. In fact, as we discuss in subsection 3.2.3, it can be seen as a spin SPT phase. Note that none of these eight phases can be connected by a path of gapped local Hamiltonians preserving P and T. However $\alpha \leftrightarrow -\alpha$ are in the same phase according to the alternative notion discussed in Section 3.1, allowing paths which smoothly change the (on-site) representation of the anti-unitary symmetry from T to PT.

$O(|\alpha|)$ symmetry of the α-chain

Here we briefly discuss a symmetry which will be useful for what follows. As had first been observed in Ref. [32], a stack of α decoupled Kitaev chains has an $O(|\alpha|)$ symmetry. Conceptually this corresponds to rotating the chains into one another. On a mathematical level this is easy to see: if $\alpha > 0$ we define $\boldsymbol{\gamma}_n = (\gamma_{\alpha n}, \gamma_{\alpha n+1} \cdots, \gamma_{\alpha n+(\alpha-1)})$ and similarly $\tilde{\boldsymbol{\gamma}}_n$, since then $H_\alpha = \frac{i}{2} \sum_n \tilde{\boldsymbol{\gamma}}_n \cdot \boldsymbol{\gamma}_{n+1}$. The Hamiltonian is invariant under the linear action of $O(\alpha)$ on the vectors and this rotation preserves the Hermitian nature and canonical commutation relations $\{\gamma_i, \gamma_j\} = 2\delta_{ij}$ and $\{\gamma_i, \tilde{\gamma}_j\} = 0$.

The 2- and 4-chain: SSH and Haldane

In the following two subsections we focus on the cases $\alpha = 2$ and 4 respectively, uncovering their relationships to other known and new models. We first summarize some relevant observations by Fidkowski and Kitaev [16]: firstly, as we have seen for $\alpha = 2$, each edge has a single complex fermionic zero mode. This is the same physics as the Su-Schrieffer-Heeger (SSH) model [28], whose Hamiltonian and properties we will soon discuss. Secondly, for $\alpha = 4$, the aforementioned $O(4)$ symmetry was realized to have an $SO(3)$ subgroup that acts projectively on the boundary. Combined with the non-trivial anti-unitary symmetry (cf. Table 3.1), the 4-chain was henceforth labeled as being in the Haldane phase, a spin SPT phase with the same algebraic structure. We discuss these statements in more detail in subsections 3.2.2 and 3.2.3.

We show that these connections can be made surprisingly simple and concrete, which we summarize here before going into detail: in subsection 3.2.2 the 2-chain is shown to *coincide* with the SSH model after a two-site change of basis. Moreover, this then implies the 4-chain can be seen as a spinful SSH model. In subsection 3.2.3 we use this to rewrite the *interacting* 4-chain as a Hubbard model of spinful fermions where in the Mott limit the charge degrees of freedom are frozen out and the effective spin-$\frac{1}{2}$ model simply has alternating Heisenberg bonds (without any phase transition). Its ground state is the fixed point limit of the Affleck-Kennedy-Lieb-Tasaki (AKLT) [25] state, a canonical example of the Haldane phase. This leads to a much simplified constructive proof of the 8-chain being adiabatically connected to a trivial chain.

It is interesting to keep track of the symmetries in the case of the 4-chain, since this gives us insights into the stability of spin SPT phases when deviating away from the Mott limit (i.e., in the presence of charge fluctuations). In subsection 3.2.3, we rewrite

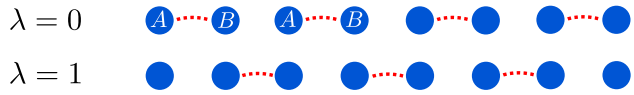

Figure 3.2.: **The Su-Schrieffer-Heeger (SSH) model** (3.9)**.** We observe fermionic edge modes for $\lambda = 1$.

the interacting 4-chain as a so-called bipartite Hubbard model, which is known to have an $SO(4)$ symmetry [145]. This coincides with the $SO(4) \subset O(4)$ symmetry of the non-interacting 4-chain mentioned above, surviving interactions. However, the $SO(3) \subset SO(4)$ which is realized projectively on its edge, does *not* correspond to spin rotation symmetry in the language of the Hubbard model. Nevertheless, in the Mott limit this $SO(3)$ does become *indistinguishable* from spin rotation symmetry (protecting the Haldane phase). This is a saving grace: it is known [139] that the Haldane phase is not stable under charge fluctuations if one preserves spin rotation symmetry, however as a by-product of our construction we see the Haldane phase *is* protected by this *other* $SO(3)$ symmetry (or a $\mathbb{Z}_2 \times \mathbb{Z}_2$ subgroup thereof). Similarly, we will see the Hubbard chain is protected by an anti-unitary sublattice/particle-hole symmetry, in the Mott limit coinciding with the usual spinful time-reversal symmetry protecting the Haldane phase.

This underlines the fact that whether or not a spin SPT phase is stable under charge fluctuations (i.e. away from the Mott limit) depends on how the symmetry acts on the charge degrees of freedom. In particular, in the Mott limit, the Haldane phase can equivalently be said to be protected by spinful time-reversal *or* fermionic sublattice symmetry—their action being indistinguishable. It is only *away* from the Mott limit that the latter—not the former—continues to protect the phase.

3.2.2. The 2-chain is the Su-Schrieffer-Heeger model

We now relate the 2-chain to the Su-Schrieffer-Heeger (SSH) [28] model. The latter is a fermionic chain with a $U(1)$ particle conservation symmetry (its Hamiltonian given by Eq. (3.9)). On the other hand, the 2-chain has superconducting terms, but as has been pointed out above it does have an $O(2)$ symmetry. Indeed if $\boldsymbol{\gamma}_n = (\gamma_{2n-1}, \gamma_{2n})$ and $\tilde{\boldsymbol{\gamma}}_n = (\tilde{\gamma}_{2n-1}, \tilde{\gamma}_{2n})$, then $H_2 = \frac{i}{2}\sum_n \tilde{\boldsymbol{\gamma}}_n \cdot \boldsymbol{\gamma}_{n+1}$. By relabeling some operators, we should be able to let the $SO(2) \subset O(2)$ act as a fermionic $U(1)$ phase symmetry. Note that this will have to involve mixing γ and $\tilde{\gamma}$, since if $c \to e^{i\alpha}c$ and $\gamma = c + c^\dagger$ then $\gamma \to \gamma\cos\alpha - \tilde{\gamma}\sin\alpha$. Let us make this more precise for the interpolation between the 2-chain and the trivial chain:

$$H_{\mathrm{SSH}} = (1-\lambda)H_0 + \lambda H_2 = (1-\lambda)\sum_n \frac{i}{2}\,\tilde{\gamma}_n\gamma_n + \lambda\sum_n \frac{i}{2}\,\tilde{\gamma}_n\gamma_{n+2}. \tag{3.7}$$

We then define A and B sublattices (i.e.: $A\ B\ A\ B\ A\ B\ ...$) and consider the new Majorana operators:

$$\begin{cases} \gamma_{A,n} &:= \gamma_{2n} \\ \tilde{\gamma}_{A,n} &:= \gamma_{2n-1} \\ \gamma_{B,n} &:= \tilde{\gamma}_{2n-1} \\ \tilde{\gamma}_{B,n} &:= -\tilde{\gamma}_{2n}. \end{cases} \tag{3.8}$$

In terms of the complex fermionic operators consisting of these new Majorana operators (i.e., $c_{A,n} = \frac{1}{2}(\gamma_{A,n} + i\tilde{\gamma}_{A,n})$), we obtain

$$H_{\mathrm{SSH}} = \sum_n \left[(1-\lambda)\, c^\dagger_{A,n}c_{B,n} + \lambda\, c^\dagger_{A,n+1}c_{B,n} + \mathrm{h.c.}\right]. \tag{3.9}$$

This is exactly the Hamiltonian of the SSH model, schematically shown in Fig. 3.2. This undergoes a quantum phase transition at $\lambda = \frac{1}{2}$ and has protected edge modes for $\lambda > \frac{1}{2}$. What about the symmetries protecting it? Relabel the 2-chain symmetries as $\mathcal{C}_B := T$ and $\mathcal{C}_A := PT$. From Eq. (3.8) we see that the way they act on these new variables is as follows:

$$\mathcal{C}_B \, c_A \, \mathcal{C}_B = c_A^\dagger \qquad \text{and} \qquad \mathcal{C}_B \, c_B \, \mathcal{C}_B = -c_B^\dagger \tag{3.10}$$

and similarly for $\mathcal{C}_A$. So our anti-unitary symmetries are particle-hole/sublattice symmetries. Despite $\mathcal{C}_B$ acting as a commuting anti-unitary symmetry on the Fock space Hamiltonian, one can check that it acts like an anti-commuting unitary on *single-particle* Hamiltonians, i.e., this corresponds to the sublattice symmetry used in the non-interacting classification. Transposing our knowledge of the symmetry fractionalization of the 2-chain, we know that for $\lambda = 1$ the $\mathcal{C}$ symmetries fractionalize with $\mathcal{C}_A$ protecting the fermionic mode on the left, and $\mathcal{C}_B$ similarly on the right (and which on general grounds must be stable until the critical point at $\lambda = \frac{1}{2}$). This also tells us that the non-interacting label $\mathbb{Z}$ for the AIII class reduces to $\mathbb{Z}_4$ in the presence of interactions. It is worth noting that the α-chains are stable under disorder whereas the SSH model is not (due to it requiring a sublattice symmetry), which is consistent with Eq. (3.8) mixing neighboring sites.

Identifying the two models

In effect the transformation (3.8) defines a local unitary U that maps the 2-chain to the SSH model. Since this unitary only acts *within* the unit cells, we know that $\mathcal{H}$, defined by $U = e^{i\mathcal{H}}$, also only acts within the unit cells. Hence one can define the local unitary evolution $U(\lambda) = e^{i\lambda\mathcal{H}}$ which smoothly connects the models at the level of the Hamiltonian. It gradually deforms the representation of the anti-unitary symmetry from T to $\mathcal{C}_B$, the crucial fact being that everywhere along this path the symmetry remains on-site (which for complex conjugation we take to mean that the basis it is defined in is on-site), which ensures that the symmetry fractionalization is everywhere well-defined. This is enough to say both models are in the same phase, as discussed in Section 3.1. The stronger statement that the unitary acts solely within the unit cells can be interpreted as the models not merely being in the same phase, but being virtually identical. To appreciate these facts, contrast it to the Kitaev chain mapping to the trivial chain under the local mapping $\gamma_n \to \gamma_{n-1}$, which one *cannot* implement by a local unitary evolution. Similarly, one can contrast it to how the 2-chain can be mapped to the trivial chain by a local unitary evolution, but such a path cannot keep the representations of the symmetries to be on-site.

3.2.3. The 4-chain as a Hubbard model and the AKLT chain

To gain insight into the interacting 4-chain, we first show how it can be rewritten as a bipartite Hubbard model, smoothly connecting to a simple spin chain in its Mott limit. As we noted above, the 4-chain does not have a non-interacting representation without accidental degeneracies: the perturbation $\gamma_1\gamma_2\gamma_3\gamma_4$ lifts the fourfold degeneracy of the left edge into a twofold one, which according to Table 3.1 cannot be lifted further if we preserve P and T. So let us consider $H_{\text{Hub}} = H_4 + V + \tilde{V}$ where

$$V = \frac{U}{4} \sum_{m=1}^{\frac{N}{4}} \gamma_{4m-3}\gamma_{4m-2}\gamma_{4m-1}\gamma_{4m} \tag{3.11}$$

and similarly for $\tilde{V}$ with $\gamma \leftrightarrow \tilde{\gamma}$. The key idea is that we should be able to see the 4-chain as a stack of two SSH chains, or alternatively as a single SSH model with an extra spin-$\frac{1}{2}$ degree of freedom. To make this more explicit, we first redefine $\gamma_{2n} = \gamma_{n,\downarrow}$ and

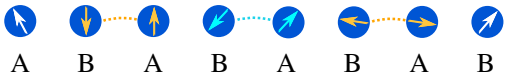

Figure 3.3.: **The bipartite Hubbard chain, Eq.** (3.13)**, where each edge is occupied by a single spinful fermion.** For $U = 0$ this is a double copy of the SSH state ($\lambda = 1$) in Fig. 3.2. For $U \to \infty$ this reduces to the AKLT fixed point state in Fig. 3.4.

$\gamma_{2n-1} = \gamma_{n,\uparrow}$ and then perform the transformation shown in Eq. (3.8) for each spin sector. For clarity, we summarize the resulting mapping:

$$\begin{cases} c_{A,n,\uparrow} = \frac{1}{2}\left(\gamma_{4n-1} + i\gamma_{4n-3}\right) & c_{A,n,\downarrow} = \frac{1}{2}\left(\gamma_{4n} + i\gamma_{4n-2}\right) \\ c_{B,n,\uparrow} = \frac{1}{2}\left(\tilde{\gamma}_{4n-3} - i\tilde{\gamma}_{4n-1}\right) & c_{B,n,\downarrow} = \frac{1}{2}\left(\tilde{\gamma}_{4n-2} - i\tilde{\gamma}_{4n}\right). \end{cases} \tag{3.12}$$

In these new variables we obtain

$$H_{\text{Hub}} = \sum_{n,\sigma}\left(c^\dagger_{A,n+1,\sigma}c_{B,n,\sigma} + \text{h.c.}\right) + U\sum_{\lambda,n}\left(n_{\lambda,n,\uparrow} - \frac{1}{2}\right)\left(n_{\lambda,n,\downarrow} - \frac{1}{2}\right), \tag{3.13}$$

where $\lambda = A, B$ is the sublattice index. So we see the interacting 4-chain is in fact a bipartite Hubbard chain, shown in Fig. 3.3. We note that this topological chain was investigated in Ref. [146] using Green's functions. As long as $U > 0$, the edges will prefer single occupancy, giving a twofold degeneracy on each edge. It can straightforwardly be proven that the gap of Eq. (3.13) does not close as we increase U (see e.g. the discussion by Anfuso and Rosch [139]), in the Mott limit giving an antiferromagnetic spin chain $H_{\text{Hub}} \xrightarrow{\text{large } U} \frac{4}{U}\sum_n \boldsymbol{S}_{B,n} \cdot \boldsymbol{S}_{A,n+1}$. Its ground state is simply a string of disjoint singlets with free spin-$\frac{1}{2}$ modes on the edges.

Relation to the AKLT model

The AKLT model [25] is given by the spin-1 Hamiltonian $H = \sum_n \boldsymbol{S}_n \cdot \boldsymbol{S}_{n+1} + \frac{1}{3}\left(\boldsymbol{S}_n \cdot \boldsymbol{S}_{n+1}\right)^2$. This is in the same phase as the spin-1 Heisenberg chain, but the difference is that its ground state is exactly known. In fact, it is the *same* as the ground state of the above (large-U) bipartite Hubbard chain, with an additional spin-1 projector on every 'AB' unit cell. The projection is in a sense immaterial: it leaves the entanglement spectrum *between* the unit cells unchanged, moreover the projector naturally disappears under the renormalization group flow as defined in Ref. [147]. In this sense one can say that the ground state of the above Hubbard chain in the Mott limit is exactly the fixed point limit of the AKLT state. This simple ground state is naturally in the Haldane phase: while the bulk is invariant under $SO(3)$ and T_{spin} (both of which are non-projective when applied to the unit cells), the edges transform as spin-$\frac{1}{2}$'s. The topological invariants of that projective representation define the celebrated Haldane phase. However, if we instead look at the relevant symmetries from the fermionic perspective, a different story emerges.

Hubbard chain protected by sublattice symmetry

As a direct spin-off of subsection 3.2.2, we know that the Hubbard chain is an SPT phase protected by the anti-unitary sublattice/particle hole symmetry $\mathcal{C}_A$ defined in (3.10), which leaves the spin degree of freedom untouched. On first sight this seems unrelated to the symmetries of the Haldane phase, but in the Mott limit this reduces to $T_{\text{spin}} = e^{i\pi S^y}K$ which is known to protect the edge modes. Indeed: if $\boldsymbol{S} \coloneqq \frac{1}{2}c^\dagger_s \boldsymbol{\sigma}_{ss'} c_{s'}$ then by Eq. (3.10) we see that $\mathcal{C}_{A,B}$ are anti-unitaries that map $\boldsymbol{S} \to -\boldsymbol{S}$. (Moreover for any SPT phase protected by T_{spin}, globally $T^2_{\text{spin}} = 1$, even if it squares to -1 on-site.) Hence we can say

that in the Mott limit we cannot distinguish between T_{spin} and $\mathcal{C}_A$ (or $\mathcal{C}_B$). However, away from the Mott limit, their difference is essential, as we discuss now.

Fragility versus stability of spin SPT phases

In Ref. [139], it was shown that one can adiabatically connect the Haldane phase to the trivial phase if one allows for paths with fermionic degrees of freedom (i.e., away from the Mott limit). This is possible even if one preserves T_{spin}, which was interpreted as a sign of fragility of (bosonic) SPT phases with respect to charge fluctuations. However, here we see there is no fragility if we replace T_{spin} by $\mathcal{C}_A$. Let us briefly repeat the reason why the Haldane phase is not stable against charge fluctuations [35, 36] in the presence of T_{spin}. The reason it *is* protected in the Mott limit, is because $T_{\text{spin}}^2 = 1$ in the bulk—since we have an even number of spin-$\frac{1}{2}$s—from which one can deduce that on the edge it has to square to ± 1, giving us a well-defined discrete invariant. But if every site no longer has exactly one fermion, we instead have $T_{\text{spin}}^2 = P$, where P denotes the parity of the number of fermions, from which one can argue that its square on the edge can be smoothly deformed from -1 to 1. It is then clear why $\mathcal{C}_A$ *does* manage to protect the edge modes: it *always* squares to the identity. Hence, there is no fragility with respect to this symmetry.

Hubbard chain protected by $\mathbb{Z}_2 \times \mathbb{Z}_2$

Instead of time-reversal symmetry, the Haldane phase can also be protected by rotation symmetry: the global π-rotations $R_x = e^{i\pi S_x}$ and $R_y = e^{i\pi S_y}$ form a $\mathbb{Z}_2 \times \mathbb{Z}_2$ group (note that $R_z = R_x R_y$) that fractionalizes as spin-$\frac{1}{2}$ representations on the boundaries, i.e. $R_x^L R_y^L = -R_y^L R_x^L$. However, similarly to above [35, 36], this does not protect the phase under charge fluctuations due to $R_x^2 = P$. As in the previous paragraph, one might wonder: although R_x and R_z do not protect the SPT phase, there might be a $\mathbb{Z}_2 \times \mathbb{Z}_2$ symmetry of the Hubbard chain which in the Mott limit becomes indistinguishable from the above spin rotation symmetry. Indeed, we introduce two unitary symmetries $\tilde{R}_x$ and $\tilde{R}_y$ which *always* obey a $\mathbb{Z}_2 \times \mathbb{Z}_2$ group structure and in the Mott limit reduce to R_x and R_y. This automatically proves that they protect the Hubbard ladder for arbitrary interaction U. We define $\tilde{R}_x$ and $\tilde{R}_y$ as the unitary operators that square to one and act as:

$$\tilde{R}_x \, c_\uparrow \, \tilde{R}_x \;=\; c_\downarrow \qquad \text{and} \qquad \tilde{R}_y \begin{Bmatrix} c_{A,\sigma} \\ c_{B,\sigma} \end{Bmatrix} \tilde{R}_y = \begin{Bmatrix} c_{A,\sigma}^\dagger \\ -c_{B,\sigma}^\dagger \end{Bmatrix} . \tag{3.14}$$

Then $\tilde{R}_x$ maps $\boldsymbol{S} \to (S_x, -S_y, -S_z)$ and $\tilde{R}_y$ maps $\boldsymbol{S} \to (-S_x, S_y, -S_z)$. Hence for large U the actions of $\tilde{R}_x$ and $\tilde{R}_z$ are indistinguishable from R_x and R_y. In conclusion, in the large U limit we can identify the symmetries R_x, R_y and T_{spin} with $\tilde{R}_x$, $\tilde{R}_y$ and $\mathcal{C}_B$, but the latter set protects the Haldane phase even in the presence of charge fluctuations. (Moreover, note that $\mathcal{C}_B = \tilde{R}_y K$, extending $T_{\text{spin}} = R_y K$.)

It is known that the bipartite Hubbard model in fact has a much bigger on-site $SO(4)$ symmetry [145]. In terms of our original Majorana description in Eq. (3.11), if we define the vector $\boldsymbol{\gamma}_n = (\gamma_{4n-3}, \gamma_{4n-2}, \gamma_{4n-1}, \gamma_{4n})$ and similarly $\tilde{\boldsymbol{\gamma}}_n$, then each element of $A \in SO(4)$ simply acts *linearly* on this vector. Indeed, $H_4 = \frac{i}{2} \sum_n \tilde{\boldsymbol{\gamma}}_n \cdot \boldsymbol{\gamma}_{n+1}$ is rotationally invariant and the interaction terms are of the form $\gamma_1\gamma_2\gamma_3\gamma_4 = \epsilon_{i_1 i_2 i_3 i_4} \gamma_{i_1}\gamma_{i_2}\gamma_{i_3}\gamma_{i_4}$ such that $V \to \det(A)\, V$, thus the non-interacting $O(4)$ symmetry is broken down to $SO(4)$. The above $\mathbb{Z}_2 \times \mathbb{Z}_2$ symmetry group is a subgroup of this $SO(4)$: one can rewrite the action of Eq. (3.14) in terms of matrices which act linearly on the original Majorana variables, i.e.

$$\tilde{R}_x = \begin{pmatrix} \sigma_x & 0 \\ 0 & \sigma_x \end{pmatrix}, \qquad \tilde{R}_y = \begin{pmatrix} -\mathbb{I}_2 & 0 \\ 0 & \mathbb{I}_2 \end{pmatrix}. \tag{3.15}$$

In addition, we can write these in terms of generators of the Lie algebra $\mathfrak{so}(4)$, i.e. $\tilde{R}_{x,y} = \exp\left(i\pi\tilde{S}_{x,y}\right)$ where

$$\tilde{S}_x = \frac{i}{2}\begin{pmatrix} 0 & -\mathbb{I}_2+\sigma_x \\ \mathbb{I}_2-\sigma_x & 0 \end{pmatrix}, \qquad \tilde{S}_y = \begin{pmatrix} \sigma_y & 0 \\ 0 & 0 \end{pmatrix}. \tag{3.16}$$

Note $\tilde{R}_z = \tilde{R}_x\tilde{R}_y = \exp\left(i\pi\tilde{S}_z\right)$ where $i\tilde{S}_z = [\tilde{S}_x, \tilde{S}_y]$. These operators satisfy the angular momentum algebra $[\tilde{S}_a, \tilde{S}_b] = i\varepsilon_{abc}\tilde{S}_c$, generating an $SO(3)$ subgroup of $SO(4)$. Thus there is the chain of symmetry groups $\mathbb{Z}_2 \times \mathbb{Z}_2 \subset SO(3) \subset SO(4)$, each of which can be said to protect the edge modes. This agrees with the observation by Fidkowski and Kitaev that the $SO(4)$ symmetry of the interacting 4-chain has an $SO(3)$ subgroup which transforms the edges under a spin-$\frac{1}{2}$ representation [32]. In terms of the variables of the Hubbard chain (3.13), in the Mott limit the above $SO(3)$ is indistinguishable from spin rotation acting on the unit cells.

Connecting the 8-chain to the trivial chain

We note that having connected the 4-chain to the Haldane phase gives an alternative construction of an adiabatic path from a stack of eight Kitaev chains to the trival phase, which is considerably less technically involved than the original construction of Ref. [32]. Interestingly, the path which we consider here in detail, was already sketched in Ref. [146]. More precisely: one first tunes the 8-chain to a stack of two decoupled spin chains with alternating (intra-chain) Heisenberg bonds. Now adiabatically turn off the intra-chain couplings and turn on the inter-chain Heisenberg couplings. This does not close the gap since it reduces to the four-spin problem $H = t\,(\boldsymbol{S}_1\cdot\boldsymbol{S}_2 + \boldsymbol{S}_3\cdot\boldsymbol{S}_4) + (1-t)\,(\boldsymbol{S}_1\cdot\boldsymbol{S}_3 + \boldsymbol{S}_2\cdot\boldsymbol{S}_4)$, whose distinct eigenvalues—there are maximally six due to $\frac{1}{2}\otimes\frac{1}{2}\otimes\frac{1}{2}\otimes\frac{1}{2} = 0\oplus 0\oplus 1\oplus 1\oplus 1\oplus 2$—can be obtained after some algebra, giving the gap $\sqrt{3\left(t-\frac{1}{2}\right)^2+\frac{1}{4}}$. The resulting phase is trivial: turning off the interactions leads us to a spinful version of Hamiltonian (3.9) with $\lambda = 0$.

Relation to previous work

As we have already mentioned at the end of subsection 3.2.1, Fidkowski and Kitaev [32] had observed that the algebraic properties of the interacting 4-chain resemble those of the well-known Haldane phase. The new result here is that the path from the 4-chain to such a spin chain is very simple and dictated by symmetries, directly leading to a close cousin of the AKLT model. This concrete path simultaneously raised and resolved the apparent paradox of the (in)stability of the Haldane phase with respect to charge fluctuations. We now point out the work of two other groups on the physics of the 4-chain.

In 2012, Rosch [35] showed how one can trivialize the 4-chain (seen as superconducting spinless fermions) if one allows couplings to spin*ful* fermions. More concretely, starting from a stack of a trivial spin chain and four Kitaev chains, a path to a completely trivial chain was constructed without breaking time-reversal symmetry (TRS). Indeed, if we only preserve TRS in the presence of charge fluctuations, we can first adiabatically transform our trivial spin chain to be in the Haldane phase. By the above, we now have a stack of *two* Haldane chains, which can clearly be trivialized. Interestingly, that work defined variables very similar to the above (3.12) but did *not* rewrite the Hamiltonian in terms of it. This is presumably due to a difference in philosophy: after defining the new variables, they were not seen as spinful fermions since the TRS of the original 4-chain does not act as TRS on these variables. Our approach, however, is to consider (3.12) as defining genuine spinful fermions, and conclude that the Hubbard chain (3.13) is simply not protected by TRS but instead by the sublattice/particle-hole symmetry $\mathcal{C}_A$.

We also mention the field theoretic works by You et al. [148, 149]. They showed that starting from the 4-chain, one can define spin operators out of these Majoranas whose effective continuum action—upon integrating out the fermionic degrees of freedom—is the *same* non-linear sigma model that is known to describe the Haldane phase [22]. Note that the work of Anfuso and Rosch [139] has shown it can be subtle to draw conclusions about topological properties of a gapped phase after having integrated out other gapped degrees of freedom if these sectors were not completely decoupled to begin with. In the works by You et al. this decoupling is ensured by requiring the condensation of a particular $\mathbb{Z}_2$ gauge field. Without a physical mechanism to ensure this condensation (unlike the Hubbard chain (3.13) which ensures the gauge constraint $\gamma_1\gamma_2\gamma_3\gamma_4 = -1$ for large U), one cannot *directly* transfer insights from the effective spin chain to the original fermionic one. It can however give very useful hints, and in Ref. [149] the knowledge of how to trivialize a stack of two Haldane chains was used to explicitly construct a path of the interacting 8-chain to the trivial phase. Nevertheless, although this leads to a natural *construction*, to actually *confirm* the presence of a gap one still has to solve a rather complicated problem involving 16 Majoranas, for which exact diagonalization (ED) was used. This is similar to the original path proposed by Kitaev and Fidkowski [32], where in addition to ED there was also a non-trivial analytic argument involving perturbation theory and the representation theory of $SO(8)$. Hence, to the best of our knowledge, having rewritten the 4-chain as (3.13) has led to the simplest explicit path from the 8-chain to the trivial chain, since it allows us to *directly* use the spin chain results. It would be interesting to see if this approach can be helpful for the general program laid out in Ref. [149], which elucidates the effect of interactions on fermionic SPT phases in higher dimensions by using known results for bosonic SPT phases.

3.3. Topological spin chains

3.3.1. The α-chains map to generalized cluster models

We now turn to spin SPT phases, focusing on spin chains which despite being *mathematically* equivalent to the above fermionic α-chains, are *physically* quite distinct. To this purpose, recall that in one dimension, the non-local Jordan-Wigner transformation relates fermionic chains to spin-$\frac{1}{2}$ chains (with open boundary conditions) and vice versa:

$$\begin{cases} \gamma_n = Z_1 Z_2 \cdots Z_{n-1} X_n \\ \tilde{\gamma}_n = Z_1 Z_2 \cdots Z_{n-1} Y_n. \end{cases} \tag{3.17}$$

This transformation is compatible with the property that under complex conjugation ($T = K$) we have $T\gamma_n T = \gamma_n$ and $T\tilde{\gamma}_n T = -\tilde{\gamma}_n$. A priori it is not clear that such a non-local transformation preserves locality of the Hamiltonian. There is however a simple criterion: a fermionic Hamiltonian is local if and only if the corresponding spin Hamiltonian is local and commutes with spin-flip symmetry $P = \prod_n Z_n$. Let us now consider what the α-chain is mapped to under Eq. (3.17).

In the simplest case one can take the 0-chain, which under Jordan-Wigner (JW) maps to a polarizing field $H = \sum_n Z_n$. More interesting is the well-known fact that the JW dual of the Kitaev chain H_K, i.e. the 1-chain, is the Ising chain $H_I = -\sum_n X_n X_{n+1}$. This illustrates how, despite the JW transformation not changing the energy levels, the non-local mapping typically changes the physics: here it relates an SPT phase to a symmetry-broken phase. As a next step, consider the JW dual of the 2-chain. Compared to the Kitaev chain, the Majorana operators are now one site further apart and hence one Z of the JW string is not canceled, leading to the cluster model $H_C = -\sum_n X_{n-1} Z_n X_{n+1}$. This structure naturally extends to all α-chains as shown in Table 3.2, where we see that

Fermionic α-chain $2H_\alpha$ (3.4)	Spin Hamiltonian after Jordan-Wigner (3.17)	$f(z)$
$\vdots$	$\vdots$	$\vdots$
$\sum i\tilde{\gamma}_n\gamma_{n-2}$	$-\sum Y_n Z_{n+1} Y_{n+2}$	z^{-2}
$\sum i\tilde{\gamma}_n\gamma_{n-1}$	$-\sum Y_n Y_{n+1}$	z^{-1}
$\sum i\tilde{\gamma}_n\gamma_n$	$\sum Z_n$	1
$\sum i\tilde{\gamma}_n\gamma_{n+1}$	$-\sum X_n X_{n+1}$	z
$\sum i\tilde{\gamma}_n\gamma_{n+2}$	$-\sum X_n Z_{n+1} X_{n+2}$	z^2
$\vdots$	$\vdots$	$\vdots$
$\sum i\tilde{\gamma}_n\gamma_{n+\alpha}$	$-\sum X \underbrace{Z \quad \cdots \quad Z}_{\alpha-1} X$	z^α

Table 3.2.: **The α-chain and its Jordan-Wigner transform.** For convenience, we also list the associated polynomial $f(z)$ introduced in Chapter 2. This polynomial easily allows to solve any Hamiltonian which is a sum of these fermionic or bosonic Hamiltonians, as explained in Section 2.3.

the spatial inversion ($\alpha \leftrightarrow -\alpha$) on the fermionic side corresponds to $X \leftrightarrow Y$ on the spin side.

These generalized cluster models first appeared in the literature in 1971 as the quantum chains dual to certain two-dimensional classical dimer models [27] (there referred to as generalized XY models). In modern times they have resurfaced in studies of their phase transitions: first in context of exact results for their critical entanglement scaling [135] and more recently concerning conjectures for their conformal field theories [138, 150]. On the other hand, it seems the physics of these *gapped* spin chains has been left relatively unexplored. In particular, it is interesting to check how the physics of these spin models resembles or differs from the SPT structure of their fermionic counterparts. We will see these generalized cluster models exhibit rich physics despite their simplicity.

The cluster model ('XZX') and the 2-chain

The special case of $\alpha = 2$, the cluster model, is known [134] to be in an SPT phase protected by the $\mathbb{Z}_2 \times \mathbb{Z}_2$ symmetry group generated by $P_1 = \prod_{n \text{ odd}} Z_n$ and $P_2 = \prod_{n \text{ even}} Z_n$. However, we now show that the mapping (3.17) between the 2-chain and the cluster model uncovers a hitherto-unknown symmetry which also protects the model. In subsection 3.2.1, we saw that the right edge of the 2-chain has a Kramers pair with respect to $T = K$, and the left edge with respect to PT. Since the Jordan-Wigner transformation (3.17) has its string starting at the left edge, the leftmost region of the 2-chain and the cluster model should have the *same* local physics. We conclude that the cluster model has a Kramers pair on the left edge with respect to $PT = (\prod_n Z_n)\, K$. As discussed in subsection 3.2.1, for a bosonic system an anti-unitary symmetry squares to the same sign on both edges. Hence, unlike the 2-chain, PT protects *both* edges: the Jordan-Wigner transformation (3.17), which is highly non-local near the right edge, has changed the physics.

To see these statements within the spin language, first consider that Section 3.1 implies $P = P_L P_R$ with $P_L = Y_1 X_2$ and $P_R = X_{N-1} Y_N$ (where we have used $P = P_1 P_2$). Secondly, in subsection 3.3.3 we show that the fractionalization of T is trivial, i.e. $T = U_L U_R$ with $U_L = U_R = 1$ when acting on some local basis of edge states. The latter implies that when acting on this same basis, $PT = V_L V_R$ with $V_{L,R} = P_{L,R}$. Hence on the left PT squares to $(PT)V_L(PT)V_L = -Y_1 X_2 Y_1 X_2 = -1$, and similarly on the right. This is summarized in row '$\alpha = 2$' of Table (3.3). The fact that PT protects the cluster model explains why, for example, $H_C + \varepsilon \sum_n Y_n$ still has well-defined edge modes, as can be verified using perturbation theory or the numerical density matrix renormalization group (DMRG) [12]

α	P	T	PT	total degeneracy
-3	broken	Kramers pair: left, right	broken	8
-2		left, right		4
-1	broken	broken		2
0				1
1	broken		broken	2
2			left,right	4
3	broken	broken	left,right	8
4		left, right	left, right	4

Table 3.3.: **Symmetry breaking and fractionalization of the spin chains in Table 3.2.** This is with respect to $P = \prod Z_n$ and $T = K$. 'Kramers pair on left' means the anti-unitary symmetry squares to -1 there.

method. This new non-trivial symmetry can guide us to further insights—which we discuss in subsection 3.3.2.

Symmetry fractionalization of the generalized cluster models

We now ask what the fractionalization is of these symmetries, P and T, for any of these generalized cluster models. We repeat that this is different from the fermionic results in Table 3.1 since the non-local nature of the JW transformation mixes the edge with the bulk. Table 3.3 was derived using the analytic methods introduced in subsection 3.3.3, and numerically confirmed with DMRG [12] using the entanglement perspective discussed in Ref. [151]. Note that the results are in line with what one would expect based on the Jordan-Wigner transformation: as discussed before, the Jordan-Wigner transformation whose string starts from the left end, should map the 2-chain to an SPT protected by PT. Similarly, starting from the right end should map it to a spin model protected by T. This is the same as starting from the left end but taking the spatially inverted 2-chain, i.e. the (-2)-chain, as confirmed by Table 3.3. Also note that Table 3.1 says that—at least in a particular gauge—the left end of the Kitaev chain ($\alpha = 1$) is protected by PT. This corresponds to the fact that the corresponding Ising chain spontaneously breaks $PT = (\prod_n Z_n)\, K$, whereas the dual of the (-1)-chain, $H = -\sum_n Y_n Y_{n+1}$, spontaneously breaks T.

The first symmetry of the resulting table is that like its fermionic dual, it only depends on $\alpha \mod 8$. The second symmetry is that swapping the T and PT columns is the same as changing the sign of α: from Table 3.2, $\alpha \leftrightarrow -\alpha$ is equivalent to $X \leftrightarrow Y$, which is achieved by the anti-unitary operator $\mathcal{O} = e^{i\frac{\pi}{4}\sum_n Z_n} K$, and indeed $\mathcal{O}\, T\, \mathcal{O} = PT$.

Symmetry breaking and/or SPT order

Before discussing generalized cluster models for specific α, let us observe their overall symmetry breaking and SPT properties. Every odd α has $\mathbb{Z}_2$ symmetry breaking. This is to be expected: the degeneracy ($= 2^\alpha$) is then not a multiple of 4, meaning we cannot associate it to bosonic modes on each edge. Hence there must be a degeneracy even with periodic boundaries, which for gapped phases in one dimension is always due to spontaneous symmetry breaking. In subsection 3.3.3 we show a general argument for the absence or presence of symmetry breaking that is self-contained in the spin language.

On the other hand, even α give rise to (purely) SPT phases. The four inequivalent even-α phases have a $\mathbb{Z}_2 \times \mathbb{Z}_2$ structure: each is its own inverse, and stacking any two non-trivial chains generates the third. This is to be contrasted with the $\mathbb{Z}_8$ of the eight fermionic SPT phases. The non-local JW transformation does not commute with the

procedure of stacking, in the sense that, for example, a stack of two cluster models does not correspond to a stack of two 2-chains under JW.

The symmetries of Table 3.3 imply that the only new phases (at least with respect to these symmetries) are $\alpha = 3, 4$, since the negative α are related to positive α by a symmetry transformation. In fact the models related by $\alpha \leftrightarrow -\alpha$ are in the same phase if we allow for paths of gapped local Hamiltonians that smoothly change the on-site representation of the symmetries, transforming T into PT (where, again, by 'on-site anti-unitary' we mean that the basis for complex conjugation is on-site). Hence, before turning to the cluster model in more detail in subsection 3.3.2, we discuss the physics of $\alpha = 3, 4$.

The '$XZZX$' cluster model

Interestingly, $\alpha = 3$ has both symmetry breaking *and* SPT order. In particular we find that the symmetry breaking order parameter[6] is a cluster-type term, $X_{n-1}Y_nX_{n+1}$, such that a symmetry-broken sector has the effective Hamiltonian $H_\pm = \pm\sum_n X_{n-1}Y_nX_{n+1}$. This still has PT as a symmetry and it turns out that its symmetry fractionalization is the same as for $\alpha = 2$. More generally: for odd $0 < \alpha < 4$, the α-chain spontaneously breaks into a ground state sector which is in the same phase as the $(\alpha - 1)$-chain with respect to the unbroken symmetry (and similarly for negative α). A particular manifestation is that the symmetry-broken ground state of the Ising chain is trivial.

The '$XZZZX$' cluster model

The case $\alpha = 4$ is again purely an SPT phase (and similar to the fermionic 4-chain one needs extra terms to lift accidental degeneracies: the Jordan-Wigner transform of Eqn. (3.11) gives terms of the form $X_nY_{n+1}X_{n+2}Y_{n+3} + (X \leftrightarrow Y)$). If one compares the symmetry fractionalization tables of the fermionic α-chain (Table 3.1) and the generalized cluster models (Table 3.3), the only non-trivial line that coincides is $\alpha = 4$. Hence one might be tempted to conclude these two are in the same phase. This is in fact not true, the fundamental reason being that the 'P' in the fermionic case is fermionic parity symmetry, which is intrinsic to the Hilbert space, whereas the 'P' in the spin models is spin-flip symmetry which one can explicitly break. More concretely: there can be no path of gapped local Hamiltonians connecting the fermionic $\alpha = 4$ to the bosonic $\alpha = 4$, even if we allow the on-site representation of the relevant symmetries to smoothly change. The difference becomes even more striking: in the following section, we show how the cluster model is in fact in the Haldane phase with all its discrete symmetries. Combining this with subsection 3.2.3, we know that there is a path connecting the fermionic 4-chain to the cluster model ($\alpha = 2$), which then proves there cannot be a path to the generalized cluster model with $\alpha = 4$.

3.3.2. The cluster state is the AKLT fixed point limit

The above showed that there are two sets of symmetries protecting the cluster model $H_C = -\sum_n X_{n-1}Z_nX_{n+1}$: firstly a pair of commuting unitary symmetries squaring to one (P_1 and P_2), and secondly an anti-unitary symmetry that squares to one (PT). For the SPT phase to survive, one needs to only preserve one of these sets. There is another well-known bosonic SPT phase with the same algebraic properties: the Haldane phase. As encountered in section 3.2, it is an SPT phase protected by either the group of π-rotations which *in the bulk* square to one (generated by $R_x = e^{i\pi S_x}$ and $R_y = e^{i\pi S_y}$) or by the time-reversal symmetry that squares to one ($T_{\text{spin}} = R_yK$).

[6] Indeed: a state with $XYX = \pm 1$ will satisfy $XZZX = 1$ since $(X_nY_{n+1}X_{n+2})(X_{n+1}Y_{n+2}X_{n+3}) = X_nZ_{n+1}Z_{n+2}X_{n+3}$.

Figure 3.4.: **The AKLT state.** The spins connected by dashed lines form spin singlets. The AKLT state has spin-1 projectors on the gray ovals [25] which disappear in the renormaliation group fixed point limit [147].

This similarity is in fact not accidental: the cluster state is actually in the Haldane phase! For this to be a meaningful statement, we first need to perform a change of basis so that the symmetry operators map to each other:

$$P_1 \to R_x, \qquad P_2 \to R_y, \qquad PT \to T_{\text{spin}}. \tag{3.18}$$

Note that this is possible because the operators share the same group properties. It turns out that after this change of basis, the spin cluster ground state is actually mapped exactly to the fixed point limit of the AKLT state encountered before, sketched in Fig. 3.4: each oval denotes a unit cell such that it has a linear representation of rotation and time-reversal symmetry. The dashed lines denote spin singlets on the bonds, with unconstrained spin-$\frac{1}{2}$'s on each edge, protected by the projective representations of the bulk symmetries.

Identifying symmetries

To make this connection more precise, let us start with our spin-$\frac{1}{2}$ cluster Hamiltonian $H_C = -\sum_n X_{n-1}Z_nX_{n+1}$. Note that although this is translation invariant, the symmetry P_1 is not, so if we want a new basis where this symmetry acts as R_x, then we need to artificially work with unit cells of two spins. We now define a unitary operator U which is a tensor product over these unit cells, acting in each cell as follows:

$$\begin{aligned}
|\uparrow\uparrow\rangle &\xrightarrow{U} & |s\rangle &\coloneqq \tfrac{1}{\sqrt{2}}(|\uparrow\downarrow\rangle - |\downarrow\uparrow\rangle),\\
|\uparrow\downarrow\rangle &\xrightarrow{U} & |x\rangle &\coloneqq \tfrac{1}{\sqrt{2}}(|\uparrow\uparrow\rangle - |\downarrow\downarrow\rangle),\\
|\downarrow\uparrow\rangle &\xrightarrow{U} & -|y\rangle &\coloneqq \tfrac{i}{\sqrt{2}}(|\uparrow\uparrow\rangle + |\downarrow\downarrow\rangle),\\
|\downarrow\downarrow\rangle &\xrightarrow{U} & i|z\rangle &\coloneqq \tfrac{i}{\sqrt{2}}(|\uparrow\downarrow\rangle + |\downarrow\uparrow\rangle).
\end{aligned} \tag{3.19}$$

The labels $|s, x, y, z\rangle$ which we define on the right-hand side of Eq. (3.19) imply their symmetry properties, e.g. $|y\rangle$ goes to minus itself under R_x or T_{spin}, but is invariant under R_y. Note that the unitary U is naturally determined by the symmetry considerations of (3.18): if we, for example, apply P_1 on the left-hand side of Eq. (3.19), then this is equivalent to applying R_x on the right-hand side. More concretely, its defining characteristics are $UP_1U^\dagger = R_x$, $UP_2U^\dagger = R_y$ and $U(PT)U^\dagger = T_{\text{spin}}$, accomplishing (3.18). Moreover, note that this can be done *smoothly*, similar to as we discussed in subsection 3.2.2.

The resulting Hamiltonian

Having used symmetries to obtain the relevant change of basis, we can now see how it affects the cluster model. Curiously, the unitary has the effect of factorizing the Hamiltonian: e.g.[7] $-X_1Z_2X_3$ becomes Y_2Y_3, and $-X_2Z_3X_4$ becomes X_2X_3. Thus the Hamiltonian in this basis is a sum of *disjoint* operators, which moreover turn out to be projectors:

$$\begin{aligned}
U\, H_C\, U^\dagger &= \sum_n (X_{2n}X_{2n+1} + Y_{2n}Y_{2n+1}) \\
&= -\sum_{\text{bond}} (|s\rangle\langle s| - |z\rangle\langle z|)
\end{aligned} \tag{3.20}$$

[7] More precisely, X_{2n} becomes X_{2n} and $Z_{2n-1}X_{2n}$ becomes $-X_{2n-1}$. Similarly $X_{2n-1} \Rightarrow Y_{2n-1}$ and $X_{2n-1}Z_{2n} \Rightarrow -Y_{2n}$.

The ground state of this is the state with a singlet $|s\rangle$ on each *bond* connecting the unit cells as in Fig. 3.4. As mentioned in subsection 3.2.3, it is obtained from the original AKLT state by a block-spin RG flow which does not change the bipartition entanglement spectrum [147]. An alternative way of checking that the cluster state and the fixed point limit of the AKLT state are the same is by comparing their matrix product state description[8]. As an aside, note that the cluster state is translation invariant, but its symmetries have a two-site unit cell. The change of basis swaps this: the AKLT state (Fig. 3.4) has a two-site unit cell, but its symmetries are on-site.

Consequences

This mapping can teach us a few things: for example the Haldane phase is also known to be protected by link inversion symmetry, which is lattice inversion about the center of a bond. So we can conclude that the cluster state is similarly protected by such a symmetry[9].

Moreover, it is known that the AKLT state is symmetric under continuous spin rotation. The fact that the cluster ground state must *also* have an $SO(3)$ symmetry is a priori surprising, given its definition. Similarly this implies the 2-chain and the SSH model ($\lambda = 1$), whose $O(2)$ symmetry we already discussed in Section 3.2, has a ground state with $SO(3)$ symmetry. Note that this is completely unrelated to the symmetries we discussed in Section 3.2 having to do with rotating the Kitaev chains into one another: that concerned symmetries of the Hamiltonian, whereas this $SO(3)$ is an emergent symmetry in the ground state. (It is worth pointing out that one can adiabatically turn on the $Z_{2n}Z_{2n+1}$ component in Eq. (3.20) without affecting the ground state, until one reaches an $SO(3)$-symmetric Hamiltonian: the alternating Heisenberg chain we have encountered before in Section 3.1 and subsection 3.2.3.)

In the other direction, the cluster state has been mainly investigated in the context of its power for measurement-based quantum computation. It was only later that it was realized that the AKLT state [152] and more generally the Haldane phase [153, 154] offer a similar resource. Our mapping makes this more direct, and illustrates how by identifying symmetries one can construct natural maps that relate seemingly different models. Note that both the cluster state and the AKLT state have been generalized to 2D, both of particular interest to measurement-based quantum computing, and it would be interesting to see to what extent this kind of symmetry-guided mapping can generalize.

Identifying 'XZX', 'AKLT', 'SSH' and the 2-chain

In Fig. 3.1 we summarize a few of the mappings related to the 2-chain. In particular we complete the circle by noting that if we use the JW transformation to map back our spin model in the new basis to fermions, we obtain the SSH model. Let us take this step by step: starting with the linear interpolation between the trivial chain and cluster model,

$$H = (1-\lambda)\sum_n Z_n \; - \lambda \sum_n X_{n-1}Z_nX_{n+1}, \tag{3.21}$$

then under Eq. (3.19) this maps to the alternating spin-$\frac{1}{2}$ XY-chain (which moreover continuously connects to the alternating Heisenberg chain):

$$UHU^\dagger = (1-\lambda)\sum_{n\text{ odd}}(X_nX_{n+1}+Y_nY_{n+1}) + \; \lambda \sum_{n\text{ even}}(X_nX_{n+1}+Y_nY_{n+1}). \tag{3.22}$$

[8] The MPS matrices for either state are $\mathbb{I}, X, iY, Z$. For the cluster state this is in the basis $|\uparrow\uparrow\rangle, |\uparrow\downarrow\rangle, |\downarrow\downarrow\rangle, |\downarrow\uparrow\rangle$. For the fixed point limit of the AKLT state this is in the $|s\rangle, |x\rangle, i|y\rangle, |z\rangle$ basis.

[9] It is however a bit unnatural: one inverts the lattice of unit cells but not the unit cells themselves; moreover there is a -1 factor for every unit cell in state $|\uparrow\uparrow\rangle$. Example: $|\downarrow\uparrow,\uparrow\uparrow\rangle \Rightarrow -|\uparrow\uparrow,\downarrow\uparrow\rangle$. Usual lattice inversion does not protect the cluster SPT phase.

Note that with respect to the unit cells which group together $(2m-1, 2m)$, this is trivial for $\lambda < \frac{1}{2}$ and in the Haldane phase for $\lambda > \frac{1}{2}$. After the usual Jordan-Wigner map (3.17), Eq. (3.22) coincides with the SSH model as shown in Eq. (3.9). Remember that the SSH model is protected by the sublattice/particle-hole symmetries $\mathcal{C}_{A,B}$ as defined in (3.10). One can check that $\mathcal{C}_A$ on the fermionic side (which protects the left edge) maps to T_{spin} on the spin side (which protects both edges), and similarly $\mathcal{C}_B$ (which protects the right edge) maps to PT_{spin} (which protects nothing). Again we see that the JW transformation changes the physics.

Note that Fig. 3.1 does not contain the connection between the interacting 4-chain and the AKLT state as discussed in subsection 3.2.3, which implies that the fermionic 4-chain can be adiabatically connected to the cluster model.

'$XZZZX$' is not in the Haldane phase

Similarly, one can subject the generalized cluster model with $\alpha = 4$ (which is also symmetric under P_1, P_2 and T) to the same mapping (3.19). We then obtain

$$H = \sum_{n \text{ even}} \left(X_n Z_{n+1} Z_{n+2} X_{n+3} + Y_n Z_{n+1} Z_{n+2} Y_{n+3}\right). \tag{3.23}$$

This is now a spin chain with the *same* discrete symmetries as the Haldane phase, i.e. R_x, R_y and T_{spin}, yet it is in a *different* symmetry class. It is protected by T_{spin}—like the Haldane phase—but *also* by $R_{x,y,z}T_{\text{spin}}$—unlike the Haldane phase. Moreover, it is *not* protected by π-spin rotations alone. In particular, one can derive $R_x^L = X_1 Z_2 Y_3$ and $R_y^L = Y_1 Z_2 X_3$, which clearly commute. This shows it is very different from the fermionic 4-chain, despite both on first sight sharing a similar symmetry fractionalization in Tables 3.1 and 3.3. This illustrates the physical subtleties of the Jordan-Wigner transform.

3.3.3. Kramers-Wannier dualities for the generalized cluster models

The generalized cluster models are all exactly soluble in terms of fermions, but it can often be cumbersome to extract the relevant information in the spin language. Here, we present a way of extracting the physics we have discussed so far—directly in the spin language. Many properties simply drop out, such as the occurrence of spontaneous symmetry breaking (only) for α odd and the symmetry fractionalization of the topological phases. Concretely, we show how any of the generalized cluster models can be mapped to a trivial spin chain using a type of Kramers-Wannier transformation. The original transformation [155] is a duality of the quantum Ising chain which relates the symmetry-broken phase to the trivial phase and vice versa. Here we generalize this mapping, which in particular will show that for periodic boundary conditions the ground state is unique for α even and twofold degenerate for α odd, implying symmetry breaking. Note that before repeating the original mapping, we first treat the case where α is even since it is simpler.

The case for α even

For clarity, we consider the cluster model (i.e. $\alpha = 2$), but the argument extends to other $\alpha = 2m$. Define the new spin operators $\tilde{X}_n = X_n$ and $\tilde{Z}_n = X_{n-1} Z_n X_{n+1}$. These indeed obey the Pauli algebra. Then $H_C = -\sum_n X_{n-1} Z_n X_{n+1} = -\sum_{n=1}^{N} \tilde{Z}_n$. Clearly the ground state is unique! Note that for open boundary conditions, $\tilde{Z}_1$ and $\tilde{Z}_N$ would not appear in the Hamiltonian, giving the correct edge degeneracies. This allows for a slightly different derivation of the symmetry fractionalization, e.g., $P_1 = \prod_{\text{odd}} Z = \prod_{\text{odd}} \tilde{Z} = \tilde{Z}_1 = X_N Z_1 X_2$, which we already knew. However, it also allows to calculate other fractionalizations such as that of $T = K$: since the mapping preserves complex

conjugation and the ground state subspace condition $\tilde{Z}_{2\leq n\leq N-1} = 1$ is also real, one easily obtains that $T = K'$, where K' is complex conjugation in the low energy subspace. I.e., T is trivial for the cluster state.

The case for α odd

Inspired by the above, one might similarly define $\tilde{Z}_n = X_n X_{n+1}$ for $H = -\sum_n X_n X_{n+1}$, but then there is no choice of $\tilde{X}_n$ that satisfies the Pauli algebra. However, if we redefine $\tilde{Z}_N = X_N$ for the last site, then choosing the domain-wall operators $\tilde{X}_n = Z_1 Z_2 \cdots Z_n$ gives the correct algebra. For periodic boundary conditions we obtain

$$H_I = -\sum_{n=1}^{N} X_n X_{n+1} = -\sum_{n=1}^{N-1} \tilde{Z}_n - \prod_{n=1}^{N-1} \tilde{Z}_n. \tag{3.24}$$

Now the ground state is clearly twofold degenerate. This constructions works for all odd α by extending it to $\tilde{Z}_n = X_n Z \cdots Z X_{n+\alpha}$ and $\tilde{Z}_N = X_N Z_1 \cdots Z_{\alpha-1}$, which indeed defines a consistent Pauli algebra with $\tilde{X}_n = \prod_{k=1}^{n} X_k Z \cdots Z X_{k+\alpha-1}$. The Hamiltonian is again of the form of Eq. (3.24) with a twofold degeneracy. Note that for open boundary conditions, the harmless product term drops away and $\alpha - 1$ terms disappear from the sum, giving a 2^α-fold degeneracy for these models.

4. Interacting gapless topological phases: symmetry-enriched criticality

The topological invariants studied in Chapter 3 relied on the presence of a bulk gap. More precisely, we required a finite bulk correlation length—which follows from having a gap [15]. This can also be seen phenomenologically: the zero-energy edge modes studied in Chapter 3 usually have a localization length ξ_{loc} equal to the bulk correlation length ξ. However, in Chapter 2, we already saw that it is possible that $\xi_{\text{loc}} < \xi$; in fact, ξ can blow up whereas ξ_{loc} remains finite (e.g., see Fig. 2.2). There are also *interacting* examples of critical chains hosting topologically protected edge modes, with either algebraic or exponential finite-size splitting [41–58]. This chapter provides a unifying framework for this phenomenon, placing it into the more general context of *symmetry-enriched quantum criticality*, which we introduce. The idea is simple: a given universality class can split into various *distinct* classes when additional symmetries are imposed. These can be distinguished by symmetry properties of either local or nonlocal scaling operators. The latter case provides a *topological invariant* and can imply emergent edge modes!

This novel concept unifies in two respects. First, as already mentioned, it offers a framework that incorporates previously studied examples, giving a common explanation for the observed edge modes at criticality—whilst also introducing qualitatively novel instances. Second, the invariants we introduce are direct generalizations of those studied in the gapped case, protecting edge modes in both settings. In particular, SPT and spontaneously symmetry-breaking phases correspond to the special cases where the bulk universality class is chosen to be trivial. This puts in perspective how much is left to be explored: one can repeat the study and classification for any choice of universality class. In this chapter, we focus on universality classes described by conformal field theories (CFTs).

Examples of symmetry-enriched criticality are hiding in plain sight. These tend to occur at phase transitions where the neighboring gapped phases are non-trivial (similar to the non-interacting case studied in Chapter 2). For example, a paradigmatic SPT phase is the Haldane phase, realized in the spin-1 Heisenberg chain [18, 22–24, 26, 156], discussed in Chapter 3. By introducing an easy-axis anisotropy, this can be driven to an Ising phase:

$$H_{\text{XXZ}} = J \sum_n \left(S_n^x S_{n+1}^x + S_n^y S_{n+1}^y + \Delta S_n^z S_{n+1}^z \right). \tag{4.1}$$

These two gapped phases are separated by an Ising critical point at $\Delta_c \approx 1.1856$ [157]. We point out that, although the bulk correlation length diverges, a twofold degeneracy with open boundaries remains exponentially localized, shown in Fig. 4.1. In this chapter, we show that this Ising CFT is topologically *enriched* by π-rotations around the principal axes (a $\mathbb{Z}_2 \times \mathbb{Z}_2$ group), explaining the observed edge modes.

These concepts apply to symmetry-enriched CFTs with a general on-site symmetry group G; we refer to them also as G-enriched CFTs, or G-CFTs for short. This is not only relevant for condensed matter systems—such as the example described above—but also to high-energy physics; in particular, G-CFTs can be related to discrete torsion of orbifold CFTs, arising in string theory [158–160], although edge modes had not yet been pointed out in that context. For illustrative purposes, we focus on two particular symmetry groups in this chapter: the unitary group $\mathbb{Z}_2 \times \mathbb{Z}_2$ and the anti-unitary $\mathbb{Z}_2 \times \mathbb{Z}_2^T$ (where complex conjugation is defined relative to an on-site basis). In particular, for the Ising CFT,

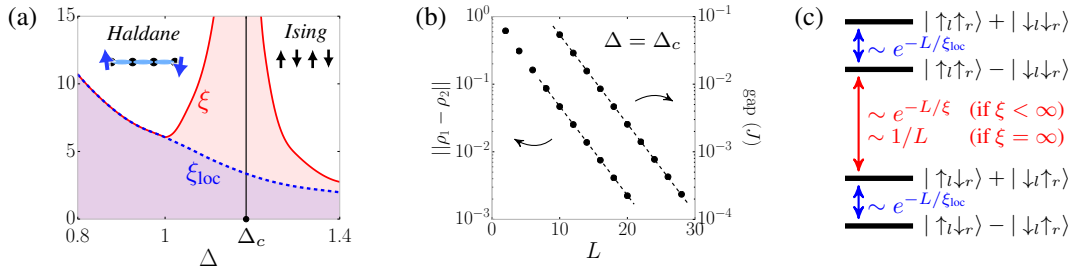

Figure 4.1.: **Persistent edge mode in spin-1 XXZ chain at criticality.** (a) The bulk correlation length ξ blows up, whereas the edge mode localization length ξ_{loc} stays finite. (b) The latter can be measured in two ways: firstly, the two ground states $|\uparrow_l\downarrow_r\rangle \pm |\downarrow_l\uparrow_r\rangle$ have a splitting which is exponentially small in system size L, or, equivalently, the two states differ by an operator which is exponentially localized near the edges (L is the region we trace out near an edge before calculating the distance of the two density matrices). The dashed lines are proportional to $\exp(-L/\xi_{\text{loc}})$ with $\xi_{\text{loc}} \approx 3.3$. (c) For $\Delta < \Delta_c$, the other states are split by the bulk correlation length, leading to an algebraic splitting at $\Delta = \Delta_c$. See Ref. [52] for the same physics in a different model.

the former (latter) gives rise to edge modes whose finite-size splitting is exponentially (algebraically) small in system size. For the algebraic splitting, we show that the power is remarkably high, $\sim 1/L^{14}$. We also discuss the classification of such symmetry-enriched CFTs, providing a complete answer for the Ising CFT with a general symmetry group G.

This chapter is organized as follows. Since the essential concepts can be readily understood, we give an overview in Section 4.1. This provides a self-contained summary for the reader in a hurry, and can serve as a guide to the other sections. In particular, it introduces and motivates the notion of *symmetry flux*: this is the key player throughout this chapter and allows us to define topological invariants at criticality. Moreover, Section 4.1 gives a sense of how this invariant protects edge modes at criticality. Symmetry fluxes and edge modes are discussed more systematically in Sections 4.2 and 4.3, respectively. Section 4.4 concerns the classification of G-enriched CFTs. In Section 4.5, we employ this concept of symmetry-enriched quantum criticality to show that some of the topologically non-trivial critical Majorana chains we discussed in Chapter 2 remain non-trivial in the presence of interactions. Finally, in Section 4.6, we show how previous works fit into our framework.

4.1. A conceptual overview

In this overview, we present the main messages of this chapter, introducing and motivating the relevant concepts by using the symmetry group $G = \mathbb{Z}_2 \times \mathbb{Z}_2^T$ as an illustrative example ($\mathbb{Z}_2^T$ denotes the group generated by an anti-unitary symmetry that squares to the identity). This overview can serve as a guide to the other sections—where definitions, examples and results are discussed in detail. Here we consider spin-1/2 chains, denoting the Pauli matrices by X, Y and Z as we have done in Chapter 3, and representing the symmetry group $\mathbb{Z}_2 \times \mathbb{Z}_2^T$ by the spin-flip $P \equiv \prod_n X_n$ and an anti-unitary symmetry given by complex conjugation in this basis, $T \equiv K$.

4.1.1. Bulk invariants from symmetry properties of operators

The key idea is that *symmetry properties of both local and nonlocal operators allow us to define discrete invariants*—even for critical systems. The simplest example is given by the

two critical Ising chains:

$$\begin{array}{rcl} H & = & -\sum_n (Z_n Z_{n+1} + X_n), \\ H' & = & -\sum_n (Y_n Y_{n+1} + X_n). \end{array} \tag{4.2}$$

Both are known to be described by the Ising universality class, or, equivalently, the conformal field theory (CFT) with central charge $c = 1/2$ [37]. This universality class has a *unique local* operator $\sigma(x)$ with scaling dimension $\Delta_\sigma = 1/8$ (meaning that $\langle \sigma(x)\sigma(0)\rangle \sim 1/x^{2\Delta_\sigma}$) [37]. There are various choices of microscopic operators on the lattice that generate this operator in the low-energy effective theory, e.g., $\sigma(x) \sim Z_n$ for H and $\sigma(x) \sim Y_n$ for H'. We observe that these two operators transform *differently* under complex conjugation T. We say that these two Ising CFTs are *enriched* by the $\mathbb{Z}_2^T$ symmetry T, with the former CFT obeying $T\sigma T = +\sigma$ and the latter $T\sigma T = -\sigma$. Indeed, one can argue that this charge is always *discrete*, i.e. $T\sigma T = \pm\sigma$, and that it is *well-defined*, i.e., all choices of lattice operators that generate σ in the low-energy effective theory have the same charge/sign *if* T is an unbroken symmetry[1]. This discrete invariant cannot change as long as we stay within the Ising universality class.

What is the consequence of such an invariant? It means that any G-symmetric path of gapless Hamiltonians connecting H and H' must at some point go through a different universality class. For example, consider the interpolation $\lambda H + (1-\lambda)H'$ (with $0 \le \lambda \le 1$): this is everywhere in the Ising universality class *except* at the halfway point $\lambda = 1/2$, where the system passes through a multi-critical point (with a dynamical critical exponent $z_{\text{dyn}} = 2$). Alternatively, $\lambda H - (1-\lambda)H'$ passes through a Gaussian fixed point (central charge $c = 1$) at $\lambda = 1/2$. (These claims can be straightforwardly derived using the tools of Chapter 2 and the correspondence[2] in Table 3.2.) It is at these non-Ising points that the property $T\sigma T = \pm\sigma$ changes. Of course, the G-symmetry of the path is key: H and H' are unitarily equivalent by a rotation around the x-axis, $e^{-i\alpha\sum_n X_n}$ $(0 \le \alpha \le \pi/4)$, but this path violates complex conjugation symmetry T.

The above examples could be distinguished by symmetry properties of *local* operators. The more interesting case, however, is when two enriched critical points can only be distinguished by the symmetry properties of *nonlocal* operators. Such an example is given by:

$$\begin{array}{rcl} H & = & -\sum_n (Z_n Z_{n+1} + X_n), \\ H'' & = & -\sum_n (Z_n Z_{n+1} + Z_{n-1} X_n Z_{n+1}). \end{array} \tag{4.3}$$

These two systems cannot be distinguished by a local operator; in particular, both are described by the Ising universality class with $\sigma(x) \sim Z_n$ [126], i.e., $T\sigma T = +\sigma$. However, the Ising CFT also has a *nonlocal* operator $\mu(x)$ with scaling dimension $\Delta_\mu = 1/8$—this is related to the local $\sigma(x)$ under Kramers-Wannier duality. For the usual critical Ising chain, this is known to be the string operator $\mu(x) \sim \cdots X_{n-2}X_{n-1}X_n$ at any position n. For H'', however, one can show that $\mu(x) \sim \cdots X_{n-2}X_{n-1}Y_nZ_{n+1}$ [126]. This suggests that the two models are two distinct G-enriched Ising CFTs distinguished by $T\mu T = \pm\mu$. To establish this, we need to ensure that the charge of μ is well-defined, i.e., that it is independent of our choice of operator on the lattice. This requires us to introduce the notion of a *symmetry flux*.

To motivate the idea of a *symmetry flux*, let us first observe that the above nonlocal lattice operators corresponding to μ are of the form $\prod_{m<n} X_m \mathcal{O}_n$, i.e., their strings consist of the same on-site unitaries that form the $\mathbb{Z}_2$ symmetry $P = \prod X_n$. The endpoint operator $\mathcal{O}_n$ chosen such that the resulting object has the slowest possible decay ($\mathcal{O}_n = X_n$ for H and $\mathcal{O}_n = Y_nZ_{n+1}$ for H''). Indeed, for the Ising CFT it is known that $\Delta = 1/8$ is

[1] Both statements follow from that the fact that if $\mathcal{O}_1$ and $\mathcal{O}_2$ both generate σ, then $\langle \mathcal{O}_1\mathcal{O}_2\rangle \neq 0$ (following from the fusion rule $\sigma \times \sigma = 1 + \varepsilon$) which must be real if T is unbroken.

[2] Note that before appealing to Table 3.2, rotate $(X_n, Y_n, Z_n) \to (Z_n, Y_n, -X_n)$.

the smallest possible scaling dimension [37]. We call such a string operator with slowest possible decay *the symmetry flux of P.* One can argue—as we do in Section 4.2—that once one fixes the $\mathbb{Z}_2$ symmetry under consideration (here P), then the Ising universality class has a *unique* symmetry flux, even in the presence of additional gapped degrees of freedom[3]! This means that we have a well-defined charge $T\mu T = \pm\mu$. We say that the above two models, H and H'', realize two distinct $\mathbb{Z}_2 \times \mathbb{Z}_2^T$-enriched Ising CFTs. Moreover, since this is based on charges of nonlocal operators, we say that they are *topologically distinct.*

We thus propose that distinct symmetry-enriched CFTs can be distinguished by how symmetry fluxes of $g \in G$ are charged under the other symmetries in G. For the models in Eq. (4.3), the discrete invariant is the sign picked up when conjugating the symmetry flux of P by T. The beauty of this invariant is that it works equally well for gapped phases. In that case, asking for the slowest possible decay is asking for long-range order. In other words, the aforementioned symmetry flux now coincides with the string order parameter for gapped symmetry-protected topological (SPT) phases [151, 161]. The connection between the gapless and gapped case can be made even more direct: the Ising universality class can be perturbed[4] into a symmetric gapped phase by condensing the symmetry flux $\mu(x)$, i.e., the gapped phase will have long-range order $\lim_{|x-y|\to\infty}\langle\mu(x)\mu(y)\rangle \neq 0$. Hence, we see that the usual Ising critical chain H can be perturbed into the trivial phase with string order parameter $\cdots X_{n-2}X_{n-1}X_n$, whereas H'' will flow to a non-trivial SPT phase with string order parameter $\cdots X_{n-2}X_{n-1}Y_nZ_{n+1}$ (this is the cluster phase which we discussed in the previous chapter). In the gapped symmetry-preserving case, one can argue that the symmetry flux is *always* unique in one spatial dimension; this follows from the principle of symmetry fractionalization [16, 17]. Indeed, the symmetry properties of its endpoint operator $\mathcal{O}_n$ encode the projective representation (or, equivalently, the second group cohomology class) labeling the gapped phase.

4.1.2. Edge modes from charged symmetry fluxes

If a symmetry flux has a non-trivial charge under another symmetry, then this can be linked to ground state degeneracies in the presence of open boundary conditions. We argue this more generally in Section 4.4; here we illustrate this for the lattice model H'' in Eq. (4.3), taking a half-infinite system with sites $n = 1, 2, \cdots$. We show that the boundary of this critical chain spontaneously magnetizes (see Ref. [52] for a related system). Indeed, on the lattice we see that Z_1 commutes with H''; the spontaneous edge magnetization $Z_1 = \pm 1$ thus gives a twofold degeneracy. To see that this magnetization is not a mere artifact of our fine-tuned model, we can study its stability in the Ising CFT starting with $\langle\sigma(x \approx 0)\rangle \neq 0$ (with the boundary at $x = 0$). If we add the P-symmetry flux $\mu(0)$ to the Hamiltonian, this would connect the two ordering directions and hence destabilize them. This is what would happen for the usual Ising chain H, where the symmetry flux is condensed near the boundary, $\langle\mu(0)\rangle \neq 0$, giving us a symmetry-preserving boundary condition, $\langle\sigma(0)\rangle = 0$ [162]. However, if $T\mu T = -\mu$, the $\mathbb{Z}_2^T$ symmetry prevents us from adding this perturbation, and, remarkably, the edge magnetization is stable! Indeed, in Section 4.3 we show that all symmetry-*allowed* perturbations correspond to operators with scaling dimension greater than one—implying that they are irrelevant for the boundary RG flow. In summary, the zero-dimensional edge spontaneously breaks P symmetry, stabilized by the $\mathbb{Z}_2 \times \mathbb{Z}_2^T$-enriched bulk CFT.

It is important to note that this degeneracy crucially relies on the presence of an edge.

[3] E.g., consider a gapped SPT phase with long-range order in a string order parameter $\mathcal{A}_n$ which is odd under T. If this is stacked on top of a critical chain, then μ and $\mu\mathcal{A}$ have the *same* scaling dimension $\Delta = 1/8$ yet *distinct* charges. Fortunately, they are distinguished by their string, i.e., they are symmetry fluxes for *distinct* symmetries.

[4] By adding $\varepsilon(x) \sim -\mu(x)\mu(x+a) + \sigma(x)\sigma(x+a)$ to the Hamiltonian.

The key reason for this is that, while $\mu(x)$ is *nonlocal* in the bulk, it is *local* near a boundary, i.e., its string can terminate[5]; see Section 4.3 for how this enters the general argument. Indeed, H'' has a unique ground state with periodic boundary conditions. In fact, in that case H and H'' are related by the unitary transformation $U = \prod_n (CZ)_{n,n+1}$, where CZ is the control-Z gate—and it is well-established that H has a unique ground state. This unitary transformation also relates the trivial *gapped* phase to the non-trivial *gapped* cluster phase [31]; in fact, this is a special case of the class of transformation discussed in subsection 3.3.3 of the previous chapter.

Thus far, we have focused on a single end, giving the complete story for a half-infinite system. For a finite system of length L, we need to consider the finite-size splitting of the symmetry-preserving states which entangle both edges:

$$|\uparrow_l\uparrow_r\rangle \pm |\downarrow_l\downarrow_r\rangle \quad \text{and} \quad |\uparrow_l\downarrow_r\rangle \pm |\downarrow_l\uparrow_r\rangle. \tag{4.4}$$

In general, to analytically determine such finite-size splitting, it is useful to start in the scale-invariant RG fixed point limit and then consider what additional perturbations are necessary to distinguish the states. For example, if the system is gapped, then all four states in Eq. (4.4) are degenerate in the fixed point limit. The only way a local perturbation can then couple the two edges is at L^{th} order in perturbation theory. Indeed, for gapped SPT phases, the finite-size splitting is exponentially small in system size, as discussed in Chapter 3. For critical systems, however, the RG fixed point limit is richer, being described by a CFT. In particular, it is known [163] that the two anti-ferromagnetic states in Eq. (4.4) are split from the ferromagnetic ones at the energy scale[6] $\sim 1/L$, the same as the finite-size *bulk* gap. This is due to the spontaneous boundary magnetizations sensing their (mis)alignment through the critical bulk. The remaining two states, $|\uparrow_l\uparrow_r\rangle \pm |\downarrow_l\downarrow_r\rangle$, are exactly degenerate within the CFT. They can be split by perturbing away from the fixed point limit by adding RG-irrelevant perturbations. The splitting can already occur at second order in perturbation theory (intuitively, each edge has to couple to the critical bulk). Nevertheless, we show that the dominant contribution has a surprisingly large power $\sim 1/L^{14}$, caused by the so-called *seventh descendant* of μ; see Section 4.3 for a derivation.

The above twofold degeneracy with open boundaries is the generic result for a topologically non-trivial symmetry-enriched Ising CFT. The nature of its finite-size splitting depends on the protecting symmetry. In the above case, where μ is odd under an anti-unitary symmetry, we found an algebraic splitting $\sim 1/L^{14}$. In other scenarios, μ may be odd under a symmetry associated to additional gapped degrees of freedom, which by the same perturbative argument would lead to an exponentially small finite-size splitting. This is in agreement with the observations in Ref. [52], and is also what we observe in Fig. 4.1. Both scenarios are discussed in detail in Section 4.3.

4.1.3. Classifying G-CFTs

In the above, we defined discrete invariants. Two natural questions arise: given a universality class, how many distinct invariants can one realize; and are these invariants complete? More precisely, if all local operators and symmetry fluxes have the same symmetry properties, can the models be smoothly connected whilst preserving their universality class? We explore this in Section 4.4, arguing that it is indeed complete for the Ising CFT. In particular, we discuss the case for the symmetry group $G = \mathbb{Z}_2 \times \mathbb{Z}_2$ for illustrative purposes. We first recall the six distinct *gapped* phases in this symmetry class, after which we study the universality classes that naturally arise at the $\binom{6}{2} = 15$ direct transitions between these

[5] Note that terminating its string in the bulk would effectively lead to a *two*-point operator $\mu(x)\mu(y)$.
[6] This is the *only* possible nonzero energy scale at a fixed point limit.

phases. In particular, we find nine distinct $\mathbb{Z}_2 \times \mathbb{Z}_2$-enriched Ising ($c = 1/2$) universality classes, whereas we show that *all* $\mathbb{Z}_2 \times \mathbb{Z}_2$-enriched Gaussian ($c = 1$) transitions can be connected (if they have minimal codimension, as explained in Section 4.4). For the $c = 1$ case, we construct exactly-solvable models that allow us to connect symmetry-enriched CFTs which have seemingly distinct symmetry properties. This is possible since—unlike for the Ising CFT—there is a *connected* family of different $c = 1$ universality classes along which scaling dimensions can cross, such that the symmetry properties of symmetry fluxes need not be invariant for $c = 1$. However, as we discuss in Sections 4.4 and 4.6, there are still non-trivial G-CFTs for $c \geq 1$.

4.1.4. Majorana edge modes at criticality

The edge mode encountered in the spin chain H'' in Eq. (4.3) is rather unusual from the gapped perspective. Firstly, the ground state is unique with periodic boundary conditions, and *twofold*[7] degenerate with open boundaries. There is no gapped bosonic SPT phase with this property. Moreover, while the ground states $|\uparrow_l\uparrow_r\rangle \pm |\downarrow_l\downarrow_r\rangle$ can be toggled by a local edge mode operator $Z_1 \sim \sigma(0)$, such cat states are unstable and the system would collapse into $|\uparrow_l\uparrow_r\rangle$ or $|\downarrow_l\downarrow_r\rangle$ (i.e., the zero-dimensional edges exhibits spontaneous symmetry breaking, which is not possible in the absence of a bulk). In this collapsed basis, one would need an extensive operator P to toggle between them.

In Section 4.5 we give a fermionic example where the edge mode is more conventional: this is simply one of the critical Majorana chains introduced in Chapter 2 in the non-interacting context. The bulk is a free Majorana $c = \frac{1}{2}$ CFT, and each boundary hosts a localized zero-energy Majorana edge mode. This has the same ground state degeneracy as the usual gapped Kitaev chain. Moreover, similar to the latter, there is an edge Majorana operator that toggles between the two (stable) ground states. We show that the system is characterized by the symmetry flux of fermionic parity symmetry being odd under spinless time-reversal symmetry. In other words, this is a non-trivial symmetry-enriched Majorana CFT, which means that the edge mode is stable beyond the non-interacting setting of Chapter 2.

This critical Majorana chain arises as a phase transition from the gapped phase with two Majorana modes (per edge) protected by spinless time-reversal, to the Kitaev chain phase with one Majorana mode (per edge). In Chapter 2 we saw that in that case, one edge mode delocalizes at the transition—becoming the bulk critical mode—whereas the other mode remains localized. This fermionic system is in fact related to H'' by a Jordan-Wigner transformation (e.g, using[2] Table 3.2). In the spin chain language, starting from the gapped cluster phase, two of the four degenerate ground states with open boundary conditions have a splitting that is determined by the *bulk* correlation length: these become delocalized at the critical point toward the Ising phase, with only the above twofold degeneracy remaining. Entering the gapped Ising phase, we have an edge magnetization which gradually merges with the bulk magnetization as we go deeper into the phase; see also Ref. [164].

4.1.5. A unified language

There is already a considerable body of work on critical one-dimensional systems with topological edge modes [41–58]. Section 4.6 is devoted to demonstrating how our formalism allows us to unify previous works. We illustrate this for Refs. [41, 46, 52, 165], showing how the models introduced therein can be interpreted as G-enriched Ising or Gaussian CFTs. This automatically identifies novel discrete bulk invariants for these systems in terms of their symmetry fluxes, ensuring the presence of protected edge modes.

[7] We do not count the states whose finite-size splitting scales as the bulk gap $\sim 1/L$.

4.2. Symmetry fluxes and topological invariants

In this section, we explain how to define discrete topological invariants for both gapped and gapless systems. We do this by introducing the notion of symmetry fluxes; their charges will be the invariants. In subsection 4.2.2, we illustrate how this indeed associates a topological invariant to the Ising critical point of the spin-1 XXZ chain encountered in Fig. 4.1. These invariants constrain the possible structure of phase diagrams, as we illustrate in subsection 4.2.3. This section is devoted to *bulk* properties; the related phenomenon of topological edge modes is discussed in Section 4.3.

4.2.1. Defining symmetry fluxes and their charges

Consider a symmetry element $g \in G$, where G is the symmetry group of the Hamiltonian. If this is represented on the lattice by an *unbroken* on-site unitary operator $U^g = \prod_n U_n^g$, we can associate to it a so-called *symmetry flux*. This is defined to be a (half-infinite) string operator of the form $\mathcal{S}_n^g \equiv \cdots U_{n-3}^g U_{n-2}^g U_{n-1}^g \mathcal{O}_n^g$ where the *local* endpoint operator $\mathcal{O}_n^g$ is chosen such that the resulting correlator,

$$\langle \mathcal{S}_m^{g\dagger}\, \mathcal{S}_n^g \rangle = \langle \mathcal{O}_m^{g\dagger} U_m^g U_{m+1}^g \cdots U_{n-1}^g \mathcal{O}_n^g \rangle, \tag{4.5}$$

has the slowest possible decay as a function of $|n-m|$, with leading positive[8] term. In practice, the correlator in Eq. (4.5) has two possible functional forms, depending on whether or not U^g is associated to gapped degrees of freedom—meaning that all particles charged under this symmetry are massive. If this is the case, its symmetry flux has long-range order (i.e., it tends to a finite positive value). Otherwise, there is algebraic decay, $\langle \mathcal{S}_m^g \mathcal{S}_n^g \rangle \sim 1/|n-m|^{2\Delta_g}$. (Note that any decay faster than algebraic would imply symmetry breaking.) The exponent Δ_g is called the scaling dimension of $\mathcal{S}_g$ and is by definition as small as possible; long-range order can be seen as the special case $\Delta_g = 0$. The universality class of the system determines the value of Δ_g.

An obvious and important question is whether—for a given model—the above definition specifies a *unique* symmetry flux. To make this question precise—and to avoid a trivial overcounting[9]—we can naturally define an inner product between symmetry fluxes:

$$\langle \tilde{\mathcal{S}}^g | \mathcal{S}^g \rangle_{\text{sym}} \equiv \lim_{|n-m|\to\infty} |n-m|^{2\Delta_g} \langle \tilde{\mathcal{O}}_m^{g\dagger} U_m^g \cdots U_{n-1}^g \mathcal{O}_n^g \rangle, \tag{4.6}$$

where $\mathcal{S}_n^g$ and $\tilde{\mathcal{S}}_n^g$ are two symmetry fluxes obeying the above definition. We see that norms are strictly positive, $\langle \mathcal{S}^g | \mathcal{S}^g \rangle_{\text{sym}} > 0$, making the above inner product *positive definite*. This gives us a notion of whether two symmetry fluxes are linearly dependent or not. We thus have a *vector space* spanned by the symmetry fluxes of $g \in G$, and its *dimension* D_g is a property of the universality class, as we will soon discuss (e.g., it is one-dimensional for gapped systems and for the Ising universality class).

Charges of symmetry fluxes

The group G has a natural action on symmetry fluxes via $U^h \mathcal{S}^g U^{h\dagger}$. It is easy to see that this is a symmetry flux for hgh^{-1}. It is hence natural to take h from the subgroup of all elements commuting with g—the *stabilizer* $C(g)$—such that $U^h \mathcal{S}^g U^{h\dagger}$ is again a symmetry flux for g. In particular, if the space of symmetry fluxes of g is one-dimensional, then this new flux must be linearly dependent on $\mathcal{S}^g$. We define the relative phase to be *the charge of the symmetry flux of g under h*. In general, we can define this through the inner product:

[8] This can be ensured by absorbing spatially varying phase factors into $\mathcal{O}_n$.

[9] E.g., multiplying any symmetry flux by an operator which has a nonzero expectation value would not change its decay.

$\langle \mathcal{S}^g | U^h \mathcal{S}^g U^{h\dagger} \rangle_{\text{sym}} = \chi_g(h) \in U(1)$. However, in practice one chooses the endpoint operator $\mathcal{O}^g$ to transform nicely under $C(g)$, in which case we can directly read off the charge from $U^h \mathcal{S}^g U^{h\dagger} = \chi_g(h) \mathcal{S}^g$. If G is abelian, it can be shown that these charges are classified by $H^2(G, U(1))$; see Appendix C.1 for details.

The charges under anti-unitary symmetries are slightly more subtle, since they seemingly change if we redefine $\mathcal{S}^g \to i\mathcal{S}^g$. We thus need to fix a gauge. If g is of order m (i.e., $g^m = 1$), then $(\mathcal{S}^g)^m$ is a *local* operator (i.e., the string has disappeared). This means that it is sensible to calculate its vacuum expectation value—which is generically nonzero—and we fix the gauge by requiring this to be positive: $\langle (\mathcal{S}^g)^n \rangle > 0$.

The above showed that charges are straightforwardly defined if the symmetry flux is unique, directly giving access to discrete invariants. We now show that this uniqueness is indeed guaranteed if, for example, the bulk is gapped or described by the Ising universality class. We also touch upon the more general case where the space of symmetry fluxes is higher-dimensional.

Symmetry fluxes for gapped phases

In the gapped case, the symmetry flux for any unbroken symmetry $g \in G$ is *unique*, i.e., any two symmetry fluxes are linearly dependent. This follows from the concept of *symmetry fractionalization* (see Appendix C.1.3 for a proof). Indeed, in this case the above definition of the symmetry flux coincides with the well-known notion of a string order parameter characterizing the phase [151, 161]. Note that this uniqueness applies even to *critical* systems as long as U^g acts non-trivially only on *gapped* degrees of freedom. The uniqueness of this symmetry flux implies we have well-defined charges $\chi_g(h)$.

As discussed in Chapter 3, gapped phases are classified by topologically distinct projective representations of G which are labeled by a so-called cocycle $\omega \in H^2(G, U(1))$. The above charges $\chi_g(h)$ can be expressed in terms of this cocycle (see Appendix C.1.3). The converse is also true for, e.g., abelian groups G: in Appendix C.1.3 we prove that the cocycle can be reconstructed from knowing the charges. This is not true for arbitrary groups G. Nevertheless, in practice knowing the charges is often equivalent to knowing the projective representations (the simplest known counter-example involves a group of 128 elements [151]).

Symmetry fluxes for the Ising universality class

We now show that if one is given a G-symmetric lattice model where some degrees of freedom are described by the Ising universality class and other degrees of freedom (if present) are gapped, then any $g \in G$ has a *unique* symmetry flux $\mathcal{S}^g$. Firstly, the Ising CFT is known to have an emergent $\mathbb{Z}_2$ symmetry (i.e., this makes no reference to what the symmetries of the lattice model might be) and it is known that this has a *unique*[10] symmetry flux μ which moreover has scaling dimension $\Delta_\mu = 1/8$ [37]. Secondly, this is the *only* unitary on-site symmetry of the Ising CFT [166], hence any lattice symmetry which acts non-trivially on the local degrees of freedom of the CFT must coincide—for the gapless part of the spectrum—with the emergent $\mathbb{Z}_2$ symmetry, thereby inheriting the uniqueness of its symmetry flux. A part of the symmetry can of course also act non-trivially on additional *gapped* degrees of freedom, but as we just argued in the above, this does not affect the conclusion of uniqueness.

In summary, for any $g \in G$ we have a unique symmetry flux. Its scaling dimension is $\Delta_g = 1/8$ if g acts non-trivially on the CFT, otherwise $\Delta_g = 0$. As described in Section 4.2.1, this uniqueness gives us well-defined charges $\chi_g(h) \in U(1)$ under any symmetry

[10] This is because the partition function in the sector twisted by the emergent $\mathbb{Z}_2$ symmetry has a unique ground state.

h that commutes with g. These charges form a *discrete invariant* of the symmetry-enriched Ising CFT. We will see an example of this in subsection 4.2.2.

Symmetry fluxes for general universality classes

In the above two cases, for each $g \in G$, the vector space of symmetry fluxes happened to be one-dimensional. More generally, it might have some dimension D_g, such that each basis of symmetry fluxes $\mathcal{S}^g_\alpha$ come with an additional label $\alpha = 1, \ldots, D_g$. Hence, the subgroup of elements that commute with g (the stabilizer of g) has a higher-dimensional representation on this space of fluxes, $U^h \mathcal{S}^g_\alpha U^{h\dagger} = R^g_{\alpha,\beta}(h)\mathcal{S}^g_\beta$. For example, $D_g > 1$ generically happens at transitions between distinct SPT phases (or between G-CFTs), where the different symmetry fluxes become degenerate.

A higher-dimensional representation can of course still come with discrete labels (in particular, there are cases where all degenerate fluxes have the *same* charges; see Section 4.6), but extra care has to be taken before one can conclude that these give *invariants* of the G-enriched CFT. In particular, some CFTs allow for marginal perturbations which can change D_g. For example, the $c = 1$ $\mathbb{Z}_2$-orbifold CFT allows for one-dimensional vector spaces of symmetry fluxes ($D_g = 1$), but this CFT can be smoothly tuned to a compact boson CFT where this representation becomes two-dimensional. Such a process is explored in a lattice model in Section 4.4 where we use this to connect apparently distinct G-CFTs with $c = 1$.

Implications for phase diagrams

Identifying *discrete* invariants for symmetry-enriched universality classes has strong implications for the possible structure of phase diagrams. In particular, if two models are described by the same CFT at low energies but by distinct *symmetry-enriched* CFTs, then these two transitions cannot be smoothly connected in a larger phase diagram. This means that any path attempting to connect them must have an intermediate point where the universality class discontinuously changes—either to a distinct CFT (necessarily of higher central charge) or to something that is not a CFT (e.g., a gapless point with dynamical critical exponent $z_{\text{dyn}} \neq 1$). Examples are discussed in subsection 4.2.3.

4.2.2. Topological invariant for the critical spin-1 anisotropic XXZ chain

Having laid out the general structure of symmetry fluxes, we are now in a good position to apply this to a concrete model: the spin-1 XXZ chain. As mentioned in the introduction and as shown in Fig. 4.1, as one tunes the easy-axis anisotropy Δ from the topological Haldane phase to the symmetry-breaking Ising phase, there remains a localized edge mode at the Ising critical point. Here we identify a bulk topological invariant at criticality, establishing that it indeed forms a novel symmetry-enriched Ising CFT. This invariant also explains its edge behavior, as discussed in Section 4.3.

The gapped Haldane phase is known to be protected by, for example, the $\mathbb{Z}_2 \times \mathbb{Z}_2$ group of π-rotations (represented by $R_\gamma = \prod_n e^{i\pi S^\gamma_n}$ for $\gamma = x, y, z$). This SPT phase has long-range order in $\langle S^\gamma_i \exp(i\pi \sum_{i<k<j} S^\gamma_k) S^\gamma_j \rangle$. The symmetry flux of R_γ is thus $\prod_{m<n} e^{i\pi S^\gamma_m} S^\gamma_n$. Its long-range order is shown in Fig. 4.2(a) for $\gamma = x$, which indeed vanishes at the critical point $\Delta = \Delta_c$. In the Ising phase for $\Delta > \Delta_c$ we have the local order parameter S^z_n, characterizing the spontaneous breaking of R_x and R_y.

Despite the vanishing of the long-range order of these order parameters, they still play an important role at criticality: they are identified by their scaling dimension $\Delta = 1/8$, as shown in Fig. 4.2(b). We thus conclude that—similar to the known gapped case—the symmetry flux of R_x at criticality is still the Haldane string order parameter. As discussed

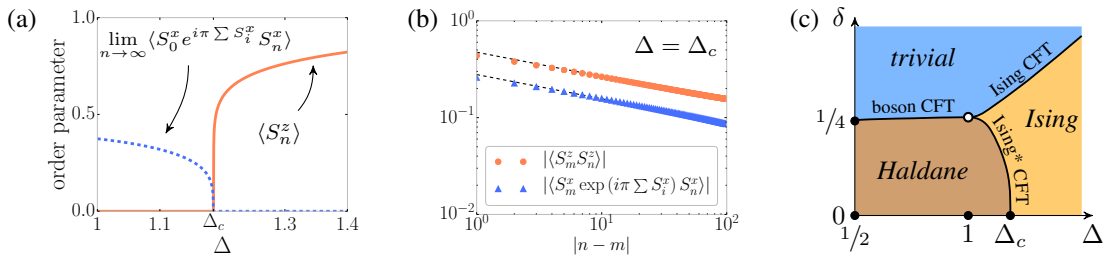

Figure 4.2.: **Symmetry fluxes for the spin-1 XXZ chain and transitions between topologically distinct Ising universality classes.** (a) The Haldane string order parameter and Ising order parameter have long-range order in the SPT and symmetry-breaking phase, respectively. (b) At criticality, the long-range order is replaced by algebraic decay. Both operators have the same scaling dimension (i.e., their correlators decay as $\sim 1/|n-m|^{2\Delta}$ with $\Delta = 1/8$; the dashed lines are a guide to the eye) and in the continuum limit correspond to the μ and σ operators of the Ising CFT, respectively. We conclude that μ has non-trivial charge under other symmetries, which functions as a topological invariant. (c) Phase diagram upon introducing bond-alternation. There is a $c = 1$ transition between the topologically distinct $c = \frac{1}{2}$ transitions. The tricritical point (hollow marker) is a WZW $SU(2)_1$ CFT, where the trivial and Haldane string order parameters both have scaling dimension 1/8.

in subsection 4.2.1, this means that the Ising critical point is non-trivially enriched by $\mathbb{Z}_2 \times \mathbb{Z}_2$-symmetry. More concretely, if we denote the symmetry flux of R_x by μ (using the traditional notation of scaling operators of the Ising CFT)[11], we have the non-trivial charge $R_z \mu R_z = -\mu$.

In passing, we note that the gapped Haldane phase is also known to be protected by time-reversal symmetry $T_{\text{spin}} = R_y K$ (where K is complex conjugation in the local z-basis). Similarly, the Ising criticality at $\Delta = \Delta_c$ is enriched by the $\mathbb{Z}_2 \times \mathbb{Z}_2^T$ symmetry generated by R_x and T_{spin}. Indeed, we see that $T_{\text{spin}} \mu T_{\text{spin}} = -\mu$. It would be interesting to define a notion of symmetry flux for anti-unitary symmetries.

4.2.3. Implications for phase diagrams: bond-alternating spin-1 XXZ chain

Having identified the discrete invariant $R_z \mu R_z = -\mu$ for the spin-1 XXZ chain at criticality, we can distinguish it from a trivial Ising criticality where $R_z \mu R_z = \mu$. Whereas the former appears at a phase transition between an Ising phase and a non-trivial SPT phase, the latter appears as one tunes from/to a trivial SPT phase[12]. The discreteness of $R_z \mu R_z = \pm\mu$ means that these two Ising criticalities cannot be smoothly connected, constraining the possible structure of phase diagrams containing such Ising transitions. This can be illustrated by adding, e.g., bond-alternation:

$$H = J \sum_n (1 - \delta(-1)^n) \left(S^x_n S^x_{n+1} + S^y_n S^y_{n+1} + \Delta S^z_n S^z_{n+1} \right). \tag{4.7}$$

The two-parameter phase diagram, obtained with iDMRG [12, 167], is shown in Fig. 4.2(c) (see also Refs. [168, 169]). For large δ we can realize a trivial Ising CFT where the symmetry flux of R_x is *not* charged, being given by $\mu \sim e^{i\pi \sum_{m<n} S^x_m}$. We observe that the

[11] In principle we should label it by μ_{R_x}, since the symmetry flux of R_y also has scaling dimension $\Delta = 1/8$ and may be denoted by μ_{R_y}.

[12] Condensing μ would lead to a symmetric gapped phase, with its symmetry properties determining its phase.

two topologically-distinct symmetry-enriched Ising CFTs (with central charge $c = 1/2$) are separated by a point where the universality class changes (hollow white marker). In this case, this 'transition of transitions' is described by the Wess-Zumino-Witten $SU(2)_1$ CFT with central charge $c = 1$. Here, the symmetry flux of R_x still has scaling dimension $\Delta_{R_x} = 1/8$, but this space is now *two-dimensional* (i.e., there are two linearly independent symmetry fluxes of R_x). Indeed, one symmetry flux is non-trivial, $e^{i\pi \sum_{m<n} S^x_m} S^x_n$, and the other, trivial, $e^{i\pi \sum_{m<n} S^x_m}$. This degeneracy of symmetry fluxes is in fact true along the whole line of $c = 1$ CFTs separating the trivial and Haldane SPT phase, which is natural given the emergent duality symmetry at this transition.

4.3. Edge modes at criticality

In the previous section, we introduced the notion of a symmetry flux and its corresponding charge. In this section, we relate this bulk property to degeneracies in the presence of open boundary conditions. This section is naturally divided in two: in subsection 4.3.1 we focus on a *single* boundary of a half-infinite system, where we explain how a charged symmetry flux can lead to the boundary spontaneously breaking a symmetry; in subsection 4.3.2, we study the coupling between such boundary magnetizations and calculate the finite-size splitting of the degeneracy. Throughout this section, we use the Ising CFT as an illustrative example, but the method which we lay out is generally applicable. In fact, at the end of every subsection, we indicate what the necessary analysis would be for a general CFT.

4.3.1. Half-infinite chain: a single boundary

Let us consider a *half-infinite* system, allowing us to study a single edge. We furthermore presume that the system is described by the Ising universality class. To study what happens near its boundary, we use the fact that all possible *boundary RG fixed points*—describing the (0+1)-dimensional edge of this CFT—are known [163, 170]. There are three distinct fixed points, as sketched in Fig. 4.3; these have different behavior with respect to the $\mathbb{Z}_2$ symmetry intrinsic to the Ising CFT:

1. The *free* boundary fixed point: this preserves the $\mathbb{Z}_2$ symmetry. The symmetry flux of this $\mathbb{Z}_2$ symmetry, denoted by $\mu(x)$, can be said to have condensed. Indeed[13], $\langle \mu(x_{\text{boundary}}) \rangle \neq 0$ [162].

2. The (explicitly) *fixed*$^{\pm}$ boundary fixed point: this requires explicitly breaking the $\mathbb{Z}_2$ Ising symmetry at the level of the Hamiltonian (near its boundary). The local spin operator $\sigma(x)$ points up or down near the edge, $\langle \sigma(x_{\text{boundary}}) \rangle \neq 0$; its sign depends on the explicit breaking of the $\mathbb{Z}_2$ symmetry. This fixed point is *excluded* by enforcing $\mathbb{Z}_2$ symmetry of the Hamiltonian.

3. The *spontaneously fixed* boundary fixed point: the symmetry is not broken at the level of the Hamiltonian, but the ground state spontaneously magnetizes. More precisely, it is a *two-dimensional* Hilbert space which is the direct sum of the two symmetry-broken orderings.

The latter fixed point[14] is not often mentioned in the literature, but this is for a good reason: it is usually an *unstable*[15] RG fixed point. A generic perturbation would condense

[13] Note that in the bulk the one-point function of $\mu(x)$ is not well-defined due to it being nonlocal. However, near the boundary $\mu(x)$ becomes local.

[14] Note that this is not a Cardy state in the boundary conformal field theory.

[15] Consider, for example, $H = -\sum_{n=1}^{\infty} Z_n Z_{n+1} - \sum_{n=2}^{\infty} X_n$ with its spontaneous boundary magnetization $Z_1 = \pm 1$. This is unstable against the perturbation $X_1 \sim \mu(0)$, flowing to a unique ground state.

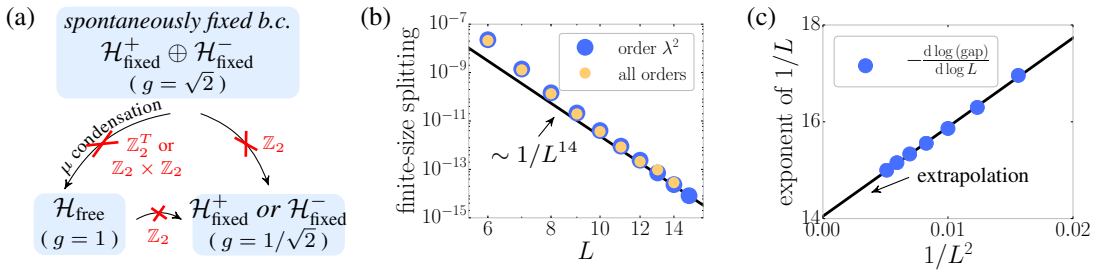

Figure 4.3.: **Topologically protected edge modes in the Ising CFT.** (a) Boundary RG flow for the Ising CFT: usually the free boundary condition is stable (when preserving global $\mathbb{Z}_2$), but it can be prevented when μ is charged under additional symmetries. In that case, the spontaneously fixed boundary condition (with a global twofold degeneracy) is stable! (b) If a unitary symmetry protects the edge mode, finite-size splitting is exponentially small in system size (see Fig. 4.1). For an anti-unitary symmetry, however, the field theory analysis in the main text suggests a splitting $\sim 1/L^{14}$. We confirm the latter numerically in a spin chain model where μ is charged under $\mathbb{Z}_2^T$. Note that for $L = 15$, the gap is around machine precision. (c) To separate out higher-order corrections present in (b), we extrapolate the leading exponent of $1/L$; the data agrees with the predicted splitting $\sim 1/L^{14} \times \left(1 + \alpha/L^2\right)$.

$\mu(x)$ near the boundary, flowing to the free fixed point. From the RG perspective, this is due to the *boundary scaling dimension* of $\mu(x_{\text{boundary}})$ being $1/2$; this is smaller than one, implying it is *relevant* for $0+1$-dimensional RG flows. However, if $\mu(x)$ is charged under some *additional* symmetry, then this RG flow is prohibited and the spontaneous fixed boundary condition—along with its twofold degeneracy—is stabilized! The above is summarized in Fig. 4.3.

One can in principle repeat the above analysis for any CFT. The necessary information to set up the problem is the list of possible conformal boundary conditions, as well as the boundary condition changing operators and their (boundary) scaling dimensions. Supplemented by the symmetry properties of these operators, one can study which boundary RG fixed points are stable and (non)degenerate.

4.3.2. Finite-size splitting: coupled boundaries

As argued in the previous subsection, if the $\mathbb{Z}_2$-symmetry flux $\mu(x)$ of the Ising CFT is charged under an additional symmetry, the boundary spontaneously magnetizes. We now investigate the resulting degeneracy—and its finite-size splitting—for a *finite* chain of length L (with $x \in [0, L]$). Since the bulk gap vanishes as $\sim 1/L$, we can only meaningfully speak of degeneracies whose finite-size splitting decays *faster* than this. There are four candidate degenerate ground states, labeled by their boundary magnetizations:

$$|\uparrow_l\uparrow_r\rangle,\ |\uparrow_l\downarrow_r\rangle,\ |\downarrow_l\uparrow_r\rangle,\ |\downarrow_l\downarrow_r\rangle. \tag{4.8}$$

However—presuming the model under consideration has a ferromagnetic sign—the antiferromagnetic states in Eq. (4.8) are split from the ferromagnetic ones at the scale $\sim 1/L$ [163, 170]. Intuitively, this is because the edges can sense their (mis)alignment through the critical bulk. We thus only have *two* ground states: $|\uparrow_l\uparrow_r\rangle$ and $|\downarrow_l\downarrow_r\rangle$. In fact, *within the CFT*, these are exactly-degenerate eigenstates. This does not mean that they have no splitting in realistic systems: by definition, a CFT has no length scales, hence the only quantity with units of energy is $1/L$. If we perturb the CFT with RG-irrelevant

perturbations—present in any realistic system—then the twofold degeneracy could be split by the smaller energy scales $\sim \xi^\alpha/L^{1+\alpha}$ or $\sim \exp(-L/\xi)$ (where ξ is a constant with units of length). As a consistency check, note that in the RG fixed point limit, $\xi/L \to 0$, confirming that splittings which are faster than $1/L$ are indeed not visible in the CFT.

The purpose of this section is to determine whether the finite-size splitting of the aforementioned twofold degeneracy is algebraic or exponential in system size. This comes down to analyzing the possible perturbations V one can add to the CFT Hamiltonian, $H = H_{\text{CFT}} + V$, mixing $|\uparrow_l\uparrow_r\rangle \leftrightarrow |\downarrow_l\downarrow_r\rangle$. To connect these two states which break the Ising symmetry, we need to perturb with the corresponding symmetry flux. Indeed, $\mu(x_{\text{boundary}})$ is known to be a *boundary-condition-changing* (bcc) operator toggling between the two fixed$^\pm$ boundary conditions [163, 170]. We have already established that we cannot add $\mu(x)$ due to it being charged under an additional symmetry. However, there is a whole *tower* of bcc operators: the *descendants* of $\mu(x)$, with scaling dimensions $\Delta_n = 1/2 + n$ (where $n = 1, 2, 3, \cdots$). Note that since $\Delta_n > 1$, these are RG-irrelevant for the $(0+1)$-dimensional edge. This means they do not affect the analysis in Fig. 4.3, but they can indeed contribute to finite-size splitting. Whether it is possible to add such descendants of $\mu(x)$ depends on the the protecting/enriching symmetry. Determining which descendant—if any—is allowed, determines whether the splitting is exponential or algebraic (along with its power), as we explain now.

Exponential splitting

If $\mu(x)$ is charged under a symmetry U which is associated to gapped degrees of freedom (d.o.f.), then all its descendants have the same non-trivial charge. To see this, note that the descendants are created by applying the *local* Virasoro generators L_n to $\mu(x)$, and U acts trivially on local gapless d.o.f.. In conclusion, there is no perturbation within the low-energy CFT that can couple $|\uparrow_l\uparrow_r\rangle \leftrightarrow |\downarrow_l\downarrow_r\rangle$. Any effective interaction must hence be mediated through gapped d.o.f., which at most can lead to a finite-size splitting $\sim \exp(-L/\xi)$. This applies whenever the protecting symmetry is *unitary*: the only unitary symmetry of the Ising CFT is its $\mathbb{Z}_2$ symmetry [166], such that any additional unitary symmetry must be associated to gapped d.o.f.. A case in point is the critical spin-1 XXZ chain, where $\mu(x)$ is charged under R_z (see Section 4.2.2). This explains the exponentially-localized edge mode observed in Fig. 4.1. A similar conclusion was drawn in the work by Scaffidi, Parker and Vasseur [52], where gapped degrees of freedom stabilized a spontaneous boundary magnetization in a critical Ising chain.

Algebraic splitting

In case $\mu(x)$ is charged under an anti-unitary symmetry T, then the charge of its descendants can be different. More generally, if $\mathcal{O}_n$ is the lattice operator for a continuum operator $\varphi(x)$, then its first descendants can be realized by $\partial_x\varphi(x) \sim \mathcal{O}_{n+1} - \mathcal{O}_n$ and $\partial_t\varphi(x) \sim i[H, \mathcal{O}_n]$. Hence, we see that $\partial_x\varphi(x)$ has the *same* charge under T as $\varphi(x)$, whereas it is opposite for $\partial_t\varphi(x)$. For the boundary operator $\mu(0)$, we only have the time-like derivative, i.e., $\mu(0)$ has a unique first descendant with charge $T\partial_t\mu(0)T = +\partial_t\mu(0)$.

We are hence allowed to add a perturbation $H = H_{\text{CFT}} + \lambda\partial_t\mu(0)$. Remarkably, however, this descendant cannot split the twofold ground state degeneracy. Indeed, the perturbation *disappears* after a well-chosen change of basis:

$$H = H_{\text{CFT}} + i\lambda[H, \mu(0)] = \underbrace{e^{-i\lambda\mu(0)} H_{\text{CFT}} e^{i\lambda\mu(0)}}_{\equiv \tilde{H}_{\text{CFT}}} + O(\lambda^2). \tag{4.9}$$

Note that since $T\mu(0)T = -\mu(0)$, our rotated Hamiltonian $\tilde{H}_{\text{CFT}}$ is still symmetric: $T\tilde{H}_{\text{CFT}}T = \tilde{H}_{\text{CFT}}$. Eq. (4.9) tells us that the perturbed Hamiltonian H is equivalent

to a Hamiltonian with the *same spectrum* as the unperturbed case (plus perturbations given by *higher* descendants at order $O(\lambda^2)$). In particular, the ground state degeneracy is not split by the first descendant.

To summarize the above: the *zeroth* descendant (i.e., $\mu(0)$) was not allowed by symmetry, whereas the symmetry-allowed *first* descendant could be "rotated" away using the zeroth descendant. Interestingly, this pattern continues for a while, but not indefinitely. Firstly, it can be shown that any *even* descendant is T-odd [171] and is hence excluded by symmetry. Secondly, whilst all *odd* descendants are allowed by symmetry, many of them can be removed by using the fact that even descendants generate symmetry-preserving rotations. More precisely, if we denote the number of n^{th} descendants of $\mu(0)$ as N_n (which have scaling dimension $\Delta_n = 1/2 + n$), then only $N_{2m+1} - N_{2m}$ descendants[16] at level $2m+1$ cannot be rotated away and can hence actually cause a finite-size splitting! We thus need to determine the smallest *odd* n such that $N_n > N_{n-1}$. Fortunately, the number of descendants of $\mu(0)$ can be read off from the (chiral) partition function, i.e., $\sum_n N_n q^n = q^{-\frac{23}{48}}\chi_{1,2}(q)$ [37], where

$$q^{-\frac{23}{48}}\chi_{1,2}(q) = 1 + q + q^2 + q^3 + 2q^4 + 2q^5 + 3q^6 + 4q^7 + \cdots \tag{4.10}$$

We see that $N_7 - N_6 = 4 - 3 = 1$, leaving us with a single symmetry-allowed seventh descendant of $\mu(0)$, which we denote by $\mu^{(-7)}(0)$, that cannot be rotated away. We conclude that the perturbation $V = \lambda(\mu^{(-7)}(0) + \mu^{(-7)}(L))$ can split the degeneracy. Since we need to flip *both* edges in order to couple $|\uparrow_l\uparrow_r\rangle \leftrightarrow |\downarrow_l\downarrow_r\rangle$, we have to go to second order in λ to observe a splitting, i.e., λ^2/L^β. Since this has to have units of energy, we can conclude that $\beta = 1 - 2[\lambda]$, where the unit of λ is $[\lambda] = 1 - \Delta_7$. In summary, we find an algebraic splitting with power $\beta = 2\Delta_7 - 1 = 14$.

This remarkably fast algebraic decay can be confirmed in the spin model introduced in Section 4.1, $H'' = -\sum_{n=1}^{L-1} Z_n Z_{n+1} - \sum_{n=1}^{L-2} Z_n X_{n+1} Z_{n+2}$. This fine-tuned model has exact boundary magnetizations $Z_1 = \pm 1 = Z_L$. For this system,

$$\begin{aligned} \mu(x) &\sim \cdots X_{n-2}X_{n-1}Y_nZ_{n+1}, \\ \partial_t\mu(x) &\sim \cdots X_{n-2}X_{n-1}X_n. \end{aligned} \tag{4.11}$$

In particular, we see that $\partial_t\mu(0) \sim X_1$. This operator is allowed by symmetry but does not contribute to the splitting, as discussed above. We consider a dressed operator, $X_1Z_2Z_3$, which should generically contain all possible descendants of $\mu(0)$ which are T-even. Our perturbed Hamiltonian is thus $H = H'' + \lambda(X_1Z_2Z_3 + Z_{L-2}Z_{L-1}X_L)$. In Fig. 4.3(b) we see the finite-size splitting obtained with exact diagonalization for $\lambda = 0.1$. The data is consistent with the CFT prediction $\sim 1/L^{14}$. We can also analytically predict the next-to-leading order contribution, which arises from acting with the seventh descendant of μ on one end and with the ninth descendant on the other, generating a splitting $\sim 1/L^{\Delta_7+\Delta_9-1} = 1/L^{16}$. The gap thus scales as $\sim 1/L^{14} + \alpha/L^{16}$, which means that the effective exponent of the algebraic decay is L-dependent: $-\mathrm{d}\log(\text{gap})/\mathrm{d}\log L \approx 14 + 2\alpha/L^2$ for large L. The numerical data in Fig. 4.3(c) shows perfect agreement with this formula.

The above focused on the illustrative example of the Ising CFT, but the principle is much more general. Once one has studied the boundary RG flow diagram and concluded the presence of edge modes due to charged symmetry fluxes (as in subsection 4.3.1), one can study the finite-size splitting by determining the dominant symmetry-allowed bcc operator. In the anti-unitary case, one can use the fact that the contributions of descendants can be rotated away by other descendants—which applies to any CFT. One important difference will be the counting appearing in the tower of states such as in Eq. (4.10).

[16] All N_{2m} descendants generate *independent* rotations since otherwise a linear combination of descendants would be *conserved*—in conflict with the nonzero scaling dimension Δ_{2m}.

4.4. Classifying symmetry-enriched CFTs

The previous sections have shown how a given bulk universality class (with, in particular, a fixed central charge c) can split up into distinct classes when additional symmetries are enforced. The concept of a symmetry flux—and its associated charge—allows to distinguish such symmetry-enriched CFTs. However, there are *various* invariants one can associate to G-symmetric universality classes:

1. **Spontaneously broken symmetries.** At the coarsest level, there is the phenomenon of *symmetry breaking*. The invariant this allows us to define is the subgroup $G_{\text{eff}} \subset G$ of *unbroken symmetries* (one can think of the quotient group G/G_{eff} as constituting the broken symmetries). In particular, absence of symmetry-breaking means $G_{\text{eff}} = G$.

2. **Charges of symmetry fluxes.** As defined and discussed in Section 4.2, to any $g \in G_{\text{eff}}$ we can associate a symmetry flux $\mathcal{S}^g$. We can measure the charge of S^g with respect to any other symmetry $h \in G_{\text{eff}}$ which commutes with g. The universality class tells us whether this charge is an invariant of the phase (e.g., if the space of g-symmetry fluxes is one-dimensional).

3. **Gapped symmetries.** Another robust invariant of the phase is the list of the unbroken symmetries which act only on *gapped degrees of freedom*, forming a subgroup $G_{\text{gap}} \subset G_{\text{eff}}$. We refer to symmetries in G_{gap} as being *gapped*. (Note that having a larger G_{gap} is not necessarily correlated with having a smaller central charge; it does, however, usually imply that the critical degrees of freedom are more *unstable*.)

4. **Charges of local scaling operators.** Lastly, for any unbroken symmetry $g \in G_{\text{eff}}$ which is *not* gapped (i.e., $g \notin G_{\text{gap}}$), we can study the charges of *local* low-energy CFT observables under g. Similar to the charges of symmetry fluxes, these charges can lead to invariants of the phase (e.g., a unique local operator with a particular scaling dimension has an invariant charge). For example, recall the Ising operator σ from Section 4.1 that was either real or imaginary.

For gapped phases, the third and fourth invariants are trivial (since $G_{\text{gap}} = G_{\text{eff}}$). Indeed, in most practical cases, the first two provide a complete classification of gapped one-dimensional phases protected by an on-site symmetry group G [16–19]. A natural question is whether the above invariants are also complete for G-enriched CFTs. We show that this is the case for the Ising CFT, which we illustrate for the symmetry group $\mathbb{Z}_2 \times \mathbb{Z}_2$. For Gaussian CFTs, we give a *partial* answer, showing that the $c = 1$ transitions arising between gapped $\mathbb{Z}_2 \times \mathbb{Z}_2$-symmetric phases can all be smoothly connected. We also use the latter as an instructive example for the more subtle points encountered in Section 4.2, showing that G-CFTs with *apparently* distinct charges for their symmetry fluxes can be part of the *same* G-CFT. In this section, we limit ourselves to unitary symmetries.

Throughout this section, we discuss the example $G = \mathbb{Z}_2 \times \mathbb{Z}_2$ in the context of a spin-1/2 chain, with the symmetries realized by the group of π-rotations, $R_\gamma = \prod_n R_\gamma^{(n)}$, where

$$R_x^{(n)} = X_{2n-1}X_{2n},\ R_y^{(n)} = Y_{2n-1}Y_{2n},\ R_z^{(n)} = Z_{2n-1}Z_{2n}.$$

Note that the way we write these symmetries betrays that we have fixed a *unit cell*, such that the $R_\gamma^{(n)}$ symmetries indeed *commute*. This ensures that this defines a *linear*, *on-site* representation of $\mathbb{Z}_2 \times \mathbb{Z}_2$. (We have already emphasized the importance of this in Chapter 3.)

In subsection 4.4.1, we recall the six gapped phases that can occur for this symmetry group, along with solvable models which are used in the following two subsections. In

subsection 4.4.2, we classify the symmetry-enriched Ising CFTs. In subsection 4.4.3, we discuss the case of the Gaussian CFT.

4.4.1. Gapped bulk

To keep this chapter self-contained, we briefly review the gapped phases with this symmetry group. According to the classification for spin chains with $\mathbb{Z}_2 \times \mathbb{Z}_2$ symmetries, there are exactly two gapped phases where the ground state preserves the full symmetry group [16–19]. These are the trivial phase and the topological Haldane phase, which can be realized in a spin-1/2 chain, respectively, as follows:

$$H_1 = \sum_n \left(X_{2n-1}X_{2n} + Y_{2n-1}Y_{2n}\right),$$
$$H_{\text{Hal}} = \sum_n \left(X_{2n}X_{2n+1} + Y_{2n}Y_{2n+1}\right).$$

For both Hamiltonians, the ground state is a product of singlets, but for H_1 each singlet is *within* a unit cell, whereas for the latter it is *across* unit cells. The latter is reminiscent of the ground state of the well-known spin-1 Affleck-Kennedy-Lieb-Tasaki (AKLT) model; indeed, by introducing a term that penalizes spin-0 states in each unit cell, H_{Hal} can be adiabatically connected to the AKLT model [25, 172] (which in turn can be connected to the spin-1 Heisenberg chain in Eq. (4.1)). Relatedly, while both models clearly have a unique ground state for periodic boundary conditions, H_{Hal} has a zero-energy spin-1/2 degree of freedom at each open boundary. (Note that to keep the *on-site* representation of $\mathbb{Z}_2 \times \mathbb{Z}_2$ well-defined, we can only cut the chain *between* unit cells.) These two symmetric phases can be distinguished by their symmetry fluxes: e.g., for H_1 the symmetry flux of R_x is $\mathcal{S}^x = \cdots R_x^{(n-2)} R_x^{(n-1)} R_x^{(n)}$, whereas for H_{Hal} it is $\mathcal{S}^x = \cdots R_x^{(n-2)} R_x^{(n-1)} X_{2n-1}$. These clearly have different charges under R_y and R_z.

In addition to these two symmetry-*preserving* phases, there are four symmetry-*breaking* phases (which can be labeled by G_{eff}). Three of these preserve a $\mathbb{Z}_2$ subgroup generated by one of the $R_{\gamma=x,y,z}$:

$$H_x = \sum_n X_n X_{n+1}, \quad H_y = \sum_n Y_n Y_{n+1}, \quad H_z = \sum_n Z_n Z_{n+1}.$$

We label these three Ising phases as I_x, I_y and I_z, respectively. The fourth breaks the complete $\mathbb{Z}_2 \times \mathbb{Z}_2$ symmetry group (i.e., $G_{\text{eff}} = \{1\}$) and is realized by

$$H_0 = -\sum_n \left(X_{2n-1}X_{2n+1} + Y_{2n}Y_{2n+2}\right). \tag{4.12}$$

These six Hamiltonians satisfy a very useful duality property: there is a nonlocal change of variables which effectively interchanges $H_x \leftrightarrow H_1$, $H_y \leftrightarrow H_{\text{Hal}}$ and $H_z \leftrightarrow H_0$. We give an explicit lattice construction in Appendix C.2. Physically, this transformation can be interpreted as gauging R_z (whilst keeping R_x fixed).

Lastly, we remind the reader of the fact that phases of matter can be *stacked*. This was discussed in Chapter 3, but we briefly summarize it here. Two G-symmetric models can be combined into a two-leg ladder; the new on-site symmetry is simply the tensor product of the two individual on-site symmetries. One can then study what phase the stacked model belongs to. E.g., stacking the trivial phase onto any other phase leaves the latter invariant; it acts as the identity element, explaining our notation H_1. Oppositely, stacking any phase onto the phase that breaks all symmetries, remains in the latter phase; it hence acts as the zero element[17], explaining the label H_0.

[17] Together with the relations $\text{Hal} * \text{Hal} = 1$, $I_\gamma * \text{Hal} = I_\gamma$ and $I_\gamma * I_\gamma = I_\gamma$, the abelian semigroup of $\mathbb{Z}_2 \times \mathbb{Z}_2$-phases is completely specified.

4.4.2. Ising criticality ($c = 1/2$)

We classify $\mathbb{Z}_2 \times \mathbb{Z}_2$-enriched Ising CFTs, with a straightforward generalization to general symmetry groups G. This will show that the four invariants mentioned above form a *complete* set of invariants for this universality class. Our principal focus is on symmetry-enriched Ising CFTs which naturally occur as phase transitions between the aforementioned gapped phases. Practically, this means that such Ising CFTs have a *single* symmetry-allowed bulk perturbation which can open up a gap (a *relevant* operator). I.e., only one parameter needs to be tuned to achieve criticality; such CFTs are said to have *codimension one*. Ising CFTs with higher codimension can occur but physically correspond to accidental criticalities in a phase diagram—we will discuss them at the end of this subsection. Ising CFTs of codimension one are characterized by having an *unbroken* symmetry $\mathbb{Z}_2 \subset G_{\text{eff}}$ which anticommutes with the local Ising scaling operator σ (i.e., this $\mathbb{Z}_2 \not\subset G_{\text{gap}}$). Indeed, this forbids us from adding σ as a perturbation, such that there is only one relevant symmetric operator which can open up a gap (commonly denoted by ε).

We now demonstrate how the four labels we proposed allow us to derive that there are *at least nine* codimension one Ising CFTs—afterwards we confirm that this list is complete. Firstly, we have to determine the group of unbroken symmetries. If there *is* symmetry-breaking at the critical point, we have $G_{\text{eff}} \cong \mathbb{Z}_2$ (the symmetry group cannot be completely broken if we consider a codimension one CFT). There are *three* choices for the unbroken symmetry R_γ ($\gamma = x, y, z$). Note that the remaining invariants are already determined: σ must be odd under this remaining symmetry, and a single bosonic $\mathbb{Z}_2$ symmetry flux cannot be charged under itself, i.e., $\chi_g(g) = 1$. We can also determine which gapped phases this CFT can be perturbed into. If we condense σ (corresponding to perturbing with, say, $-\varepsilon$), we arrive at the phase breaking *all* symmetries (labeled by 0), whereas if we condense μ (perturbing with $+\varepsilon$) then we flow to a gapped phase with a single $\mathbb{Z}_2$ symmetry R_γ, which can only be the Ising phase I_γ. We use the shorthand notation [0,I_γ] to denote this transition, which is realized by, for example, the lattice Hamiltonian $H_0 + H_\gamma$.

If there is *no* symmetry-breaking, then $G_{\text{eff}} = \mathbb{Z}_2 \times \mathbb{Z}_2$. We can then continue to determine its gapped subgroup G_{gap}. This cannot be empty, since it is known that the Ising CFT (without gapped degrees of freedom) does not have a $\mathbb{Z}_2 \times \mathbb{Z}_2$ symmetry at low energies [166]. Moreover, G_{gap} cannot be the full group if we are to have a codimension one Ising CFT. We thus conclude that $G_{\text{gap}} \cong \mathbb{Z}_2$. There are *three* choices for this gapped symmetry R_γ ($\gamma = x, y, z$). Note that this implies that σ is odd under the non-gapped symmetries. Physically, one side of the Ising transition—where we condense σ—is thus the Ising phase I_γ. The remaining invariant of the G-CFT is the charge of the symmetry fluxes. These symmetry fluxes determine the nearby gapped *symmetric* phase (where μ is condensed), hence we know that there are only *two* distinct choices, labeled by whether the symmetry flux of R_γ is even or odd under one of the other symmetries. We thus arrive at the transitions [1,I_γ] and [Hal,I_γ], respectively; these are realized by $H_1 + H_\gamma$ and $H_{\text{Hal}} + H_\gamma$.

These nine distinct symmetry-enriched CFTs are summarized in Fig. 4.4(a). Three of these, namely [Hal,I_γ] ($\gamma = x, y, z$), are topologically non-trivial with exponentially localized edge modes. We identify the critical spin-1 XXZ chain in Eq. (4.1) as being in the class [Hal,I_z]. A priori, it could have been that there are additional (codimension one) Ising CFTs which cannot be smoothly connected to one of these nine, meaning that they would fall outside our proposed set of invariants. However, one can prove (see Appendix C.3) that once one fixes the unbroken symmetry group G_{eff} and a list of charges for σ, then any G-enriched Ising CFT can be obtained by stacking with (and coupling to) a G-symmetric gapped phase; see Fig. 4.4(b). Note that the previous list is already closed under this action—e.g., stacking the Haldane phase on top of [1,I_γ] gives us [Hal,I_γ]—and

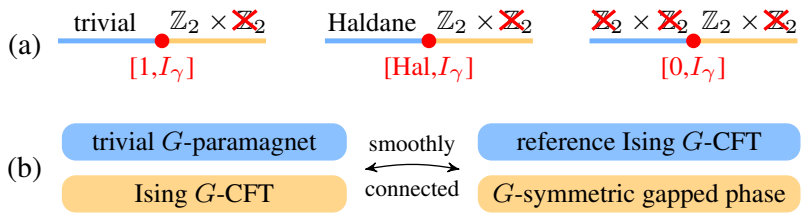

Figure 4.4.: **Classifying $\mathbb{Z}_2 \times \mathbb{Z}_2$-enriched Ising CFTs.** (a) There are nine distinct $\mathbb{Z}_2 \times \mathbb{Z}_2$-(Ising CFTs) of codimension one, coming in groups of three: one side is in the trivial/non-trivial SPT phase or the phase that breaks the *full* $\mathbb{Z}_2 \times \mathbb{Z}_2$; the other side is an Ising phase preserving a $\mathbb{Z}_2$ symmetry R_γ ($\gamma = x, y, z$). All nine can be distinguished by symmetry properties of local operators and/or symmetry fluxes. (b) To see that these nine exhaust all options, we prove that all G-enriched Ising CFTs (Ising G-CFTs, in short) can be obtained by stacking gapped phases on top of a reference Ising G-CFT; the latter is chosen to be a transition between the trivial gapped phase and an Ising phase.

is hence complete.

To generalize the above discussion to a general symmetry group G, note that the first step involved determining the unbroken symmetry group G_{eff}. The possible choice of gapped symmetries, G_{gap}, was then constrained by ensuring that our Ising CFT would have codimension one. The only remaining non-trivial labels are the charges of symmetry fluxes, which can be related to the topological properties of the nearby gapped phases. Altogether, this straightforwardly leads to a general classification (which is complete due to the *bait-and-switch lemma*; see Fig. 4.4(b) and Appendix C.3):

Classification of symmetry-enriched Ising CFTs of codimension one for a unitary group G: *these CFTs are labeled by a choice of nested subgroups $G_{gap} \subset G_{eff} \subset G$ such that $G_{eff}/G_{gap} \cong \mathbb{Z}_2$, and by an element $\omega \in H^2(G_{eff}, U(1))$, i.e., a class of projective representations of G_{eff}.*

Note that the quotient of unbroken symmetries and gapped symmetries, $G_{\text{eff}}/G_{\text{gap}}$, can be identified with the $\mathbb{Z}_2$ symmetry that is intrinsic to the Ising CFT, which ensures that the CFT has codimension one (note that σ is odd under any $g \in G_{\text{eff}} - G_{\text{gap}}$). The projective class specifies the symmetry fluxes of G_{eff} such that if we condense μ, we enter the gapped phase labeled by this projective class. If we instead condense σ, we break the symmetry group down to G_{gap}, with the resulting gapped phase identified by $\omega|_{G_{\text{gap}}} \in H^2(G_{\text{gap}}, U(1))$. Let us illustrate the above general classification for $G = \mathbb{Z}_2 \times \mathbb{Z}_2$. One choice of nested subgroups is $G_{\text{gap}} = \{1\} \subset G_{\text{eff}} = \mathbb{Z}_2 \subset G = \mathbb{Z}_2 \times \mathbb{Z}_2$, with *three* choices for the unbroken symmetry G_{eff} and *no* choice for an element in $H^2(\mathbb{Z}_2, U(1)) \cong \{1\}$. The other choice is $G_{\text{gap}} = \mathbb{Z}_2 \subset G_{\text{eff}} = G$, with *three* choices for the gapped symmetry G_{gap} and *two* choices of $\omega \in H^2(\mathbb{Z}_2 \times \mathbb{Z}_2, U(1)) \cong \mathbb{Z}_2$. We thus recover all $3 + 3 \times 2 = 9$ distinct $\mathbb{Z}_2 \times \mathbb{Z}_2$-enriched Ising CFTs of codimension one.

Let us briefly comment on G-enriched Ising CFTs of codimension two. These occur if $G_{\text{gap}} = G_{\text{eff}}$, since then both σ and ε can open up a gap. This is the maximal codimension. Since such an Ising CFT requires the fine-tuning of two parameters, it generically appears in two-dimensional phase diagrams as an isolated point (with a first-order line emanating from it). The symmetry group acts only on gapped degrees of freedom, and the latter can realize any of its phases labeled by a choice of $G_{\text{eff}} \subset G$ and $\omega \in H^2(G_{\text{eff}}, U(1))$. For $\mathbb{Z}_2 \times \mathbb{Z}_2$, there are thus six such symmetry-enriched Ising CFTs. More generally,

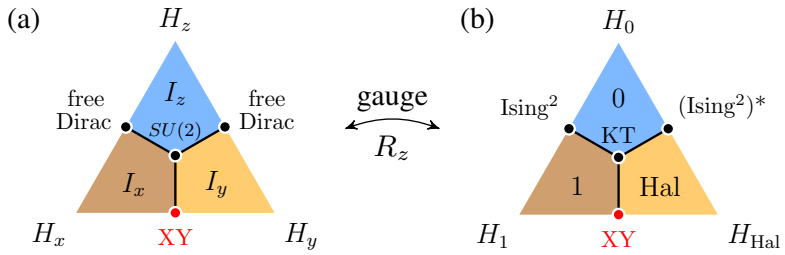

Figure 4.5.: **Classifying $\mathbb{Z}_2 \times \mathbb{Z}_2$-enriched Gaussian CFTs.** All $\mathbb{Z}_2 \times \mathbb{Z}_2$-CFTs with $c = 1$ can be connected (for $G_{\text{gap}} = \{1\}$ and $G_{\text{eff}} = G$). The $U(1)$-symmetric spin-1/2 XY chain appears in *both* panels (red dot). (a) The black lines are $c = 1$ CFTs whose (dominant) *local* operators have different symmetry properties; nevertheless, these operators become degenerate at the $SU(2)$-symmetric point, smoothly connecting these $c = 1$ CFTs. (b) Obtained from the former by a (nonlocal) unitary transformation which can be interpreted as gauging R_z symmetry. Two of the three $c = 1$ lines are described by orbifold CFTs; the dominant symmetry flux is symmetry-even (Ising^2) or symmetry-odd ((Ising^2)*), becoming degenerate at the KT point.

for any CFT one can consider the symmetry-enrichment where $G = G_{\text{gap}}$. However, this is not a very interesting example: it recovers the gapped classification and the CFT is a mere spectator. In particular, one can apply the usual mechanism of symmetry fractionalization, implying that the degeneracies with open boundary conditions (and their finite-size splitting) exactly coincide with that of the purely gapped case.

4.4.3. Gaussian criticality ($c = 1$)

There are six gapped phases for $\mathbb{Z}_2 \times \mathbb{Z}_2$-symmetric Hamiltonians and hence $\binom{6}{2} = 15$ direct transitions. We have already encountered nine of these in subsection 4.4.2: these were all distinct $\mathbb{Z}_2 \times \mathbb{Z}_2$-enriched Ising CFTs. We now demonstrate that the remaining six transitions are Gaussian CFTs. Remarkably, all six belong to the *same* $\mathbb{Z}_2 \times \mathbb{Z}_2$-enriched Gaussian CFT: they are smoothly connected. The six different types of direct transitions can be realized as direct interpolations between the fixed point Hamiltonians introduced in subsection 4.4.1, as shown in Fig. 4.5. We first discuss these transitions from the lattice perspective, which has the benefit of being concrete and constructive. Afterwards, we rephrase it in the field-theoretic language, which emphasizes the generality of these examples and makes a direct link with established CFT methods.

A lattice perspective

The six direction transitions have minimal codimension, which for a Gaussian CFT with $\mathbb{Z}_2 \times \mathbb{Z}_2$ symmetry means *codimension two*. I.e., one generically needs to tune two parameters to find these direct transitions—otherwise they split up into two separate Ising transitions. It also means that each transition shown in Fig. 4.5 is proximate to *two other gapped phases*, which are not shown. The clearest instance of this is the XY model $H_{XY} = \sum_n (X_n X_{n+1} + Y_n Y_{n+1})$ which appears *twice* in Fig. 4.5, once in each panel (red dot); indeed, $H_{XY} = H_x + H_y = H_1 + H_{\text{Hal}}$. If one breaks its $U(1)$ symmetry, one flows to one of the I_x or I_y phases (left panel). If one instead dimerizes the chain, one flows to either the trivial or topological Haldane phase (right panel); see also the discussion in subsection 4.4.1. To ensure that the CFT has codimension two, we need the full $\mathbb{Z}_2 \times \mathbb{Z}_2$ symmetry to act non-trivially on the CFT; see subsection 4.4.3. In other words,

$G_{\text{eff}} = \mathbb{Z}_2 \times \mathbb{Z}_2$ and $G_{\text{gap}} = \{1\}$. The remaining invariants which we proposed are thus the charges of local operators and of symmetry fluxes.

At first glance, such charges seem to distinguish distinct Gaussian $\mathbb{Z}_2 \times \mathbb{Z}_2$-CFTs. For instance, let us compare the $[I_x,I_y]$ transition to the $[I_x,I_z]$ transition. The former has a $U(1)$ symmetry in the xy-plane, and indeed, X_n and Y_n have the same scaling dimension $\Delta_\theta = 1/4$ for H_{XY}, whereas Z_n has $\Delta_\varphi = 1$. The roles are reversed in the latter, where Y_n is now the one with larger scaling dimension. Does this not give us a discrete invariant? I.e., for H_{XY} we can say that *all local operators of lowest scaling dimension are odd under* R_z. This *discrete* statement is surely *true*, but not *invariant*: the Gaussian CFT has a marginal tuning parameter that smoothly connects a whole line of universality classes [37, 173]. Indeed, this is well-known for the spin-1/2 XXZ chain, $H = \sum_n (X_n X_{n+1} + Y_n Y_{n+1} + \tilde{\Delta} Z_n Z_{n+1})$, which is described by a range of Gaussian CFTs for $-1 < \tilde{\Delta} \leq 1$. As one tunes $\tilde{\Delta}$ from zero to one, the scaling dimensions of X_n, Y_n and Z_n *smoothly* evolve toward the same value (this being 1/2); at $\tilde{\Delta} = 1$, the three operators are related by the $SU(2)$ symmetry of the model! All three $[I_\gamma,I_{\gamma'}]$ transitions can clearly be connected through this point, as shown in Fig. 4.5. The take-away message is that the space of local operators with smallest scaling dimension can change: this two-dimensional space becomes part of a larger-dimensional vector space at the $SU(2)$-symmetric point. The above attempt at defining a *discrete invariant charge* was thus not well-founded.

The discussion above demonstrates a subtlety in associating invariant charges to local observables. Something similar happens for the charges of symmetry fluxes. To find a Gaussian CFT whose symmetry fluxes have non-trivial charge, we need to consider transitions which are *not* invariant under stacking with the gapped Haldane phase: since the latter comes with charged symmetry fluxes, any transition that is not affected by this could not have had well-defined charges for its symmetry fluxes to begin with. To make clear what we mean, consider [1,Hal], as realized by the XY-chain. At this transition, the two distinct symmetry fluxes of R_γ for H_1 and H_{Hal}—as described in subsection 4.4.1—become scaling operators with the *same* scaling dimension $\Delta = 1/4$. We can thus not associate a unique charge to the symmetry flux of R_γ. This is related to the fact that [1,Hal]$*$Hal = [1,Hal], since it would merely interchange both sides of the transition. Similarly, the $[I_\gamma,I_{\gamma'}]$ transitions considered above would also *absorb* such an SPT phase (since $I_\gamma * \text{Hal} = I_\gamma$).

We can, however, find $c = 1$ transitions which are (seemingly) not invariant under such a stacking: consider the transition between the trivial phase and the phase that completely breaks $\mathbb{Z}_2 \times \mathbb{Z}_2$, i.e., [1,0], realized by $H_1 + H_0$. Conceptually, one can think of this as two separate Ising transitions occuring at the same point. Indeed, the field theory describing this critical point is not a usual *Gaussian CFT*, but rather the direct product of *two Ising CFTs*, usually denoted by $(\text{Ising})^2$. Accordingly, each R_γ has a *unique* symmetry flux and hence a well-defined charge! For [1,0], these fluxes commute with all symmetries, whereas for [Hal,0], they anticommute. Indeed, stacking with the Haldane phase interchanges these two transitions. However, despite having distinct discrete charge in these two cases, these models can be smoothly connected by tuning to $H_1 + H_{\text{Hal}} + H_0$, as shown in Fig. 4.5(b). The catch is that at this special point, the space of symmetry fluxes becomes two-dimensional, and the aforementioned charge is no longer well-defined—this arises naturally from a careful study of the Gaussian universality class (see subsection 4.4.3). Note that the novel phase diagram in Fig. 4.5(b) can be obtained from the known phase diagram in Fig. 4.5(a) by applying the duality transformation mentioned in subsection 4.4.1.

In conclusion, all $\mathbb{Z}_2 \times \mathbb{Z}_2$-enriched CFTs with central charge $c = 1$ can be smoothly connected if they are of codimension two. For higher codimension, there are multiple classes. Such a examples have already appeared in the literature [41, 57], and we will touch upon this in Section 4.6.

A field-theoretic perspective

We now give a field-theoretic interpretation of Fig. 4.5, which is complementary to the previous discussion.

Let us recall the compact boson CFT (also known as the one-component Luttinger liquid), which contains a phase field $\theta(x)$ and its conjugate field $\partial_x\varphi(x)$ that generates shifts in $\theta(x)$, i.e., $[\partial_x\varphi(x), \theta(y)] = 2\pi i\delta(x-y)$ [37, 173]. Both fields are 2π-periodic and the Hamiltonian is given by

$$H = \frac{1}{2\pi}\int \left(\frac{1}{4K}(\partial_x\varphi)^2 + K(\partial_x\theta)^2\right) \mathrm{d}x. \tag{4.13}$$

Here, K is the stiffness or Luttinger liquid parameter (sometimes one instead speaks of the compactification radius[18] $r_c = \sqrt{K}$). There is thus a one-parameter family of compact boson CFTs with a duality $K \leftrightarrow \frac{1}{4K}$ which interchanges the two fields. Particularly important are the primary vertex operators $e^{\pm i(m\varphi+n\theta)}$ which have scaling dimension $\Delta_{m,n} = m^2K + n^2/(4K)$ (and conformal spin $s_{m,n} = mn$). These vertex operators are local if and only if $n, m \in \mathbb{Z}$.

To see how the $\mathbb{Z}_2 \times \mathbb{Z}_2$ symmetry acts in this field theory, it is useful to use a lattice-continuum correspondence. Let us consider the XY-chain $H_{XY} = -\sum_n (X_nX_{n+1} + Y_nY_{n+1})$: this can be mapped to free fermions, allowing for a straight-forward continuum limit of the lattice model, which ends up with the compact boson CFT where $K = r_c = 1$, also called the *free Dirac CFT*. This route gives a direct relationship between lattice operators and operators of the CFT [14, 40, 174]. For instance, the generator of the on-site lattice $U(1)$ symmetry, Z_n, maps to the generator in the continuum, $\partial_x\varphi$. Similarly useful correspondences are $X_n \sim \cos\theta$ and $Y_n \sim \sin\theta$. From such relations—and from knowing how the symmetries act on the lattice operators—we can infer that R_x, R_y and R_z act in the continuum as

$$R_x : \begin{cases} \varphi \to -\varphi \\ \theta \to -\theta, \end{cases} \qquad R_y : \begin{cases} \varphi \to -\varphi \\ \theta \to \pi - \theta, \end{cases} \qquad R_z : \begin{cases} \varphi \to \varphi \\ \theta \to \theta + \pi. \end{cases} \tag{4.14}$$

(Note that $R_z = R_xR_y$, as required.) Enforcing these symmetries constrains the possible perturbations of the CFT. In fact, only two relevant operators commute with this symmetry, namely the vertex operators[19] $\cos(2\theta)$ and $\cos(\varphi)$ with scaling dimension $\Delta = 1 < 2$ at $K = 1$. Hence, this $\mathbb{Z}_2 \times \mathbb{Z}_2$-enriched $c = 1$ CFT has *codimension two*. For example, $\sin(2\theta)$—which is also relevant—is odd under R_x and is thus forbidden[20]. We note that $\pm\cos(2\theta)$ drives to I_x and I_y, whereas $\pm\cos(\varphi)$ drives to the trivial and Haldane phase; this is consistent with the red dot in Fig. 4.5(a) and (b).

The above action of $\mathbb{Z}_2 \times \mathbb{Z}_2$ was established at $K = 1$, but we see that it must continue to hold for any value of K (since $R_\gamma^2 = 1$). Nevertheless, we obtain other actions when considering, e.g., a transition $[I_x,I_z]$ instead of $[I_x,I_y]$. Indeed, for $H = -\sum_n (X_nX_{n+1} + Z_nZ_{n+1})$ we would *also* arrive at the Dirac CFT in the continuum limit, where we now denote the fields by $\tilde\varphi$ and $\tilde\theta$ to avoid confusion. The lattice-continuum correspondence, including $Y_n \leftrightarrow \partial_x\tilde\varphi$ and $Z_n \leftrightarrow \sin(\tilde\theta)$, implies

$$R_x : \begin{cases} \tilde\varphi \to -\tilde\varphi \\ \tilde\theta \to -\tilde\theta, \end{cases} \qquad R_y : \begin{cases} \tilde\varphi \to \tilde\varphi \\ \tilde\theta \to \tilde\theta + \pi. \end{cases} \qquad R_z : \begin{cases} \tilde\varphi \to -\tilde\varphi \\ \tilde\theta \to \pi - \tilde\theta, \end{cases} \tag{4.15}$$

The *same* lattice symmetries $R_{\gamma=x,y,z}$ thus act *differently* in the low-energy compact boson CFTs for these distinct transitions, as evidenced by Eqs. (4.14) and (4.15). In particular,

[18] This name arises due to the rescaled field $\tilde\theta \equiv \sqrt{K}\theta$ being $2\pi r_c$-periodic.
[19] On the lattice, these correspond to $X_nX_{n+1} - Y_nY_{n+1}$ and $(-1)^n(X_nX_{n+1} + Y_nY_{n+1})$, respectively.
[20] The lattice-continuum correpondence is $X_nY_{n+1} + Y_nX_{n+1} \sim \sin(2\theta)$.

this tells us that the local vertex operators of these CFTs (identified by their scaling dimensions) carry seemingly distinct charges, as already observed in the previous subsection.

Nevertheless, these two compact boson CFTs are merely two extremes of a single unified CFT. To see this, we use that tuning K preserves criticality. This corresponds to the black lines in Fig. 4.5(a) emerging from the phase diagram's edges. As $K \to 1/2$, we reach the center of the phase diagram. To see that the CFTs in terms of φ, θ and $\tilde{\varphi}, \tilde{\theta}$ truly *coincide* at this point, we use the fact that the self-dual point $K = 1/2$ is known to have an emergent $SU(2) \times SU(2)$ symmetry. As we show in Appendix C.4, this allows to perform a change of variables that leaves the action invariant:

$$\partial_x \tilde{\theta} = -2 \cos\theta \sin\varphi, \qquad \partial_x \tilde{\varphi} = -2 \sin\theta \cos\varphi. \tag{4.16}$$

Note that under this correspondence, Eq. (4.14) and (4.15) coincide! The identification in Eq. (4.16) tells us how these seemingly distinct compact boson CFTs are glued together. This can also be understood from the fact that at $K = 1/2$, the CFT has *nine* marginal perturbations [173]. Only *three* of these are compatible with $\mathbb{Z}_2 \times \mathbb{Z}_2$ symmetry, corresponding to the three gapless lines emanating from this point in Fig. 4.5(a).

Let us now consider the other $c = 1$ transitions, shown in Fig. 4.5(b). As mentioned in the previous subsection, this phase diagram is obtained from Fig. 4.5(a) by a nonlocal change of variables which maps the XY-chain to itself (see Appendix C.2). In the field theory, this can be interpreted as gauging R_z, the effect of which depends on how R_z acts on the fields. If R_z is a subset of the $U(1)$ rotation $\theta \to \theta + \alpha$—as happens for $[I_x,I_y]$ (see Eq. (4.14))—then gauging R_z amounts[21] to $r_c \to 1/r_c$, or, equivalently, $K \to 1/K$ [173]. This indeed keeps the free Dirac point with $K = 1$ invariant (the red dots in Fig. 4.5). The self-dual point $K = 1/2$—in the middle of the phase diagram—maps to $K = 2$, which is called the Kosterlitz-Thouless (KT) point since at this point there are *no* relevant $U(1)$-symmetric operators. However, if R_z negates the fields—as happens for $[I_x,I_z]$ (see Eq. (4.15))—then it is known that gauging this is *no longer the usual compact boson CFT*. Instead, we obtain a so-called *orbifold CFT* (this can also be seen as the boson CFT compactified on $S^1/\mathbb{Z}_2$) [173]. In particular, the free Dirac CFT in Fig. 4.5(a) maps to a stack of two Ising CFTs in Fig. 4.5(b), usually denoted by $(\text{Ising})^2$, which is a $c = 1$ orbifold CFT with orbifold radius $r_{\text{orbifold}} = 1$ [173]. This remains critical as one tunes $r_{\text{orbifold}} \to 1/\sqrt{2}$, reaching the center of the phase diagram. Indeed, it is known that at the particular value $r_{\text{orbifold}} = 1/\sqrt{2}$, the $c = 1$ orbifold CFT *coincides* with the aforementioned KT point of the compact boson CFT [173]. The interpolation between the three models H_1, H_{Hal} and H_0 thus provides a concrete lattice realization—incidentally solvable by Bethe ansatz—of the of the deep fact that the $c = 1$ orbifold CFT and compact boson CFT can be connected by a marginal perturbation, which in this case also preserves $\mathbb{Z}_2 \times \mathbb{Z}_2$.

Lastly, we comment on symmetry fluxes from the perspective of field theory. For the compact boson CFT, the space of symmetry fluxes for R_γ is two-dimensional. This is easiest to see for R_z in the case where it acts as $\theta \to \theta + \pi$ (see Eq. (4.14)). The two independent fluxes are then $\cos(\varphi/2)$ and $\sin(\varphi/2)$ with dimension $\Delta = K/4$ (on the lattice, these correspond to $\cdots Z_{n-2}Z_{n-1}Z_n$ with n even and odd, respectively). The former (latter) is even (odd) under R_x and R_y. We thus cannot associate a unique charge to the symmetry flux of R_z. The situation is seemingly different for the orbifold CFT, which we illustrate for the $(\text{Ising})^2$ CFT as realized by $H = H_1 + H_0$ (appearing in Fig. 4.5(b)). Recalling the definition of H_0 in Eq. (4.12), we see that if σ_i denotes the spin operators of the two copies of the Ising CFT, then σ_1 is odd under R_y and R_z (but even under R_x), and similarly for σ_2 with R_x and R_y interchanged. From this, we can infer that

[21] This can be seen as a concatenation of halving the compactification radius and a duality transform: $r_c \to r_c/2 \to \frac{1}{2(r_c/2)} = 1/r_c$.

the symmetry flux for R_z is $\mu_1\mu_2$ (with dimension $\Delta = 1/4$). Most importantly: this is *unique*. Indeed, its dimension is well-separated[22] from that of $(\mu_1\mu_2) \times (\sigma_1\sigma_2) \sim \psi_1\psi_2$ for which $\Delta = 1$. As discussed in Section 4.2, we can associate charges to unique symmetry fluxes. For the transition [1,0], it is easy to see that the symmetry flux of R_z is *even* under R_x and R_y, whereas for [Hal,0] it is *odd*. Hence, the two orbifold lines in Fig. 4.5(b) seem topologically distinct! The catch, however, is that both lines connect to the compact boson line, as discussed above. At that point, the scaling dimensions of $\mu_1\mu_2$ and $\psi_1\psi_2$ meet, coinciding with the aforementioned $\cos(\varphi/2)$ and $\sin(\varphi/2)$. Hence, to realize topologically non-trivial symmetry-enriched $c = 1$ CFTs, one either needs to go to higher codimension, or larger symmetry groups; examples for both are discussed in Section 4.6.

4.5. A fermionic example: the interacting version of Chapter 2

Thus far, we have discussed examples of bosonic G-CFTs. However, the concept also applies to fermionic systems. In fact, the critical Majorana chains introduced in Chapter 2 provide examples of this. Although that chapter concerned *non-interacting* systems, here we point that they realize Majorana CFTs enriched by fermionic parity symmetry $\mathbb{Z}_2^F$ and spinless time-reversal symmetry $\mathbb{Z}_2^T$. This directly implies that various cases studied in Chapter 2 indeed remain non-trivial in the presence of interactions.

For concreteness, we consider the two models

$$\begin{array}{rcccl} H & = & 2(H_0 + H_1) & = & i\sum_n \tilde{\gamma}_n(\gamma_n + \gamma_{n+1}), \\ H'' & = & 2(H_1 + H_2) & = & i\sum_n \tilde{\gamma}_n(\gamma_{n+1} + \gamma_{n+2}). \end{array} \tag{4.17}$$

To wit, this notation uses the basis of Majorana modes $\gamma_n = c_n^\dagger + c_n$ and $\tilde{\gamma}_n = i(c_n^\dagger - c_n)$, where c_n are spinless fermions satisfying $\{c_n^\dagger, c_m\} = \delta_{nm}$. The Hamiltonians in Eq. (4.17) are sketched in Fig. 2.2 of Chapter 2, with H'' having a zero-energy Majorana mode per edge. In that chapter, we proved that these two non-interacting chains are topologically distinct, despite both being described by the $c = 1/2$ Majorana CFT. In particular, we defined the topological invariant ω in terms of the roots of a particular polynomial $f(z)$ (for details, see Section 2.3). This invariant—and its associated edge modes—were well-defined as long as we preserved fermionic parity symmetry $P = \prod P_n$ (where $P_n = i\tilde{\gamma}_n\gamma_n$) and spinless time-reversal symmetry T (acting as $T\gamma_n T = \gamma_n$ and $T\tilde{\gamma}_n T = -\tilde{\gamma}_n$). In addition, the formalism of $f(z)$ allowed to derive that the edge modes are exponentially localized in this non-interacting setting (see Theorem 1 in Section 2.4).

We will illustrate that these two critical chains are indeed distinct symmetry-enriched Majorana CFTs. In fact, one could argue that this follows from our analysis of the bosonic case, since using[2] the Jordan-Wigner correspondence detailed in Table 3.2 of Chapter 3, the above models map to the models H and H'' encountered in Section 4.1. Nevertheless, while such a mapping can be very useful, it is not always the most insightful route due to the nonlocal nature of the Jordan-Wigner transformation which affects the physical interpretation. Here, we keep the discussion self-contained in the fermionic language.

Let us now explain how these two critical models in Eq. (4.17) are distinguished by the charges of the symmetry fluxes of P. Interestingly, for fermionic systems it is possible for a symmetry flux to be charged *under itself*: the symmetry flux of fermionic parity can itself be fermionic. Indeed, both H and H'' have one symmetry flux of P which is *odd* under P, and one which is *even*. The former is the same for both models, being given by $\cdots P_{n-2}P_{n-1}\gamma_n$ (with scaling dimension $\Delta = 1/8$) [126]. Physically, this corresponds to both phases being proximate to the topological Kitaev phase where this symmetry flux

[22] Similarly, the unique symmetry flux of R_x is μ_2 with $\Delta = 1/8$; its subdominant flux is $\sigma_1\mu_2$ with $\Delta = 1/4$.

has long-range order. The symmetry flux of P which is *even* under P (with the same scaling dimension), is given by [126]

$$\begin{array}{rcll} \mathcal{S}_n^P & = & \cdots P_{n-2}P_{n-1}P_n & (\text{for } H), \\ \mathcal{S}_n^P & = & \cdots P_{n-2}P_{n-1}(i\gamma_n\gamma_{n+1}) & (\text{for } H''). \end{array} \tag{4.18}$$

(The prefactors were chosen such that $\langle(\mathcal{S}_n^P)^2\rangle$ is positive; see Section 4.2.) We observe that the former is *even* under T, whereas the latter is *odd* under T. This defines a discrete bulk invariant. Analogous to the discussion in Section 4.3, the latter protects a Majorana edge mode at each boundary, giving a global two-fold degeneracy with a finite-size splitting $\sim 1/L^{14}$. Indeed, this is consistent with the above claim that the models in Eq. (4.17) are mapped onto the spin chains in Eq. (4.3) using a nonlocal Jordan-Wigner transformation—which is exact for *open* boundary conditions (as discussed in Chapter 3).

The above concerned $c = 1/2$ Majorana CFTs. In Chapter 2, we saw that there were an *infinite* number of topologically distinct versions of this CFT, labeled by a topological invariant $\omega \in \mathbb{Z}$. Using the formalism of symmetry-enriched CFTs, one can argue that with interactions there are only eight classes. For more general CFTs ($c \geq 1$), a case-by-case study is necessary. In the non-interacting case, one could have any central charge $c \in \frac{1}{2}\mathbb{Z}$, each having an infinite number of distinct symmetry-enriched versions (with P and T symmetry). With interactions, some remain non-trivial, others do not, and this can be determined by examining the symmetry action on the higher-dimensional space of symmetry fluxes. We leave an exhaustive analysis of these more general situations to future work.

4.6. Application to previous works

In this last section, we demonstrate how previous works on critical systems with edge modes can be fit into the framework of symmetry-enriched CFTs proposed in this thesis. Considering the extent of the literature on topologically non-trivial gapless phases [41–58], a *complete* demonstration would constitute a work on its own. Here, we limit ourselves to a few (chronologically-ordered) case studies. We point out how these systems can be interpreted as non-trivial symmetry-enriched CFTs, for which we identify bulk invariants.

For clarity, let us mention that in 2011 there were several contemporaneous works discussing algebraically-ordered superconductors with topological edge modes [42–44]. However, these are *not* examples of edge modes protected by a symmetry-enriched CFT. This can be seen from the fact that in these cases, the edge modes have algebraic finite-size splitting $\sim 1/L^\beta$ where the power β is proportional to the Luttinger liquid parameter K. This means that the edge modes can be destroyed by *smoothly* tuning K to a small enough value. Hence, there cannot be a *discrete bulk invariant* associated to the $c = 1$ CFT. This is consistent with symmetries not being important to stabilize the edge modes in Refs. [42–44] (aside from the $U(1)$ symmetry stabilizing criticality).

"Prediction of a gapless topological Haldane liquid phase in a one-dimensional cold polar molecular lattice"

In Ref. [41], Kestner, Wang, Sau and Das Sarma introduced a gapless analogue of the spin-1 Haldane phase. Due to the context of the work (i.e., dipolar gases), long-range interactions were considered. Nevertheless, a nearest-neighbor model is straight-forward:

$$H = \sum_n \left[(S_n^x S_{n+1}^x + S_n^y S_{n+1}^y)(S_n^z + S_{n+1}^z)^2 + \Delta S_n^z S_{n+1}^z\right]. \tag{4.19}$$

The Hamiltonian looks similar to the spin-1 XXZ chain, with an extra factor in the spin-hopping term such that $\sum_n (S_n^z)^2$ is conserved—which makes all the difference. For $0 <$

$\Delta < 1$, the system is critical with central charge $c = 1$, and using the methods of Ref. [41], it can be shown that the system is topologically non-trivial: there is still long-range order in the Haldane string order parameter $\cdots R^z_{n-2}R^z_{n-1}S^z_n$ and the ground state is twofold degenerate with open boundary conditions.

We note that this model is an example of a $c = 1$ CFT enriched by the $\mathbb{Z}_2\times\mathbb{Z}_2$ group of π-rotations R^x, R^y and R^z. Indeed, the fact that $\cdots R^z_{n-2}R^z_{n-1}S^z_n$ has long-range order, tells us, firstly, that the symmetry flux of R^z is *unique* and, secondly, that it has a non-trivial charge with respect to R^x and R^y. This thus gives us a *discrete topological invariant* for the critical bulk. In section 4.4.3 we saw that there are no topologically non-trivial $\mathbb{Z}_2\times\mathbb{Z}_2$-enriched CFTs of minimal codimension. Indeed, Eq. (4.19) is of higher codimension and is not naturally interpreted as a critical point between phases with $\mathbb{Z}_2 \times \mathbb{Z}_2$ symmetry.

However, it *is* a $\mathbb{Z}_2 \times \mathbb{Z}_2 \times \mathbb{Z}_2^T$-enriched CFT of minimal codimension! More precisely, it occurs as a direct transition between two gapped phases which are *topologically distinct* with respect to $T_{\text{spin}} = R^yK$ but which are *topologically identical* and *non-trivial* with respect to $\mathbb{Z}_2 \times \mathbb{Z}_2$. To see this—and to shed light on the unusual conservation law—it is useful to consider the unitary $U \equiv \exp\left(i\frac{\pi}{2}\sum_n(S^z_n)^2\right)$. It can be shown that this commutes with $R^{\gamma=x,y,z}$ but not with T_{spin}, i.e., $UT_{\text{spin}}U^\dagger = R^xK \neq T_{\text{spin}}$. Hence, if H_{XXZ} is the spin-1 XXZ chain—which is non-trivial with respect to π-rotations *and* time-reversal—then $UH_{\text{XXZ}}U^\dagger$ is still non-trivial with respect to the former, but *not* the latter. Remarkably, the model in Eq. (4.19) is exactly the halfway interpolation between these two, $H = \frac{1}{2}\left(H_{\text{XXZ}} + UH_{\text{XXZ}}U^\dagger\right)$. Indeed, since U toggles between the two gapped phases, the transition must occur at the $\sum(S^z_n)^2$-symmetric point. Lastly, note that both gapped phases have the same symmetry flux for R^z (this can hence remain long-range ordered at criticality) but have distinct symmetry fluxes for R^x, i.e., $\cdots R^x_{n-2}R^x_{n-1}S^x_n$ and $\cdots R^x_{n-2}R^x_{n-1}\{S^y_n, S^z_n\}$. At the critical point, the latter two become algebraically ordered with the same scaling dimension. The symmetry flux of R^x is thus degenerate, but both have the same non-trivial charges with respect to R^y and R^z, consistent with this being a non-trivially-enriched CFT.

"Quantum Criticality in Topological Insulators and Superconductors: Emergence of Strongly Coupled Majoranas and Supersymmetry"

One of the phase transitions considered by Grover and Vishwanath in Ref. [165] is between a topological superconductor in class DIII (protected by an anti-unitary symmetry satisfying $T^2 = P$) and an Ising phase which spontaneously breaks T. It was demonstrated that the edge flows to an unusual fixed point, exhibiting itself in unusual fermionic correlations near the boundary (as a function of time).

We point out that this transition is an Ising CFT enriched by T and fermionic parity symmetry P. The clearest way of seeing this is that the symmetry flux of P (which has long-range order for this bosonic transition) can be shown to be *odd* under T. In an approximate converse, the μ operator of the Ising CFT is *odd* under fermionic parity symmetry: $P\mu P = -\mu$; see Appendix C.5 for details. As discussed in Fig. 4.3, this stabilizes the spontaneously-fixed boundary condition. According to the analysis in Section 4.3, we thus expect that this class of transition generically has a global twofold degeneracy for open boundaries whose finite-size splitting is exponentially small in system size.

"Gapless symmetry-protected topological phase of fermions in one dimension"

In Ref. [46], Keselman and Berg show that spinful fermions with attractive triplet-pairing stabilize a $c = 1$ CFT with exponentially-localized edge modes protected by fermionic parity symmetry P and time-reversal symmetry T (obeying $T^2 = P$). In addition to a

field-theoretic analysis, this was numerically demonstrated in a simple lattice model:

$$H = -\sum_{n,\sigma} \left(c^\dagger_{n,\sigma} c_{n+1,\sigma} + h.c. \right) + U \sum_n \Delta^\dagger_n \Delta_n, \tag{4.20}$$

where $\sigma \in \{\uparrow, \downarrow\}$ and $\Delta_n = c_{n,\uparrow} c_{n+1,\downarrow} + c_{n,\downarrow} c_{n+1,\uparrow}$ (on the lattice, the symmetries are given by $P = \prod_j P_j$ where $P_j = e^{i\pi(n_{j,\uparrow}+n_{j,\downarrow})}$ and $T = \prod_j e^{i\pi S^y_j} K$ with $S^y_j = \frac{i}{2}(c^\dagger_{j,\downarrow} c_{j,\uparrow} - c^\dagger_{j,\uparrow} c_{j,\downarrow})$). For $U < 0$, the spin sector is gapped, whereas charges remain gapless. The stability of the edge mode was argued to be a consequence of the gap to single-fermion excitations (which moreover implies that the phenomenon persists upon adding spin-orbit coupling). Moreover, in Ref. [46] it was shown that fermionic parity symmetry anticommutes with T *near the edges*, implying edge modes.

We remark that this $c = 1$ CFT is non-trivially enriched by P and T. We find that for $U < 0$, the symmetry flux of P has long-range order and is given by $\mathcal{S}^P_j = \cdots P_{j-2} P_{j-1} (n_{j,\uparrow} - n_{j,\downarrow})$, which obeys $T \mathcal{S}^P T^{-1} = -\mathcal{S}^P$. See Appendix C.5 for numerical details. This generalizes the observation of Ref. [46] that P and T anticommute near the *boundary* to a topological invariant *in the bulk*. This moreover confirms that the phase is protected by virtue of P being a gapped symmetry. The fact that the non-trivial symmetry flux is for a *gapped* symmetry is naturally related to the exponentially small finite-size splitting observed in Ref. [46].

"Gapless symmetry-protected topological order"

In Refs. [52, 57], Scaffidi, Parker and Vasseur extended the well-known mechanism of creating gapped SPT phases by decorating domain walls [175] to critical systems. The idea is illustrated straightforwardly with an example (their mechanism also applies to higher dimensions, but here we limit ourselves to one dimension). Let U be the unitary which maps the gapped $\mathbb{Z}_2 \times \mathbb{Z}_2$-paramagnet to the $\mathbb{Z}_2 \times \mathbb{Z}_2$-SPT phase. As a starting point, take a Hamiltonian H which consists of trivial gapped degrees of freedom decoupled from a critical bulk; moreover, presume that *one* of the $\mathbb{Z}_2 \subset \mathbb{Z}_2 \times \mathbb{Z}_2$ acts only on the former gapped chain. The claim is then that $UHU^\dagger$—which is clearly still critical—is topologically non-trivial, which was diagnosed in terms of edge properties. In particular, in the above case, the ground state will be twofold degenerate for open boundary conditions (with exponentially small finite-size splitting). Through a combination of perturbative arguments and numerical calculations, this topological phenomenon was shown to be stable.

The above procedure—which can be applied for any symmetry group G—indeed creates non-trivial G-enriched CFTs. This can be seen from the perspective of symmetry fluxes: by construction, part of the symmetry group will be *gapped*, which ensures that the associated symmetry fluxes are *unique*. This means that the non-trivial charge endowed by the SPT-entangler U will be a well-defined topological invariant, even at criticality, as discussed in Section 4.2. Using the boundary RG analysis of Section 4.3, this non-trivial symmetry flux can be used to argue the presence of edge modes. The notion of *charged symmetry flux* thus gives a *topological bulk invariant* for the cases studies in Refs. [52, 57]. We note that the presence of gapped degrees of freedom are not essential to make domain wall decoration work at criticality: the models H and H'' in Section 4.1 are related by the SPT-entangler $U = \prod_n (CZ)_{n,n+1}$; in this case, we found the finite-size splitting to be algebraic.

Part II.

Excitations in two-dimensional magnets

Overview of Part II

As mentioned in the introduction, Part II of this thesis studies excitations of two-dimensional quantum spin models at zero temperature.

Chapter 5: Spectral functions and quasiparticles

The main tool we will use to investigate such excitations is the *dynamic (spin) structure factor*, which we also simply refer to as the *spectral function*. This quantity is of interest since it is obtainable by calculating time-dependent correlation functions and gives direct insight into the spectrum of the Hamiltonian and various physical properties of its quasiparticles. Being measurable by inelastic neutron scattering, it also forms an indispensable bridge between theory and experiment. In the first part of Chapter 5, we review the definition of the dynamic structure factor and its most important properties.

The second part of this chapter is devoted to introducing a novel numerical matrix-product-state-based algorithm that computes the spectral function for two-dimensional lattice models. The essential idea is to place the system on a cylinder, such that one can use powerful *one-dimensional* methods, namely the density matrix renormalization group (DMRG) [12, 106] to obtain the ground state and matrix product operator time-evolution methods [108]. This way, we obtain time-dependent correlation functions for the two-dimensional system, which gives us the spectral function after Fourier transforming. In Chapter 5, we explain what it means to put the system on a cylinder, the physical consequences of doing so, and, finally, the numerical aspects of this method.

Chapter 6: Kitaev-Heisenberg on the honeycomb lattice: proximate spin liquids

This chapter serves a dual purpose: we benchmark the method introduced in Chapter 5 and we use it to identify a *proximate spin liquid*.

The Kitaev model on the honeycomb lattice [95] is an exactly-solvable interacting spin-1/2 model realizing highly-nontrivial topological phases of matter (so-called spin liquids). Even its spectral function has been obtained analytically [176]. This thus forms a challenging benchmark for *any* numerical method for calculating spectral functions. In Chapter 6, we show that the method of Chapter 5 gives a good agreement with this exact solution.

Having benchmarked the method for an integrable model, we study the spectral function after adding non-integrable perturbations. A particularly important perturbation is given by adding a Heisenberg term. The resulting Kitaev-Heisenberg model rose to prominence after being suggested as a minimal model for quantum magnets with strong spin-orbit coupling [177], including certain iridates [178] and α-$RuCl_3$ [179]. In Chapter 6, we numerically study its spectral function. If the Heisenberg term is dominant, we find that the spectral properties are well-described by spin wave theory. However, when the Heisenberg and Kitaev terms are of comparable strength, we find that the ground state still has conventional symmetry-breaking order, but its excitations no longer seem to be simple spin waves. In particular, we find considerable weight in broad smeared-out features whose form resembles that of the pure Kitaev model. This establishes the notion of a *proximate spin liquid* and phenomenologically agrees with aspects of recent inelastic neutron scattering data for α-$RuCl_3$ [96, 97, 180].

Chapter 7: Heisenberg on the square lattice: interacting spin waves

Despite nearly a century of study of the spin-1/2 Heisenberg model on the square lattice, there is still disagreement on the nature of its high-energy excitations. More precisely, while its Néel ground state order and the accompanying low-energy Goldstone modes are well-described by spin wave theory (SWT), it has been observed that the upper part of the magnon dispersion has features which are not reproduced by SWT calculations. This has been referred to as *anomalous* [87] and some have argued that this is due to a nearby spin liquid in the phases diagram [87, 181–184]—i.e., a more benign version of the extreme case studied in Chapter 6—whereas others proclaim that it can be explained by incorporating magnon interactions [93, 94] (of course these claims need not be mutually exclusive).

Using the method of Chapter 5, we shed light on these spectral features by tracking them as we tune the Hamiltonian toward the exactly soluble Ising limit. In the latter limit, the interactions are due to a simple counting of domain walls—these are indeed nonperturbative, but nevertheless quite intuitive. This thus gives a simple interpretation of the the attractive magnon interactions of the Heisenberg model. Remarkably, a semi-quantitative description of certain observed features arises already at the lowest non-trivial order in perturbation theory around the Ising limit. Moreover, our analysis uncovers that high-energy magnons are localized on a single sublattice, which is related to the entanglement properties of the ground state. This localized nature of the high-energy magnons is presumably at the root of why the local energetic domain wall considerations of the Ising model persist to the Heisenberg limit.

Chapter 8: Heisenberg on the triangular lattice: avoided decay from strong interactions

Unlike the square lattice antiferromagnet of Chapter 7, the triangular lattice Heisenberg antiferromagnet (TLHAF) is *frustrated*—a triangle does not allow for three strictly-antiferromagnetic bonds[23]. Its ground state still spontaneously magnetizes (in a non-collinear 120° pattern) [186, 187], but there is considerable quantum entanglement due to the aforementioned frustration. It is hence unclear whether its magnon excitations are accurately described by SWT, which is an expansion around the (semi-)classical limit $S \to \infty$. Studies of the leading and next-to-leading order contributions in SWT suggest that for more than half of the Brillouin zone, the magnon dispersion is inside the two-magnon continuum, leading to a finite lifetime [75, 76, 188–191]. In other words, according to SWT, the THLAF is an archetype for *magnon decay* [75, 76, 191]. However, in Chapter 8, we numerically obtain the spectral function (according to Chapter 5) in a slightly perturbed model for which SWT still predicts decay, and we find none. Instead, the magnon seems to have been repelled out of the aforementioned continuum.

This is an instance of a very general phenomenon which we call *avoided quasiparticle decay*: if quasiparticles are strongly-interacting[24], then they are generically pushed out of the continuum which would otherwise cause their decay. To illustrate and emphasize the generality of avoided decay, in Chapter 8, we first explain this hitherto-unacknowledged principle before discussing the particular case of the TLHAF. This principle arises as a straightforward generalization of the notion of level repulsion and we illustrate it numerically in a tractable many-body Ising ladder. Finally, we point out that the phenomenology of avoided decay can be identified in existing experimental data for the triangular lattice magnet [77] $Ba_3CoSb_2O_9$ and even superfluid helium [78–83].

[23] For the same reason, the classical triangular lattice antiferromagnetic Ising model has finite entropy at zero temperature [185].

[24] This applies to the TLHAF: due to the small spin, spin waves are strongly-coupled, and due to $SU(2)$ symmetry being completely broken, there are no quantum numbers forcing matrix elements to vanish.

5. Spectral functions and quasiparticles

As already outlined in the overview of Part II of this thesis, in Chapters 6, 7 and 8 we will study the dynamic spin structure factor of two-dimensional spin models. This chapter presents the necessary background for this: Section 5.1 introduces the dynamic structure factor, and Section 5.2 presents a novel numerical method to calculate this. The latter is based on bringing together two recent developments in the field of tensor networks: on the one hand, obtaining two-dimensional ground states by using the density matrix renormalization group (DMRG) method [12, 106] on a cylinder [192] and, on the other hand, obtaining spectral functions by time-evolving one-dimensional systems [108, 193].

5.1. Dynamic structure factor: from correlations to excitations

Let us consider a lattice model where each site (at location $\boldsymbol{r}$) carries an effective spin-1/2 denoted by the Pauli matrices $\sigma^\alpha_{\boldsymbol{r}}$ ($\alpha = x, y, z$). We define the *dynamic spin structure factor* [66, 67] in terms of the plane waves $\sigma^\alpha_{\boldsymbol{k}} \equiv \frac{1}{\sqrt{\mathcal{N}}} \sum_{\boldsymbol{r}} e^{-i\boldsymbol{k}\cdot\boldsymbol{r}} \sigma^\alpha_{\boldsymbol{r}}$ (where $\mathcal{N}$ is the total number of sites) as follows:

$$\mathcal{S}^{\alpha\beta}(\boldsymbol{k}, \omega) = \frac{1}{2\pi} \int_{-\infty}^{\infty} e^{i\omega t} \left\langle \sigma^\alpha_{\boldsymbol{k}}(t) \sigma^\beta_{-\boldsymbol{k}}(0) \right\rangle \, \mathrm{d}t. \tag{5.1}$$

At this point, we have not assumed a particular structure of the lattice. As a consequence, the above $\boldsymbol{k}$ should not yet be interpreted as a (quasi-)momentum. We will return to this issue in subsection 5.1.2. Throughout this thesis, we will also refer to $\mathcal{S}^{\alpha\beta}(\boldsymbol{k}, \omega)$ as the *dynamic structure factor* and the *spectral function*. These terms are in principle broader, but since the dynamic spin structure factor is the only type of spectral function we consider in this thesis, there can be no confusion.

This spectral function contains considerable physical information. The most direct way of seeing this is by rewriting it in the so-called Lehmann representation.

5.1.1. Connection to the many-body spectrum: the Lehmann representation

From the definition in Eq. (5.1), it directly follows that $\left(\mathcal{S}^{\alpha\beta}(\boldsymbol{k}, \omega)\right)^* = \mathcal{S}^{\beta\alpha}(\boldsymbol{k}, \omega)$. In particular, $\mathcal{S}^{\alpha\alpha}(\boldsymbol{k}, \omega)$ is real. In fact, it turns out to be *positive*. To see this, we rewrite Eq. (5.1) using that $\mathcal{O}(t) = e^{iHt} \mathcal{O} e^{-iHt}$ and inserting a resolution of the identity $\mathbb{I} = \sum_n |n\rangle\langle n|$ with $|n\rangle$ being an energy eigenstate (i.e., $H|n\rangle = \omega_n |n\rangle$, setting the ground state energy to zero, $\omega_0 = 0$):

$$\mathcal{S}^{\alpha\alpha}(\boldsymbol{k}, \omega) = \frac{1}{2\pi} \int_{-\infty}^{\infty} e^{i\omega t} \left\langle \sigma^\alpha_{\boldsymbol{k}} e^{-iHt} \left(\sum_n |n\rangle\langle n| \right) \sigma^\alpha_{-\boldsymbol{k}} \right\rangle \, \mathrm{d}t \tag{5.2}$$

$$= \sum_n \left(\frac{1}{2\pi} \int_{-\infty}^{\infty} e^{i(\omega - \omega_n)t} \mathrm{d}t \right) \langle 0 | \sigma^\alpha_{\boldsymbol{k}} | n \rangle \langle n | \sigma^\alpha_{-\boldsymbol{k}} | 0 \rangle \tag{5.3}$$

$$= \sum_n \delta(\omega - \omega_n) \, |\langle n | \sigma^\alpha_{-\boldsymbol{k}} | 0 \rangle|^2. \tag{5.4}$$

This is the *Lehmann representation* of the dynamic structure factor. It tells us that if $\mathcal{S}^{\alpha\alpha}(\boldsymbol{k}, \omega) \neq 0$ for a particular value of $\boldsymbol{k}$ and ω, then there *exists* an energy eigenstate with energy ω (which is moreover created by acting with $\sigma^\alpha_{-\boldsymbol{k}}$ on the ground state).

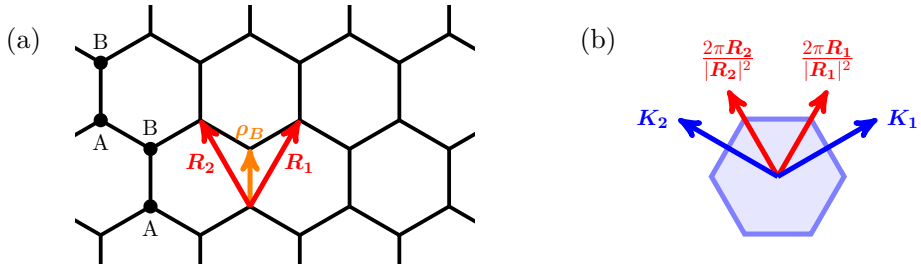

Figure 5.1.: **Honeycomb lattice.** (a) The lattice vectors $\boldsymbol{R_1}$ and $\boldsymbol{R_2}$ generate the periodic lattice where each unit cell has two sites, denoted by A and B. The vectors are shown relative to an A-site; note that $\boldsymbol{\rho_A} = \boldsymbol{0}$ and $\boldsymbol{\rho_B} = \frac{1}{3}(\boldsymbol{R_1} + \boldsymbol{R_2})$. (b) The reciprocal lattice vectors are defined by $\boldsymbol{K_i} \cdot \boldsymbol{R_j} = 2\pi\delta_{ij}$. The shaded region is the first Brillouin zone.

5.1.2. Momentum and unit cells

Let us now specify the situation further: we presume that the lattice is periodic with respect to a unit cell of $\mathcal{N}_{\text{uc}}$ sites. This will allow us to (1) give a more concrete interpretation of the weight in the Lehmann representation, (2) rewrite the spectral function to make it amenable to numerical calculations, and (3) make a direct link with experiment.

For concreteness, we will work in two spatial dimensions. Let $\boldsymbol{R_1}$ and $\boldsymbol{R_2}$ be the lattice vectors. We can then write the positions as $\boldsymbol{r} = r_1\boldsymbol{R_1} + r_2\boldsymbol{R_2} + \boldsymbol{\rho_\lambda}$ where $(r_1, r_2) \in \mathbb{Z}\times\mathbb{Z}$ and λ is the sublattice index which can take one of $\mathcal{N}_{\text{uc}}$ values. Here $\boldsymbol{\rho_\lambda}$ specifies the position *within* the unit cell. As an example (which is pertinent to the next chapter), consider the honeycomb lattice in Fig. 5.1(a), where $\mathcal{N}_{\text{uc}} = 2$. Labeling the two sublattices as A and B and taking A as the reference site, we have that $\boldsymbol{\rho_A} = \boldsymbol{0}$ and $\boldsymbol{\rho_B} = \frac{1}{3}(\boldsymbol{R_1} + \boldsymbol{R_2})$.

Let T_i be the translation by the vector $\boldsymbol{R_i}$. This is a symmetry of the lattice and the plane wave $\sigma^\alpha_{\boldsymbol{k}}$ defined above has a well-defined momentum $-\boldsymbol{k}$ under this, i.e., $T_i\sigma^\alpha_{\boldsymbol{k}}T_i^{-1} = \frac{1}{\sqrt{\mathcal{N}}}\sum_{\boldsymbol{r}} e^{-i\boldsymbol{k}\cdot\boldsymbol{r}}\sigma^\alpha_{\boldsymbol{r}+\boldsymbol{R_i}} = e^{i\boldsymbol{k}\cdot\boldsymbol{R_i}}\sigma^\alpha_{\boldsymbol{k}}$. Moreover, let us presume that this translation symmetry is also a symmetry of the Hamiltonian and is not spontaneously broken by the ground state. (Otherwise, one can simply increase the aforementioned unit cell[1].) We can then associate a momentum $\boldsymbol{k_n}$ to each eigenstate (with the ground state having $\boldsymbol{k_0} = \boldsymbol{0}$) such that $T_i|n\rangle = e^{-i\boldsymbol{k_n}\cdot\boldsymbol{R_i}}|n\rangle$. This allows us to rewrite Eq. (5.4) as

$$\mathcal{S}^{\alpha\alpha}(\boldsymbol{k},\omega) \propto \sum_n \delta(\omega-\omega_n)\delta(\boldsymbol{k}-\boldsymbol{k_n})\left|\langle n|\left(\textstyle\sum_\lambda e^{-i\boldsymbol{k_n}\cdot\boldsymbol{\rho_\lambda}}\sigma^\alpha_{\lambda,\boldsymbol{0}}\right)|0\rangle\right|^2, \tag{5.5}$$

where we use the notation $\sigma^\alpha_{\lambda,\boldsymbol{R}} \equiv \sigma^\alpha_{\boldsymbol{R}+\boldsymbol{\rho_\lambda}}$. The spectral function thus tells about the existence of eigenstates with energy ω and momentum $\boldsymbol{k}$. (Note that it cannot tell us about the *absence* of such states, since the weight may simply vanish.)

The lattice vectors $\boldsymbol{R_i}$ come with a corresponding reciprocal lattice vectors $\boldsymbol{K_j}$ such that $\boldsymbol{K_j}\cdot\boldsymbol{R_i} = 2\pi\delta_{ij}$ (see Fig. 5.1(b)). However, if the unit cell is non-trivial (i.e., $\mathcal{N}_{\text{uc}} > 1$), the spectral function is not periodic with respect to $\boldsymbol{K_j}$. It is useful to split it up into contributions which do have this symmetry. First, we split up the plane wave

$$\sigma^\alpha_{\boldsymbol{k}} = \frac{1}{\sqrt{\mathcal{N}_{\text{uc}}}}\sum_\lambda e^{-i\boldsymbol{k}\cdot\boldsymbol{\rho_\lambda}}\underbrace{\left(\sqrt{\frac{\mathcal{N}_{\text{uc}}}{\mathcal{N}}}\sum_{\boldsymbol{R}} e^{-i\boldsymbol{k}\cdot\boldsymbol{R}}\sigma^\alpha_{\lambda,\boldsymbol{R}}\right)}_{\equiv\sigma^\alpha_{\lambda,\boldsymbol{k}}}. \tag{5.6}$$

[1] Alternatively, one can sometimes find a *modified* translation operator, e.g., the Neel state on the square lattice is symmetric with respect to $\tilde{T}_i = \left(\prod_{\boldsymbol{r}} e^{i\pi S^x_{\boldsymbol{r}}}\right) T_i$ (if the ordering is in the z-direction).

We can then define the *sublattice* spectral functions $\mathcal{S}^{\alpha\beta}_{\lambda\mu}(\boldsymbol{k},\omega)$ by replacing $\sigma^\alpha_{\boldsymbol{k}} \to \sigma^\alpha_{\lambda,\boldsymbol{k}}$ in Eq. (5.1). The total spectral function is then

$$\boxed{\mathcal{S}^{\alpha\beta}(\boldsymbol{k},\omega) = \frac{1}{\mathcal{N}_{\text{uc}}} \sum_{\lambda,\mu} e^{-i\boldsymbol{k}\cdot(\boldsymbol{\rho}_{\boldsymbol{\lambda}}-\boldsymbol{\rho}_{\boldsymbol{\mu}})} \mathcal{S}^{\alpha\beta}_{\lambda\mu}(\boldsymbol{k},\omega)}\,. \tag{5.7}$$

Each of these sublattice spectral functions is periodic on the reciprocal lattice and allows for a simple expression in terms of the real-space spins:

$$\boxed{\mathcal{S}^{\alpha\beta}_{\lambda\mu}(\boldsymbol{k},\omega) = \frac{1}{2\pi} \sum_{\boldsymbol{R}} \int_{-\infty}^{\infty} e^{i(\omega t - \boldsymbol{k}\cdot\boldsymbol{R})} \left\langle \sigma^\alpha_{\lambda,\boldsymbol{R}}(t) \sigma^\beta_{\mu,\boldsymbol{0}}(0) \right\rangle \, \mathrm{d}t}\,. \tag{5.8}$$

This satisfies $\int_{\text{BZ}} \mathrm{d}^D\boldsymbol{k} \int_{-\infty}^{\infty} \mathrm{d}\omega \mathcal{S}^{\alpha\alpha}_{\lambda\lambda}(\boldsymbol{k},\omega) = \int_{\text{BZ}} \mathrm{d}^D\boldsymbol{k} = V_{\text{BZ}}$ (the α and λ indices are *not* summed over). The boxed equations (5.7) and (5.8) are how one calculates the spectral function in practice. The benefit of Eq. (5.8) is that it explicitly incorporates translation symmetry such that one only needs to sum over *one* spatial index. This will be crucial in Section 5.2 since we only need to time-evolve a *single* state $\sigma^\beta_{\mu,\boldsymbol{0}}|0\rangle$ (for a given spin component β and sublattice index μ).

5.1.3. Experimental detection via inelastic neutron scattering

As evidenced above, the spectral function is already a very useful theoretical tool since it allows to gain insight into the spectrum of a Hamiltonian by calculating correlation functions. In addition, it is also of considerable experimental significance, being measurable through inelastic neutron scattering. More precisely, one can argue that the cross-section for scattering (unpolarized) neutrons of a sample obeys [66, 67]

$$\frac{\mathrm{d}^2\sigma(\boldsymbol{k},\omega)}{\mathrm{d}\omega\mathrm{d}\Omega} \propto \sum_{\substack{\alpha,\beta,\\ \lambda,\mu}} \underbrace{\left(\delta_{\alpha\beta} - \frac{k_\alpha k_\beta}{|\boldsymbol{k}|^2}\right)}_{\text{polarization factor}} \times \underbrace{F_\lambda(\boldsymbol{k})^* F_\mu(\boldsymbol{k})}_{\substack{\text{magnetic}\\ \text{form factors}}} \times e^{-i\boldsymbol{k}\cdot(\boldsymbol{\rho}_{\boldsymbol{\lambda}}-\boldsymbol{\rho}_{\boldsymbol{\mu}})} \mathcal{S}^{\alpha\beta}_{\lambda\mu}(\boldsymbol{k},\omega). \tag{5.9}$$

This is for the special case where the lattice is rigid, i.e., it neglects the effects of spatial disorder and phonons (which can be included by an effective Debye-Waller factor [66, 67]). The magnetic form factors in Eq. (5.9) depend on the details of the atomic or molecular orbitals which are essential in understanding how the *effective* spin arises from the intrinsic and orbital angular momentum of the microscopic constituents. Since we study effective spin models in this thesis, we do not consider such form factors.

5.1.4. Example: Ising chain and fractionalization

To illustrate spectral functions and what one can learn from them, it is instructive to consider the quantum Ising chain $H = -\sum_n \left(\sigma^x_n\sigma^x_{n+1} + g\sigma^z_n\right)$.

As mentioned in Chapter 3, this can be mapped to a free-fermion chain, which in the notation of Chapter 2 would be $H = 2H_1 - 2gH_0$ (where H_α is the α-chain we introduced). In particular, the physical information of this Hamiltonian is encoded in the polynomial $f(z) = 2z - 2g$. For instance, the quasiparticle dispersion relation is

$$\varepsilon_k = |f(e^{ik})| = \sqrt{f(e^{ik})f(e^{-ik})} = \sqrt{4(e^{ik}-g)(e^{-ik}-g)} = 2\sqrt{1+g^2-2g\cos k}. \tag{5.10}$$

We read off that the gap is $2|1-g|$. Indeed, for $|g| > 1$ the system is in a gapped, symmetry-preserving phase, whereas for $|g| < 1$ the $\mathbb{Z}_2$ Ising symmetry is spontaneously broken.

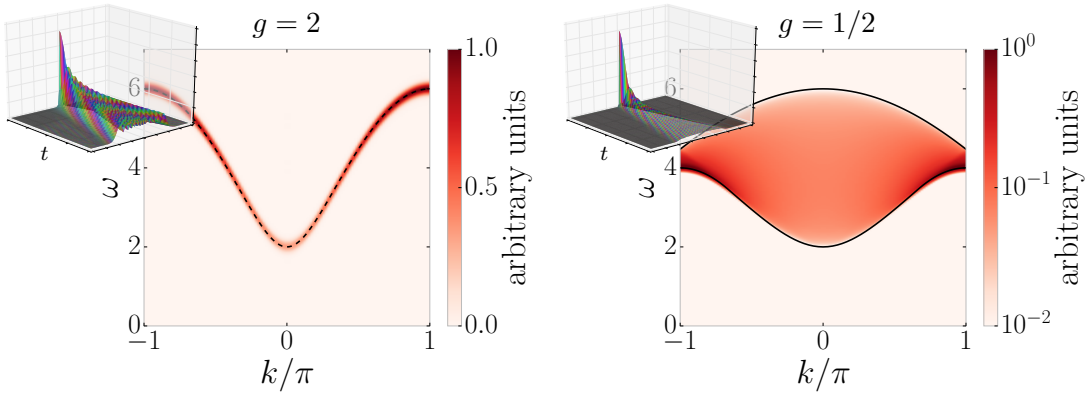

Figure 5.2.: **Spectral function of the Ising chain.** The insets show the spin-spin correlation function in space and time; the main panels show the Fourier transform, i.e., the spectral function. (a) This is in the disordered phase ($g = 2$), where the quasiparticles are local magnons; the dashed line is the analytic result for the magnon dispersion. (b) This is in the ordered phase ($g = 1/2$), where the quasiparticles are nonlocal domain walls: a local operator fractionalizes into a continuum of two domain walls; the solid lines denote the (analytically-determined) extent of the two-particle continuum.

We will consider the spectral function[2]

$$\mathcal{S}^{yy}(k,\omega) = \frac{1}{2\pi}\sum_n \int_{-\infty}^{\infty} e^{i(\omega t - kn)} \langle \sigma_n^y(t)\sigma_0^y(0)\rangle \mathrm{d}t. \tag{5.11}$$

In principle, it is possible to obtain this from the free-fermion solution, but this is highly non-trivial since σ_n^y is a nonlocal operator in the fermionic variables. Instead, we numerically obtain the spectral function by calculating the correlation function $\langle \sigma_n^y(t)\sigma_0^y(0)\rangle$ using standard density matrix renormalization group (DMRG) methods [12, 167, 193]. This involves first obtaining the ground state using DMRG, then applying the spin operator σ_0^y and subsequently time-evolving the state [13]. We defer numerical details to Section 5.2, where we will discuss the more challenging two-dimensional setting.

In Fig. 5.2, the insets show the numerically-obtained correlation functions in space and time for the values $g = 2$ and $g = 1/2$ (the color carries information about the complex phase). Their Fourier transforms give the main panels, i.e., the spectral function $\mathcal{S}^{yy}(k,\omega)$. We now clarify the physical information contained in these plots, relying on the Lehmann representation

$$\mathcal{S}^{yy}(k,\omega) = 2\pi \sum_i \delta(\omega - \omega_i)\ \delta(k - k_i)\ |\langle i|\sigma_0^y|0\rangle|^2. \tag{5.12}$$

The disordered phase: magnons

For $g = 2$, we are in the symmetry-preserving phase. This is adiabatically connected to the fixed point limit $H = -\sum_n \sigma_n^z$, where it is clear that a single spin-flip is a quasiparticle. We thus expect that applying σ_0^y to the ground state should give a nonzero overlap with a *single* quasiparticle. This is confirmed in Fig. 5.2(a), where we see weight along the dashed line, the latter being the theoretically obtained dispersion in Eq. (5.10). The finite

[2] We choose σ_n^y since it flips spins in both possible ground state orderings; however, one can repeat the analysis for any choice of operator.

broadness in Fig. 5.2(a) is related to the fact that we only have data for a *finite* time window (for details, see subsection 5.2.4). For larger time windows, this will approximate a delta function.

The ordered phase: domain walls and fractionalization

In Fig. 5.2(b) (for $g = 1/2$) we see a completely different result in the spectral function: instead of a sharp quasiparticle, we see a broad continuum. This can also be understood from considering the fixed point limit, which is now $H = -\sum_n \sigma_n^x \sigma_{n+1}^x$. In this limit, flipping a spin (by acting with σ_0^y) will create *two* deconfined domain walls. In other words, for $g = 1/2$, we do not expect that $\sigma_0^y|0\rangle$ has overlap with *single* quasiparticle states, but rather states with *two* domain walls. From the dispersion in Eq. (5.10), we can kinematically determine the region of energy-momentum space that such two-particle states would occupy. These are plotted as solid black lines in Fig. 5.2(b), exactly agreeing with the numerical result.

More generally, sharp features in spectral functions are indicative of the operator creating a single particle, whereas broad features are indicative of a multi-particle continuum. In general, any spectral function will contain a multi-particle continuum; e.g., even Fig. 5.2(a) has a three-particle continuum, but its density is not visible with the naked eye[3]. However, if the system exhibits so-called *fractionalization*, then one can see *only* broad responses[4] (Fig. 5.2(b) being an example). Fractionalization means that a single quasiparticle cannot be created by a local operator; hence, any local operator necessarily creates multiples of such quasiparticles. In one dimension this is generic for symmetry-breaking phases: quasiparticles are nonlocal domain walls. In higher dimensions, however, this is more exotic (it does not occur in symmetry-breaking phases since a domain has an energy cost scaling with its domain wall). For instance, fractionalization occurs in phases with topological order—we discuss this in Chapter 6.

5.2. Numerical method

In this thesis, we numerically obtain spectral functions of two-dimensional spin models by calculating spin-spin correlations in space and time and plugging them into Eqs. (5.7) and (5.8). To calculate these correlation functions, we need to numerically obtain the ground state, apply a spin operator and time-evolve the resulting state. In this section, we explain how to do this efficiently. In principle, this could be done using two-dimensional tensor network methods (so-called *projected entangled pairs states* (PEPS)), but (at the time of writing this thesis) it is numerically very costly to time-evolve such states. On the other hand, one-dimensionsal tensor-network-based methods (using *matrix product states* (MPS)) allow for very efficient[5] time evolution [13, 107]. The way to use such one-dimensional methods for a two-dimensional problem is by wrapping the latter onto a cylinder, as we explain now.

5.2.1. The cylinder: interpolating from 1D to 2D

As introduced in subsection 5.1.2, let $\boldsymbol{R_1}$ and $\boldsymbol{R_2}$ be the lattice vectors that span the two-dimensional lattice. If we enforce that a multiple of, e.g., $\boldsymbol{R_2}$ brings us back to where we started, then this is topologically equivalent to putting the system on a cylinder. Let us

[3] For $g = 2$, roughly 1% of the weight in $\mathcal{S}^{yy}(\boldsymbol{k}, \omega)$ is in the multi-particle continuum.

[4] The converse does not hold. E.g., due to symmetries one can have a spectral function that only contains an even number of local quasiparticles (such as in the longitudinal dynamic structure factor for a collinear magnet).

[5] This is in part due to the existence of a so-called *canonical form* of MPS.

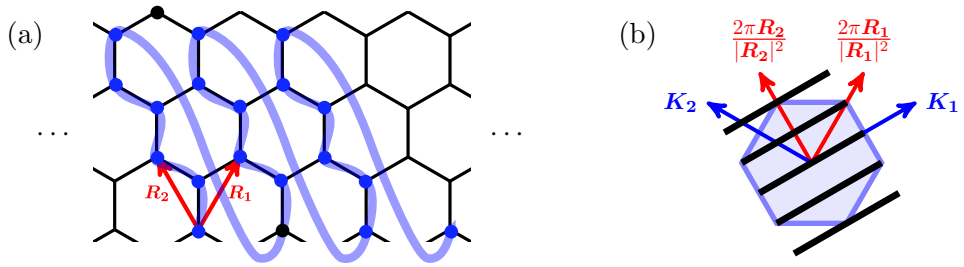

Figure 5.3.: **The honeycomb lattice on a cylinder.** (a) As an example, we take the honeycomb lattice to be periodic over $3\boldsymbol{R_2}$; this means that the two black dots are the *same* site. This is an infinite cylinder with $L_{\text{circ}} = 6$ sites per circumference. This can be seen as a one-dimensional system by snaking through the lattice as shown. Note that sites which used to be neighbors on the honeycomb lattice can be far apart along this one-dimensional snake. (b) The condition that $3\boldsymbol{R_2} \equiv \boldsymbol{0}$ imposes a quantization in momentum space: the two-dimensional Brillouin zone is reduced to the one-dimensional cuts shown .

illustrate this for the honeycomb lattice (shown in Fig. 5.1). In Fig. 5.3(a), we set $3\boldsymbol{R_2} \equiv \boldsymbol{0}$. Since every unit cell has two sites, we say that this is a cylinder with circumference $L_{\text{circ}} = 6$ (which is precise using the notion of Manhattan distance). For any finite circumference L_{circ}, one can interpret this as a one-dimensional system. More precisely, the sites can be given a one-dimensional numbering by snaking through the cylinder, as illustrated in Fig. 5.3(a). Hence, once L_{circ} is fixed, one is now free to apply one-dimensional methods to analyze the system.

The success story of numerical methods in one dimension is the density matrix renormalization group (DMRG), introduced by Steven White in 1992 [12, 106]. It efficiently obtains ground states of local, one-dimensional Hamiltonians[6]. Already in 1996, White used this to study ground states of *two-dimensional* systems using the above cylinder trick [194]. Since then, it has become a staple in the study of two-dimensional ground states [192]. On a different track, in 2008 Stoudenmire and White used DMRG (supplemented with time-evolution methods [13]) to obtain dynamical correlation functions (and hence spectral functions) for one-dimensional systems [193].

Our contribution is to bring these two developments—i.e., the use of DMRG for two-dimensional ground states and one-dimensional spectral functions—together. More concretely, we use DMRG to obtain the ground state on a cylinder, apply a local spin operator and subsequently time-evolve this state to obtain the spectral function. What made this possible is a recent work introducing a numerical time-evolution method for systems with long-range interactions [108]. This is indeed essential, since even if the original two-dimensional model is short-range, once one snakes through the cylinder (as in Fig. 5.3(a)), the effective one-dimensional system typically has an interaction range that scales with the circumference L_{circ}. The first model to which we apply this method is the Kitaev-Heisenberg model in Chapter 6, after which we turn to Heisenberg models on the square and triangular lattice in Chapters 7 and 8, respectively.

Self-evidently, the principal interest is in the *two-dimensional* system, and not in any given circumference. Ideally, one would hence be able to perform a finite-circumference scaling in L_{circ}. In practice, this is difficult (but possible [192]): DMRG easily allows to study *long* cylinders (or even *infinitely long*, using so-called infinite DMRG [167]),

[6] It is strictly speaking a method for gapped systems, but in practice it can even be used at criticality.

but the numerical cost scales exponentially in the *circumference*[7]. One is thus limited in the number of available circumferences. It is hence important to know how a given circumference impacts the spectral function. One of the main effects is that the finite circumference enforces a quantization condition in momentum space. This is illustrated in Fig. 5.3(b): one can only access one-dimensional cuts of the full two-dimensional BZ, the number of which grow linearly with L_{circ}. If one simulates a free-fermion system, this is the *only* effect due to having a (finite) circumference. In interacting systems, there can of course be additional effects, as we will explore in the following sections.

In the remainder of this chapter, we discuss numerical aspects of this method.

5.2.2. Matrix product states and bond dimension

The modern understanding of DMRG is that it is a variational method which relies on the ground state being written as a *matrix product state* (MPS) [107]. There are already many excellent introductions to the concept of MPS (see, e.g., Ref [195]), and since in the following chapters we will focus on the physics of concrete models rather than their tensor network description, we will not add to this surplus. For our purposes, the main point is that an MPS approximation to any state depends on a *bond dimension* χ, which represents the dimension of a particular tensor. Any state can be captured exactly if $\chi \to \infty$, but gapped ground states can be approximated by a finite χ (for any choice of error threshold) [102]. The numerical cost of DMRG and the time evolution[8] both scale as $O(\chi^3)$ [13, 107, 108, 195]. In practice, when obtaining a spectral function (for a given L_{circ}), we do this for increasing values of χ until the physical result no longer changes (at the scale and resolution of interest); in addition, in the following chapters we will mention the concrete values of χ which we used. Note that it is sometimes thought that one runs into problems when time-evolving a perturbed MPS due to a gradual blow-up in χ; we address this misconception in subsection 5.2.5.

A particularly useful aspect of an MPS description of a state is that it allows one to explicitly incorporate translation symmetry. This means that the ground state of an *infinitely-long* system can be encoded into a *finite* number of tensors [196]; such a representation is commonly called an infinite MPS (iMPS) [167] or uniform MPS (uMPS) [197]. Similarly, we obtain the ground state for infinitely long cylinders whilst only having to encode the state on a finite number of rings (which we refer to as the *unit cell*). However, applying a spin operator spoils this translation invariance. We resolve this by working with an iMPS whose unit cell typically consists of hundreds of rings and time evolving this, giving $|\psi^\alpha(t)\rangle = e^{-iHt}\sigma^\alpha_{\mathbf{0}}|0\rangle$. In practice, the necessary length of this unit cell is determined by ensuring that the ballistic entanglement cone emerging from the perturbed site never reaches the boundary of this unit cell (within a few correlation lengths[9]). At particular time instances, we calculate correlation functions $\langle 0|\sigma^\alpha_{\boldsymbol{n}}(t)\sigma^\alpha_{\mathbf{0}}|0\rangle = \langle 0|\sigma^\alpha_{\boldsymbol{n}}|\psi^\alpha(t)\rangle$. For this, one would ideally cap off the ends of the cylinder with fixed point vectors representing the infinite left- and right-environments. However, in practice one can choose *random* vectors: these quickly converge to the fixed point tensor as one contracts the tensor network over a few correlation lengths.

5.2.3. Discretization of time

In the above, we have discussed two important numerical parameters: the circumference L_{circ} and the bond dimension χ. A third is the timestep dt. In particular, we use the $\hat{W}^{II}$

[7] The advantage over exact diagonalization is clear: the cost of the latter is exponential in *both* dimensions.
[8] We apply the time evolution matrix product operator in a variational way.
[9] Note that when simulating a critical system using MPS, each finite bond dimension χ introduces an effective, finite correlation length $\xi(\chi)$.

time-evolution method introduced in Ref. [108]. This gives an approximation $e^{-iHt} \approx \left(\hat{W}^{II}(dt)\right)^N$ where $t = Ndt$. The error density per dt-evolution is $O((dt)^2)$ which results in an error density $O(N(dt)^2) = O(dt)$ over a time t. However, as mentioned in Ref. [108], this can be improved by instead using complex timesteps $\hat{W}^{II}(dt) \to \hat{W}^{II}\left(\frac{1+i}{2}dt\right)\hat{W}^{II}\left(\frac{1-i}{2}dt\right)$. The error per timestep is then $O((dt)^3)$, or equivalently, an error $O((dt)^2)$ over a time t. In practice, we calculate the spectral function for ever-decreasing values of dt until we no longer observe a difference in the outcome.

We note that the above time-evolution operator $\hat{W}^{II}(dt)$ is a matrix product operator (MPO), which comes with its own bond dimension χ_W. If one naively applies this to the MPS, the cost would be cubic in χ_W. However, a variational way of applying this MPO to the MPS has only a *quadratic* cost in χ_W; see the references in Ref. [108]. This improvement is especially important for the cylinder set-up, since in practice $\chi_W \sim L_{\text{circ}}$. More precisely, from the construction in Ref. [108] we see that $\chi_W = \chi_H - 1$ where χ_H is the bond dimension of the MPO that encodes the Hamiltonian. This underlines the fact that when building an MPO representation of the Hamiltonian, one should try to keep its bond dimension as small as possible. In practice, we find that the bond dimensions of the Hamiltonian ($\chi_H \sim L_{\text{circ}}$) and the state ($\chi \sim \exp L_{\text{circ}}$) determine how large we can push the circumference.

5.2.4. Gibbs phenomenon, smoothening and linear prediction

Thus far, we have discussed how to obtain the ground state on a cylinder, time-evolve the perturbed state and obtain the correlation functions in space and time[10]. The last step is to Fourier transform this, giving the spectral function. Whilst the numerical cost of this last step is negligible, it comes with its own set of subtleties. In particular, it is clear that we can only numerically compute the correlation function over a *finite* window of time $-T \leq t \leq T$. Hence, effectively one has the desired correlation function multiplied by a box function. Fourier transforming this (in time) is equivalent to a convolution of the desired spectral function with the sinc function $\propto \sin(\omega T/\pi)/\omega$. The latter oscillatory function will introduce ringing in the spectral function; this is known as the Gibbs phenomenon or Gibbs oscillation.

To minimize the effects of Fourier transforming a finite-time window, we use linear prediction [193] to increase the time window, after which we multiply the data with a Gaussian envelope $\propto e^{-t^2/(2\sigma^2)}$. The width σ of the Gaussian is chosen such that there is only little weight on the data generated by linear prediction—the main purpose of the latter is to make space for the tail of the Gaussian. In practice, we choose $\sigma = T/g$ with $2 \leq g \leq 2.5$. To the extent that one can think of the resulting real-time data as being the desired correlation function multiplied with a Gaussian, the Fourier transform will be the convolution of the desired spectral function with a Gaussian of width $\sigma_\omega = 1/\sigma$. This effectively introduces an artificial broadening of the spectral function with a full-width-at-half-maximum $\approx 2.355\sigma_\omega$.

5.2.5. A comment about entanglement growth

It is sometimes thought that perturbing the ground state of a Hamiltonian leads to a persistent (even linear) growth of entanglement entropy as a function of time. This is true for *global quenches*, i.e., where one adds a finite amount of *energy density*. The first general class of models for which this was argued were conformal field theories, where one can derive that the entanglement entropy grows linearly in time after a global quench

[10] Note that if the Hamiltonian has an anti-unitary symmetry, one can determine the negative-time data from the positive-time data (if the spin operators transform in a simple way under this symmetry).

[198]. Ref. [199] was one of the first works arguing this for non-integrable lattice models. In general, this linear growth is due to quantum information generically spreading *ballistically*. By now it has also been demonstrated in random unitary networks [200] and in generic integrable models where there is an intuitive argument in terms of quasiparticle spreading [201].

Such linear growth of entanglement entropy implies that any MPS approximation of the state quickly breaks down due to requiring an *exponentially fast* growing bond dimension. To see this, note that the maximal entanglement for an MPS with bond dimension χ is $\ln \chi$. Hence, $S \leq \ln \chi$. If we know that $S \sim \alpha t$, then $\alpha t \leq \ln \chi$, or equivalently, $\chi \geq e^{\alpha t}$. This growth is indeed generic for global quenches of thermalizing systems[11].

This is *not* true for local quenches—where one only inserts a finite amount of energy in an infinitely large system. The type of local quench that is most commonly studied consists of suddenly changing the Hamiltonian over a finite region of space; see Ref. [204] for a review. In gapless systems, the entanglement entropy can then *grow logarithmically* in time, or even *saturates* after a finite time—this depends on whether one perturbs the Hamiltonian with an irrelevant or relevant operator, respectively [205]. Even though a logarithmic growth still means that after a long enough time any MPS approximation must break down, in practice it is still useful for a large window of time since the bond dimension only needs to grow *linearly* in time (as opposed to *exponentially*).

However, the type of local quench that we study is of a different nature: we do not deform the Hamiltonian, but rather we apply a local operator on the ground state and time-evolve the resulting state. This type of local quench seems to have not yet been studied in great depth. Nevertheless, it has been argued that for a wide class of conformal field theories, perturbing the ground state with a local operator only leads to a *finite* growth of entanglement, i.e., $\lim_{t\to\infty} S(t) < \infty$, even in an infinite system [206]. In fact, one can read off universal information from the long-time value (i.e., quantum dimensions of conformal blocks), as explained in Ref. [206]. This has also been confirmed on the lattice for the particular case of the critical Ising chain [207]. This certainly deserves to be studied in more detail and generality. Phenomenologically, we indeed observe that perturbing the ground state with a local operator only leads to a *finite* amount of entanglement growth (as $t \to \infty$). It would be interesting to give an argument for this, as well as study the long-time value and the functional form of how this is approached. For completeness, we remark that for *holographic conformal field theories* (which are characterized by a central charge $c \to \infty$), it has been argued this type of local quench leads to a logarithmic growth $S \sim \ln t$ [208].

[11] This can be avoided in systems that do not thermalize, a notable example being many-body localization (MBL), where there is instead a logarithmic growth in time [202, 203].

6. Kitaev-Heisenberg on the honeycomb lattice: proximate spin liquids

In this chapter, we apply the method introduced in Chapter 5 to obtain the spectral function of a model exhibiting a spin liquid phase, characterized by the fractionalization of local excitations (a concept which we already touched upon in subsection 5.1.4 of the previous chapter). Understanding how such excitations can be probed through experimentally-accessible quantities like the dynamic spin structure factor is an important question, especially as the hunt for experimental realizations of spin liquids—and their unambiguous identification—continues. A closely related question is how a nearby spin liquid in the phase diagram can affect the properties of excitations in conventionally ordered phases of matter. The Kitaev-Heisenberg model (KHM) allows to explore these questions, in addition to offering exactly solvable points which can be used to benchmark the method we introduced in the previous chapter. This spin-1/2 model is defined as [209]

$$H = \sum_{\langle \boldsymbol{m},\boldsymbol{n}\rangle_\gamma} \underbrace{K_\gamma S^\gamma_{\boldsymbol{m}} S^\gamma_{\boldsymbol{n}}}_{\text{Kitaev}} + J \sum_{\langle \boldsymbol{m},\boldsymbol{n}\rangle} \underbrace{\boldsymbol{S}_{\boldsymbol{m}} \cdot \boldsymbol{S}_{\boldsymbol{n}}}_{\text{Heisenberg}} . \tag{6.1}$$

The first term is the pure Kitaev model exhibiting strongly anisotropic spin exchange coupling [95]. Neighboring spins couple depending on the direction of their bond γ with S^xS^x, S^yS^y or S^zS^z; see Fig. 6.1(a). The second is the $SU(2)$-symmetric Heisenberg term. The KHM serves as a putative minimal model for several materials including Na_2IrO_3, Li_2IrO_3 [178], and α-$RuCl_3$ [179]. Note that the spin Hamiltonian describing these materials might be vastly more complicated; what motivates us is whether a relatively simple Hamiltonian like the KHM can reproduce salient features observed for these real-world materials.

The pure Kitaev model ($J = 0$) is an exactly solvable spin-1/2 model stabilizing two different Kitaev quantum spin liquids (KSL) with *anyonic*[1] excitations: a gapped (gapless) $\mathbb{Z}_2$ spin liquid with gapped (gapless) Majorana and gapped flux excitations [95]. These are commonly referred to as the A and B phase of the Kitaev model, respectively, and their Majorana and flux quasiparticles are nonlocal, which means that local operators necessarily create pairs of them. This is an instance of *fractionalization* (as encountered in the previous chapter in a simpler one-dimensional setting).

If not stated otherwise, we use the parametrization $J = \cos\alpha$ and $K_\gamma = K = 2\sin\alpha$. For $\alpha = \pm\frac{\pi}{2}$, we obtain the pure Kitaev model in the B phase, which is stable under time-reversal symmetric perturbations as pointed out by Kitaev in Ref. [95] (to obtain the A phase, one must choose, e.g., $K_z > K_x + K_y$). Numerical studies of the ground state phase diagram of the KHM have shown an extended QSL phase for small J and four symmetry broken phases for larger J [178].

The dynamical response functions of the pure Kitaev model are known exactly and reveal characteristic features [98, 210], such as a spectral gap in the dynamical spin structure factor due to a spin flip not only creating gapless Majorana but also gapped flux excitations. This feature is perturbatively stable to small J [211], but the influence of J on high-energy features (or non-perturbatively at low energies) is unclear and of ongoing interest [212]. More pressingly, there appear to be proximate spin liquids detected in ex-

[1] A quasiparticle whose particle statistics is not bosonic or fermionic is often referred to as an *anyon*. Strictly speaking, such statistics is only well-defined for gapped phases of matter [95].

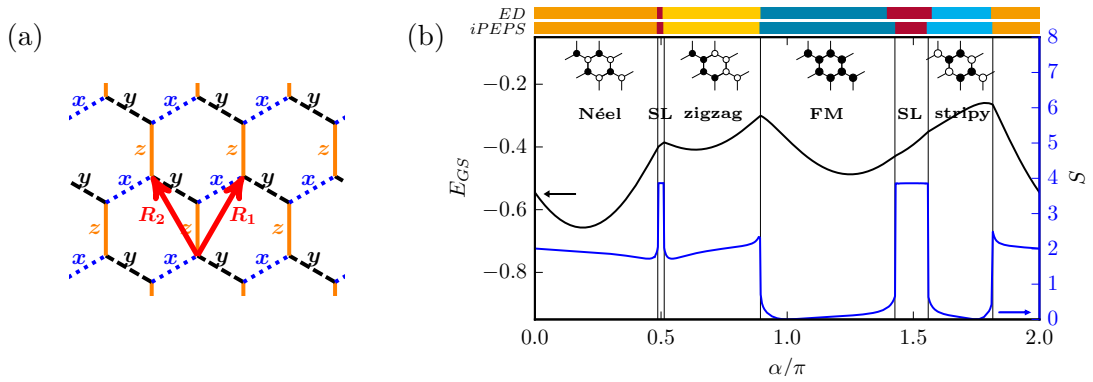

Figure 6.1.: **The Kitaev-Heisenberg model.** (a) Blue (dotted), black (dashed) and orange (solid) edges of the honeycomb lattice correspond to Kitaev exchange couplings $S^\gamma_{\boldsymbol{m}} S^\gamma_{\boldsymbol{n}}$ with $\gamma = x, y, z$, respectively. (b) Phase diagram for infinite cylinder with circumference $L_{\text{circ}} = 12$, showing the ground state energy density (black line) and the entanglement entropy for bipartitioning the cylinder (blue line). The insets illustrate the ordering pattern of the magnetic phases. Two spin liquid (SL) phases exist around the pure Kitaev models ($\alpha = 0.5\pi$ and 1.5π). The results of ED [178] and iPEPS [226] are illustrated on top.

perimental measurements [96, 97], such as possibly the currently much-studied α-$RuCl_3$ [97, 179, 180, 213–220], whose low-energy physics is consistent with spin waves on an ordered background, but whose broad high-energy features resemble those of a KSL. (There are indications that one can drive α-$RuCl_3$ into a spin liquid phase by tuning a magnetic field [213, 221–225]; we do not focus on this aspect here.) In particular, for intermediate energy scales there are star-like features [180] apparently arising from a combination of spin wave and QSL physics. A natural question is whether such a proximate spin liquid can be uncovered in a theoretical model consisting of a Kitaev model perturbed into a symmetry-breaking phase.

In this chapter, we first revisit the ground state phase diagram in Section 6.1 and confirm the previously found phases. The infinite cylinder geometry allows us to numerically confirm that the gaplessness of the KSL is robust throughout the entire phase. In Section 6.2, we then use the methods of Chapter 5 to obtain the dynamical spin structure factor. We first benchmark our method by comparing to exact results for the Kitaev model and find a good agreement. Subsequently, we calculate the spectra of different (non-soluble) phases of the KHM. Most notably, we identify broad high energy continua even in ordered phases, which are moreover similar to the high energy features in the nearby spin liquid phase. This provides a concrete realization of the concept of a proximate spin liquid, which was recently invoked in the context of neutron scattering experiments on α-$RuCl_3$. Note that we do not claim that this spectral response indicates that the ordered phase has fractionalized particles—there is no known mechanism that would allow for that. One possibility could be that the fractionalized excitations are *nearly* deconfined in the ordered phase. We leave the interpretation in terms of quasiparticles (if it exists) as part of a future work; here the goal is to point out that, phenomenologically, the high-energy spectral response is that of the nearby Kitaev spin liquid.

6.1. Ground state phase diagram

In subsection 5.2.1 of the previous chapter, we discussed how ground state phase diagrams of two-dimensional systems can be obtained by putting the system on an infinitely-long

cylinder and then using iDMRG. Here, we apply this to the KHM. We choose the cylinder geometry shown in Fig. 5.3(a). In particular, we choose the circumference L_{circ} to be a multiple of six: then the corresponding $L_{\text{circ}}/2$ momentum cuts in Fig. 5.3(b) will go through all the corners of the Brillouin zone. The gapless Majorana cones of the exactly solvable KSL are known to live on these corners [95], and the full KHM has a C_6 symmetry which means that these cones cannot shift as we turn on a Heisenberg perturbation [211]. Hence, our $L_{\text{circ}} \times \infty$ system size is such that the KSL on the cylinder should also be gapless. We go up to $L_{\text{circ}} = 12$ in this chapter.

The phase diagram for this largest circumference, $L_{\text{circ}} = 12$, is shown in Fig. 6.1(b) (for the iDMRG simulations we keep $\chi = 1200$ states), which agrees with previous studies [178, 209, 226–229]. For this circumference, the system is compatible with the sublattice transformation that maps zigzag to AF and stripy to FM [209]. Plotted are the ground state energy and the entanglement or von-Neumann entropy $S = -\text{Tr}\rho^{\text{red}} \log \rho^{\text{red}}$ of the reduced density matrix ρ^{red} for a bipartitioning of the cylinder by cutting along a ring. Both the cusps in the energy density and the discontinuities of the entanglement entropy indicate first order transitions. A careful finite size scaling is difficult because of the large bond dimension needed; it is thus not possible to make definite statements about whether the transitions remain first order in the limit $L_{\text{circ}} \to \infty$.

The symmetry broken phases can be identified by measuring the local magnetization. We identify a Néel phase ($-0.185 < \alpha/\pi < 0.487$) that extends around the pure antiferromagnetic Heisenberg[2] point, the corresponding zigzag phase ($0.513 < \alpha/\pi < 0.894$), a ferromagnetic phase around the pure FM Heisenberg point ($0.894 < \alpha/\pi < 1.427$), and its stripy phase ($1.559 < \alpha/\pi < 1.815$). The two KSLs between the Néel and zigzag phases as well as between FM and stripy phases are confirmed to be gapless, as expected for the B phase. In particular, if L_{circ} is a multiple of six, we use the finite entanglement scaling approach [133, 231, 232] and extract the expected central charge $c = 1$ for both KSLs; each of the two Majorana cones contributes $c = 1/2$. See Appendix D.2 for numerical details. Note that when a gapless spin liquid is placed on a cylinder, the gauge field generically adjusts to open a gap [233]. In order to see gapless behaviour, we have to initiate the iDMRG simulations in the gapless sector to access a metastable state; the gapped ground state, which has a non-zero flux through the cylinder, overestimates the stability of the QSL phases (see Appendix D.3 for additional details). It is remarkable how well the phase boundaries agree with those from the infinite projected entangled pair state (iPEPS) simulations [226], as shown in Fig. 6.1(b).

6.2. Dynamical spin structure factor

We now consider the dynamical spin structure factor $\mathcal{S}^{\alpha\alpha}(\boldsymbol{k}, \omega)$ as introduced in Section 5.1 of the previous chapter. We can numerically obtain this on the cylinder using the method introduced in Section 5.2. As explained in subsection 5.2.4, this comes with an artificial broadening (due to smoothening the real-time data in order to avoid Gibbs oscillations upon Fourier transforming) which we choose to be $\sigma_\omega \approx \frac{2.3}{T}$ (with T being the time window for which we time-evolve the perturbed ground state). If not stated otherwise, we present results for $\mathcal{S}(\boldsymbol{k}, \omega) \equiv \sum_\gamma \mathcal{S}^{\gamma\gamma}(\boldsymbol{k}, \omega)$.

[2] Note that due to the mapping of the 2D lattice onto a 1D chain, Mermin-Wagner-Coleman [230] applies at the pure AF-Heisenberg point and suppresses long range Néel order. In fact, it is replaced by a gapped symmetry-preserving state, which extends over a finite region in parameter space. For further discussion, see Appendix D.1.

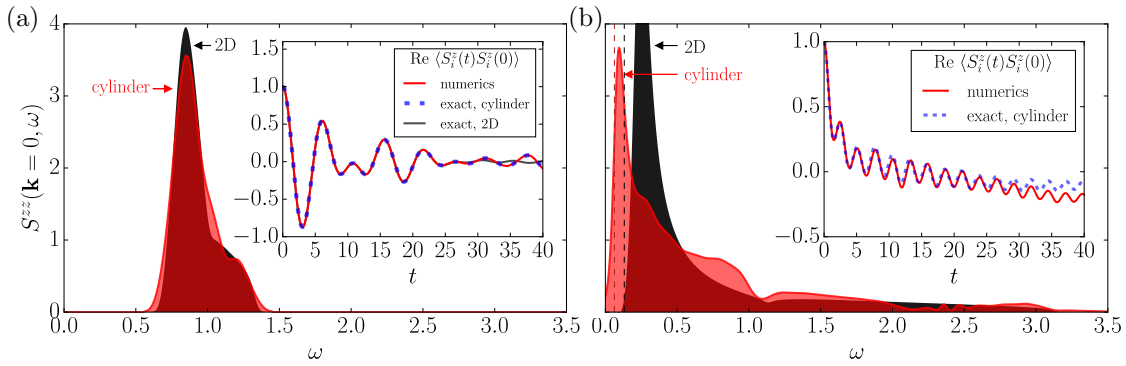

Figure 6.2.: **Dynamical spin structure factor of the Kitaev model.** The spectral function $\mathcal{S}^{zz}(\boldsymbol{k}=\mathbf{0},\omega)$ obtained from dynamical DMRG is compared to exact results (insets show real time data). The latter were obtained following Ref. [98], except for the blue curve in (b) [234]. (a) Gapped KSL, "A phase", on a cylinder with $L_{\text{circ}}=10$ and anisotropic couplings $K_x=-2$ and $K_y=K_z=-\frac{1}{3}$. (b) Gapless isotropic KSL, "B phase", with $L_{\text{circ}}=6$ and $\alpha=\frac{3\pi}{2}$.

6.2.1. Benchmarking for the Kitaev model

We benchmark the method by comparing our numerical approach to exact results for the pure Kitaev model. Figure 6.2(a) shows a comparison for the gapped Kitaev model in the "A phase" with $K_x/K_{y,z}=6$, with the exact solution for $\mathcal{S}^{zz}(\boldsymbol{k}=0,\omega)$ shown in black. Our numerics (with resolution $\sigma_\omega\approx 0.06$ in units shown) for an infinite cylinder with $L_{\text{circ}}=10$ (red) agrees well with such features as gap, bandwidth and total spectral weight. In the real-time data (inset), whilst the numerics agrees with the exact solution for the cylinder geometry, it overlaps with the 2D result only until a characteristic time scale corresponding to the perturbation traveling around the cylinder and then feeling the static fluxes inserted by the spin-flip. More generally, we expect such timescales (after which 2D physics becomes 1D) to be particularly significant for systems with fractionalization.

For Fig. 6.2(b) we take $K_x=K_y=K_z=-2$ being in the gapless KSL phase, "B phase", at $\alpha=\frac{3\pi}{2}$. Comparing the exact 2D result (black) to our numerics for a cylinder of circumference $L_{\text{circ}}=6$ (red), we see qualitative similarities, such as a spectral gap (dashed lines; slightly obscured by our finite-time window), a dip where the fluxes suppress the van Hove singularity of the Majorana spectrum [98], comparable bandwidth and strong low-energy weight. The broadening corresponds to $\sigma_\omega\approx 0.045$ in units shown. Two striking quantitative differences are (i) the spectral gap which for this circumference is approximately half that of the 2D limit, and (ii) the presence of a delta-peak on this gap ($\approx 4\%$ of total spectral weight). The latter, present for any cylinder, vanishes[3] as $L_{\text{circ}}\to\infty$. The inset compares exact real-time results on the cylinder [234] with our numerics. Despite approximating the ground state of the gapless sector using MPS, we find good agreement for appreciable times.

6.2.2. Symmetry-broken phases

After this benchmarking, we explore $\mathcal{S}(\boldsymbol{k},\omega)$ in different phases of the KHM shown in Fig. 6.3, all with $\sigma_\omega\approx 0.06$. The pure Heisenberg FM ($\alpha=\pi$) can be solved in terms of

[3] We used free-fermion exact diagonalisation (which allows for system sizes of thousands of sites) to extract the weight of this peak for $L_{\text{circ}}=6$ and confirmed that it vanishes as $L_{\text{circ}}\to\infty$ being consistent with analytic results in the 2D limit [98].

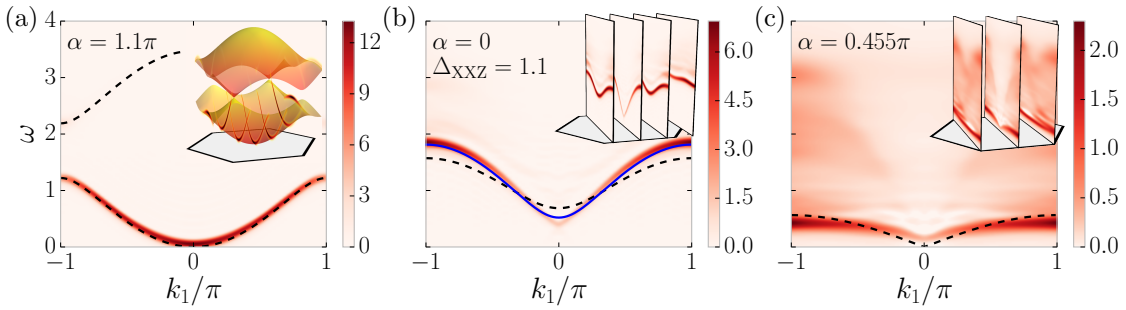

Figure 6.3.: **Dynamical spin structure factor in symmetry-broken phases.** $\mathcal{S}(\boldsymbol{k}, \omega)$ for $\boldsymbol{k} = (k_1/\pi)\boldsymbol{K_1}$ in different phases of the KHM with a ω-resolution $\sigma_\omega \approx 0.06$. Dashed lines show results from LSWT. Insets show the data for all momentum cuts (for given L_{circ}). (a) FM phase for a cylinder with $L_{\text{circ}} = 12$. (b) Antiferromagnet with small spin anisotropy without Kitaev term ($L_{\text{circ}} = 8$). The solid blue line shows next order spin wave calculations [235]. (c) AF phase in proximity of the KSL ($L_{\text{circ}} = 6$).

linear spin wave theory (LSWT) and numerically captured with bond dimension $\chi = 2$. Instead of this special point, in Fig. 6.3(a) we show results for $\alpha = 1.1\pi$ (corresponding to $K = 0.65J$) where we still find excellent agreement with LSWT. Note that there is small gap ($\approx 0.05|J|$) which is (erroneously) absent in LSWT despite the presence of SU(2)-breaking Kitaev coupling [178]. We do not observe any strong cylinder effects on the dynamics, which is presumably related to the short correlation length and the absence of fractional excitations.

The pure Heisenberg AFM (with small XXZ anisotropy) in Fig. 6.3(b) shows appreciable deviations from LSWT, with second order SWT [235] giving better agreement. Moreover, the weight in the spin waves is approximately halved, indicating the importance of higher order magnon contributions. Staying within the Néel phase but approaching the QSL, LSWT cannot even qualitatively describe Fig. 6.3(c), with considerable weight in very broad high energy features unaccounted for.

6.2.3. The zigzag phase, α-$RuCl_3$ and proximate spin liquids

Lastly, we focus on a parameter regime producing zigzag ordering—the same order found in α-$RuCl_3$ at low temperatures [97, 180, 213]. (Note that it might well be the case that for the full Hamiltonian describing α-$RuCl_3$, the Kitaev coupling would have an opposite sign as the one discussed here [214, 236–238]. Here, our goal is not to quantitatively describe α-$RuCl_3$, but rather to qualitatively reproduce observed features with a simple Hamiltonian.) Fig. 6.4 shows $\mathcal{S}(\boldsymbol{k}, \omega)$ for four different choices of α: the first column contains the exact solution for the pure AFM Kitaev model, and the subsequent column are all numerical results within the zigzag phase with increasing α. For each α we show $\mathcal{S}(\boldsymbol{k}, \omega)$ at three fixed values of ω: the rows display representative low-, mid- and high-energy features, with parameters $L_{\text{circ}} = 12$ and time cut-off $T = 10$ corresponding to a broadening $\sigma_\omega \approx 0.23$ (in units shown). We average over the three different symmetry broken directions of the ground state.

The first row shows the low-energy physics of the Kitaev model being reconstructed into spin wave bands, with minima on the edges of the first Brillouin zone. For $\alpha = 0.7\pi, 0.8\pi$ these obey the C_6-symmetry, indicating that the cylinder geometry locally looks like 2D. Interestingly, the high-energy physics of the ordered phases is very similar to that of the pure Kitaev model: broad features are centered around the symmetric Γ-point, $\boldsymbol{k} = 0$,

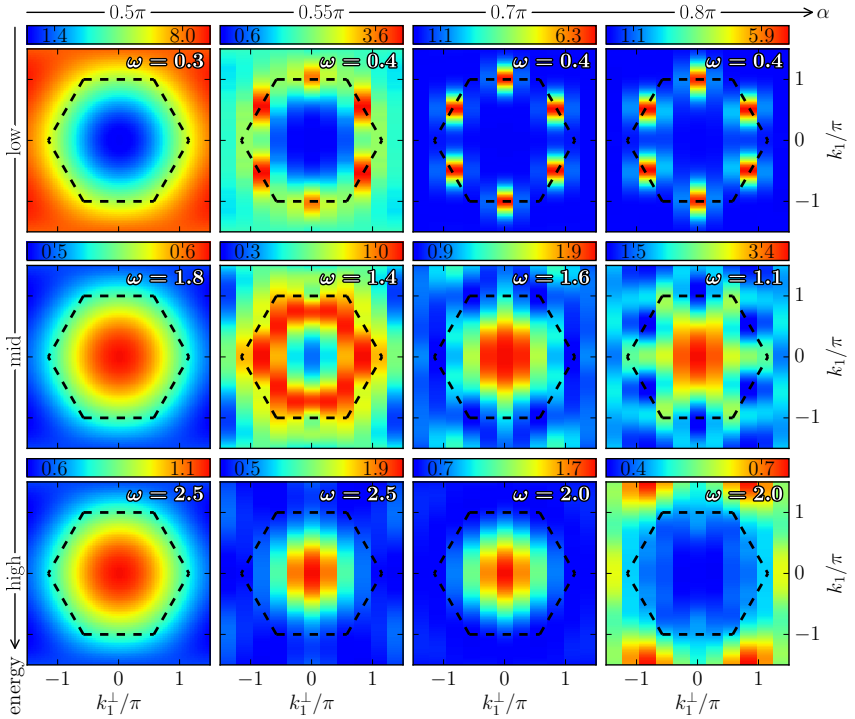

Figure 6.4.: **Proximate spin liquid in the zigzag phase.** The spectral function $\mathcal{S}(\boldsymbol{k}, \omega)$ at three different energy scales for the KSL at $\alpha = 0.5\pi$ (analytic result, 2D) and the zigzag phase at $\alpha = 0.55\pi, 0.7\pi, 0.8\pi$ ($L_{\text{circ}} = 12$). We observe broad continua in energy space which are structurally akin to those of the KSL.

with its characteristic energy and width simultaneously decreasing as α increases. The interplay between these low- and high- energy features then gives rise to different mid-energy shapes. In fact the six spin wave bands start on the edges of the first Brillouin zone. As the energy increases, these bands become increasingly diffuse, eventually overlapping in a broad blob at Γ. These features sharpen upon moving away from the nearby QSL.

In Appendix D.4, we show the spectral function at the Gamma point $\boldsymbol{k} = 0$ as a function of energy obtained for $T = 40$ with $L_{\text{circ}} = 6$, which allows for a finer resolution $\sigma_\omega \approx 0.06$. We find that, even at this higher resolution, the high-energy features stay very broad in energy-space.

The persistence of the broad high energy features characteristic of the QSL across the transition into the zigzag phase are the essence of the idea of a proximate spin liquid. This concept was recently invoked for the putative Kitaev-compound α-$RuCl_3$ [97, 178–180]. However, as mentioned above, its detailed microscopic Hamiltonian—while not yet universally agreed upon—likely contains important terms beyond the KHM studied here [214, 236–238]. Note that in Fig. 6.4, for $\alpha = 0.7\pi$ at intermediate energies, there is a six-pointed-star whose arms point towards the edges of the first Brillouin zone. A similar feature was observed in experimental measurements on α-$RuCl_3$ [180].

It is interesting to note that if we do not average over different symmetry broken directions, the low-energy physics strongly breaks the C_6 symmetry yet the six-pointed star at intermediate energies persists: thus even if we interpret these high energy features as the overlap of broad spin waves, at this point the effect of symmetry breaking has disappeared. Under what conditions such a symmetry restoration occurs more generally is an interesting question, as is the issue in what settings a broad response at intermediate and high energies may generally be expected to occur, and to what extent it may nonetheless be amenable to a quasi-particle description.

7. Heisenberg on the square lattice: interacting spin waves

At its ripe age of 91 years [239], the square lattice antiferromagnetic Heisenberg model has had its dynamical properties studied intensely. Spin wave theory was in large part developed to investigate this model's low-energy properties [240–242]. Its anomalous terms lead to a 'relativistic' (linear and isotropic) low-energy dispersion, related to coupling the two sublattices of the ground state's spontaneous Néel ordering [243]. While evading an exact treatment, its dynamics has been studied numerically via quantum Monte Carlo simulations [88, 89] and exact diagonalization [92]; also several high-order perturbative expansions have been devised, such as around the Ising limit [90, 91, 244, 245] or via continuous unitary transformations (CUT) [93, 94]. In addition, a number of ad-hoc approaches have been motivated by a range of different physical pictures. Moreover, this model is related to experimental systems, not least to the parent states of the cuprates [182, 246–248], the study of which has led to much of the modern theory of quantum magnetism.

It may thus seem all the more surprising that there is still no consensus on the appropriate physical picture for certain regions in momentum space. Proposals include strongly-interacting magnons [93, 94], deconfined spinons [87, 181–184], all the way to a connection to deconfined quantum criticality [89]. The disagreement is not limited to the underlying physical mechanism, but also pertains to quantitative aspects of spectral properties. One uniting factor, at least, is a need to go beyond a perturbatively-dressed single-magnon picture.

Our intention is not to propose yet another scenario. Rather, we adopt the perspective that away from the unassailable hydrodynamic limit—accounting for the low-energy Goldstone modes [71, 243]—other features which have caught the attention of the community may not even be uniquely described by one picture as opposed to another. Instead, we seek to provide a simple account of salient features of the intermediate and high-energy part of the spectrum.

Perhaps the most controversial region concerns magnons with momenta $|k_x| + |k_y| = \pi$. Spin wave theory predicts that these are dispersionless, in disagreement with both experiment [85–87] and theoretical methods. What is instead observed, is a local mininum at $\boldsymbol{k} = (\pi, 0)$—commonly referred as the *roton mode*, in analogy with the quasi-particle dispersion in liquid Helium [84] discussed in Chapter 8. Moreover, spin wave theory is unable to account for the high spectral weight in the continuum just above this mode.

In this chapter, we advance along two complementary tracks. First, we determine the dynamical structure factor using the DMRG-based method introduced in Chapter 5, with systematic errors distinct from those of previous approaches. This novel method has at least two welcome features: it confirms that the phenomenology of the roton mode is indeed beyond the dressed single-magnon picture, and it uncovers a hitherto-unrecognized property of magnons with $|k_x| + |k_y| = \pi$, which we refer to as *sublattice-localization*. We also clarify how the latter is related to the entanglement of the ground state.

Second, we use existing data from an Ising expansion developed by Singh and Gelfand [90, 244, 245]—and pushed further by Zheng, Oitmaa and Hamer [91]—to point out that some known results at the isotropic point are already semi-quantitatively accounted for by the lowest non-trivial order. Moreover, our numerical method allows us to study such

an XXZ model (with dominant easy-axis anisotropy) without any perturbative approximation.

The main message of this chapter is that aspects of the attractive magnon interactions, i.e., the physics beyond spin wave theory, arise naturally from domain-wall-counting in the Ising limit, sometimes connecting all the way to the isotropic Heisenberg point. In particular, the numerical results show this at a phenomenological level, but a simple perturbative calculation also sheds light on, e.g., the small-yet-nonzero magnitude and shape of the roton mode's dispersion. Moreover, even the aforementioned phenomenon of sublattice-localization can be accounted for within a low-order perturbative picture. In addition, we provide a quantitative analysis of the roton mode.

This chapter is structured as follows. In Section 7.1, we give a brief overview of the model's salient features, relating them to previous literature whenever possible. The spectral functions obtained using DMRG are shown in Section 7.2: first for the Heisenberg model, which is then connected to the Ising limit. Section 7.3 supplements this by showing how various features, such as the roton minimum or sublattice-localization, naturally arise within a low-order perturbative picture. The apparently hitherto-unexplored phenomenon of sublattice-localization is studied numerically in Section 7.4, emphasizing its link to entanglement (or absence thereof). Section 7.5 contains a quantitative analysis of the roton mode with comparison to results from the literature.

7.1. Square lattice Heisenberg model

We study the spin-$\frac{1}{2}$ antiferromagnetic Heisenberg model on the square lattice, allowing for easy-axis anisotropy:

$$H = J \sum_{\langle \boldsymbol{n},\boldsymbol{m}\rangle} \left(S^z_{\boldsymbol{n}} S^z_{\boldsymbol{m}} + \lambda \left[S^x_{\boldsymbol{n}} S^x_{\boldsymbol{m}} + S^y_{\boldsymbol{n}} S^y_{\boldsymbol{m}} \right] \right) \tag{7.1}$$

where $J > 0$. We are principally interested in the isotropic point $\lambda = 1$, where the Néel order of the ground state spontaneously breaks the $SU(2)$ symmetry down to a $U(1)$ group generated by $S^z_{\text{tot}} = \sum_{\boldsymbol{n}} S^z_{\boldsymbol{n}}$ (where we define the ordering direction to be along the spin z-axis). As we will argue, it is also useful to consider $0 \leq \lambda < 1$, where the model is in a gapped Ising phase which spontaneously breaks the $\mathbb{Z}_2$ symmetry $R_x = \prod_{\boldsymbol{n}} \exp\left(i\pi S^x_{\boldsymbol{n}}\right)$.

7.1.1. Dynamical structure factor and quantum numbers

In Chapter 5, we have already extolled the virtues of the dynamic spin structure factor. Here, we give a few additional details that are particular to this model. Since the ground state has a two-site unit cell, one should in principle resort to the sublattice spectral functions defined in subsection 5.1.2. However, since in this chapter we will focus on the *transverse* spectral function, we can work with the simpler expression

$$\mathcal{S}^{\gamma\gamma}(\boldsymbol{k},\omega) = \frac{1}{2\pi} \sum_{\mathbf{r}} \int_{-\infty}^{\infty} e^{i(\omega t - \mathbf{k}\cdot\mathbf{r})} C^{\gamma\gamma}(\mathbf{r},t)\, \mathrm{d}t, \tag{7.2}$$

with $C^{\gamma\gamma}(\boldsymbol{r},t) = \langle \sigma^\gamma_{\boldsymbol{r}}(t)\sigma^\gamma_{\boldsymbol{0}}(0)\rangle = 4\langle S^\gamma_{\boldsymbol{r}}(t) S^\gamma_{\boldsymbol{0}}(0)\rangle$. The transverse spectral function is then given by

$$\mathcal{S}^t(\boldsymbol{k},\omega) = \mathcal{S}^{xx}(\boldsymbol{k},\omega) + \mathcal{S}^{yy}(\boldsymbol{k},\omega). \tag{7.3}$$

Indeed, if $\gamma = x, y$, one can show[1] that

$$\mathcal{S}^{\gamma\gamma}(\boldsymbol{k},\omega) = \sum_{\alpha} \delta(\omega - (\omega_\alpha - \omega_0))\, |\langle \alpha | \tilde{S}^\gamma_{\boldsymbol{k}} | 0\rangle|^2 \tag{7.4}$$

[1] To argue that $\langle 0|\tilde{S}^\gamma_{-\boldsymbol{k}}|\alpha\rangle\langle\alpha|S^\gamma_{\boldsymbol{0}}|0\rangle = \langle \tilde{S}^\gamma_{-\boldsymbol{k}}|\alpha\rangle\langle\alpha|\tilde{S}^\gamma_{\boldsymbol{k}}|0\rangle$, one can use that $\tilde{S}^\gamma_{\boldsymbol{k}}$ has a well-defined quantum number with respect to the *modified* translation operator $R^\gamma_\pi T_{x,y}$.

where $\tilde{S}^\gamma_{\boldsymbol{k}} = \sum_{\boldsymbol{r}} e^{i\boldsymbol{k}\cdot\boldsymbol{r}} S^\gamma_{\boldsymbol{r}}$, thanks to the fact that the system still has an unbroken modified translation operator $R^\gamma_\pi T_{x,y}$. It is natural to choose a basis $|\alpha\rangle = |\boldsymbol{k}, S^z_{\text{tot}}, \beta\rangle$, where $\boldsymbol{k}$ is the momentum with respect to the translation symmetry $T_{1,\pm 1}$ of the *two-site unit cell*. Eq. (7.4) tells us that the spectral function gives information about the existence of energy eigenstates with momentum $\boldsymbol{k}$ and and $S^z_{\text{tot}} = \pm 1$.

Note that when labeling states, $\boldsymbol{k}$ lives in the reduced (magnetic) Brillouin zone, $|k_x| + |k_y| \leq \pi$, but the spectral function itself is periodic only with respect to the original (lattice) Brillouin zone, $-\pi \leq k_x, k_y \leq \pi$ (taking the lattice constant to be unity).

7.1.2. Spin wave theory

In terms of the above quantum numbers, spin wave theory predicts two bands[2]. These exactly coincide and are distinguished by $S^z_{\text{tot}} = \pm 1$. The dispersion relation to order[3] $1/S^0$, i.e., linear spin wave theory (LSWT), is [241, 249]

$$\varepsilon^{\text{LSWT}}_{\boldsymbol{k}} = \sqrt{4 - \lambda^2(\cos(k_x) + \cos(k_y))^2}. \tag{7.5}$$

Hence for $\lambda = 1$, there are two linearly-dispersing Goldstone modes at the zone center (in sectors $S^z_{\text{tot}} = \pm 1$), consistent with two of three generators of $SU(2)$ being spontaneously broken [71]. However, based on general sum rules [250], it is known that $||S^{x,y}_{\boldsymbol{k}}|0\rangle|| \sim |\boldsymbol{k}|$ as $\boldsymbol{k} \to \boldsymbol{0}$, such that the Goldstone modes will have vanishing intensity in the transverse spectral function $\mathcal{S}^t(\boldsymbol{k}, \omega)$ at the zone center. Instead, they show up near the ordering wavevector $\text{M} = (\pi, \pi)$, since the same sum rules imply an (integrable) divergence $||S^{x,y}_{\text{M}+\boldsymbol{k}}|0\rangle|| \sim 1/|\boldsymbol{k}|$ as $\boldsymbol{k} \to \boldsymbol{0}$.

The first order corrections to the dispersion within spin wave theory are [251, 252]

$$\varepsilon^{\text{LSWT}+1/S}_{\boldsymbol{k}} = a\, \varepsilon^{\text{LSWT}}_{\boldsymbol{k}} - (1 - \lambda^2)\, b \left(\frac{2}{\varepsilon^{\text{LSWT}}_{\boldsymbol{k}}} - \frac{\varepsilon^{\text{LSWT}}_{\boldsymbol{k}}}{2} \right) \tag{7.6}$$

where a and b are (λ-dependent) constants[4]. At the isotropic point, this correction is only a momentum-independent rescaling. Higher-order corrections ($1/S^2$ and $1/S^3$) are also known [253–255], which we discuss in Section 7.5.

7.1.3. Phenomenology of diagonal magnons: a short review

The purpose of this section is to give a brief (and, unavoidably, partial) overview of some of the salient features which have been the focus of much of the previous work on the excitations of this model.

There is a peculiar property of the LSWT prediction: $\varepsilon_{\boldsymbol{k}}$ is constant along $|k_x| + |k_y| = \pi$. For convenience, we refer to magnons with these momenta as being *diagonal*. This dispersionless feature is a consequence of the more basic fact that at these momenta, the low-order spin wave Hamiltonian vanishes. This also means that the Bogoliubov rotation, which normally mixes the bosons of the two sublattices, is absent there. We thus arrive at the fact that, within LSWT, the diagonal magnons are purely *localized on a single sublattice*.

In fact, this one-dimensional flatness in the spectrum means that one has a freedom in choosing a basis of energy eigenstates. By Fourier transforming the momentum eigenstates

[2] One could instead work in a local frame where there is only one band, but this obscures some of the physics. In particular, then S^z_{tot} is no longer a good quantum number.

[3] To wit, the Holstein-Primakoff transformation is $S^+ = \sqrt{2S}\sqrt{1 - \frac{a^\dagger a}{2S}}\, a$. The dominant term of the square root $\sqrt{1 - \frac{a^\dagger a}{2S}}$ is of order $1/S^0$, which leads to LSWT.

[4] $a = 2 - \frac{1}{2}\int \frac{\mathrm{d}\boldsymbol{q}}{4\pi^2}\, \varepsilon^{\text{LSWT}}_{\boldsymbol{q}}$ and $b = \int \frac{\mathrm{d}\boldsymbol{q}}{4\pi^2}\, \frac{(\cos(q_x)+\cos(q_y))^2}{\varepsilon^{\text{LSWT}}_{\boldsymbol{q}}}$, where the integration is over $[-\pi, \pi] \times [-\pi, \pi]$.

along one direction, one can thus construct eigenstates which are spatially *localized onto a single diagonal* (of a given sublattice), with alternating signs along this diagonal. In summary, at low order in SWT, diagonal magnons are localized on both a sublattice and a diagonal. (In Section 7.3, we show that the same features arise naturally at low order in the Ising expansion.)

Despite being flat in LSWT and LSWT+$1/S$, the diagonal magnons acquire a finite but very small dispersion in higher-order spin wave theory [253–256]. Equivalently, this means that magnons can no longer be confined onto a single diagonal. However, it has not yet been investigated whether the aforementioned sublattice-localization persists. We study this both numerically (Section 7.4) and perturbatively (subsection 7.3.5).

The SWT predictions at diagonal momenta, $|k_x|+|k_y| = \pi$, do not agree well with other methods or experiments [85–87]—both with respect to single- and multi-magnon features. Examples of previous studies include methods based on quantum Monte Carlo (QMC) combined with analytic continuation [88, 89], series expansions in λ (up to 14th order) [90, 91], exact diagonalization (ED) [92] and the continuous unitary transform (CUT) [93, 94]. All these methods predict a more pronounced local minimum of the magnon at $\boldsymbol{k} = (\pi, 0) = X$, referred to as the roton mode, although they do not agree on its exact magnitude or shape (a quantitative discussion is deferred to Section 7.5). More strikingly, they also predict an unusually large weight in the continuum above this local minimum.

The latter phenomenology is also observed in experiment [86, 87, 257], and exotic scenarios have been given to explain it. For example, it has been argued that near $\boldsymbol{k} \approx X$, the magnon can be seen as two (nearly) deconfined spinons [87, 89, 182, 184]. This interpretation has subsequently been challenged by the CUT method [93, 94], which reproduces various salient features based on a picture of strongly-interacting magnons. The intuitive nature of said strong interactions, however, has not yet been clarified. We will argue that an Ising-like domain-wall interaction naturally accounts for it.

7.2. Spectral functions

In this section we discuss the transverse spectral function $\mathcal{S}^t(\boldsymbol{k}, \omega)$ as defined in Eq. (7.3). This is obtained using the method outlined in Chapter 5; we need only mention the details here that are specific to this chapter. The model is put on an infinitely long cylinder whose finite, periodic direction is along a zigzag/staircase path. We define the circumference L_{circ} in Manhattan distance, i.e., the minimal number of bonds needed to wrap around the cylinder. In this work $L_{\text{circ}} = 8, 10$. For a given circumference, we confirm that our results are converged in both bond dimension and inverse time-step by increasing both until the results no longer change. Due to the expensive nature of time-evolving large cylinders, in this work we are limited to bond dimension $\chi \approx 400$ for the largest circumference considered ($L_{\text{circ}} = 10$). A typical size that we used for the time-step is $dt = 0.01/J$. The conservation of S^z_{tot} was implemented explicitly.

7.2.1. Isotropic/Heisenberg model

Fig. 7.1 shows the transverse spectral function at the isotropic point ($\lambda = 1$). Because of the cylindrical geometry, momentum is discrete along one direction and continuous along the other. This is indicated by the red lines in the Brillouin zone in Fig. 7.1(a). Since the periodic direction is along a zigzag/staircase path, the momentum cuts are lines of constant $k_x - k_y$. This means we can directly access a line of diagonal magnons (as defined in Section 7.1), in the figure denoted by the line segment Y–X, where $X = (\pi, 0)$ and $Y = \left(\frac{\pi}{2}, -\frac{\pi}{2}\right) \cong \left(\frac{\pi}{2}, \frac{\pi}{2}\right)$ (by symmetry). In fact, while it is true that $\left(\frac{\pi}{2}, -\frac{\pi}{2}\right)$ and $\left(\frac{\pi}{2}, \frac{\pi}{2}\right)$ are symmetry-equivalent in 2D, this is not strictly true on the cylinder geometry.

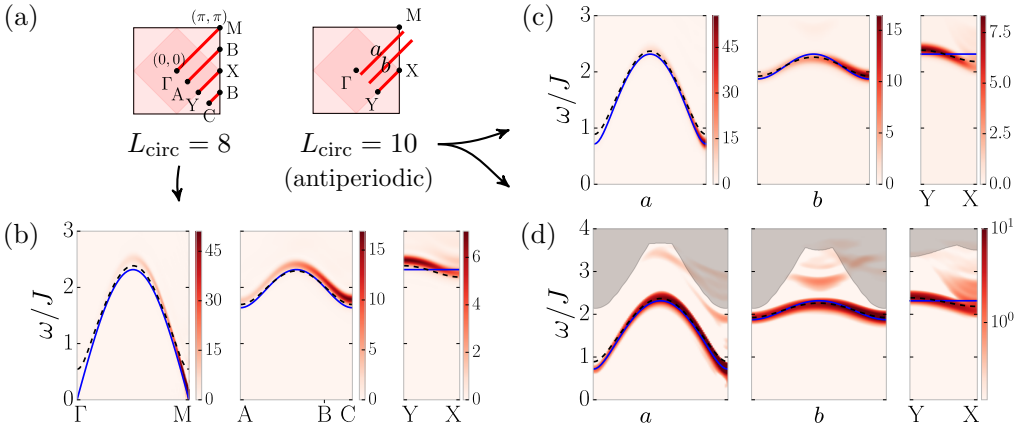

Figure 7.1.: **Symmetry-inequivalent momentum cuts of the transverse spectral function for the Heisenberg model ($\lambda = 1$).** Dashed black line is the series expansion result up to twelfth order evaluated at $\lambda = 1$ [91, 258]; solid blue line is LSWT+$1/S$ [251, 252]. (The maximum of the color scale is set by the largest value of the spectral function, except along the $\Gamma - \mathrm{M}$ line, where we reduced it by 90%.) (a) The accessible momentum cuts for cylinder circumferences $L_{\text{circ}} = 8, 10$. (b) The spectral function for $L_{\text{circ}} = 8$; the effective broadening due to the finite time window is $\sigma_\omega \approx 0.055J$. (c) The spectral function for $L_{\text{circ}} = 10$ and $\sigma_\omega \approx 0.05J$. (d) Same as (c) but in log-scale. The shaded region denotes the *kinematic* three-magnon continuum (for this geometry). The continuum above the roton mode ($\boldsymbol{k} \approx X$) is outside the kinematic region and it is instead related to (quasi-)bound state physics.

However, we have confirmed that such finite-size effects are small. The same line of diagonal magnons, X–Y, can be accessed for $L_{\text{circ}} = 10$ if there are antiperiodic boundary conditions along the finite direction, shifting the momentum cuts as shown.

We numerically observe the Goldstone modes at the zone center and the ordering wavevector $\mathrm{M} = (\pi, \pi)$. Moreover, the intensity vanishes at the zone center, and diverges at M, consistent with the sum rules discussed in Section 7.1. This agrees with the Goldstone modes predicted by LSWT+$1/S$ (solid blue line), whereas the naive evaluation of the series expansion data (up to λ^{12}) does not reproduce this[5] (dashed black line).

On the other hand, along the Y–X line, the series expansion data fares better at reproducing the local minimum at $\mathrm{X} = (\pi, 0)$. As discussed in Section 7.1, SWT predicts a flat dispersion along Y-X. Moreover, even in this linear color scale, we can see spectral weight above the single-magnon curve near $\boldsymbol{k} \approx \mathrm{X}$. These single- and multi-magnon features at the isotropic point are analyzed in more detail in Section 7.5. Here, we limit ourselves to a few general, conceptual remarks.

For $L_{\text{circ}} = 8$ (Fig. 7.1(b)), the system is gapless at the zone center, hence the multi-magnon continuum starts at the one-magnon branch (up to the miniscule gap introduced by using a finite bond dimension). For the $L_{\text{circ}} = 10$ geometry (Fig. 7.1(c)), however, the antiperiodic boundary condition imply that we do not pass through the Goldstone mode, such that the multi-magnon continuum is separated from the one-magnon branch. Nevertheless, these antiperiodic boundary conditions have some useful side-effects. Due to now simulating a gapped system, it is easier to converge the numerics in the bond dimension parameter of the matrix product state describing the ground state. Moreover, it

[5] More sophisticated extrapolation techniques could be and have been used for the low-energy modes near the isotropic point [90, 91], however in this work we focus on the high-energy modes.

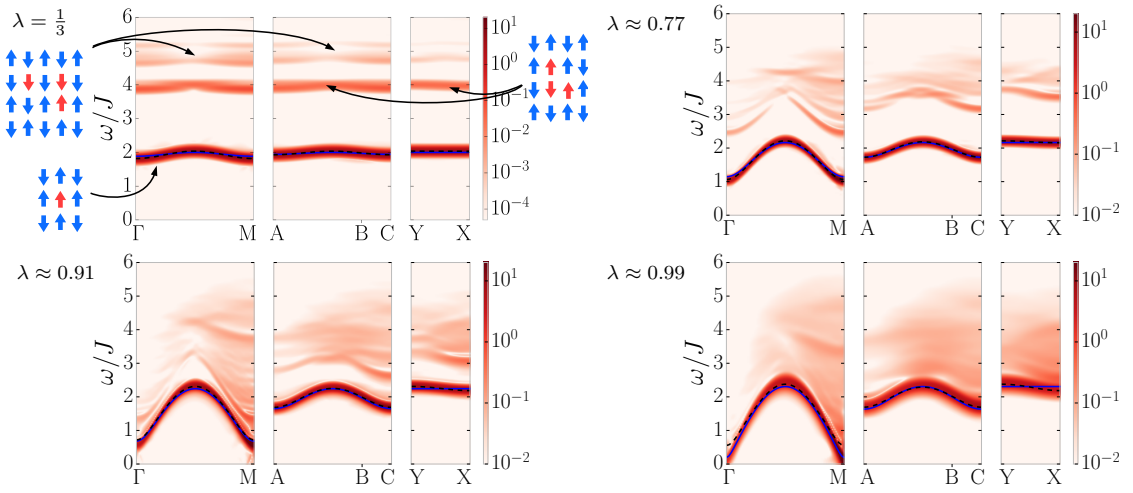

Figure 7.2.: **The transverse spectral function as a function of λ ($L_{\text{circ}} = 8$, log-scale).** Spectral features at the $SU(2)$ point ($\lambda = 1$) can be connected back to the Ising limit ($\lambda = 0$). Near the Ising limit, we identify the one-magnon branch, three-magnon bound states and three-magnon continuum based on domain-wall counting. Solid blue line is SWT+$1/S$ [251, 252], dashed black line is series expansion[91, 258] up to order λ^{12}. For the labeling of the momentum directions, see Fig. 7.1(a).

allows the ground state to spontaneously break the symmetry, even at the isotropic point. This is non-trivial given our set-up, since the cylinder is effectively a one-dimensional system (with a large unit cell), such that the Mermin-Wagner-Coleman theorem [230, 259] should prevent ordering. The catch is that the antiperiodic boundary conditions explicitly break the $SU(2)$ symmetry, although this is not locally noticeable.

This effective gap for $L_{\text{circ}} = 10$ can give us further insight into the physics beyond that of a single magnon. In Fig. 7.1(d), we show the same data of Fig. 7.1(c) in log-scale. We see a continuum right above the single-magnon branch near $\boldsymbol{k} \approx X$. However, this continuum does *not* fall within the frequency region of the kinematic (non-interacting) three-magnon continuum[6]. To emphasize this, we have plotted the three-magnon continuum *for this cylinder geometry* in the grey shaded region. Hence, the continuum above the roton mode is instead related to (quasi-)bound states. More precisely, using the insights from the upcoming subsection 7.2.2, this continuum is a combination of closely packed three-magnon (quasi-)bound states and a continuum made out of a single magnon and a two-magnon (quasi-)bound state. This is strongly suggestive that the roton mode arises by being repelled from these strongly-interacting states. This agrees with the conclusions of the CUT approach [93, 94].

7.2.2. Interpolating between the Ising and Heisenberg limits

Fig. 7.1 confirms that the DMRG method can reproduce the roton mode and the strong presence of multi-magnon features near $\boldsymbol{k} \approx X$. However, to gain insight into *how* and *from where* these features appear, it is useful to interpolate from the Ising limit ($\lambda = 0$) to the $SU(2)$-symmetric point ($\lambda = 1$). This is illustrated in Fig. 7.2 for $L_{\text{circ}} = 8$. In particular, we demonstrate that the features at the isotropic point can be traced back to those in the Ising limit.

[6] Note that due to parity symmetry, the transverse spectral function does not pick up the two-magnon continuum.

To this end, let us first identify the spectral features close to the Ising limit ($\lambda = \frac{1}{3}$). We can do this by using simple energetic arguments. Note that when $\lambda = 0$, a 'magnon' corresponds to a single localized spin flip with energy cost $\frac{J}{2}$ per bond, totaling $2J$. In Fig. 7.2, we see that for for $\lambda = \frac{1}{3}$ the magnon has gained some dispersion, but its energy is still roughly $2J$. Since the transverse spectral function picks up states with $S^z_{\text{tot}} = \pm 1$, the next excitation contains three magnons. Energetically, these magnons prefer to form a bound state whose domain wall counts eight bonds. Indeed, we observe bound states at energy $8 \times \frac{J}{2} = 4J$. There are several such states at this energy due to the internal degree of freedom corresponding to orientation and shape. At even higher energies, there is the kinematic continuum made out of a two-magnon bound state ($6 \times \frac{J}{2}$) and a free magnon ($2J$) with total energy around $5J$.

Having identified all spectral features for $\lambda = \frac{1}{3}$, we track their evolution as we tune $\lambda \to 1$ in Fig. 7.2. When $\lambda \approx 0.77$, some of the three-magnon bound states have merged, whereas others have already been absorbed into the three-magnon continuum. Closer to the isotropic point, $\lambda \approx 0.91$, the three-magnon continuum continues to come down in energy. This trend gradually continues up to $\lambda \approx 0.99$.

We see that the spectral features vary continuously as a function of λ. In particular, we see that there is no restructuring of the magnon near $\boldsymbol{k} \approx (\pi, 0)$ for any $\lambda < 1$. This was a priori not a given. Read backwards, this means that the features near the isotropic point can be continuously traced back to those in the Ising limit. Relatedly, it is worth pointing out that even at the isotropic point, the multi-magnon continuum is not featureless. We discuss this substructure more quantitatively in Section 7.5.

In Fig. 7.1(d), we saw how for $L_{\text{circ}} = 10$, there is a continuum above the roton mode which is not made out of kinematic combinations of magnons. In subsection 7.2.1, we claimed that it is instead a continuum made up out of (quasi-)bound states. The justification for this claim is that by smoothly decreasing λ, the observed continuum indeed splits up into three-magnon bound states and a continuum made up out of a magnon and a two-magnon bound state.

7.3. Perturbative understanding from the Ising limit

In Section 7.2, we saw that we could connect spectral features of the isotropic model to those near the Ising limit. The purpose of this section is to complement this by gaining insights from low-order perturbation theory in λ. The point is not to see how well the isotropic point can be described *quantitatively* by a series expansion in λ [90, 91]. Instead, we ask what the lowest order processes are that *qualitatively* explain certain features at the isotropic point. Intriguingly, this already naturally leads to a *semi-quantitative* description.

We rewrite the Hamiltonian in Eq. (7.1) as $H = H_0 + \lambda V$ with

$$H_0 = J \sum_{\langle \boldsymbol{n}, \boldsymbol{m} \rangle} S^z_{\boldsymbol{n}} S^z_{\boldsymbol{m}} \qquad \text{and} \qquad V = \frac{J}{2} \sum_{\langle \boldsymbol{n}, \boldsymbol{m} \rangle} \left(S^+_{\boldsymbol{n}} S^-_{\boldsymbol{m}} + S^-_{\boldsymbol{n}} S^+_{\boldsymbol{m}} \right). \tag{7.7}$$

The Ising limit $\lambda = 0$ is exactly solvable: the ground state is a Néel product state, and the single-magnon excitations consist of localized spin flips. The perturbation λV introduces dynamics to these static excitations. Before going through this in detail, let us give the broad brush strokes to emphasize the simplicity of both the ingredients and results.

7.3.1. Overview and summary of the perturbative picture

As we will argue, the effective Hamiltonian has contributions at *even* order in λ only. The Ising magnons start to hop at order λ^2 by going through a virtual three-magnon bound

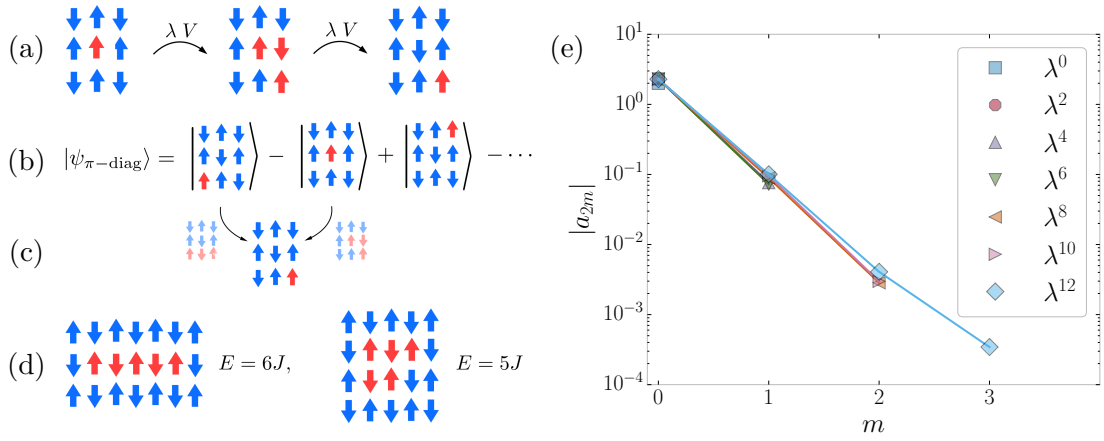

Figure 7.3.: **Perturbation theory around the Ising limit.** The A-(B-)sublattice is defined by where spins point down (up) in the ground state. (a) An A-magnon can hop at order λ^2 through a virtual three-magnon bound state. (b) This one-magnon state, localized on a single diagonal, cannot hop off it at order λ^2 due to the destructive interference shown in (c). (d) No destructive interference at order λ^4: different intermediate five-magnon bound states do not have the same energy. (e) The size of the Fourier coefficients of the dispersion of the diagonal magnons, $\varepsilon_{\pi-k,k} = J\sum_m a_{2m}\cos(2mk)$, obtained from series expansion up to different orders λ^n, evaluated at $\lambda = 1$. This is based on data from Refs. [91, 258]. We observe that the higher harmonics die off exponentially fast.

state (see Fig. 7.3(a)). Nevertheless, as we explain in subsection 7.3.3, magnons with diagonal momentum $|k_x| + |k_y| = \pi$ are still dispersionless at this order. This is equivalent to the statement that if one builds a one-magnon state which is entirely localized on a single diagonal and has momentum π along it (see Fig. 7.3(b)), then it cannot hop off due to destructive interference (see Fig. 7.3(c)).

The key to the destructive interference traces back to the fact that all three-magnon bound states have the same energy, and hence the virtual paths—half of which come with opposite signs due to the π-momentum—can cancel exactly. Thus from the viewpoint of the Ising expansion, such destructive interference and the resulting flatness of the diagonal magnons seems accidental. It is hence not surprising that if one goes to next-to-leading order, i.e., λ^4, the diagonal magnons acquire a dispersion. Indeed, now virtual five-magnon bound states appear, which can have differing energies (see Fig. 7.3(d)).

Since the emergence of the roton mode is due to the physics of (virtual) bound states, one can indeed say that this phenomenology is due to the attractive interactions between magnons. Since this interaction is so natural in the Ising language, the qualitatively correct physics arises rather easily. Indeed, the resulting dispersion at order λ^4 does not just correctly reproduce the qualitative features of having a local minimum[7] at $\boldsymbol{k} = (\pi, 0)$ and a maximum at $\boldsymbol{k} = \left(\frac{\pi}{2}, \frac{\pi}{2}\right)$, but evaluating it at $\lambda = 1$ even gives a semi-quantitative description for the isotropic model, as we discuss in subsection 7.3.4. It is moreover in remarkable proximity to the CUT prediction [93, 94], which is a sophisticated framework for strongly-interacting magnons. This success at relatively low order is in contrast with higher-order SWT.

That yet-higher-order corrections don't radically change the physics at hand can be

[7] One might have guessed that $(\pi, 0)$ would be special since this is where two flat directions (in momentum space) intersect, i.e., the lines $(\pi - q, q)$ and $(\pi - q, -q)$.

confirmed by repurposing results from previous studies [90, 91]. In Fig. 7.3(e), we show how the dispersion along the line of diagonal magnons has certain 'harmonics' generated at distinct orders in λ^n (the first non-trivial harmonic appearing at λ^4). We see that the higher harmonics die off exponentially fast, justifying a low-order picture. Note that such an exponential decay is a priori not obvious, considering that perturbation theory generically leads to an exponential proliferation of the number of terms.

Lastly, we also consider the perturbed wavefunctions at leading order. In particular, the ground state is dressed by pairs of correlated spin flips, introducing entanglement. This would usually allow one to create magnons associated with one sublattice by acting on the other sublattice. Surprisingly, our perturbative analysis implies that this is *not* possible for diagonal magnons. In other words, they seem to be localized on a given sublattice. This is discussed in subsection 7.3.5. (We also revisit and confirm such sublattice-localization numerically in Section 7.4.)

We now provide the details of the story as just described.

7.3.2. Ising limit and defining magnons

In the Ising limit $\lambda = 0$, the ground state is a Néel (product) state. We define the A-(B-) sublattice to be where spins point *down* (*up*) in the ground state. For any product state in the spin-z basis, we can count the number of flipped spins on the A-sublattice, relative to the ground state, which we denote by N_A (similarly for N_B). Hence, the ground state corresponds to $N_A = 0 = N_B$, whereas the single-magnon states have $N_A = 1$, $N_B = 0$ (called A-magnons) or $N_A = 0$, $N_B = 1$ (B-magnons).

The perturbation V will mix states with different N_A and N_B, however $N_A - N_B = S^z_{\text{tot}}$ remains a well-defined quantum number. If we perturb the system such that, for a given momentum, the one-magnon energy scale does not overlap with multi-magnon states, we can *non-perturbatively* label the single-magnon states by $N_A - N_B = 1$ or $N_A - N_B = -1$, referred to as A- and B-magnons, respectively. Since V thus cannot connect A-magnons to B-magnons, we can limit our study to A-magnons. More precisely, we are interested in the *effective* Hamiltonian H_{eff} on $\mathcal{H}_0$, the Hilbert space of states satisfying $N_A = 1$ and $N_B = 0$.

Note that these Ising magnons are exactly those encountered in Fig. 7.2. As discussed in Section 7.2, a single magnon has a domain wall crossing four bonds and hence has energy $E_0 = 4 \times \frac{J}{2} = 2J$ relative to the ground state (in the unperturbed Ising limit).

7.3.3. Dispersionless diagonal magnons at leading-order

The single-magnon states are completely static and localized in the Ising limit. They moreover stay immobile at first order in λ. More precisely, denoting the projector onto $\mathcal{H}_0$ as P_0, then at first order we have $P_0 V P_0 = 0$. This is because V creates a pair of A- and B-magnons out of the vacuum: it, e.g., maps $|\uparrow\downarrow\rangle \xrightarrow{V} \frac{J}{2}|\downarrow\uparrow\rangle$, whereas it *annihilates* ferromagnetic bonds. More generally, V flips the *parity* of $N_{A,B}$, hence the conservation of $N_A - N_B$ shows that there are *no* contributions to H_{eff} at any odd order λ^{2n+1}.

Thus, by standard perturbation theory, the lowest-order effective Hamiltonian on $\mathcal{H}_0$ is

$$H_{\text{eff}} = E_0 P_0 + \lambda^2 P_0 V G_0 V P_0 + \mathcal{O}(\lambda^4), \tag{7.8}$$

where $G_0 = (E - H_0)^{-1}$. This indeed introduces hopping, as shown in Fig. 7.3(a): the A-magnon can hop to any of the eight nearest sites (on the same sublattice) by going through a virtual three-magnon bound state. As discussed in Section 7.2, such a bound state involves eight *ferromagnetic* bonds, with total energy cost $8 \times \frac{J}{2} = 4J$—whereas the cost of a single magnon is $E_0 = 2J$. Thus, the path shown in Fig. 7.3(a) carries a weight $\frac{\lambda J}{2} \times \frac{1}{2J - 4J} \times \frac{\lambda J}{2} = -\lambda^2 \frac{J}{8}$.

Magnons can thus hop at order λ^2. However, certain superpositions are immobile due to destructive interference. Consider, for example, the state shown in Fig. 7.3(b): it is localized on a single A-diagonal, with an alternating sign structure. (We can say its momentum along the diagonal is π.) The magnon is unable to hop off the diagonal at order λ^2. This is illustrated in Fig. 7.3(c), showing two destructively interfering paths. It is important that both paths go through a virtual three-magnon bound state (both with energy $4J$), such that the two weights cancel exactly. Equivalently, all A-magnon momentum eigenstates with $|k_x| + |k_y| = \pi$—which we referred to as diagonal magnons in the previous sections—have constant energy. In summary, the diagonal magnons are dispersionless in the Ising expansion up to order $\mathcal{O}(\lambda^4)$. It is interesting to note that this coincides with the LSWT$(+1/S)$ predictions in Section 7.1.

7.3.4. Roton mode at next-to-leading order

It is hence important to see what happens at sub-leading order in λ. Here we follow the perturbative scheme by Kato [260] and Takahashi [261]. In terms of H_0 and V, they constructed a general-purpose unitary mapping $\Gamma_\lambda : \mathcal{H}_0 \to \mathcal{H}$ which embeds the unperturbed states into the space spanned by the true eigenstates (the latter being λ-dependent). This object gives us access to the effective Hamiltonian

$$H_{\text{eff}} := \Gamma_\lambda^\dagger H \Gamma_\lambda =: \sum_{n=0}^{\infty} \lambda^n H_{\text{eff}}^{(n)}. \tag{7.9}$$

As argued before, $H_{\text{eff}}^{(2n+1)} = 0$. Moreover, $H_{\text{eff}}^{(0)} = E_0 P_0$ and $H_{\text{eff}}^{(2)} = P_0 V G_0 V P_0$. From knowing the aforementioned object Γ_λ (which, for completeness, we reproduce as a function of H_0 and V in Appendix E), one can derive that

$$H_{\text{eff}}^{(4)} = P_0 V \tilde{G}_0 V \tilde{G}_0 V \tilde{G}_0 V P_0 - \frac{1}{2} \left\{ H_{\text{eff}}^{(2)}, P_0 V \tilde{G}_0^2 V P_0 \right\} \tag{7.10}$$

where $\tilde{G}_0 = Q_0 G_0 Q_0 = Q_0 (E - H_0)^{-1} Q_0$ and $Q_0 = 1 - P_0$.

From this, one can calculate that the diagonal magnons acquire a dispersion at this order. The reason for this is in fact simple, as hinted at in subsection 7.3.1. Fig. 7.3(d) shows two possible virtual five-magnon bound states that can appear as intermediate states. These two states have domain walls extending over, respectively, twelve and ten bonds. Their energy is thus different, and one should not expect perfect destructive interference.

More precisely, the resulting dispersion at order λ^4 is described by a simple cosine-like dispersion for the diagonal magnons: $\varepsilon_{\pi-k,k} = a + b\lambda^2 - c\lambda^4(d + \cos(2k)) + \mathcal{O}(\lambda^6)$ with $a, b, c, d > 0$. This has a local (roton) minimum at $\boldsymbol{k} = (\pi, 0)$ and a maximum at $\boldsymbol{k} = \left(\frac{\pi}{2}, \frac{\pi}{2}\right)$. Moreover, evaluating this at $\lambda = 1$ already gives a semi-quantitative description of the isotropic model. We refer the reader interested in quantitative details to Section 7.5, which is devoted to an in-depth comparison between various different methods.

In summary, the roton mode naturally appears in the Ising expansion. Through the property of all three-magnon bound states having the same energy, the local minimum at $\boldsymbol{k} = (\pi, 0)$ is absent at leading order, already indicating that it is less pronounced at the isotropic point. At the same time, its salient features readily appear at next-to-leading order, leading to a semi-quantitatively correct description. From this point of view, it is indeed an interacting-magnon effect, where the interaction is based on a simple domain-wall counting in the Ising limit.

7.3.5. Sublattice-localization of diagonal magnons

Aside from looking at the effective Hamiltonian, it can be instructive to consider how the eigenstates evolve with λ. This is exactly the information encoded in Γ_λ. In Fig. 7.4 we

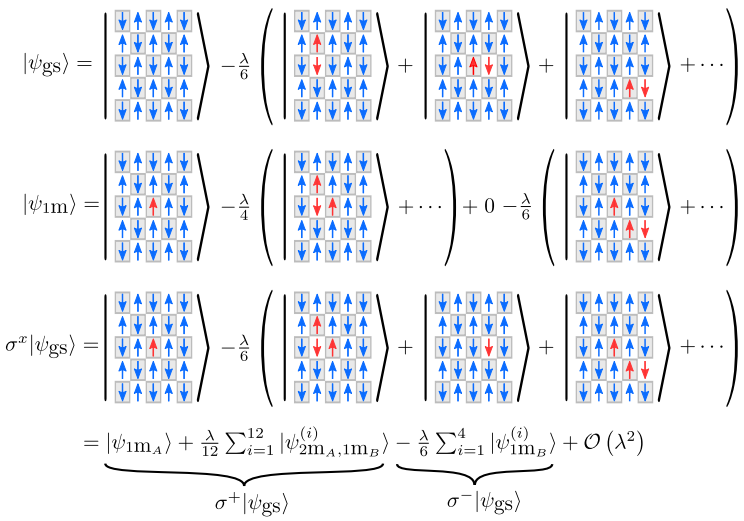

Figure 7.4.: **Dressing of the Ising limit ground state and a single A-magnon at leading order in perturbation theory.** The gray boxes denote the A-sublattice. The entanglement structure of the above states can be used to understand why the diagonal magnons seem to be localized on a given sublattice, as discussed and observed numerically in Section 7.4.

show the leading-order results, both for the ground state as well as a localized A-magnon. (One would have to Fourier transform the latter to obtain an energy eigenstate.) We see that these states are dressed with 'pair fluctuations' whilst staying within a well-defined $N_A - N_B = \sum S^z_{\mathrm{tot}} = 0, 1$ sector.

Having access to the perturbed states, we can ask what excitations are created upon acting with a local operator on the ground state. Fig. 7.4 shows that at this order, a σ^x operator does not just create a single magnon, but also three-magnon bound states. This is to be expected and is directly in line with the spectral weight observed in Fig. 7.2.

It is more interesting to consider what happens when applying σ^- on the A-sublattice. This brings us into the sector $N_A - N_B = -1$. In other words, by acting with this operator on the A-sublattice, we create a B-magnon. This is not possible in the product state Ising limit $\lambda \to 0$, where acting with σ^- on the A-sublattice annihilates the ground state. But as shown in Fig. 7.4, the perturbation V introduces entanglement, such that $\sigma^-_{\boldsymbol{n}}|\psi_{\mathrm{gs}}\rangle$ is nonzero and has a B-magnon on the four B-sites adjacent to the original site $\boldsymbol{n} \in A$.

However, something unusual happens for diagonal momenta. Note that for any given B-site, there are four adjacent A-sites. If the operator we acted with on the A-sublattice has momentum $|k_x| + |k_y| = \pi$, then half of these four sites carry a positive sign, and half a negative sign, so that there would be perfect cancellation. In other words: we are not able to create a B-magnon with $|k_x| + |k_y| = \pi$ by acting on the A-sublattice.

The above used an explicit calculation, but the essential mechanism at play should hold at all orders. If we act on a given site of the A-sublattice, then by the 90° symmetry of the model, the signs and weights will be the same in all four directions. However, this is incompatible with the alternating sign structure of diagonal momenta. This argument suggests that as long as we act on a single site of the A-sublattice, we *cannot* create a B-magnon with a diagonal momentum. We investigate this claim of *sublattice-localization* non-perturbatively in the following section, detailing its relationship to entanglement.

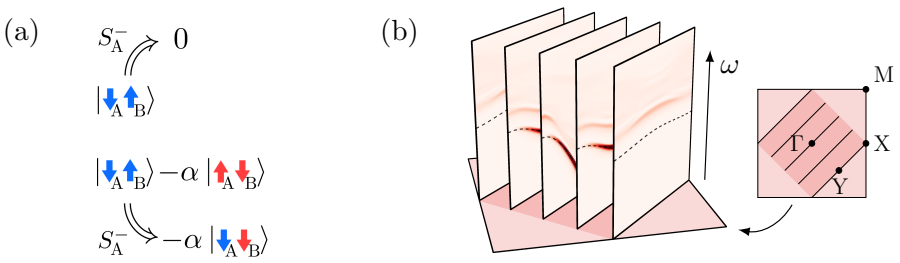

Figure 7.5.: **Sublattice-localization of diagonal magnons.** (a) If there is entanglement in the ground state (due to pair fluctuations), then it is generically possible to create a B-magnon by acting on the A-sublattice. (b) The *sublattice spectral function* $\mathcal{S}_{A\to B}(\boldsymbol{k},\omega)$ obtained with DMRG is shown: this measures whether acting on the A-sublattice can create B-magnons. As defined in Eq. (7.11), we act with S^- exclusively on the A-sublattice (where the expectation value already points down). The ground state entanglement is responsible for the non-zero spectral weight on the single-magnon branch (dashed line). Surprisingly, there is *no* weight on the diagonal magnons (edge of shaded square). The plot is for $\lambda = 0.95$ and $L_{\text{circ}} = 8$. The same conclusion seems to hold when acting with multi-site operators.

7.4. Entanglement and sublattice-localization of diagonal magnons

In this section we discuss a peculiar property of the entanglement in this model. As before, we define the A-sublattice where the spins point down in the ground state (opposite for the B-sublattice). The ground state is in the sector $S^z_{\text{tot}} = 0$, and a magnon associated with the B-sublattice, a *B-magnon*, is in the sector $S^z_{\text{tot}} = -1$.

If the ground state had *no* entanglement between the two sublattices, then by acting on the A-sublattice, one could *not* create a B-magnon. The intuitive idea is sketched in Fig. 7.5(a), but the more precise wording is as follows: if $|\Psi_{\text{gs}}\rangle = |\psi_A\rangle \otimes |\psi_B\rangle$ (where $|\psi_{\alpha=A,B}\rangle$ lives on the α-sublattice), then, e.g., $S^-_{\boldsymbol{n}}$—which puts us in the S^z_{tot} sector of a B-magnon—*annihilates* the ground state if $\boldsymbol{n} \in A$. To argue this, note that since the ground state is an eigenstate of S^z_{tot}, then the factorization implies that $|\psi_{\gamma=A,B}\rangle$ must be an eigenstate of $S^z_{\gamma=A,B} := \sum_{\boldsymbol{n}\in\gamma} S^z$. Moreover, since the product Néel state has a finite[8] overlap with $|\Psi_{\text{gs}}\rangle$, this fixes the eigenvalue of S^z_A to be as (algebraically) small as possible. Hence, acting with the lowering operator on A must annihilate the state.

The actual ground state will of course have entanglement; for example, at leading order in λ, there are two-site spin-flips ('pair fluctuations') which entangle the two sublattices, see, e.g., Fig. 7.5(a) or Fig. 7.4. Thus, it is indeed generically possible to create a B-magnon by acting on the A-sublattice. However, this does not seem to be true for diagonal magnons, i.e., when $|k_x| + |k_y| = \pi$. To make this precise, we introduce what we call the *sublattice spectral function*,

$$\mathcal{S}_{A\to B}(\boldsymbol{k},\omega) = \sum_{\alpha} \delta(\omega - (\omega_\alpha - \omega_0))\ |\langle\alpha|\tilde{S}^-_{A,\boldsymbol{k}}|0\rangle|^2 \tag{7.11}$$

where $\tilde{S}^-_{A,\boldsymbol{k}} = \sum_{\boldsymbol{r}\in A} e^{i\boldsymbol{k}\cdot\boldsymbol{r}} S^-_{\boldsymbol{r}}$. There are two crucial differences that distinguish it from the usual transverse spectral function as in Eq. (7.2). Firstly, we only act on the A-sublattice,

[8] For overlaps to be well-defined, one can apply the argument to finite systems.

where spins point down in the symmetry-broken ground state. Secondly, we act with the lowering operator S^-, putting us in the S^z_{tot} sector of B-magnons.

In Fig. 7.5, we show this sublattice spectral function $\mathcal{S}_{A\to B}(\boldsymbol{k},\omega)$. For convenience, we consider $\lambda = 0.95$ instead of the isotropic point, as this allows us to tell the one-magnon branch straightforwardly apart from the multi-magnon sector. We see that the response is non-zero on almost the whole single-magnon branch (dashed lines). However, the spectral weight is exactly zero for any of the diagonal magnons (i.e., along the border of the shaded region in the Brillouin zone). We conclude that the diagonal magnons appear to be localized on their respective sublattices.

In subsection 7.3.5 we gave a symmetry-based argument for the sublattice-localization within the perturbative framework, using the fact that we act with a single-site operator. However, we have also numerically confirmed that the same absence of spectral weight occurs even if we act with *multi-site* operators localized on the A-sublattice (not shown). We have not found an explanation for this and it would be interesting to study this in more detail. It is an open question whether there is a probe that could directly access $\mathcal{S}_{A\to B}(\boldsymbol{k},\omega)$ in an experimental set-up.

7.5. Quantitative analysis at diagonal momenta

In this section, we analyze the roton mode at $\boldsymbol{k} = (\pi, 0) \cong X$ and its associated multi-magnon features in more quantitative detail, including a comparison to previous work.

7.5.1. Depth of the anomalous mode at $\boldsymbol{k} = (\pi, 0)$

In Fig. 7.6(a), we consider the depth of the roton mode, i.e. the maximum of the dispersion at $\boldsymbol{k} = \left(\frac{\pi}{2}, \frac{\pi}{2}\right) \cong Y$ relative to the local minimum at $\boldsymbol{k} = (\pi, 0) \cong X$. This is shown as a function of the parameter λ. As derived in Section 7.3, we expect the dispersion to scale as $\sim \lambda^4$ for small λ. For that reason, we scale our axis accordingly. The numerical results obtained with our DMRG-based method for $L_{\text{circ}} = 10$ (up to $\chi = 400$) are shown as yellow dots. At the isotropic point ($\lambda = 1$), we plot the predictions of QMC [88, 89] (extrapolated from up to $N = 48 \times 48$), CUT [93, 94], ED [92] (extrapolated from up to $N = 36$) and SWT [241, 249, 251–255].

This quantity is extracted from the spectral function by fitting the single-magnon response with a Gaussian[9]. Near the isotropic point, this fitting is somewhat subtle, as the one-magnon response is not easily separated from the multi-magnon weight. Fitting the (quasi-)bound states just above the single-magnon branch—which are highly relevant near $\boldsymbol{k} \approx (\pi, 0)$—as well, we obtain results which are stable with respect to the numerical parameters.

At the isotropic point, the method that DMRG is closest to is QMC. For $L_{\text{circ}} = 10$, we obtain $\varepsilon_{\frac{\pi}{2},\frac{\pi}{2}} \approx 2.40J$ and $\varepsilon_{\pi,0} \approx 2.06J$-$2.07J$. This can be compared to the QMC [89] extrapolations $\varepsilon_{\frac{\pi}{2},\frac{\pi}{2}} \approx 2.40J$ and $\varepsilon_{\pi,0} \approx 2.13J$. We are unable to perform a finite-circumference analysis, since for $L_{\text{circ}} = 6$ there are domain-wall excitations (wrapping around the circumference), while for $L_{\text{circ}} = 8$ the system is gapless such that we expect stronger finite-circumference effects. However, one can compare our results to the finite-size QMC data with linear dimension 10, corresponding to our largest cylinder circumference. In that case, QMC obtains [89] $\varepsilon_{\pi,0} \approx 2.2J$. Taking this to give a rough finite-size estimate, we note that we are within the same distance to the extrapolated QMC data (although at the opposite extreme).

It is illuminating to not just focus on the isotropic case, but to track the evolution as a function of λ as shown in Fig. 7.6(a). The dashed lines are from series expansions [90, 91]

[9] Note that the width of the Gaussian is known; see Section 7.2.

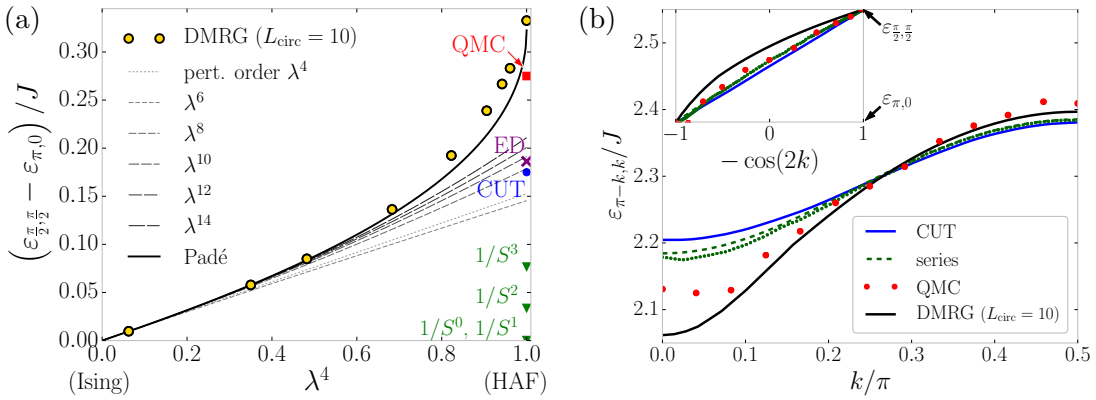

Figure 7.6.: **Depth and dispersion of the roton mode.** (a) Its depth is shown as a function of λ. Yellow dots are the DMRG results ($L_{\mathrm{circ}} = 10$). Dashed lines are series expansion results to various orders [90, 91]. We obtain the solid line by rewriting series expansions in terms of $\delta = 1 - \sqrt{1-\lambda^2}$ and subsequently making a Padé approximant (details in main text). At the isotropic point ($\lambda = 1$), we compare to QMC [88, 89], CUT [93, 94], ED [92] and SWT [241, 249, 251–255]. (b) Dispersion at the istropic point ($\lambda = 1$). The solid black line is the DMRG result ($L_{\mathrm{circ}} = 10$). The green lines are the series expansion results: the dashed line [91, 258] is the result to order λ^{12} evaluated at $\lambda = 1$, whereas the dotted green line is extracted from the plot in Ref. [91]. We also compare to QMC [88, 89] and CUT [93, 94]. Inset: rescaled dispersions to compare functional forms.

to different orders in λ. If we track the lowest-order result $\sim \lambda^4$ toward the isotropic point $\lambda = 1$, we already obtain the correct order of magnitude. This is moreover in striking proximity to the CUT prediction. As we include higher order terms, we see that the dispersion gradually creeps up, showing no real sign of convergence. However, since SWT results are analytic in the modified parameter $\delta = 1 - \sqrt{1-\lambda^2}$, it is suggestive to rewrite the series expansion in terms of δ. Doing so, and building a Padé approximant out of it, we obtain the solid line in Fig. 7.6(a).

We find that the Padé approximant is remarkably robust: the approximants $[3,3]$, $[4,2]$, $[5,2]$, $[4,3]$, $[3,4]$ all give virtually indistinguishable results! This stability suggests that the solid line could be a reasonable prediction for the true evolution of the dispersion as a function of λ. Exactly *at* the isotropic point, there is a small caveat: any power series in λ, when rewritten in terms of δ, generically predicts a diverging slope at $\delta = 1$. Hence, also in this case, we find that the dashed curve is finite at $\delta = 1$ but its slope is vertical. It is not clear whether this particular feature is physical or not. Other than that, we expect that the Padé approximant should be reliable and we are encouraged by the fact that our numerical results agree so well with the Padé curve, indicating that finite-size corrections for $L_{\mathrm{circ}} = 10$ are already rather small.

It would be interesting to investigate to what extent the Padé approximant gives the correct prediction. In particular, it might be worthwhile to test and compare the other methods[10] at $0 < \lambda < 1$.

[10] We note that applying the CUT method developed in Refs. [93, 94] to $\lambda < 1$ would be distinct from the CUT method that was applied to the XXZ model in Ref. [262]: in the latter case, the CUT method was perturbative in the parameter λ, hence being an alternative way of calculating the series expansion coefficients.

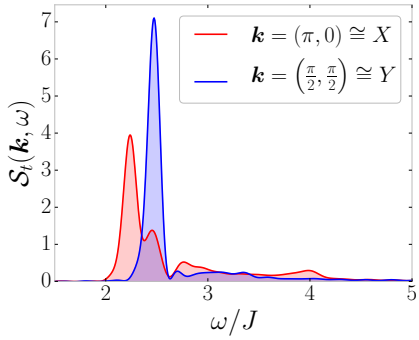

Figure 7.7.: **Weight in the continuum above diagonal magnons.** Transverse spectral function $\mathcal{S}^t(\boldsymbol{k}, \omega)$ for the Heisenberg model ($\lambda = 1$) with $L_{\text{circ}} = 8$ and broadening $\sigma_\omega \approx 0.055J$. The second peak for $\boldsymbol{k} = (\pi, 0) \cong X$ is the three-magnon (quasi-)bound state.

7.5.2. Dispersion relation

Aside from studying the depth of the roton mode, we also consider its shape. Our numerical result is shown in Fig. 7.6(b) (solid black line). We compare it to the functional forms obtained by CUT, QMC and series expansion. As discussed in Section 7.3, the lowest-order non-trivial prediction from the Ising expansion is a simple cosine-like dispersion. This is not significantly altered at higher orders in λ (or at the very least, only very slowly so), as was shown in Fig. 7.3(e). The purpose of the inset is to show a comparison with this simple cosine.

Remarkably, the CUT result is perfectly fit by a single harmonic. In conjunction with subsection 7.5.1, we thus conclude that the fourth order extrapolation from the Ising expansion seems to be in striking proximity to the CUT prediction of the roton dispersion. Our result, on the other hand, while being dominated by the same cosine, also contains the higher harmonics (which are qualitatively generated in the Ising expansion). We point out that the QMC curve has more structure near $\boldsymbol{k} \approx X$, with a possible small subsidiary maximum at the X point itself; it would be interesting to investigate its origin.

7.5.3. Multi-magnon features

Lastly, in Fig. 7.7 we show a more detailed slice of the transverse spectral function $\mathcal{S}^t(\boldsymbol{k}, \omega)$ first shown in in Fig. 7.1. At two values of the momentum, $\boldsymbol{k} = (\pi, 0) \cong X$ and $\boldsymbol{k} = \left(\frac{\pi}{2}, \frac{\pi}{2}\right) \cong Y$, we show the spectral weight as a function of ω. This numerical data is for the smaller circumference $L_{\text{circ}} = 8$, since as discussed in Section 7.2, in that case the system is gapless. Being gapless, one expects there to be more significant finite-size effects on a *quantitative* level, but the *qualitative* shape should look more like the 2D limit than the $L_{\text{circ}} = 10$ data would.

For either momentum, we clearly see the single-magnon peak (broadened due to our finite-time window, as explained in Section 7.1) and a broad three-magnon continuum. Moreover, for $\boldsymbol{k} = (\pi, 0) \cong X$, we recognize a second, smaller peak. This is a three-magnon (quasi-)bound state.

We would like to comment on the following two features of Fig. 7.7. Firstly, there is considerable weight in the multi-magnon sector at $\boldsymbol{k} = (\pi, 0)$, and not at $\boldsymbol{k} = \left(\frac{\pi}{2}, \frac{\pi}{2}\right)$. Due to not having a tight grasp on finite-size effects for $L_{\text{circ}} = 8$, we do not believe there is great value in quoting precise numbers, but at $\boldsymbol{k} = (\pi, 0)$, only roughly half the weight is on the single magnon. Secondly, there is certainly a substructure to the multi-magnon weight. This seems to be in contrast to the featureless spectral function observed

in a recent Monte Carlo study [89], which however considers the sum of the transverse and longitudinal spectral function. We do not expect the longitudinal contribution to completely smear out the substructure; in fact, the CUT analysis indicates the presence of strong resonances in the latter [93, 94]. Due to the absence of a finite-size analysis, the substructure we observe is not conclusive and it would be interesting to investigate this further.

8. Heisenberg on the triangular lattice: avoided decay from strong interactions

In the introduction of this thesis, we touched upon the concept of a *quasiparticle*: a large number of microscopic degrees of freedom moving in unison as a single emergent entity. Chapters 6 and 7 considered the specific cases of anyons and magnons, but the concept is much more general. When they exist, a multitude of physical properties of the system can be readily understood in terms of them—not least transport and finite temperature properties. Hence, an important question in the theory of condensed matter is to know when quasiparticles are indeed a good description of the excitations of many-body systems.

Over the decades, various approximate and perturbative schemes have been developed in an effort to describe the quasiparticles on top of various distinct ground state orders. Two notable examples are spin wave theory [240–242] for describing magnons on top of spontaneously ordered magnets—in part developed to describe the square lattice antiferromagnet of Chapter 7—and slave-particle mean-field theory [9, 263, 264] for describing the anyonic excitations on top of quantum spin liquids. What makes such approximations tractable is that they treat the quasiparticles as non-interacting (which can then be perturbatively corrected). Hence, at leading order, the quasiparticles in such schemes are well-defined by construction. However, if one finds that for a given momentum and energy of the quasiparticle, there are multi-particle states with the same energy and momentum (i.e., the quasiparticle is said to be in the multi-particle continuum) then a nonzero matrix element[1] between the two will lead to *quasiparticle decay*. In particular, the quasiparticle will no longer be well-defined—in the best case scenario, it can still be identified as a finite-lifetime resonance. For a review of this in the context of quantum magnets, see Ref. [76].

The above conventional picture is true for *weak* interactions, where a perturbative treatment is justified. In this chapter, however, we show that this is far from the whole story: *strong* interactions *generically* stabilize quasiparticles by pushing them out of the continuum. This general mechanism is straightforwardly illustrated in an exactly solvable model in Section 8.1; in fact, the main message can be summarized in a single figure (see Fig. 8.1). In subsection 8.1.3, we numerically confirm this prediction of avoided decay in an Ising ladder where we can tune between the weakly- and strongly-interacting limits. In Section 8.2, we show that the triangular lattice Heisenberg antiferromagnet (with a slight anisotropy for ease of numerics) also displays *avoided magnon decay*, in contradiction with naive SWT predictions. Turning to *existing* experimental data in Section 8.3, we identify the detailed phenomenology of avoided quasiparticle decay in the triangular lattice magnet [77] $Ba_3CoSb_2O_9$, and even in liquid helium [78–83]—one of the earliest instances of quasiparticle decay [74].

8.1. The principle of avoided quasiparticle decay

The idea of avoided decay is easily summarized, which we do in Fig. 8.1. The claim is that for strong enough interactions between the quasiparticle and the continuum, the former

[1] Symmetries and quantum numbers might force matrix elements to be zero; in this chapter, we will consider the generic case where this does not happen.

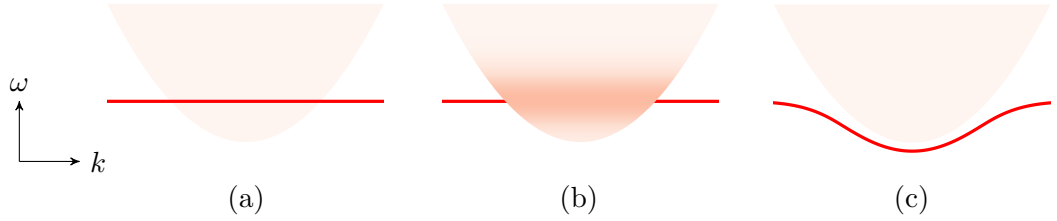

Figure 8.1.: **The concept of avoided decay.** (a) As a starting point, a non-interacting quasiparticle (red line) partially overlaps with a multi-particle continuum of states (shaded region). (b) Weakly coupling the quasiparticle to the continuum leads to decay, manifesting itself through line broadening. (c) We point out that for strong enough interactions, the quasiparticle will be pushed out of the continuum. Decay is now forbidden due to energy and momentum conservation.

will be repelled out of the latter. In this sense, the quasiparticle *avoids* or even *undoes* its decay. This concept, which we now discuss in more detail, is a direct generalization of the well-known notion of level repulsion.

8.1.1. Level-level repulsion: avoided crossing

It is a fundamental insight of quantum mechanics that energy levels repel. This is commonly illustrated by letting two levels with unperturbed ('bare') energies $\pm E_b$ interact with one another through a coupling γ, i.e.,

$$\hat{H} = \begin{pmatrix} E_b & \gamma \\ \gamma & -E_b \end{pmatrix}. \tag{8.1}$$

The resulting energies of $\hat{H}$ are $\pm\sqrt{E_b^2 + \gamma^2}$. Hence, repulsion leads to a minimal separation of the levels of $2|\gamma|$, no matter how small the initial separation $2|E_b|$. In particular, if we tune E_b through zero—such that the bare energies cross—we see that the energies of the interacting systems never meet. This is sometimes referred to as an *avoided crossing*.

A natural question is whether the above notion of level repulsion extends to the case of a discrete level coupled to a continuum of states. The question might seem moot, since the common expectation is that a bare level inside a continuum will be *dissolved* by interactions (see Fig. 8.1(b)), becoming a finite-lifetime resonance or worse, no hint of it remaining. If the bare level represents a quasiparticle, its broadening and disappearance in the many-particle continuum is known as quasiparticle decay. In the case of non-topological[2] quantum magnets, the expectation of magnon decay [76] has—surprisingly only recently—been borne out in inelastic neutron scattering experiments [265–269].

8.1.2. Level-continuum repulsion: avoided decay

Here, we show that this expectation of quasiparticle decay is wrong when interactions are strong enough. Rather, with increasing interaction strength, an infinitely long-lived state re-emerges out of the continuum of states (see Fig. 8.1(c)). This happens via a simple generalization of the familiar level repulsion, Eq. (8.1). We couple a bare state $|\psi\rangle$ with bare energy E_b to a continuum of states $|\varphi_\alpha\rangle$ with bare energies E_α. I.e., $\hat{H} = \hat{H}_0 + \gamma\hat{V}$,

[2] I.e., an ordered magnet or a non-topological paramagnet.

where

$$\hat{H}_0 = E_b\,|\psi\rangle\langle\psi| + \int \mathrm{d}\alpha\; E_\alpha|\varphi_\alpha\rangle\langle\varphi_\alpha|, \tag{8.2}$$

$$\hat{V} = \int \mathrm{d}\alpha\;\left(|\psi\rangle\langle\varphi_\alpha| + |\varphi_\alpha\rangle\langle\psi|\right). \tag{8.3}$$

The continuous label α satisfies $\langle\varphi_\alpha|\varphi_\beta\rangle = \delta(\alpha-\beta)$ and we denote the density of states (DOS) of the continuum by $\nu(E)$. For convenience, we say the onset of the continuum is at $E=0$ (i.e., $\nu(E)=0$ for $E<0$). Physically, this model represents states with a fixed value of *total* momentum—the continuous index α corresponds to the *relative* momentum of multi-particle states.

We now show that, for large enough coupling $|\gamma|$, there is a single discrete state $|\psi^*\rangle$ with an energy *below* the continuum, $E^*<0$. Moreover, the contribution of the unperturbed state $|\psi\rangle$ to this final discrete state, denoted by the weight $Z=|\langle\psi|\psi^*\rangle|^2$, can be large—for a continuum of finite support, the weight approaches $Z\to 1/2$ for large $|\gamma|$. This is experimentally important: a vanishing Z implies that the state $|\psi^*\rangle$ bears little relationship to the original quasiparticle. However, a *large* Z ensures that any experimental set-up—e.g., neutron scattering—for detecting the original quasiparticle $|\psi\rangle$ also detects $|\psi^*\rangle$. Hence, while existence of $|\psi^*\rangle$ and *finiteness* of Z for this simple model have been pointed out before [270], its phenomenology and in particular its relevance to quasiparticles in strongly-interacting quantum systems seem to have been underappreciated.

The existence of a pole for strong interactions

It is useful to consider the single-particle Green's function $G(E)=\langle\psi|(E-\hat{H})^{-1}|\psi\rangle$. One can derive that $G(E)^{-1}=E-E_b-\gamma^2 g(E)$ where we have defined $g(E)\equiv\int\frac{\nu(\varepsilon)}{E-\varepsilon}\mathrm{d}\varepsilon$ (see Appendix F.1). Note that $\lim_{E\to-\infty}G(E)^{-1}=-\infty$ and $\lim_{E\to 0^-}G(E)^{-1}=-E_b-\gamma^2 g(0^-)$. Since $G'(E)>0$, the existence of a (unique) pole at E^* below the continuum (i.e., $E^*<0$) is equivalent to $G(0^-)^{-1}>0$, which in turn is equivalent to $\gamma^2>E_b/|g(0^-)|$. We conclude that if the bare quasiparticle is inside the continuum (i.e., $E_b>0$), then there is threshold value $\gamma_{\mathrm{th}}\equiv\sqrt{E_b/|g(0^-)|}$ such that there is a (unique) pole below the continuum for any coupling $|\gamma|>\gamma_{\mathrm{th}}$! (Note that $g(0^-)\neq 0$, such that $\gamma_{\mathrm{th}}<\infty$.)

In the special case that the DOS has a discontinuous onset (i.e., $\nu(0^+)\neq 0$), then the integral defining $|g(0^-)|$ diverges, such that the threshold value γ_{th} defined above is zero. Hence, in this case, *any* nonzero γ will give rise to a pole below the continuum. An equivalent treatment can be found in Ref. [270].

Quasiparticle weight Z

To obtain the single-particle weight $Z=|\langle\psi|\psi^*\rangle|^2$ (where $|\psi^*\rangle$ is the wavefunction with energy $E^*<0$), consider that the weight of the delta function $\delta(E-E_b-\gamma^2 g(E))$ is given by the inverse derivative of its argument, i.e., $Z=\frac{1}{1-\gamma^2 g'(E^*)}$. Moreover, for large $|\gamma|$, we have the relationship $E^*=\gamma^2 g(E^*)$, from which one can derive that $E^*\to-\infty$ as $|\gamma|\to\infty$. We thus have that

$$\lim_{|\gamma|\to\infty} Z = \lim_{E\to-\infty}\left(1-\frac{E\,g'(E)}{g(E)}\right)^{-1}. \tag{8.4}$$

To evaluate this, we need the asymptotic behaviour of $g(E)$. If $\nu(E)$ has finite support, then $g(E)\sim\frac{1}{E}\int\nu(\varepsilon)\mathrm{d}\varepsilon$ as $|E|\to\infty$. Plugging this into Eq. (C.25), we obtain $Z\to 1/2$ in the strongly-interacting case.

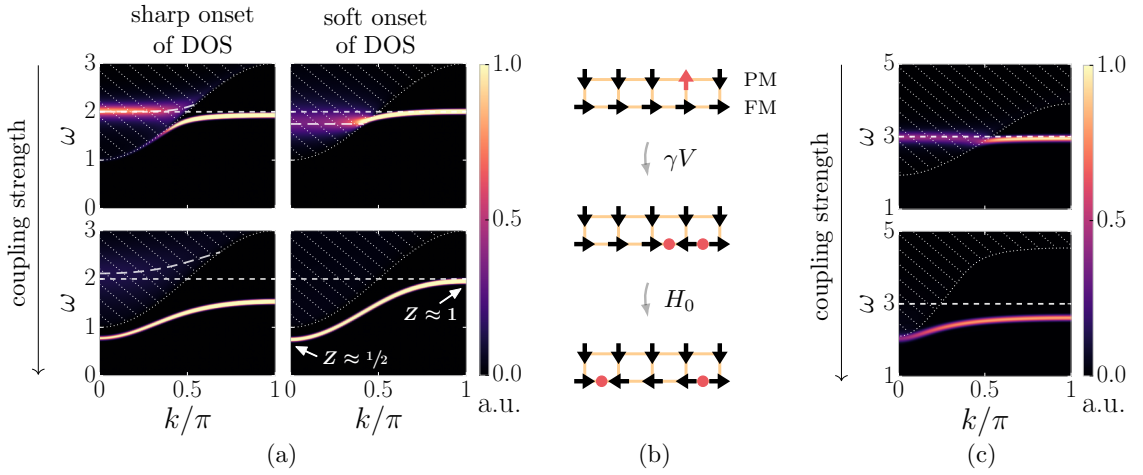

Figure 8.2.: **Avoided quasiparticle decay in toy model and Ising ladder.** (a) The bare level $|\psi_k\rangle$ (flat short-dashed line) is coupled to a continuum (shaded by dotted lines) in Eqs. (8.2) and (8.3). At weak coupling, we observe a decaying mode in the continuum (long-dashed line) with near-entrance behaviour depending on the DOS. For strong interactions, a quasiparticle $|\psi_k^*\rangle$ is pushed out with weight $Z_k = |\langle\psi_k|\psi_k^*\rangle|^2$ approaching $1/2$. (b) A paramagnet (PM) and Ising ferromagnet (FM). By coupling the two chains, a magnon can decay into two domain walls. (c) The numerically-determined dynamic structure factor for the Ising ladder. Flat dashed line is bare magnon and shaded region (dotted lines) denotes two-domain-wall continuum. At weak coupling, the magnon decays. At strong coupling, the magnon is pushed below the continuum.

If $\nu(E)$ does not have finite support but instead decays as $\nu(E) \sim a/E^\beta$ with $\beta > 0$ as $E \to +\infty$, then by the theory of Stieltjes transforms [271]

$$g(E) \sim_{E\to-\infty} \begin{cases} -b/|E|^{\min(1,\beta)} & \text{if } 0 < \beta \neq 1 \\ b(\ln|E|)/E & \text{if } \beta = 1 \end{cases} \qquad (b > 0). \tag{8.5}$$

From these asymptotics, we obtain

$$\lim_{|\gamma|\to\infty} Z = \begin{cases} 1/2 & \text{if } \beta \geq 1, \\ 1/(1+\beta) & \text{if } 0 < \beta < 1. \end{cases} \tag{8.6}$$

Note that this is lower bounded by $1/2$. For example, for $\nu(E) \propto 1/\sqrt{E}$, we obtain $Z \to 2/3$ as $|\gamma| \to \infty$.

The spectral weight and onset of DOS

The exactly solvable model defined in Eqs. (8.2) and (8.3) allows us to derive more than just the existence of the quasiparticle and its weight. It gives us access to the full spectral weight of the bare state $|\psi\rangle$ on the excited states, i.e., $\mathcal{A}(E) := \sum_n |\langle\psi|n\rangle|^2\, \delta(E-E_n)$. This is representative of what inelastic neutron scattering would measure. Using the identity $\mathcal{A}(E) = \frac{1}{\pi}\mathrm{Im}G(E-i0^+)$, a straightforward calculation—detailed in Appendix F.1—gives[3]

$$\mathcal{A}(E) = \begin{cases} \frac{1}{\pi}\frac{\Gamma(E)}{(E-E_b-\gamma^2 g(E))^2+\Gamma(E)^2} & \text{if } \nu(E) \neq 0, \\ \delta(E-E_b-\gamma^2 g(E)) & \text{if } \nu(E) = 0, \end{cases} \tag{8.7}$$

[3]For $g(E)$ to be well-defined in the continuum, one has to interpret its definition $g(E) \equiv \int \frac{\nu(\varepsilon)}{E-\varepsilon}\mathrm{d}\varepsilon$ as a *Cauchy principal value.*

where $\Gamma(E) \equiv \gamma^2 \pi \nu(E)$. Within the continuum (i.e., $\nu(E) \neq 0$), Eq. (8.7) can qualitatively be interpreted as a Lorentzian with an energy-dependent width $2\Gamma(E)$, and an energy-dependent mean $E_b + \gamma^2 g(E)$. Note that the width $2\Gamma(E) = 2\pi \times \gamma^2 \times \nu(E)$ is what one would expect from Fermi's golden rule.

In Fig. 8.2(a), we plot this spectral weight for two illustrative cases: the left (right) column has a discontinuous (continuous) onset of the DOS of the continuum. Such a (dis)continuity can—roughly speaking—be associated to dimensionality. For instance, the two-particle continuum of non-interacting particles with a parabolic dispersion has as its onset $\nu(E_{th} + \delta E) \sim (\delta E)^{D/2-1}$ in D spatial dimensions; note that this is discontinuous in one and two dimensions. We take $D = 1$ ($D = 3$) in the left (right) column of Fig. 8.2(a); see Appendix F.1 for details on how these plots are obtained.

Let us first discuss weak coupling γ. In Fig. 8.2(a) we see that the quasiparticle straightforwardly enters the continuum and decays if the onset of the continuum is soft. In the case where the DOS has a discontinuous onset, we see a different behavior. For our particular model, the state cannot enter the continuum at all [270]. Indeed, we have already remarked that if $\nu(0^+) \neq 0$, then there is a pole outside the continuum for any nonzero value of $\gamma \neq 0$. Instead, its spectral weight Z is transferred into a decaying mode in the continuum. Detecting the *residual* quasiparticle requires very sensitive and high resolution measurements (e.g., neutron spin echo spectroscopy), see Section 8.3. This singular behaviour may be regularized in a more complete model, allowing the state to terminate [74], which need not affect Fig. 8.2(a) (top left) at the resolution shown.

The main focus of the present work is on large coupling γ, where we find that the quasiparticle re-emerges, independent of the details of the DOS (bottom panels of Fig. 8.2(a)). This is accompanied by the weight $Z \to 1/2$, in agreement with our general claim.

The conditions for avoided decay

How widely applicable is this mechanism of avoided quasiparticle decay? Note that the fact we assumed γ to be independent of α is not important, since in the full solution, γ^2 and the DOS always appear together. For example, in a system with $SO(3)$ spin-symmetry, the coupling constant vanishes near the threshold as $\gamma(E_{th} + \delta E) \sim \sqrt{\delta E}$ [272]. This leads to a different power of the onset of $\gamma^2 \nu(E)$, which amounts to shifting the effective dimensionality $D \to D + 2$. Similarly, one could effectively include direct interactions *within* the continuum by using a renormalised DOS.

There are, however, two essential implicit assumptions. Firstly, we presume that there is space below the continuum to be repelled into. This is not applicable to, for example, Fermi liquids, where the continuum starts directly above the ground state energy over an *extended* region in momentum space. Second, the model does not actually treat the situation where the continuum is made of the *same* quasiparticles that it repels—making it exactly solvable. This should be a good approximation if the quasiparticle trying to enter the continuum has its momentum $\boldsymbol{k}$ well-separated from those quasiparticles whose momenta $\boldsymbol{q}$ and $\boldsymbol{k} - \boldsymbol{q}$ make up the continuum at that point. As discussed below, this turns out to be the case in the TLHAF.

8.1.3. Confirmation in a tunable Ising ladder

Before considering the challenging TLHAF, we verify our predictions in a tunable, yet *numerically* tractable, fully many-body quantum system. This consists of two spin-$\frac{1}{2}$ chains: one a perfect paramagnet in a field, $\hat{H}_0^{(A)} = -3 \sum_n \hat{S}^z_{A,n}$, the other an ordered quantum Ising ferromagnet, $\hat{H}_0^{(B)} = -\sum_n \left(4J \hat{S}^x_{B,n} \hat{S}^x_{B,n+1} + 2g \hat{S}^z_{B,n} \right)$ (with $J > g > 0$). The ground state of the paramagnet has all spins pointing up; a flipped spin is a

dispersionless magnon. The ferromagnet is ordered along the x-direction, with freely moving domain wall quasiparticles. Inter-chain coupling can allow the magnon to decay into a pair of domain walls, illustrated in Fig. 8.2(b); for this, consider the interaction $H_{\text{int}} = 4\gamma \sum_n \hat{S}^x_{A,n} \hat{S}^z_{B,n}$.

In Fig. 8.2(c), we plot the dynamical spin structure factor

$$\mathcal{S}^{xx}(k,\omega) = \frac{1}{2\pi} \int \langle 0|\hat{\sigma}^x_{A,-k}(t)\hat{\sigma}^x_{A,k}(0)|0\rangle e^{i\omega t} \mathrm{d}t = \sum_n \delta(\omega - \omega_n) |\langle n|\hat{\sigma}^x_{A,k}|0\rangle|^2. \tag{8.8}$$

The dynamical spin-spin correlations were obtained using the methods in Chapter 5 (in the simpler one-dimensional setting). We found that a timestep truncation of $dt = 0.1$ and a low bond dimension of $\chi = 30$ was enough to achieve converged results; the effective broadening (discussed in subsection 5.2.4) is $\sigma_\omega = 0.055$ in the units shown in Fig. 8.2(c). In the top panel, we take $g_B = 0.5$ and $J_B = 1$ and set the coupling to a relatively small value, $\gamma = 0.3$. The continuum is determined by numerically extracting the dispersion of a single domain wall and subsequently calculating the kinematic two-domain-wall continuum. We observe that the magnon decays in this weakly-interacting case.

The bottom panel of Fig. 8.2(c) is for the strongly-interacting case. However, ramping up the coupling strength γ effectively renormalizes the parameters of the Ising chain. This is because $\hat{H}_{\text{int}}$ is not *purely* an interaction term: it contains an $\hat{S}^z_B$ on the ordered chain, which attempts to condense the domain walls and cause a phase transition. To prevent this, whilst increasing γ we also change the parameters J_B and g_B such that the location of the continuum (shaded region in Fig. 8.2(c)) remains *roughly* unchanged. Thus, for the bottom panel, we arrive at $g_B = 0.9$, $J = 3$ and $\gamma = 3.4$. Crucially, as advertised, strong interactions prevent quasiparticle decay: the magnon re-emerges from the continuum unscathed.

8.2. Avoided decay in the triangular-lattice Heisenberg antiferromagnet

We now turn to the paradigmatic spin-1/2 TLHAF, which describes a wide range of frustrated quantum spin materials (see Ref. [273] for a recent overview). Its ground state is ordered, with neighboring spins forming a 120° angle [186, 187]. However, away from the lowest energies [75], the status of its magnon excitations remains unsettled due to the uncontrolled nature of the available analytic and numerical methods [75, 76, 188, 191]. The most venerable of these is perhaps spin wave theory (SWT), an expansion in inverse spin, $1/S$. The precise Hamiltonian we consider is

$$\hat{H} = J \sum_{\langle \boldsymbol{n},\boldsymbol{m}\rangle} \left((1-\delta)\ \hat{\boldsymbol{S}}_{\boldsymbol{n}} \cdot \hat{\boldsymbol{S}}_{\boldsymbol{m}} - \frac{\delta}{2}\ \hat{S}^{\text{loc},z}_{\boldsymbol{n}} \hat{S}^{\text{loc},z}_{\boldsymbol{m}} \right) \tag{8.9}$$

where a small easy-axis anisotropy ($\delta = 0.05$) slightly gaps out the three[4] massless Goldstone modes, making the model more numerically tractable. Here, $\hat{\boldsymbol{S}}^{\text{loc}}_{\boldsymbol{n}}$ is the spin in the basis of the rotating (local) frame.

8.2.1. Spin wave prediction and avoided decay

Spin wave theory predicts magnon decay [75] over a large region of momentum space. This has been studied in detail for the isotropic model ($\delta = 0$) [75], but it remains true for $\delta = 0.05$. In particular, the shaded region in the inset of Fig. 8.3(a) shows where

[4] We have one Goldstone mode for every broken generator of $SU(2)$ [71].

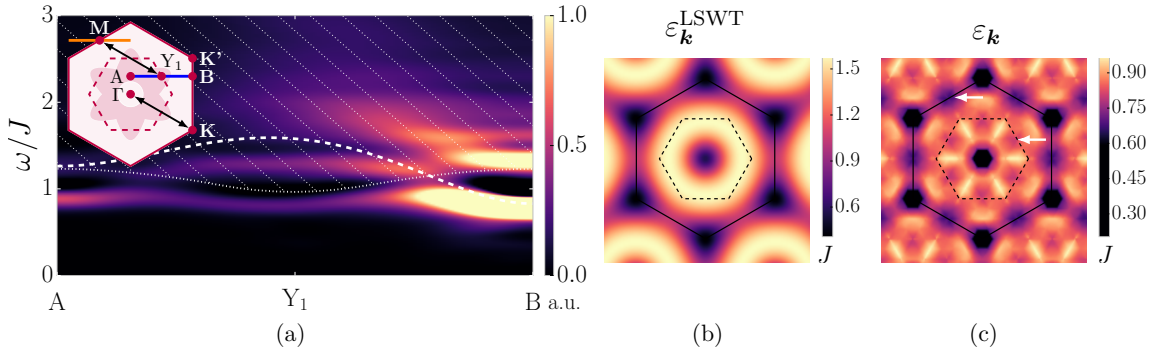

(a) (b) (c)

Figure 8.3.: **Avoided decay in the spin-$\frac{1}{2}$ TLHAF with $\delta = 0.05$.** (a) Inset: the Brillouin zone; the dashed line delineates the *magnetic* BZ. LSWT predicts magnon decay in the shaded region, dominated by $\boldsymbol{q} \to (\boldsymbol{q}-\mathrm{K})+\mathrm{K}$. The black arrow illustrates that $\mathrm{Y}_1 = \mathrm{M} + \mathrm{K}$; hence decay is possible if $\varepsilon_{\mathrm{Y}_1} > \varepsilon_{\mathrm{M}} + \varepsilon_{\mathrm{K}}$. Main panel: the out-of-plane dynamical spin structure factor along the blue line in the inset. The dotted line represents the two-magnon states consisting of a magnon along the orange line (inset) and a K-magnon. The dashed line is the magnon dispersion from LSWT. We see avoided decay, where the level-continuum repulsion induces a local minimum near Y_1. (b) LSWT prediction for the dispersion relation. (c) The numerically-obtained dispersion is most heavily renormalized where LSWT predicts decay (see inset of (a)). The local minimum at M induces a local minimum at Y_1 (white arrows).

linear SWT (LSWT) predicts decay for this value of δ. A magnon with momentum $\boldsymbol{k}$ is then predicted to decay into two magnons with momenta $\boldsymbol{q}$ and $\boldsymbol{k}-\boldsymbol{q}$, where $\boldsymbol{q} \approx \mathrm{K}$, the corner of the Brillouin zone (BZ). However, small spin and noncollinear order—breaking all symmetries and thus allowing for many interaction terms—generate strong quantum interactions. Our mechanism thus suggests an alternative to the expected scenario of magnon decay.

In Fig. 8.3(a), we consider the out-of-plane dynamical spin structure factor $\mathcal{S}^{yy}(\boldsymbol{k},\omega) = \frac{1}{2\pi}\int\langle 0|\hat{\sigma}^y_{-\boldsymbol{k}}(t)\hat{\sigma}^y_{\boldsymbol{k}}(0)|0\rangle e^{i\omega t}\mathrm{d}t$, taking the 120° order to be in the xz-plane. This was obtained using the methods in Chapter 5; for numerical aspects, see subsection 8.2.3. The momentum axis is along the A–B line (blue line in inset). Since SWT predicts decay into a K-magnon, the dotted line shows the numerically obtained two-magnon energy $\varepsilon_{\boldsymbol{q}} + \varepsilon_K$, with $\boldsymbol{q}$ along the orange line in the inset. For comparison, the dashed curve is the SWT prediction of the magnon in the non-interacting limit $1/S \to 0$ (LSWT), which travels deep into the two-magnon continuum. We observe that the numerically obtained $S = 1/2$ dispersion is pushed out completely—a crisp instance of avoided magnon decay.

8.2.2. Roton minima and interaction-induced symmetry

The magnon dispersion is known to have a local minimum at the midpoint M of the BZ edge. This appears at higher order in SWT and in series expansion methods [75, 188, 191] and is confirmed in Fig. 8.3(c). Our *novel* prediction is that the avoided decay must in turn induce a local minimum at the midpoint Y_1 of the *magnetic* BZ (MBZ) edge. This is apparent in Fig. 8.3(a,c). More precisely, absence of magnon decay implies the strong constraint[5] $|\varepsilon_{\mathrm{M}} - \varepsilon_{\mathrm{Y}_1}| \leq \varepsilon_{\mathrm{K}}$, which we find to be satisfied in our numerics—and in

[5]The decay process $\boldsymbol{k} \to \mathrm{K} + (\boldsymbol{k}-\mathrm{K})$ accounts for the *complete* decay region (as predicted by LSWT) only at the isotropic point. For $\delta \neq 0$, this process represents the core of the decay region, which is slightly extended by considering $\boldsymbol{k} \to \boldsymbol{q} + (\boldsymbol{k}-\boldsymbol{q})$ with $\boldsymbol{q} \approx \mathrm{K}$. Hence, the minimum predicted by the

disagreement with SWT.

More generally, at the isotropic point $\delta = 0$, absence of decay is *equivalent* to the magnon dispersion $\varepsilon_{\boldsymbol{k}}$ being periodic with respect to the magnetic BZ—which is three times smaller than the original BZ. (This is a direct consequence from the fact that $\varepsilon_{\mathrm{K}} = 0$ for $\delta = 0$.) This powerful criterion might help to figure out the extent of (avoided) decay at the isotropic point, be it using numerical or experimental methods.

8.2.3. Numerical aspects

Circumference

The data in Fig. 8.3 is for a cylinder with circumference $L_{\mathrm{circ}} = 6$, taking the periodic direction to be along one of the primitive vectors. We have checked that whilst the multimagnon continuum still has a dependence on L_{circ}, the single-magnon dispersion is better converged in L_{circ}—at least for the middle- and high-energy modes of interest. Appendix F.2.2 presents a study of the L_{circ}-dependence.

Bond dimension

Due to the absence of continuous symmetry in the ground state, the large coordination number of the lattice, and the fact that the isotropic point has *three* Goldstone modes, it is numerically challenging to time-evolve this highly-entangled state. For this reason we are limited in the bond dimensions that we can reach: $\chi = 450$ for long-time dynamics necessary for resolving high-energy modes, and $\chi = 800$ for short-time dynamics for low-energy modes.

More precisely, the numerical parameters for Fig. 8.3(a) correspond to a timestep truncation $dt = 0.05J$, a bond dimension $\chi = 450$, and an effective gaussian broadening with $\sigma = 0.077J$. The dotted line in Fig. 8.3(a) is the sum $\varepsilon_{\boldsymbol{q}} + \varepsilon_{\mathrm{K}}$, where $\boldsymbol{q}$ is along the orange line in the inset. Here $\varepsilon_{\boldsymbol{q}}$ was obtained by tracing the peak of the spectral function along that slice, whereas ε_{K} is a low-energy feature which could not be resolved with the bond dimension $\chi = 450$. Instead, we went up to $\chi = 800$, limiting the time-window we could obtain, leading to a larger effective broadening. However, since the low-energy mode is well-separated from other (relevant) modes, one can still reliably extract the energy from a broad response. From a scaling in bond dimension, we then obtained $\varepsilon_{\mathrm{K}} \approx 0.3J$ for the value $\delta = 0.05$. This is markedly lower than the LSWT prediction, $\varepsilon_{\mathrm{K}}^{\mathrm{LSWT}} \approx 0.41J$. For a detailed study of the convergence in bond dimension, see Appendix F.2.1.

Obtaining a two-dimensional dispersion

The magnon dispersion in Fig. 8.3(c) was obtained by tracing the low-energy peak of the spectral function—having verified that the magnon branch was resolved enough for this to be sensible. At low energies, this was supplemented by the aforementioned approach where we could go up to $\chi = 800$. Due to the cylindrical geometry on which our method is based, the dispersion we obtain is continuous along one direction, and discrete along the other. We then superimposed the momentum cuts along three different orientations and subsequently interpolated this to the full two-dimensional Brillouin zone. The fact that where these cuts intersected, they agreed, is a confirmation that the circumference $L_{\mathrm{circ}} = 6$ is large enough for the single-magnon dispersion to resemble the true two-dimensional result. As a sanity check for our interpolation method, we have verified that it gives the correct result when applied to the LSWT dispersion.

principle of avoided decay is only precisely at Y_1 at the isotropic point. Indeed, in Fig. 8.3(c) one can see that the minimum (for $\delta = 0.05$) has been slightly shifted inward.

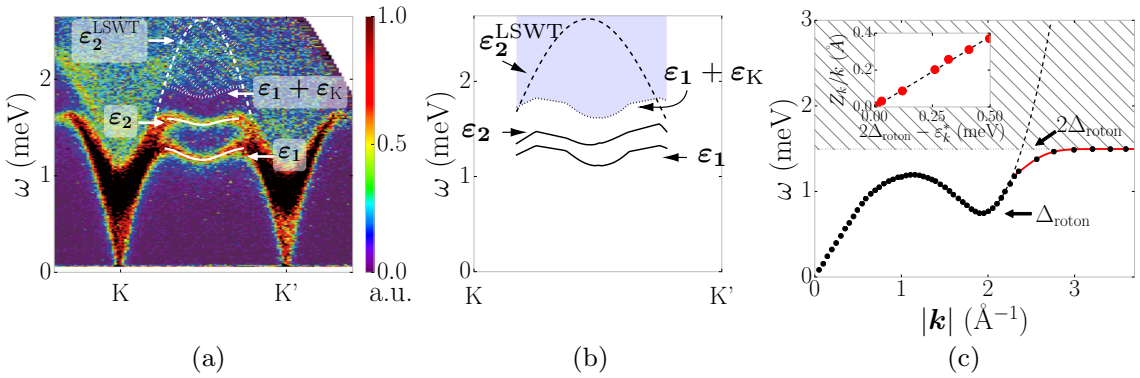

Figure 8.4.: **Avoided quasiparticle decay and level-continuum repulsion in experimental data: the triangular lattice magnet $Ba_3CoSb_2O_9$ and superfluid helium.** (a) Inelastic neutron scattering data and LSWT comparison for $Ba_3CoSb_2O_9$ [77]. The neutron data picks up all magnon bands related by momentum K; the lower branch (ε_1) goes through M, the higher branch (ε_2) through Y_1 (see Fig. 8.3 for BZ labeling). Similar to Fig. 8.3, magnon decay is avoided, with the local minimum near M inducing a local minimum near Y_1. (b) For comparison, we show the numerically obtained dispersion for model (8.9) with $\delta = 0.05$, taking $J = 1.67$ meV as in Ref. [77] and including bands related by momentum K. We stress that this Hamiltonian does *not* directly model the experiment: the former (latter) has a small easy-axis (easy-plane) anisotropy. (c) Black dots are the phonon-roton dispersion of superfluid helium extracted from Refs. [79, 80]; inset shows single-particle weight extracted from Refs. [81, 82]. Our solvable model implies that the level approaches the continuum exponentially in the bare level (red line). Moreover, the weight is predicted to go to zero proportional to the level approaching the continuum, confirmed in the inset.

8.3. Avoided decay in experiment

Quasiparticle *decay* has been observed in experiment, e.g., in two-dimensional piperazinium hexachlorodicuprate (PHCC) [265]. More recently, aspects of *level-continuum repulsion* have been reported in the gapped spin-orbit-coupled frustrated magnet $BiCu_2PO_6$ [274]: the quasiparticle still decays, but its near-entrance behavior is similar to what we observed in the top left panel of Fig. 8.2(a). This nicely fits our theoretical framework: the one-dimensional nature of $BiCu_2PO_6$ suggests a sharp discontinuous onset of the bare two-magnon DOS, preventing a smooth quasiparticle entry into the continuum. In contrast, PHCC is spin-rotation symmetric, such that our earlier argument implies that the DOS should have a soft onset, consistent with the smooth entry observed in Ref. [265].

More strikingly, we claim that the phenomenology of *avoided decay* has been observed in recent experiments on $Ba_3CoSb_2O_9$ [77]. We turn to this now, after which apply our toy model to gain insights into liquid helium.

8.3.1. $Ba_3CoSb_2O_9$

The magnetic material $Ba_3CoSb_2O_9$ is well-described by the TLHAF with a small easy-plane anisotropy, for which Fig 8.4(a) shows[6] recent inelastic neutron scattering data [77].

[6] In the experiment [77], K' was taken in the second BZ (which differs from the other choice by a reciprocal lattice vector). This difference has no bearing on the bands one picks up, so for our purposes this distinction is irrelevant. It does, however, affect the precise value of the intensity. This explains why

Since this is sensitive to the *full* dynamical spin structure factor, it picks up copies of the magnon dispersion translated by K. Fig. 8.4(a) thus shows *two* bands[7]: the bottom one (ε_1) centered at M, the top one (ε_2) centered at Y_1. Neither decay and both exhibit a local minimum, in agreement with the phenomenology of Fig. 8.3. For comparison, Fig. 8.4(b) shows the numerically obtained data for model (8.9) along the same momentum cut (i.e., this is the same data contained in Fig. 8.3). We can thus directly reinterpret apparently unrelated experimental features as being linked by avoided quasiparticle decay.

It is worth emphasizing that $Ba_3CoSb_2O_9$ has an easy-*plane* anisotropy, whereas the model we studied numerically has an easy-*axis* anisotropy (see Eq. (8.9)). Hence, the similarity between Fig. 8.4(a) and (b) illustrates that the phenomenon of avoided decay is robust, i.e., it is not sensitive to small perturbations. Of course, the difference between an easy-plane and easy-axis anisotropy would affect low-energy properties.

In contrast, magnon decay *has* experimentally been observed in a spin-2 TLHAF [267]. This is consistent with $1/S$ being a measure of interaction strength—and avoided decay requiring strong interactions.

8.3.2. Superfluid helium

Lastly, we consider the iconic quasiparticle dispersion of superfluid helium, Fig. 8.4(d). While it was originally thought that the quasiparticle would enter the two-roton continuum [74], it is now known that the dispersion instead flattens off. This is consistent with the discontinuous onset of the two-roton DOS [78, 83]. Here, we add quantitative insights into how the quasiparticle approaches the continuum. This serves as a demonstration of how the toy model in Eqs. (8.2) and (8.3) can be used to obtain insights into experimental results—even allowing to extract effective interaction strengths.

Approach to the continuum: quasiparticle energy and weight

We will work in variables which measure energy relative to the onset of the two-roton continuum, i.e., $E = \omega - 2\Delta_{\text{roton}}$. The two-roton DOS $\nu(E)$ has a jump discontinuity $\nu(0^+) \equiv \nu_0 \neq 0$. We derive this in Appendix F.3, which moreover shows that this jump is momentum-dependent, i.e., $\nu_0 = \tilde{\nu}_0/|\boldsymbol{k}| = \tilde{\nu}_0/k$. This momentum-dependence is not really noticeable in the following formulas, and one may approximate it by $\nu_0 = \tilde{\nu}_0/k_{\text{roton}}$. However, we will include it for completeness.

Let us recall that in subsection 8.1.2 we derived that $E^* = E_b + \gamma^2 g(E)$ with $g(E) = \int \frac{\nu(\varepsilon)}{E-\varepsilon} \mathrm{d}\varepsilon$. Given the aforementioned jump discontinuity, we obtain that near the onset $g(E) \approx \nu_0 \ln(-E) + \text{cst}$. If we focus on $E^* \approx 0$, we arrive at the condition $0 \approx E_b + \gamma^2 g(E^*)$, or equivalently, $E^* \propto \exp\left(-\frac{E_b}{\gamma^2 \nu_0}\right)$. The renormalized energy E^* is predicted to approach the continuum exponentially in the bare energy E_b. Moreover, in subsection 8.1.2 we obtained that the spectral weight on the quasiparticle is given by $Z^{-1} = 1 - \gamma^2 g'(E^*)$. This straightforwardly gives us $Z \approx -\frac{E^*}{\nu_0 \gamma^2}$ for small E^*, i.e., the weight is proportional to the distance to the continuum.

In conclusion, we arrive at the following predictions for the quasiparticle dispersion ε_k and weight Z_k near the continuum:

$$\varepsilon_k \approx 2\Delta_{\text{roton}} - \alpha e^{-a\, k\, \varepsilon_b} \qquad \text{and} \qquad Z_k \approx b\, k\, (2\Delta_{\text{roton}} - \varepsilon_k). \tag{8.10}$$

The fitting parameters a and b give us a measure of the effective (inverse) coupling strength. In fact, the above derivations suggest that $a = b$, but it does not make sense to expect

Fig. 8.4(a) is not left-right symmetric.

[7] In fact, there are *three* bands, but two overlap (in this resolution). Similarly, Fig. 8.4(b) should also show the left-right-inverted version of ε_2, which is left out in order to not overly complicate the figure.

this for the experimental data, as the weight Z_k extracted in that setting is usually only defined up to a global multiplicative factor.

The high-quality data of Refs. [79–82] allows us to extract the information to test these predicted functional forms. The dispersion relation was straightforwardly obtained from Refs. [79, 80] and is plotted in the main panel of Fig. 8.4(a). The weight, however, is more subtle: Refs. [81, 82] showed the data as a function of momentum, which we extracted and interpolated. We then evaluated this interpolated function at the same momenta for which Refs. [79, 80] quoted values for the energy. This allowed us to plot Z as a function of energy in the inset of Fig. 8.4(c). The predicted functional forms for ε_k and Z_k are confirmed in Fig. 8.4. In both cases, we find that $a_{\text{fit}}\, k_{\text{roton}}$ and $b_{\text{fit}}\, k_{\text{roton}}$ are comparable to the (inverse) bandwidth, in testament to the strong interactions.

A general relationship from the Hellmann-Feynman theorem

The above predictions in Eq. (8.10) satisfy an interesting property: $\mathrm{d}\varepsilon_k/\mathrm{d}\varepsilon_b = Z$ (remember that $a = b$). This is in fact a *general* relationship that holds for the model in Eqs. (8.2) and (8.3). This is easily proven:

$$\frac{\mathrm{d}E^*}{\mathrm{d}E_b} = \frac{\mathrm{d}}{\mathrm{d}E_b}\langle\psi^*|\hat{H}|\psi^*\rangle = \langle\psi^*|\frac{\mathrm{d}\hat{H}}{\mathrm{d}E_b}|\psi^*\rangle = \langle\psi^*|\psi\rangle\langle\psi|\psi^*\rangle = Z. \tag{8.11}$$

We have used the Hellmann-Feynman theorem to move the derivative inside, and from Eq. (8.2) we obtained that $\frac{\mathrm{d}\hat{H}}{\mathrm{d}E_b} = |\psi\rangle\langle\psi|$. Whilst this derivation is surprisingly simple, it is physically quite remarkable to have such a direct relationship between the dispersion and spectral weight of a quasiparticle.

We thus see that our simple toy model gives new insights into the well-studied physics of superfluid helium. Quasiparticle decay is of course inevitable, given that the bare dispersion goes arbitrarily deep into the continuum. Nevertheless, the principle of a continuum being able to push on a quasiparticle is evidenced by the persistence of the roton dispersion, whilst weight is slowly siphoned into a decaying mode in the continuum. More than just being a qualitative observation, this shows that one can—at least in principle—extract effective quasiparticle interaction strengths from such highly-resolved experimental data. It would be worthwhile to explore this quantitative aspect of our theory more systematically, especially in a tunable experimental setting. For instance, it would be interesting to explicitly break the aforementioned $SO(3)$ symmetry in PHCC and measure whether the triplon's entry into the continuum is considerably altered.

9. Conclusions and outlook

In Part I of this thesis, we showed how critical chains can still be topologically non-trivial, exhibiting localized edge modes protected by topological invariants. We elucidated this by providing novel instances as well as an overarching framework. Part II focused on the properties of excitations above ground states. To this end, we introduced a novel matrix-product-state-based method for obtaining the spectral functions of two-dimensional systems. Using the latter for quantum spin models on the honeycomb, square and triangular lattices, we uncovered new robust phenomenology of such excitations, including proximate spin liquids and avoided quasiparticle decay.

In this concluding chapter, we highlight some of the key insights of this thesis, emphasizing the remaining open questions and how we might move forward.

9.1. Topological critical points between non-trivial phases

The critical points studied in Part I of this thesis were only topologically non-trivial when all neighboring gapped phases were themselves non-trivial (i.e., either topological or symmetry-breaking). Indeed, the topology at criticality can be interpreted as a residue of that of the non-triviality of the neighboring phases. Conversely, the topological edge modes remain well-defined upon opening up a bulk gap and hence do not require fine-tuning to exist[1]. In other words, these critical points are topological *despite* being gapless. This is in stark contrast to topological semi-metals, which are only topologically non-trivial *because* they are gapless—their lower-dimensional topological invariants measure the fact that the gapless point (or nodal line or surface) is a source of topological flux [64, 65, 275, 276]. Consequently, the localized edge modes of topological semi-metals disappear when the bulk is gapped out.

The transitions between such topological and symmetry-breaking phases of matter is virgin territory beyond one spatial dimension. As discussed in Part I, there are a multitude of one-dimensional examples, which we largely unified in Chapter 4. It would be very interesting to explore higher-dimensional analogues. The only examples of transitions between a two-dimensional symmetry-breaking and symmetry-protected topological (SPT) phase of matter of which I am aware, are Refs. [52, 277–279]. Encouragingly, they find exotic edge modes in addition to the expected bulk criticality; however, a framework is missing. Much remains to be explored, especially since in two dimensions, some of the neighboring gapped phases can have intrinsic topological order. Before attempting to find a unifying framework in higher dimensions, it is paramount to propose and explore concrete models, which will undoubtedly lead to a rich phenomenology. For instance, a preliminary study of transitions between distinct integer quantum Hall plateaus suggests that chiral edge modes survive at criticality—this will be explored in future work.

Even in the one-dimensional setting there are still a variety of open questions. We have given a partial classification of symmetry-enriched conformal field theories, and it is natural to continue this program. A complementary approach would be to identify this symmetry-enrichment in tensor networks, such as infinite-dimensional matrix product states [280] or the multi-scale entanglement renormalization ansatz (MERA) [281]; in particular, a

[1] As we have seen, the edge mode might have a different interpretation upon opening up a gap, e.g., toggling between cat states of bulk symmetry-breaking phases.

classification of symmetric MERAs is desirable [282, 283]. More phenomenologically, one can ask whether there exist topologically non-trivial critical points which cannot be made topologically trivial by a finite-depth local unitary—unlike all examples in Part I. A more practical question is what the use of symmetry-enriched quantum criticality might be. One appealing aspect is that it allows one to track localized quantum information across a bulk quantum phase transition; e.g., the edge qubit of a bosonic SPT phase can be smoothly connected to the edge magnetization of an Ising phase, unharmed by the bulk passing through an Ising critical point.

9.2. An interpretation of proximate spin liquids

In Chapter 6, we observed broad high-energy spectral features akin to those of a spin liquid despite the ground state being conventionally ordered. This constitutes the first clear-cut realization of a *proximate spin liquid* in a theoretical model. This phenomenology can be useful as an indicator of there being a nearby spin liquid in the phase diagram, which one might be able to tune into. Indeed, a proximate spin liquid was experimentally observed in α-$RuCl_3$ [96, 97, 180] and subsequent studies implied that a spin liquid phase can be stabilized by tuning a magnetic field [213, 221–225].

Nevertheless, it is still unclear what the physical interpretation of such a proximate spin liquid might be. In particular, can these high-energy features be interpreted in terms of quasiparticles? If so, are they an indication that there are nearly-deconfined anyons? If the latter is correct, it would suggest that at some finer resolution, the continuum might be revealed to consist of a dense set of bound states. Of course, it is a priori not even a given that there is a simple or straightforward interpretation of high-energy features in strongly-coupled quantum magnets.

To elucidate these finer points of a proximate spin liquid, it could be useful to study the *anisotropic* Kitaev model (with Ising or Heisenberg perturbations), where there is a large separation in energy scale between the low-energy fluxes (whose condensation drives the transition) and the high-energy Majoranas—the latter are even projected out in the infinite-anisotropy limit, recovering the toric code model. Using the toric code limit as a perturbative starting point might even allow for an analytic approach to this phenomenon.

9.3. A theory of quasiparticles at finite energies

A key message of this thesis is that quasiparticles can still have *generic* or *robust* properties at finite energies (but zero energy density). The lack of knowledge of such properties is more likely due to the absence of reliable analytical and numerical methods for their study, rather than the absence of the properties themselves. Indeed, the *universal* arguments which are valid in the low-energy regime—involving such powerful concepts like the renormalization group—do not directly apply. Instead, in this thesis, we used the novel numerical method introduced in Chapter 5 to uncover robust properties of finite-energy excitations[2]. As an illustration, let us highlight three novel but simple mechanisms which have a broad application to models old and new:

1. **Generic roton modes from intersecting flat directions.** For the isotropic Heisenberg models on the square and triangular lattice as considered in Chapters 7 and 8, linear spin wave theory (LSWT) predicts a one-dimensional subset of the Brillouin zone along which magnons are dispersionless. Nevertheless, the true dispersion was found to have a minimum at the middle of the Brillouin zone boundaries. In both

[2] Of course, once a new phenomenon is uncovered using a numerical tool, it can sometimes be explained and underpinned using a simple analytic understanding; Chapter 8 is an illustration of this.

cases, this is where the predicted flat directions intersect. Hence, the LSWT dispersion can be locally approximated by a flat plane. This means that the multi-magnon continuum at these points has an enhanced density of states[3] (DOS). A larger DOS implies a bigger repulsion, naturally explaining the observed roton minimum.

2. **Avoided quasiparticle decay from strong interactions.** This principle is the focus of Chapter 8, so we will not dwell on it here. Let us simply remark that if the aforementioned mechanism naturally explains that flat directions in LSWT lead to local minima—which we may dub *roton modes of the first kind*—then avoided decay can naturally explain *roton modes of the second kind*. By the latter, we refer to the scenario where the shape of the onset of the multi-magnon continuum is determined by a roton of the first kind, such that if a non-interacting magnon inside this continuum is to avoid decay, its shape must mimic this local minimum. We observed this feature in Chapter 8 in both numerical as well as experimental data[4].

3. **Interaction-induced symmetry.** Strong interactions can enhance the symmetries of a quasiparticle dispersion relation. For example, in Chapter 8 we noted how the absence of decay in the *isotropic* triangular lattice Heisenberg antiferromagnet (TLHAF) is equivalent to the quasiparticle dispersion relation being periodic with respect to the thrice-smaller[5] *magnetic* Brillouin zone. We do not claim complete absence of decay in the isotropic model, but the degree to which decay is avoided is directly correlated with an approximate enhanced symmetry (this can already be seen by comparing Figs. 8.3(b) and (c)). Standard mechanisms for emergent symmetries rely on the renormalization group. This mechanism is entirely different, and it would be interesting to explore it further, e.g., in one-dimensional settings.

These are by no means the only mechanisms identified and discussed in this thesis[6]. They serve to show that even in strongly-interacting low-dimensional quantum matter, the excitations at finite energies need not be unstructured.

The above mechanisms are new, which naturally begs the question: what else might have been thus far overlooked? One concrete open question is to better understand the substructure in the multi-magnon continuum of strongly-interacting magnets. In particular, we do not yet understand the curious features in the continuum of the TLHAF, shown in Fig. 8.3(a). In fact, it is not even clear whether this is a true two-dimensional phenomenon, or whether it is an artifact of our cylinder method. Note that this is different for the single-magnon dispersion, whose convergence we could confirm, which was sufficient for the purposes of confirming the avoided magnon decay.

9.4. Avoided quasiparticle decay in experiment

In Chapter 8, we also identified the novel principle of avoided quasiparticle decay in existing experimental data. For the triangular lattice material $Ba_3CoSb_2O_9$ [77], this merely served a qualitative role, explaining the appearance of a seemingly-puzzling local minimum of the magnon dispersion relation. The most promising application of the principle of avoided decay, however, was for superfluid helium [79–82], showcasing that one can in principle extract effective coupling strengths by fitting quasiparticle dispersions and weights. To

[3] For both the square and triangular lattices, the predicted three- and two- magnon continuum at the zone boundary start at the one-magnon band by adding gapless Goldstone modes with zero momentum.

[4] In particular, in the inelastic neutron scattering data for $Ba_3CoSb_2O_9$ [77] in Fig. 8.4(a), the bottom (top) band is a roton of the first (second) kind.

[5] The author is not aware of a connection to Hermes Trismegistus.

[6] For instance, there is the concept of proximate spin liquids, and the fact that high-energy magnons for isotropic models can retain some spatial localization similar to Ising-like models—see Chapter 7.

explore this further, one could apply this to theoretic models where one already has some handle on the effective coupling, such that this extraction method can be benchmarked. If this indeed turns out to be a reliable tool, then it can be used to determine effective physical models based on experimental data, even for strongly-interacting systems.

It would also be interesting to find an experimental realization where one can tune between decay and avoided decay. For quantum magnets, the inverse spin $1/S$ is a measure of the magnon coupling strength, but this cannot be tuned in experiment. Instead, one could use that symmetries constrain the functional form (and hence strength) of couplings; it is easier to tune the presence or absence of symmetries. As a concrete suggestion, consider the two-dimensional $SO(3)$-symmetric piperazinium hexachlorodicuprate (PHCC) [265]. The ground state preserves this symmetry, and its triplon quasiparticle has been observed to decay in the continuum. Its smooth entrance into the continuum is allowed since an $SO(3)$-symmetric coupling has to vanish at the onset of the continuum [272], such that $\gamma^2\nu(\varepsilon)$ is small (being the decay rate per Fermi's golden rule; see Chapter 8). If one explicitly breaks this $SO(3)$ symmetry, the two-dimensional nature of the material (implying a large density of states in the continuum) can show itself, preventing a smooth entrance into the continuum. Alternatively, decay can be tuned in ferromagnets with a magnetic field and a Dzyaloshinskii-Moriya interaction; this was recently proposed by McClarty and Rau in Ref. [284], although they did not explore the strongly-interacting regime.

9.5. Pushing the numerical frontier of spectral functions

Since the novel tool for obtaining the spectral function (see Chapter 5) was essential to uncovering the aforementioned properties, it is natural to ask: how can this method be improved and extended? Thus far, we have applied it to two-dimensional spin models. In principle, the same method can be used for (spinful) fermions such as in the Hubbard model. However, this requires a doubling of the on-site Hilbert space dimension, cutting the accessible circumferences in half. The largest circumference we have accessed in the spin models was $L_{\text{circ}} = 12$ in Chapter 6; hence, a Hubbard model with $L_{\text{circ}} = 6$ in a *gapped* phase could be possible. However, a natural intermediate step between bosonic and fermionic systems would be hole-doped magnets. Similarly, the most straightforward way of simulating finite-temperature properties—i.e., by using a purification—would require doubling the on-site Hilbert space dimension.

Putting systems on cylinders is a rather common operation for field theorists who use it to impose a finite temperature—the radius functions as an inverse temperature [285]. It is suggestive and exciting to explore whether this also applies to this lattice set-up[7]. If it is indeed the case that the ground state of a two-dimensional lattice model on a cylinder tells us about the physical properties of the *infinite* two-dimensional model at *finite* temperatures, then that would turn the cylinder geometry from a curse into a blessing. This is worth exploring. As a concrete suggestion, one could compare the finite-temperature phase diagram of the two-dimensional transverse-field Ising model (TFIM) to the ground state phase diagram of the TFIM on a cylinder with a variable radius.

Lastly, deciding whether a spectral function can be simulated using a finite bond dimension matrix product state—even in principle—is an interesting open question. This is equivalent to asking whether the entanglement generated by $e^{-iHt}\,\mathcal{O}\,|\text{ground state}\rangle$ (with $\mathcal{O}$ a local operator) is bounded or grows indefinitely. Interestingly, on first sight there seem to be conflicting field theoretic works answering this question for 1+1 dimensional conformal field theories. One work implies that the entanglement always converges to a finite value [206] whereas another claims that for a particular type of conformal field theories, it grows logarithmically at late times [208]. The progress of the numerical method is

[7] I thank Ryan Thorngren for suggesting this connection.

thus intimately linked with a better physical understanding of the entanglement generated by quasiparticles, which is an exciting question in and of itself.

9.6. Concluding remarks

The study of topological phases is by now a mature field of many-body physics, recognized by the Nobel Prize in 2016 [286]. Nevertheless, it still has many surprises in store—even in the one-dimensional setting, where one might have expected such matters to be done and dusted. There is little doubt that much is still to be explored concerning topological criticality in higher dimensions, a rich vein to tap into for years to come.

A more formidable blind spot in our view on many-body systems concerns the nature of excitations above highly-entangled ground states. However, as we have seen, tensor network methods are slowly shaping up to the task of making these features numerically accessible and the necessary high-resolution scattering experiments have become available. Hence, instead of having to guess what might happen, we can simply look through these new windows onto such spectral features—a surefire way of uncovering new quasiparticle phenomenology. Indeed, nature is well-known to be more original than physicists, so we might as well turn to her for inspiration.

A. Non-interacting fermions

A.1. Solving the translation invariant model with periodic boundary conditions

Let our Hamiltonian be given by $H = \sum t_\alpha H_\alpha$. Define $f(k) = \sum_\alpha t_\alpha e^{ik\alpha}$ and $\varepsilon_k, \varphi_k \in \mathbb{R}$ such that $f(k) = \varepsilon_k e^{i\varphi_k}$. One might choose to take $\varepsilon_k \geq 0$, but we do not require this. We now prove that a Bogoliubov rotation with angle φ_k diagonalizes the Hamiltonian, with single-particle spectrum ε_k, i.e.:

$$H = \sum_k \varepsilon_k \left(\frac{1}{2} - d_k^\dagger d_k\right) \qquad \text{where} \begin{pmatrix} d_k \\ d_{-k}^\dagger \end{pmatrix} = \exp\left(i\varphi_k \frac{\sigma^x}{2}\right) \begin{pmatrix} c_k \\ c_{-k}^\dagger \end{pmatrix}, \tag{A.1}$$

with $c_k = \frac{1}{\sqrt{L}} \sum e^{-ikn} c_n$. To see this, first consider the α-chain $H_\alpha = \frac{i}{2} \sum \tilde{\gamma}_n \gamma_{n+\alpha}$. In terms of the Fourier modes, one obtains

$$H_\alpha = -\frac{1}{2} \sum_k \begin{pmatrix} c_k^\dagger & c_{-k} \end{pmatrix} H_{\alpha,k} \begin{pmatrix} c_k \\ c_{-k}^\dagger \end{pmatrix} \qquad \text{where } H_{\alpha,k} = \cos(-k\alpha)\, \sigma^z + \sin(-k\alpha)\, \sigma^y \,. \tag{A.2}$$

So for our original Hamiltonian $H = \sum_\alpha t_\alpha\, H_\alpha$ we thus obtain

$$H = -\frac{1}{2} \sum_k \begin{pmatrix} c_k^\dagger & c_{-k} \end{pmatrix} H_k \begin{pmatrix} c_k \\ c_{-k}^\dagger \end{pmatrix} \qquad \text{where } H_k = \varepsilon_k\, (\cos(-\varphi_k)\, \sigma^z + \sin(-\varphi_k)\, \sigma^y) \,. \tag{A.3}$$

We can interpret H_k as two-dimensional vector which we can align with the σ^z axis by rotating it over an angle $-\varphi_k$ around the σ^x axis. This is implemented by $U(\vartheta) = \exp(-i\vartheta S^x) = \exp(-i\vartheta\sigma^x/2)$, such that $H_k = \varepsilon_k\, U(\varphi_k)\, \sigma^z\, U(-\varphi_k)$. Hence,

$$H = -\frac{1}{2} \sum_k \varepsilon_k \begin{pmatrix} d_k^\dagger & d_{-k} \end{pmatrix} \sigma^z \begin{pmatrix} d_k \\ d_{-k}^\dagger \end{pmatrix} = -\sum_k \varepsilon_k\, d_k^\dagger d_k + \frac{1}{2} \sum_k \varepsilon_k \,. \tag{A.4}$$

A.2. Majorana edge modes: details for proof of Theorem 1

First we treat the case $\omega > 0$, i.e. the zeros strictly within the unit disk outnumber the order of the pole at the origin ($N_z > N_p$). We consider $H = \frac{i}{2} \sum_{\alpha=-\infty}^{+\infty} t_\alpha\ (\sum_{n=1}^{\infty} \tilde{\gamma}_n \gamma_{n+\alpha})$ on the half-infinite chain. Let $\{z_i\}$ denote the ω largest zeros strictly within the unit disk. We now show that for each such z_i, we can construct a real Majorana edge mode on the left edge:

$$\gamma_{\text{left}}^{(i)} = \sum_{n \geq 1} b_n^{(i)}\, \gamma_n \,. \tag{A.5}$$

Note that if the coefficients $b_n^{(i)}$ are real, this is indeed Hermitian and commutes with T. The remaining requirements are hence that, firstly, $\gamma_{\text{left}}^{(i)}$ commutes with H, secondly, that $|b_n^{(i)}| \sim |z_i|^n$, and lastly, that the different modes anti-commute, i.e. that $\left\{\gamma_{\text{left}}^{(i)}, \gamma_{\text{left}}^{(j)}\right\} = 2\delta_{ij}$. However, if the latter is not satisfied, this can be remedied by noting that $\{\cdot,\cdot\}$

defines an inner product on the space of zero modes and hence one can apply the Gramm-Schmidt process. Note that one should do this in order of ascending correlation lengths, so as to not affect the dominant part of the spatial decay. In conclusion, it is sufficient to fix one of the z_i and show that we can find real-valued $b_n^{(i)}$ such that $[\gamma_{\text{left}}^{(i)}, H] = 0$ and $|b_n^{(i)}| \sim |z_i|^n$ (the latter implying a localization length $\xi_i = -\frac{1}{\ln|z_i|}$). The resulting edge modes need to be linearly independent, which is automatic for distinct zeros (due to the distinct asymptotic forms) but we will have to take care when there are degenerate zeros.

A straight-forward calculation shows that $[\gamma_{\text{left}}^{(i)}, H] = -i\sum_{n\geq 1} \mathcal{C}_n \tilde{\gamma}_n$ with

$$\mathcal{C}_n = \sum_{a\geq 1} b_a^{(i)}\ t_{a-n} \tag{A.6}$$

giving us an infinite number of constraints $\{\mathcal{C}_n = 0\}$. Let us first consider the case $N_p = 0$, then $t_{\alpha<0} = 0$, which means that each $\mathcal{C}_n$ contains *all* the coefficients of $f(z)$. Concretely, this means that upon taking $b_a^{(i)} = z_i^{a-1}$, we have $\mathcal{C}_n = z_i^{n-1} f(z_i)$ and hence all constraints are trivially satisfied! If z_i is real, this defines a real Majorana mode, which is normalizable since $\left\{\gamma_{\text{left}}^{(i)}, \gamma_{\text{left}}^{(i)}\right\} = \sum_{n,m=1}^{\infty} z_i^{n-1} z_i^{m-1} 2\delta_{nm} = \frac{2}{1-z_i^2} \neq 0$. If z_i is complex, we can choose $b_n^{(i)} = z_i^{n-1} \pm \overline{z}_i^{n-1}$ (which are indeed also solutions due to the Hermiticity of γ_n). Hence if z_i is complex, we obtain *two* solutions, consistent with z_i and $\overline{z}_i$ being distinct zeros of $f(z)$. Another subtlety arises when z_i is degenerate. Suppose z_i has an m-fold multiplicity (i.e. there are $i_1, \cdots, i_m$ such that $z_{i_1} = \cdots = z_{i_m}$), then $b_a^{(i_l)} = \frac{\mathrm{d}^{l-1} z^{a-1}}{\mathrm{d}z^{l-1}}\big|_{z=z_i} = \frac{(a-1)!}{(a-l)!} z_i^{a-l}$ (with $l = 1, \cdots, m$) define m solutions since then $\mathcal{C}_n = \left(z^{n-1} \frac{\mathrm{d}^{l-1} f(z)}{\mathrm{d}z^{l-1}}\right)\Big|_{z=z_i} = 0$. Note that these solutions are linearly independent, yet they all have the same localization length.

We now consider the case $N_p > 0$. Let $\{\tilde{z}_s\}$ denote the N_p *smallest* zeros of $f(z)$. Since $\omega = N_z - N_p > 0$ by assumption, we know that $z_i \notin \{\tilde{z}_s\}$. We then consider the ansatz

$$b_a^{(i)} = z_i^a + \sum_{s=1}^{N_p} \lambda_s^{(i)} \tilde{z}_s^a\ . \tag{A.7}$$

Note that before we had to take the exponent of z_i to be $a-1$ instead of a to ensure normalizability in case $z_i = 0$, but when $N_p > 0$ we know that $z_i \neq 0$ (otherwise it could be substracted from the pole). Since $t_{\alpha<-N_p} = 0$, we similarly have that $\mathcal{C}_{n>N_p} = 0$ is trivially satisfied by virtue of z_i and $\{\tilde{z}_s\}$ being zeros of $f(z)$. The remaining N_p conditions are equivalent to a problem of the type $A\lambda = b$, where the $N_p \times N_p$ matrix $A_{ns} = \left(\sum_{a\geq 1} t_{a-n}\ \tilde{z}_s^a\right)$. We now show that if the zeros are not degenerate, A is invertible. Indeed: by virtue of $f(z_i) = 0$ one can rewrite $A_{ns} = -\sum_{a=n}^{N_p} t_{-a} \tilde{z}_s^{n-a}$ (using that $\tilde{z}_s \neq 0$ since $N_p > 0$), which by simple row reduction can be reduced to the Vandermonde matrix associated to $\{\tilde{z}_s\}$ with determinant $\prod(\tilde{z}_s - \tilde{z}_{s'}) \neq 0$. Hence there is a unique solution for $\{\lambda_i\}$. If there *is* a degeneracy in $\{\tilde{z}_s\}$, one can repeat the trick encountered in the case $N_p = 0$ by working with the derivatives instead. Similarly, if one of the zeros is complex, one can take the real and imaginary combinations of the above solution. In the special case that $\overline{z}_i \in \{\tilde{z}_s\}$, these two solutions are not linearly independent, which is in fact consistent with the number of edge modes claimed in the statement of the theorem.

Suppose now that $\omega \leq 0$. The above arguments show that in that case we cannot construct a real mode on the left (because the resulting recursion relation does not admit a normalizable solution). We could perhaps construct an imaginary mode on the left edge, or equivalently, a real mode on the *right* edge. This is true if and only if the spatially inverted system (i.e. where left and right are swapped) admits real zero modes on its left edge. Hence, to prove Theorem 1, it is sufficient to prove that if the original system has

topological invariant ω, then the inverted system has $\omega_{\text{inv}} = -(\omega + 2c)$. Indeed: if then $\omega_{\text{inv}} > 0$, we can conclude that the original system has $\omega_{\text{inv}} = |\omega + 2c|$ imaginary modes on its left edge, whereas if $\omega_{\text{inv}} \leq 0$ it has none. In the latter case we can make the stronger claim that it does not allow for *any* edge modes: if there were a γ such that $[\gamma, H] = 0$, we could split it into its real and imaginary components, $\gamma = \frac{\gamma + T\gamma T}{2} + \frac{\gamma - T\gamma T}{2}$, each of which would commute with the Hamiltonian.

We now prove that if $f(z)$ has topological invariant ω, then the inverted chain has a function $f_{\text{inv}}(z)$ with topological invariant $\omega_{\text{inv}} = -\omega - 2c$. First note that spatial inversion comes down to $t_\alpha \leftrightarrow t_{-\alpha}$, and hence $f_{\text{inv}}(z) = f\left(\frac{1}{z}\right)$. If we write $f(z) = \frac{1}{z^{N_p}} \prod_i (z - z_i)$ and denote the number of zeros of $f(z)$ inside the unit disk as N_z and the *total* number of zeros as N, then it is straight-forward to derive that $f\left(\frac{1}{z}\right) \propto \frac{1}{z^{N-N_p}} \prod_i \left(z - \frac{1}{z_i}\right)$. Hence $N_P^{\text{inv}} = N - N_p$. Moreover the total number of zeros is still the same, the number of zeros on the unit circle ($2c$, by definition) has not changed, and the number of zeros of $f\left(\frac{1}{z}\right)$ *outside* the unit disk is the number zeros of $f(z)$ *within* the unit disk, such that $N_Z^{\text{inv}} = N - N_z - 2c$. In conclusion, $\omega_{\text{inv}} = N_z^{\text{inv}} - N_p^{\text{inv}} = N_p - N_z - 2c = -\omega - 2c$. This finalizes the proof.

Note. On first sight the condition that $\omega < -2c$ might seem surprising, however it makes conceptual sense: if ω satisfies that criterion, then *any* neighboring gapped phase has a winding number that is more negative than $\omega + 2c$ (which corresponds to the gapped phase where we move all the zeros on the unit circle inside the unit disk), i.e. then every nearby gapped phase has at least $|\omega + 2c|$ edge modes.

Example. Let us treat one example: $H = t_0 H_0 + t_1 H_1 + t_2 H_2$ with homogeneous coordinates $t_0, t_1, t_2 \geq 0$. The associated function is $f(z) = t_2 z^2 + t_1 z + t_0$. It is useful to introduce the inhomogeneous parameters $\tau_0 = \frac{t_0}{t_2}$ and $\tau_1 = \frac{t_1}{t_2}$, such that the two zeros of $f(z)$ are given by $z_{1,2} = -\frac{\tau_1}{2} \pm \sqrt{\left(\frac{\tau_1}{2}\right)^2 - \tau_0}$. Finding the critical points of this model, comes down to characterizing when at least one of the zeros has norm one. For this it is useful to distinguish between when the square root is imaginary or real. In the first case, i.e. $\tau_0 > \left(\frac{\tau_1}{2}\right)^2$, we have $z_{1,2} = -\frac{\tau_1}{2} \pm i\sqrt{\left|\left(\frac{\tau_1}{2}\right)^2 - \tau_0\right|}$ such that $|z_{1,2}|^2 = \tau_0$. Hence, one critical line in this model, with *two* zeros on the unit circle, lies at $\tau_0 = 1$ and $\tau_1 < 2$. This is the line $t_0 = t_2$ shown in Fig. 2.4 of the main text. In the second case, i.e. $\tau_0 \leq \left(\frac{\tau_1}{2}\right)^2$, we have $|z_{1,2}| = \frac{\tau_1}{2} \mp \sqrt{\left(\frac{\tau_1}{2}\right)^2 - \tau_0}$. A straight-forward calculation shows at least one has norm unity if and only if $\tau_1 = \tau_0 + 1$. The system is critical if that condition holds, together with $\tau_0 \leq \left(\frac{\tau_1}{2}\right)^2$, but the former in fact implies the latter. Hence we obtain the critical line $t_1 = t_0 + t_2$ shown in Fig. 2.4.

Notice that on the latter line, the zeros of $f(z)$ are $z_1 = -1$ and $z_2 = -\tau_0$. Hence if $\tau_0 < 1$, we have a critical point with a Majorana edge mode $\gamma_L = \sqrt{1 - \tau_0^2} \sum_{n=1}^{\infty} (-\tau_0)^{n-1} \gamma_n$ with localization length $\xi = -\frac{1}{\ln \tau_0}$. If $\tau_0 = 0$ we obtain the special case $H = H_1 + H_2$ discussed in the main text, with a perfectly localized edge mode $\gamma_L = \gamma_1$.

A.3. Correlation length from the zero closest to the unit circle

In Eq. (2.8) of the main text, we derived that

$$\langle \tilde{\gamma}_n \gamma_{n+N} \rangle = \frac{1}{2\pi} \oint \sqrt{\frac{f(z)}{f(1/z)}}\, z^{-N-1} \mathrm{d}z. \tag{A.8}$$

Originally, the contour is along the unit circle. Gradually increase the radius of this contour until we hit a singularity of the integrand. This occurs at the zero z_0 which is closest to the unit circle; if $|z_0| > 1$, then the singularity is due to the numerator, whereas

if $|z_0| < 1$, the singularity is in the denominator. (We presume the generic setting where z_0 has multiplicity one and where $1/z_0$ is not also a zero of $f(z)$; in the special case where either of these assumptions are violated, one can indeed have cancellations such that the correlation length is determined by other zeros of $f(z)$.) For definiteness, let us presume that z_0 lies *outside* the unit circle; the argument is straightforwardly adapted to the other case. Moreover, for ease of discussion, we presume $z_0 = x_0$ lies on the positive real axis and that there is no other zero z_i with $|z_i| = |z_0|$.

Take a finite $\varepsilon > 0$ such that there are no other zeros z_i for which $x_0 < |z_i| < x_0 + \varepsilon$. We can thus push the contour out further than the radius $|z_1|$—except at the branch point where it gets snagged. In this region, we can presume that branch cut emanating from x_0 lies along the positive real axis. We thus have

$$\langle \tilde{\gamma}_n \gamma_{n+N} \rangle = \left(\int_{x_0}^{x_0+\varepsilon+i0} - \int_{x_0}^{x_0+\varepsilon-i0} \right) \sqrt{x - x_0}\, f_{\mathrm{reg}}(x)\, x^{-N} \mathrm{d}x + O\left((x_0+\varepsilon)^{-N}\right), \quad \text{(A.9)}$$

where $f_{\mathrm{reg}}(z)$ is analytic over the domain of integration. We change variables: $x = x_0 e^t$ with the domain of integration $t : 0 \to \ln(1 + \varepsilon/x_0) \equiv t_f$. For large N, we thus obtain the asymptotic expression (ignoring prefactors)

$$\langle \tilde{\gamma}_n \gamma_{n+N} \rangle \sim x_0^{-N} \int_0^{t_f} \sqrt{e^t - 1}\, f_{\mathrm{reg}}(x_0 e^t)\, e^{-tN} \mathrm{d}t. \quad \text{(A.10)}$$

By virtue of Watson's lemma, for large N the integral is an algebraic function of N. In conclusion, the two-point function asymptotically behaves as $\sim x_0^{-N}$. Since $x_0 > 1$, this thus implies an exponential decay $\sim e^{-N/\xi}$ with $\xi = 1/\ln x_0$.

A.4. Topological invariant in the case of a unit cell

Here we provide more details for the case where the system is not strictly translation invariant, but instead has a repeating unit cell structure. This material is divided into three main sections.

1. The first section concerns the *definition* of a Hamiltonian with a unit cell of N sites and its associated complex function $f(z)$ with topological invariant ω. A consistency check is required: if we have a translation invariant system (i.e. $N = 1$), the definition of ω as discussed in the main text can be used, but we are free to describe this system as having a unit cell ($N > 1$) and hence choose to use the generalized definition of ω for systems with a unit cell. We confirm that both options give the same value for ω. Moreover, we show that ω is a genuine invariant even in the case of a unit cell, i.e. that it cannot change without causing a bulk phase transition. The reasoning is analogous to that of the main text, i.e. the values of $f(z)$ on the unit circle are related to the bulk energy spectrum.

2. The second section derives the additive property of ω: if one describes two decoupled systems as one system with a larger unit cell, then the ω thus obtained is simply the sum of the two original topological invariants. This property is shared by the central charge c.

3. The third section concerns the classification of phases in the BDI class. Recall that in the main text we showed that a translation invariant system with central charge c and topological invariant ω can be tuned to have an associated complex function $f(z) = \pm\left(z^{2c} \pm 1\right) z^{\omega}$. We also explained the intuition that if we allow for paths of local Hamiltonians with a unit cell, that we should be able to connect cases

which have different signs in the above $f(z)$. Here we confirm this by construction. This completes the proof of Theorem 2 for phases which allow for a translation invariant realization. However, this collection of phases is not closed under stacking: a gapped translation invariant chain stacked on top of a critical translation invariant chain cannot be connected to a single critical translation invariant chain (indeed: the latter never has *any* gapped degrees of freedom). We thus extend the classification to the set of phases generated by stacking. The result is that two systems are in the same phase *if and only if* they have the same c and ω —possibly up to a decoupled *trivial* chain (with $c = \omega = 0$). The latter is only necessary when one attempts to connect a critical chain *without* gapped degrees of freedom to one *with* them: all the gapped degrees of freedom can then be separated out (i.e. *dumped*) into a decoupled trivial chain.

A.4.1. Definition of topological invariant

For completeness and ease of reference, we repeat the definition given in the main text. Suppose that instead of a translation invariant chain, we have a unit cell of N sites. Then our Hamiltonian is of the form $H = \frac{i}{2}\sum_n \tilde{\boldsymbol{\gamma}}_n^T T_\alpha \boldsymbol{\gamma}_{n+\alpha}$, where $T_\alpha \in \mathbb{R}^N \times \mathbb{R}^N$. The associated meromorphic function we define is

$$f(z) := \det F(z) := \det\left(\sum_\alpha T_\alpha z^\alpha\right). \tag{A.11}$$

We again define the topological invariant as $\omega = N_z - N_p$, where N_z denotes the number of zeros of $f(z)$ strictly within the unit disk, and N_p is the order of the pole at $z = 0$.

ω is well-defined, i.e. independent of blocking

A translation invariant system $H = \frac{i}{2}\sum \tilde{\gamma}_n \; t_\alpha \; \gamma_{n+\alpha}$ has an associated function $g(z) = \sum t_\alpha z^\alpha$. We could also choose to describe this system with an N-site unit cell with hopping matrix

$$T_\alpha = \begin{pmatrix} t_{N\alpha} & t_{N\alpha+1} & \cdots & t_{N\alpha+(N-1)} \\ t_{N\alpha-1} & t_{N\alpha} & \cdots & t_{N\alpha+(N-2)} \\ \vdots & \vdots & \ddots & \vdots \\ t_{N\alpha-(N-1)} & t_{N\alpha-(N-2)} & \cdots & t_{N\alpha} \end{pmatrix}, \tag{A.12}$$

with an associated function $f(z) = \det\left(\sum T_\alpha z^\alpha\right)$. We now show that $f(z)$ has the same topological invariant as $g(z)$. To see this, note that we can write

$$f\left(z^N\right) = \det F\left(z^N\right) = \begin{vmatrix} g_0(z) & g_1(z)/z & \cdots & g_{N-1}(z)/z^{N-1} \\ g_{N-1}(z)\; z & g_0(z) & \cdots & g_{N-2}(z)/z^{N-2} \\ \vdots & \vdots & \ddots & \vdots \\ g_1(z)\; z^{N-1} & g_2(z)\; z^{N-2} & \cdots & g_0(z) \end{vmatrix} \tag{A.13}$$

$$= \begin{vmatrix} g_0(z) & g_1(z) & \cdots & g_{N-1}(z) \\ g_{N-1}(z) & g_0(z) & \cdots & g_{N-2}(z) \\ \vdots & \vdots & \ddots & \vdots \\ g_1(z) & g_2(z) & \cdots & g_0(z) \end{vmatrix}, \tag{A.14}$$

where $g_i(z) = \sum_n t_{nN+i} z^{nN+i}$, giving a decomposition $g(z) = \sum_i g_i(z)$ such that $g_i(\zeta z) = \zeta^i \; g_i(z)$ where $\zeta = e^{2\pi i/N}$. The above means that $f\left(z^N\right)$ is the determinant of the circulant matrix associated to the list of numbers $(g_0(z), \cdots, g_{N-1}(z))$, whose determinant is known to be given by $\prod_{n=0}^{N-1}\sum_i \zeta^{ni} \; g_i(z)$. Hence $f\left(z^N\right) = \prod_{n=0}^{N-1}\sum_i g_i\left(\zeta^n z\right) = \prod_{n=0}^{N-1} g\left(\zeta^n z\right)$.

Note that the topological invariant of $f\left(z^N\right)$ is simply N times that of $f(z)$, hence we conclude $f(z)$ and $g(z)$ have the same topological invariant. This means ω does not depend on how we *choose* to describe our system.

As an aside, it is worth noting that $f(z)$ and $g(z)$ do *not* coincide. For example, H_0+H_2 has the associated function $g(z) = 1 + z^2 = (z + i)(z - i)$, whereas the above shows that $f(z^2) = g(z)g(-z) = (1 + z^2)^2$, such that $f(z) = (1 + z)^2$. Observe that $f(z)$ has a zero at $z = -1$ with multiplicity *two*. Unlike in the translation invariant case, this no longer implies that the dynamical critical exponent $z_{\text{dyn}} = 2$. This illustrates that if the system has a unit cell, we can no longer use the associated function to distinguish between, for example, a CFT with $c = 1$ or a single quadratic gapless point. However, it remains true that *if the bulk is a CFT*, then the central charge is given by half the number of zeros on the unit circle (counting multiplicities). This is a consequence of the relation between $f(e^{ik})$ and the energy spectrum, which we prove now.

ω cannot change without a phase transition

The values of $f(z)$ on the unit circle carry the same relevance as in the translation invariant case. In particular, a zero crossing the unit circle would correspond to changing the physics in the bulk, since $\left|f\left(e^{ik}\right)\right| = \prod_{n=1}^{N}\left|\varepsilon_k^{(n)}\right|$, where $\varepsilon_k^{(n=1,\cdots,N)}$ represent the N bands. To see this, consider the Hamiltonian with an N-site unit cell:

$$H = \frac{i}{2}\sum_{\alpha}\sum_{n}\left(\tilde{\gamma}_{n,1} \quad \tilde{\gamma}_{n,2} \quad \cdots \quad \tilde{\gamma}_{n,N}\right) T_\alpha \begin{pmatrix} \gamma_{n+\alpha,1} \\ \gamma_{n+\alpha,2} \\ \vdots \\ \gamma_{n+\alpha,N} \end{pmatrix}. \tag{A.15}$$

If we define $c_{k,\lambda} = \sqrt{\frac{N}{L}}\sum_n e^{-ikn}c_{n,\lambda}$ (where λ is the index within the unit cell and L is the *total* number of sites), then a straight-forward computation shows that

$$H = -\frac{1}{2}\sum_{k}\begin{pmatrix} c_{k,1}^\dagger & \cdots & c_{k,N}^\dagger & c_{-k,1} & \cdots & c_{-k,N}\end{pmatrix} H_k \begin{pmatrix} c_{k,1} \\ \vdots \\ c_{k,N} \\ c_{-k,1}^\dagger \\ \vdots \\ c_{-k,N}^\dagger \end{pmatrix}, \tag{A.16}$$

with

$$H_k = \begin{pmatrix} F_H(z) & F_{AH}(z) \\ -F_{AH}(z) & -F_H(z)\end{pmatrix}\Bigg|_{z=e^{ik}}, \tag{A.17}$$

where $F_H(z)$ and $F_{AH}(z)$ denote the Hermitian and anti-Hermitian part of $F(z) = \sum_\alpha T_\alpha z^\alpha$, i.e. $\frac{F(z)\pm F(z)^\dagger}{2}$. The determinant of H_k is most easily obtained by conjugating with $U = \frac{1}{\sqrt{2}}(\sigma_x + \sigma_z)\otimes\mathbb{I}_N$:

$$UH_kU^\dagger = \begin{pmatrix} 0 & F(z)^\dagger \\ F(z) & 0\end{pmatrix}\Bigg|_{z=e^{ik}} \tag{A.18}$$

such that $\det H_k = (-1)^N\left|f\left(e^{ik}\right)\right|^2$. This finishes the proof since $\det H_k = (-1)^N\prod_{n=1}^{N}\left(\varepsilon_k^{(n)}\right)^2$.

Hence even in the presence of a unit cell, we can associate a meromorphic function to the Hamiltonian. Moreover, this gives rise to a well-defined topological invariant (independent of whether the system is gapped or gapless) that can only change if the bulk undergoes a phase transition.

A.4.2. Additivity of c and ω under stacking

Take two chains, characterized by $g(z) = \det G(z) = \det\left(\sum T_\alpha^{(1)} z^\alpha\right)$ and $h(z) = \det H(z) = \det\left(\sum T_\alpha^{(2)} z^\alpha\right)$ respectively. One can stack these two on top of one another, which is equivalent to having a chain with

$$T_\alpha = \begin{pmatrix} T_\alpha^{(1)} & 0 \\ 0 & T_\alpha^{(2)} \end{pmatrix} \qquad \text{such that } f(z) = \begin{vmatrix} G(z) & 0 \\ 0 & H(z) \end{vmatrix} = g(z)h(z)\,. \tag{A.19}$$

Hence the topological invariant of $f(z)$ is the sum of those of $g(z)$ and $h(z)$. This establishes the additive property of the topological invariant under stacking —similar to the well-known property of the central charge of a CFT. Note that the central charge can only increase under addition, such that the *labeling* by $\mathbb{N}\times\mathbb{Z}$, with $c \in \frac{1}{2}\mathbb{N}$ and $\omega \in \mathbb{Z}$, is in fact a *semigroup*.

In the main text we saw that c and ω *uniquely* label all the phases which allow for at least one translation invariant representative (if translation symmetry is not enforced). Stacking such phases can in principle generate new phases, and hence it is a priori not clear that c and ω are sufficient to label them, i.e. that stacks with the same c and ω can be connected. In the next section we show that this is in fact true. This means that the set of phases can be *identified* with the semigroup $\mathbb{N}\times\mathbb{Z}$, where the operation of stacking corresponds to addition. The special case where $c = 0$ corresponds to the classification of gapped phases in the BDI class which is known to be classified by the *group* $\mathbb{Z}$, which in this context can be identified with $\{0\}\times\mathbb{Z} \subset \mathbb{N}\times\mathbb{Z}$.

A.4.3. Classification

Effect of unit cell on classification of translation invariant chains

In the main text we explained how any translation invariant model with central charge c and topological invariant ω can be tuned to the canonical form $f(z) = \pm\left(z^{2c} \pm 1\right) z^\omega$ whilst at all times preserving translation invariance. From the above we know that even if we allow for paths with an arbitrary unit cell, ω *cannot* change without causing a phase transition (whereas c is not allowed to change by virtue of our very *definition* of a phase). However, we now show that by allowing for such a unit cell, we *can* connect models with such different signs. The situation is summarized in Fig. A.1.

Regarding the first sign, one can note that defining $U(\alpha) = \exp\left(\frac{\alpha}{2}\sum_n \tilde\gamma_{2n-1}\tilde\gamma_{2n}\right) = \prod_n \left(\cos\left(\frac{\alpha}{2}\right) + \tilde\gamma_{2n-1}\tilde\gamma_{2n}\sin\left(\frac{\alpha}{2}\right)\right)$ does the trick: $U(\pi)H_\alpha U(\pi)^\dagger = -H_\alpha$ whereas $[U(\alpha), T] = 0$. Although $U(\pi)$ maps strictly translation invariant models to strictly translation invariant models, for intermediate $0 < \alpha < \pi$, the transformed Hamiltonian will have a two-site unit cell.

For the second sign, we need to find a transformation which maps $H_\omega \to -H_\omega$ and $H_{2c+\omega} \to H_{2c+\omega}$. Note that at a discrete level, this is accomplished by applying (for a chain with periodic boundary conditions)

$$V = \quad \cdots(\tilde\gamma_1\cdots\tilde\gamma_{2c})\,(\gamma_{2c+1+\omega}\cdots\gamma_{4c+\omega})\,(\tilde\gamma_{4c+1}\cdots\tilde\gamma_{6c})\,(\gamma_{6c+1+\omega}\cdots\gamma_{8c+\omega})\cdots \tag{A.20}$$

Indeed: $VH_\omega V^\dagger = -H_\omega$ and $VH_{2c+\omega}V^\dagger = H_{2c+\omega}$. We now need to show that this can be implemented gradually. To this purpose, define the local generator

$$A = \sum_{n\in\mathbb{Z}}\sum_{m=1}^{2c} \tilde\gamma_{6nc+m}\tilde\gamma_{6nc+4c+m} + \gamma_{6nc+2c+\omega+m}\gamma_{6(n+1)c+\omega+m}\,. \tag{A.21}$$

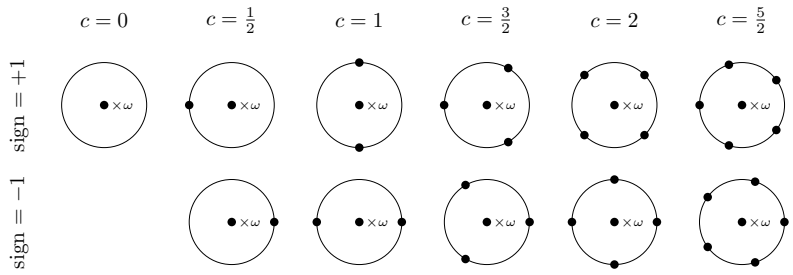

Figure A.1.: Any translation invariant Hamiltonian in the BDI class, $H = \sum t_\alpha H_\alpha$ with $f(z) = \sum t_\alpha z^\alpha$, which has central charge $c \in \frac{1}{2}\mathbb{N}$ and topological invariant $\omega \in \mathbb{Z}$, can be brought to the canonical form $H = \pm\left(H_{2c+\omega} \pm H_\omega\right)$ with $f(z) = \pm\left(z^{2c} \pm 1\right) z^\omega$ without causing a phase transition (as explained in the main text). The pattern of zeros and poles of this canonical form is illustrated above, where 'sign' denotes the choice of the relative sign in $z^{2c} \pm 1$. Including the further choice of the overall sign, one obtains a $\mathbb{Z}_2 \times \mathbb{Z}$ classification for the gapped phases ($c = 0$), and a $\mathbb{Z}_2 \times \mathbb{Z}_2 \times \mathbb{Z}$ classification for the critical phases which are described by a non-trivial CFT in the bulk. If we allow for paths which break strict translation symmetry by introducing a unit cell, we can always bring it to the form $H = H_{2c+\omega} + H_\omega$: the central charge and the topological invariant fully characterize each phase (as long as the dynamical critical exponent $z_{\mathrm{dyn}} = 1$, i.e. the zeros on the unit circle are non-degenerate).

Firstly note that $[A, T] = 0$. Secondly, all the terms in A commute, such that

$$V(\alpha) := \exp\left(\frac{\alpha}{2} A\right) \tag{A.22}$$

$$= \prod_{n\in\mathbb{Z}} \prod_{m=1}^{2c} \exp\left(\frac{\alpha}{2} \tilde{\gamma}_{6nc+m} \tilde{\gamma}_{6nc+4c+m}\right) \exp\left(\frac{\alpha}{2} \gamma_{6nc+2c+\omega+m} \gamma_{6(n+1)c+\omega+m}\right) \tag{A.23}$$

$$= \prod_{n\in\mathbb{Z}} \prod_{m=1}^{2c} \left(\cos\left(\frac{\alpha}{2}\right) + \tilde{\gamma}_{6nc+m} \tilde{\gamma}_{6nc+4c+m} \sin\left(\frac{\alpha}{2}\right)\right) \times \left(\cos\left(\frac{\alpha}{2}\right) + \gamma_{6nc+2c+\omega+m} \gamma_{6(n+1)c+\omega+m} \sin\left(\frac{\alpha}{2}\right)\right). \tag{A.24}$$

Hence this allows to smoothly apply V, since

$$V(\pi) = \prod_{n\in\mathbb{Z}} \prod_{m=1}^{2c} \tilde{\gamma}_{6nc+m} \tilde{\gamma}_{6nc+4c+m} \gamma_{6nc+2c+\omega+m} \gamma_{6(n+1)c+\omega+m} = V\,. \tag{A.25}$$

Extending the classification to stacks: a semigroup structure

We consider all phases in the BDI class which are described in the bulk by a CFT and which can be obtained by deforming a translation invariant Hamiltonian $H = \sum t_\alpha H_\alpha$ — or stackings thereof— with an arbitrary unit cell. We now prove that these are classified by the semigroup $\mathbb{N} \times \mathbb{Z}$, being uniquely labeled by the central charge $c \in \frac{1}{2}\mathbb{N}$ and the topological invariant $\omega \in \mathbb{Z}$. More precisely, given such a system, then after adding a *single* trivial decoupled chain H_0 *if need be*, we can always smoothly connect it to a chain described by H_ω stacked on top of $2c$ copies of the standard critical Majorana chain $H_0 + H_1$.

Note that given the previous section, it is sufficient to prove the above statement for a system consisting of n decoupled chains, each in the canonical form $H_i = H_{2c_i+\omega_i} + H_{\omega_i}$

with central charge c_i and topological invariant ω_i such that $c = \sum_{i=1}^n c_i$ and $\omega = \sum_{i=1}^n \omega_i$. We prove this by induction.

Consider the case $n = 1$. If $c = 0$, then the system is already described by H_ω and we are done. If $c \neq 0$, then after stacking with a trivial chain described by H_0, we can bring it to two decoupled chains H_ω and $H_0 + H_{2c}$ by virtue of Corollary 1 (an auxilliary result proved below). The latter can naturally be seen as consisting of $2c$ decoupled copies of $H_0 + H_1$.

As for the induction step: suppose the decomposition holds for n, then we prove it for $n+1$. Applying the result on the first n chains gives us $H_{\omega_1+\cdots+\omega_n}$ and $2(c_1 + \cdots + c_n)$ copies of $H_0 + H_1$. We can now use Corollary 1 to transfer the topological invariant of the $(n+1)$th chain into $H_{\omega_1+\cdots+\omega_n}$, leaving the $(n+1)$th chain to be described by $H_0 + H_{2c_{n+1}}$. If $c_{n+1} \neq 0$, the latter consists of $2c_{n+1}$ copies $H_0 + H_1$ such that we are done. If $c_{n+1} = 0$, then we end up with *two* decoupled gapped chains (in addition to the critical chains), described by H_ω and H_0. However, such a stack can locally and smoothly be connected into a single chain H_ω. One way of seeing this, is by using Corollary 1 to connect this to two copies of $H_{\frac{\omega}{2}}$ if ω is even, or to a stack of $H_{\frac{\omega-1}{2}}$ and $H_{\frac{\omega+1}{2}}$ if ω is odd. In the former case, simply interlacing the two chains gives a chain described by H_ω, whereas in the latter case the same works if one also swaps the corresponding real Majoranas of both chains. This swapping can be done locally, smoothly and in a T-preserving way by virtue of Lemma 1, which is proven below. This completes the proof.

Lemma 1 *A permutation of a finite set of Majorana modes of the same type (i.e. real or imaginary) can be implemented in a smooth and T-preserving fashion, on the condition that the same permutation cycle is applied on two disjoint systems.*

Note that a permutation of a finite number of Majoranas is automatically local. If one is interested in non-overlapping permutations cycles (whose cycle length does not depend on system size) in an arbitrarily large system, then by applying this result in parallel, one can achieve this in a local, smooth and T-preserving fashion.

Since any permutation can be decomposed into a series of transpositions, it is sufficient to prove this lemma for the special case of a swap $\gamma_1 \leftrightarrow \gamma_2$. The condition that the same permutation cycle is applied on a disjoint system, means we also want to swap $\gamma_3 \leftrightarrow \gamma_4$. To this end, let us define

$$U(\alpha) = \exp\left(\frac{\alpha}{2}\gamma_2\gamma_4\right)\exp\left(\frac{\alpha}{4}\left[\gamma_1\gamma_2 + \gamma_3\gamma_4\right]\right) \tag{A.26}$$

$$= \left[\cos\left(\frac{\alpha}{2}\right) + \gamma_2\gamma_4\sin\left(\frac{\alpha}{2}\right)\right]\left[\cos\left(\frac{\alpha}{4}\right) + \gamma_1\gamma_2\sin\left(\frac{\alpha}{4}\right)\right]\left[\cos\left(\frac{\alpha}{4}\right) + \gamma_3\gamma_4\sin\left(\frac{\alpha}{4}\right)\right]. \tag{A.27}$$

It is clear that for $\alpha \in \mathbb{R}$ we have $[U(\alpha), T] = 0$, and the Hermiticity of the Majorana modes shows that $U(\alpha)$ is unitary. It is straightforward to show that $U(\pi) = \frac{1}{2}(\gamma_2 - \gamma_1)(\gamma_4 - \gamma_3)$. This means that $U(\pi)\gamma_1 U(\pi)^\dagger = \gamma_2$ and $U(\pi)\gamma_2 U(\pi)^\dagger = \gamma_1$ (and analogously for γ_3 and γ_4). Hence, $U(\alpha)$ indeed smoothly implements the two swaps for $\alpha \in [0, \pi]$.

Note that we needed to simultaneously do the swap on γ_3, γ_4 as well, otherwise we can only define $V(\alpha) = \exp\left(\frac{\alpha}{4}\gamma_1\gamma_2\right)$, which indeed achieves $V(\pi)\gamma_2 V(\pi)^\dagger = \gamma_1$ but also $V(\pi)\gamma_1 V(\pi)^\dagger = -\gamma_2$.

We now show that this lemma implies a very useful corollary.

Corollary 1 *Given two decoupled translation invariant chains in the BDI class with topological invariants ω_1 and ω_2 respectively, there is a local, smooth and T-preserving way to shift $\omega_1 \to \omega_1 + \zeta$ and $\omega_2 \to \omega_2 - \zeta$ for arbitrary $\zeta \in \mathbb{Z}$.*

Colloquially, we say that we can transfer the topological invariant between the two chains whilst staying within the same phase.

Note that for a *single* chain we can arbitrarily modify its topological invariant by shifting each real mode $\gamma_n \to \gamma_{n+\zeta}$, which has the effect $t_\alpha \to t_{\alpha+\zeta}$ such that $f(z) \to z^\zeta f(z)$ and hence $\omega \to \omega + \zeta$. However, this discrete mapping cannot be implemented in local, smooth and T-preserving way. Indeed, we know we cannot change ω without causing a phase transition.

However, given a stack of two chains, it turns out we can implement the above shift map (in opposite directions on each chain, such that the total topological invariant is unaffected) via a series of *local* permutations. The corollary then follows by applying Lemma 1. The necessary permutations are shown in Fig. A.2.

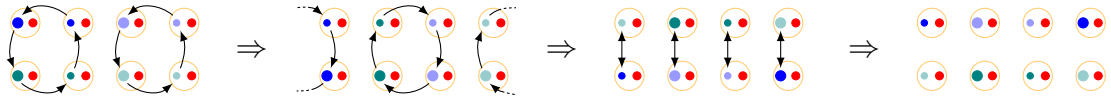

Figure A.2.: A visual proof of the statement that by *local* permutations of Majoranas of the *same* type (blue and green denote *real* Majorana modes, red denote *imaginary* modes) one can map $\gamma_n \to \gamma_{n-1}$ in the *top* layer and $\gamma_n \to \gamma_{n+1}$ in the *bottom* layer (and one can reverse the shift by changing the direction of the arrows in the figure). This implies that if the two chains were decoupled, then under this transformation $H^{(\mathrm{top})} = \sum t_\alpha^{(\mathrm{top})} H_\alpha^{(\mathrm{top})} \to \sum t_\alpha^{(\mathrm{top})} H_{\alpha-1}^{(\mathrm{top})}$ (and in the opposite direction for $H^{(\mathrm{bottom})}$). In other words: this allows to transfer the topological invariant from one chain to the other (whilst keeping the total ω unchanged). As a consequence of Lemma 1, this type of transformation can be done smoothly in a local and T-preserving way. Hence this allows, for example, to continuously connect a stack of H_0 ($\omega = 0$, $c = 0$) and $H_1 + H_2$ ($\omega = 1$, $c = \frac{1}{2}$) to a stack of H_1 ($\omega = 1$, $c = 0$) and $H_0 + H_1$ ($\omega = 0$, $c = \frac{1}{2}$).

B. The principles of symmetry fractionalization in one dimension

Consider a gapped one-dimensional system of length N invariant under a global symmetry group G. The total Hilbert space has a tensor product structure $\mathcal{H} = \otimes_n \mathcal{H}_n$ with an on-site Hilbert space dimension $\dim(H_n) = d$ (possibly after blocking). The abstract symmetry group G acts via an (anti)linear representation $\rho : G \to U(d^N)$ on the Hilbert space, where $U\left(d^N\right)$ are the $d^N \times d^N$ unitary matrices. We work in the setting where the symmetry is on-site, which means that there exists an (anti-)linear representation $\rho_n : G \to U(d)$ such that for all $g \in G$, $\rho(g) = \otimes_n \rho_n(g)$. In the case of an anti-unitary symmetry, this means that the basis in which we define complex conjugation has to be compatible with the tensor product structure. Note that such on-site symmetries are automatically well-defined if we have open boundary conditions, which is essential for our approach. Since we will be interested in faithful representations (which means $G \cong \rho(G)$), we will in fact identify G with its representation. In other words we can say 'take $U \in G$' where U is some unitary operator.

B.1. Each symmetry fractionalizes

Consider a bosonic system with open boundaries. In section 3.1 we have argued that any unitary symmetry $U \in G$ can effectively be written as $U = U_L U_R$ where $U_{L,R}$ are exponentially localized near the boundary. This means that in the thermodynamic limit, U_L and U_R have no overlap. We now argue that this means that $U_{L,R}$ are *separately* symmetries, at least in the ground state subspace (however, if $U = U_L U_R$ holds even for excited states –as is the case for strong zero modes– then the following argument applies to the full Hamiltonian). Decompose the Hamiltonian $H = H_L + H_R$ where H_L has no overlap with U_R and H_R has no overlap with U_L. This is possible due to the locality of the Hamiltonian. (Note that H_L will have overlap with H_R.) Due to the tensor product structure of the symmetry, we can also choose H_L and H_R such that U is a symmetry of each individually. This means $0 = [U, H_L] = [U_L U_R, H_L] = [U_L, H_L]U_R$. Since U_R is invertible, this means $[U_L, H_L] = 0$. The fact that U_L has no overlap with H_R also means $[U_L, H_R] = 0$. Hence $[U_L, H] = [U_L, H_L + H_R] = 0$. Similarly $[U_R, H] = 0$.

B.2. Projective representation on the edge

The previous paragraph showed that bulk symmetries $U, V \in G$ define edge symmetries U_L, V_L, U_R, V_R. We now discuss what relations hold for these edge operators, working in the bosonic setting –later we mention what changes in the fermionic case. Suppose, for example, that the original symmetries U and V are commutative, i.e. $UVU^{-1}V^{-1} = 1$, then $U_L V_L = e^{i\alpha} V_L U_L$. To see this, note that

$$\begin{aligned} 1 &= (U_L U_R)(V_L V_R)\left(U_L^{-1} U_R^{-1}\right)\left(V_L^{-1} V_R^{-1}\right) \\ &= \left(U_L V_L U_L^{-1} V_L^{-1}\right)\ \left(U_R V_R U_R^{-1} V_R^{-1}\right) \end{aligned} \tag{B.1}$$

Since the two factors act on disjoint regions, each must be proportional to the identity: $U_L V_L U_L^{-1} V_L^{-1} = e^{i\alpha}$. This proves the above claim. More generally, any group relation

that holds in G, also holds for the edge symmetries *up to a phase factor*. This means the edge transforms under a *projective* representation of G.

B.3. Gauge symmetry and classes

The phase factors of such a projective representation can have an arbitrariness to them. The defining relationship $U = U_L U_R$ is invariant under the gauge transformation $U_L \to e^{i\beta} U_L$ and $U_R \to e^{-i\beta} U_R$. However, the above $e^{i\alpha}$ is unchanged. We say the phase defined by $U_L V_L U_L^{-1} V_L^{-1}$ is gauge invariant. On the other hand, if $U^2 = 1$, then $U_L^2 = e^{i\gamma}$ which transforms under the previous gauge transformation as $U_L^2 = e^{i(2\beta+\gamma)}$. In particular, one can (partially) fix the gauge of U_L by choosing $U_L^2 = 1$. To each projective representation, one can associate its gauge-invariant phase factors. We say two projective representations belong to the same class if these factors are the same. For example, all half-integer projective representations of $SO(3)$ belong to the same class. The set of these classes itself forms a group (for example one can add two classes by multiplying their phase factors) which is mathematically denoted by $H^2(G; U(1))$ and is called the second group cohomology group with coefficients in $U(1)$. For example, $H^2_{\text{grp}}(SO(3); U(1)) = \mathbb{Z}_2$, corresponding to the two distinct classes of half-integer and integer spins. In case G is finite, it is also referred to as the Schur multiplier of G.

B.4. Topological invariants and protected edge modes

The above shows that to each gapped symmetry-preserving Hamiltonian, we can associate a list of phase factors to its edges. If one has two different Hamiltonians, each with its own set of phase factors (i.e. each is associated to a class of projective representations), then if these phase factors cannot be smoothly deformed into one another, these Hamiltonians must be in distinct phases. This happens if these phase factors can only take discrete values. Consider for example $G = \mathbb{Z}_2 \times \mathbb{Z}_2$ generated by U and V. We have already encountered the invariant $U_L V_L = e^{i\alpha} V_L U_L$. Since also $U^2 = 1$, then U_L^2 is a phase factor and hence $[U_L^2, V_L] = 0$. This means $e^{i2\alpha} = 1$, such that the projective representations of $G = \mathbb{Z}_2 \times \mathbb{Z}_2$ are labeled by $U_L V_L = \pm V_L U_L$. Such a discrete invariant cannot change smoothly and thus labels distinct phases. Note that a non-trivial projective representation always has a dimension > 1 (otherwise everything would trivially commute). In this way non-trivial phase factors are also linked to degenerate edge modes. More concretely, a d-dimensional projective representation protects a d-dimensional edge mode.

Not all distinct classes of projective representations define different phases. For example, the projective representations of $G = \mathbb{Z} \times \mathbb{Z}$ are characterized by a continuous phase $U_L V_L = e^{i\alpha} V_L U_L$. In other words, the distinct classes of projective representations are labeled by $H^2_{\text{grp}}(\mathbb{Z} \times \mathbb{Z}; U(1)) = U(1)$: there are infinitely many, but they are all smoothly connected. However, a finite-dimensional unit cell is symmetric with respect to a finite group G or a compact Lie group G, in which case $H^2_{\text{grp}}(G; U(1))$ is discrete[1]. So for the case of finite-dimensional on-site Hilbert spaces, the classes of projective representations are characterized by *discrete* invariants, i.e. they label distinct SPT phases with protected edge modes.

[1] If G is a compact Lie group, then $H^2_{\text{grp}}(G; U(1)) \cong H^2_{\text{sing}}(G; \mathbb{Z})$ which is well-known to be $\cong \mathbb{Z}^\beta \oplus T$ with $\beta \in \mathbb{N}$ and T finite.

B.5. Anti-unitary symmetries

A similar procedure works for an anti-unitary symmetry $T = UK$, where U is an on-site symmetry and K is complex conjugation defined in a tensor product basis. If one chooses a basis for the low-energy degrees of freedom (necessarily living on the edge since the bulk is gapped) which factorizes between left and right, then one can define a new notion of complex conjugation, $\tilde{K}$, with respect to this factorized basis. If we restrict ourselves to these basis states, the same argument goes through as before, i.e. the symmetry will effectively act as $T = U_L U_R$. Allowing for phase factors and superpositions, the expression becomes $T = U_L U_R \tilde{K}$ in the low-energy subspace.

If the original symmetry satisfies $T^2 = 1$, then

$$\begin{aligned} 1 &= T\,(U_L U_R \tilde{K}) \\ &= T U_L T^2 U_R T^2 \tilde{K} \\ &= T U_L T T U_R T U_L U_R \tilde{K}^2 \\ &= (\overline{U}_L U_L)(\overline{U}_R U_R) \quad \text{where } \overline{\mathcal{O}} := T\mathcal{O}T \end{aligned} \tag{B.2}$$

Since the two factors act on disjoint regions, $\overline{U}_L U_L = e^{i\kappa}$. Note that this phase factor is invariant under $U \to e^{i\alpha}U$. Moreover we see that $U_L^{-1} = e^{-i\alpha}\overline{U}_L$, and since any operator commutes with its inverse, we have that U_L and $\overline{U}_L$ commute. Hence the product $\overline{U}_L U_L$ must be real. We conclude that the projective representations of $T^2 = 1$ are labeled by $U_L\overline{U}_L = \overline{U}_L U_L = \pm 1$. Alternatively, one could have defined the invariant $U_L\tilde{K}U_L\tilde{K} = \pm 1$, and in fact for bosonic systems $(U_L T)^2 = (U_L\tilde{K})^2$ (which can be proven using $T = T^{-1} = \tilde{K}U_R^{-1}U_L^{-1}$) so the choice is irrelevant. The latter choice might seem more natural, since $U_L\tilde{K}$ can be said to be an anti-unitary operator living on the left edge, but the fermionic case (which we address soon) shows that the other invariant is preferable.

To confirm that this invariant is independent of our choice of (factorized) basis, note that any other choice leads to a complex conjugation $\tilde{K}' = W_L W_R \tilde{K} W_R^{-1} W_L^{-1}$. Each effective complex conjugation, $\tilde{K}$ and $\tilde{K}'$, leads to a fractionalization $T = U_L U_R \tilde{K} = V_L V_R \tilde{K}'$. Substituting the above expression for $\tilde{K}'$, one obtains $U_L = V_L W_L \tilde{K} W_L^{-1} \tilde{K}$ up to a phase factor which does not affect the argument. Using this one can indeed straightforwardly show that $(U_L T)^2 = (V_L T)^2$, again using the trick that $T = T^{-1}$.

B.6. What changes for fermions

So far we have used the fact that if U_L and U_R act on disjoint regions, then they commute. This clearly need not be the case for fermionic systems. This means that for each symmetry we can now have an extra phase factor: $U_L U_R = \pm U_R U_L$. Equivalently, this encodes whether U_L is bosonic or fermionic, i.e $U_L P = \pm P U_L$, where P is fermionic parity symmetry. A (projective) representation with this extra structure is called graded[16].

There is an important subtlety. In order to have a well-defined symmetry fractionalization of an anti-unitary symmetry, $T = U_L U_R \tilde{K}$, it is important that $\tilde{K}$ is chosen with respect to basis that factorizes over the edges. If this can be done, then the above proof directly applies to show the gauge invariance of $U_L\overline{U}_L$, even if U_L is fermionic. However, fermionic chains can have a non-local fermionic mode that is spread out over both edges and hence such a basis does not exist. The best one can do is a decomposition $\mathcal{H} = (\mathcal{H}_L \otimes \mathcal{H}_R) \oplus \mathcal{H}_{\text{non-local}}$, where $\dim \mathcal{H}_{\text{non-local}} = 0, 2$. This corresponds to respectively having an even or odd number of Majorana modes per edge. The definition of $\tilde{K}$ then depends on the basis one chooses in $\mathcal{H}_{\text{non-local}}$, which can possibly change the value of $U_L\overline{U}_L$. This simply means the anti-unitary symmetry protects the non-local mode (e.g.

this is the case for the Kitaev chain, which is dual to the statement that the degeneracy of the Ising chain is protected by the spontaneously broken PT symmetry). Despite $U_L\overline{U}_L$ not being gauge-invariant in that case, one can still use it to label distinct phases, even if one does *not* make consistent gauge choices –this will be illustrated in the example of the α-chain which we soon compute. Nevertheless, if one so prefers, one can consistently fix the gauge by requiring that the non-local basis vectors are chosen to be an eigenstate of P_L (where P is fermionic parity symmetry). Equivalently this means $\tilde{K}P_L\tilde{K} = P_L^{-1}$. Note that this condition on $\tilde{K}$ is independent of the gauge choice for P_L.

One might wonder how what changes if we switch between the two possible gauge choices. To this purpose, we can label the gauge by β, i.e. $\tilde{K}P_L\tilde{K}P_L = (-1)^\beta$. One can straight-forwardly prove that if $P_LP_R = P_RP_L$, then $\beta = 0$, confirming that the subtlety of fixing β only arises in the presence of a non-local mode. In the latter case, one can show that $\tilde{K}P_R\tilde{K}P_R = (-1)^{\beta+1}$, i.e. fixing this gauge is equivalent to choosing an edge, matching the fact that after a Jordan-Wigner transformation (which also chooses an edge) one obtains a spin chain where these subtleties do not arise. Suppose now that $T = U_LU_R\tilde{K}$ in a gauge labeled by β, then one can change the gauge by choosing $\tilde{K}' = P_LP_R\tilde{K}$. One can show that the new fractionalization, $T = V_LV_R\tilde{K}'$, satisfies $V_L\overline{V}_L = (-1)^{\beta+af}U_L\overline{U}_L$, where a (resp. f) denotes whether P_L (resp. U_L) is fermionic. Similarly, the same identity holds for the right-hand side if we replace $\beta \to \beta + a$. (Useful intermediate results to prove this, are $P_LTP_LT = (-1)^{\beta+f}$ and $P_LU_L = (-1)^{(a+1)f}U_LP_L$, which both straightforwardly follow from the trick of rewriting $P_L = PP_R^{-1}$ and $T = T^{-1} = \tilde{K}U_R^{-1}U_L^{-1}$.)

Another subtlety is that instead of the invariant $(U_LT)^2$ one could consider $(U_L\tilde{K})^2$. However, one can show that $(U_LT)^2 = \pm(U_L\tilde{K})^2$, where the sign corresponds to U_L being bosonic (plus) or fermionic (minus). Hence if one is merely interested in counting and distinguishing phases, the choice is irrelevant. However, in section 3.2.1 we have argued that the former choice is more natural in terms of the physics. For example, it leads one to the conclusion that the 2-chain is protected by PT on the left-hand side, which is indeed given substance by the Jordan-Wigner transformation (with its string starting at the left end) mapping the 2-chain to a spin chain protected by PT (and not T).

B.7. Symmetry fractionalization of the α-chain

The α-chain is a fermionic system with an anti-unitary symmetry $T = K$. From the above discussion, one can make an educated guess about the number of phases it has: there is an invariant for whether or not the fractionalization of P is fermionic (i.e. there are an odd number of Majorana modes per edge) and then two invariants for whether or not T protects something on the left or right. In summary we are interested in obtaining for each α-chain the following phase factors (where $T = U_LU_R\tilde{K}$):

$$P_LP_R = (-1)^aP_RP_L \tag{B.3}$$

$$TU_LTU_L = \overline{U}_LU_L = (-1)^b \tag{B.4}$$

$$TU_RTU_R = \overline{U}_RU_R = (-1)^c \tag{B.5}$$

Note that if one is given b, then the invariant c is equivalent to the information of whether or not $U_{L,R}$ is fermionic. Indeed: $1 = T^2 = TU_LU_R\tilde{K} = (TU_LT)(TU_RT)U_LU_R$, hence the fractionalization being bosonic or fermionic is equivalent to $(U_LT)^2$ having, respectively, the same or opposite sign as $(U_RT)^2$. One can rephrase this as $U_LU_R = (-1)^{a+b}U_RU_L$, and also $U_LP = (-1)^{a+b}P\,U_L$. Note that as discussed above, the values of b and c depend on the choice of complex conjugation in case of a non-local fermion (i.e. $a = 1$). One can encode this choice in $\beta = 0, 1$ where $P_L\tilde{K}P_L\tilde{K} = (-1)^\beta$. Nevertheless, we will see a, b, c successfully distinguish all eight phases *even* if one mixes choices of β.

α	a	b		c	
0	0	0		0	
1	1	0		(0)	[1]
2	0	0		1	
3	1	(0)	[1]	1	
4	0	1		1	
5	1	1		(1)	[0]
6	0	1		0	
7	1	(1)	[0]	0	

Table B.1.: The phase factors characterizing the symmetry fractionalization of P and T as defined in Eq. (B.3) and derived from Eqs. (B.8) and Eq. (B.11). If the result depends on the gauge choice $P_L\tilde{K}P_L\tilde{K} = (-1)^\beta$, we show it in parentheses. In that case, the value in round (square) brackets corresponds to $\beta = 0$ ($\beta = 1$). Note that these three columns correspond to the first two columns in Table (3.1).

A priori one might also expect PT to give extra invariants. However we now show that its fractionalization is fixed by the above information. If we write $PT = V_L V_R \tilde{K}$, then

$$(PT)V_L(PT)V_L = \begin{cases} TU_RTU_R & \text{if } a = 0 \\ (-1)^{\beta+1}TU_LTU_L & \text{if } a = 1 \end{cases} \tag{B.6}$$

This is straight-forward to derive. Firstly note that $V_L = P_L U_L$ (up to an irrelevant sign), hence

$$\begin{aligned} (PT)V_L(PT)V_L &= PTP_LU_LPTP_LU_L \\ &= PTP_LTTU_LTPP_LU_L \\ &= (-1)^{\beta+b+c+a(b+c)}PP_L^{-1}TU_LTU_LPP_L \\ &= (-1)^{\beta+b+c+a(b+c)+a}TU_LTU_L \end{aligned} \tag{B.7}$$

where we have used that $P_LTP_LT = (-1)^{\beta+b+c}$ and $U_LPP_L = (-1)^{a(b+c)}PP_LU_L$.

We now explicitly derive the expressions for $P_{L,R}$ and $U_{L,R}$ for the α-chain (where for notational convenience we choose α positive). One may easily ascertain that up to an irrelevant sign

$$P_L = \prod_{1\le n\le\alpha} \gamma_n \qquad P_R = i^\alpha \prod_{0\le n<\alpha} \tilde{\gamma}_{N-n} \tag{B.8}$$

This is a direct consequence of $P = i^N \prod \tilde{\gamma}_n\gamma_n$ and the fact that for all $1 \le n \le N-\alpha$, in the ground state subspace $\tilde{\gamma}_n\gamma_{n+\alpha} = i$. To factorize the low-energy Hilbert space made up by these modes as much as possible onto the edges, let us define

$$\begin{cases} c_1^L = \frac{1}{2}(\gamma_1 + i\gamma_2) & c_1^R = \frac{1}{2}(\tilde{\gamma}_{N-1} + i\tilde{\gamma}_N) \\ \quad\vdots & \quad\vdots \\ c_a^L = \frac{1}{2}(\gamma_{2a-1} + i\gamma_{2a}) & c_a^R = \frac{1}{2}\left(\tilde{\gamma}_{N-2a+1} + i\tilde{\gamma}_{N-2(a-1)}\right) \end{cases} \tag{B.9}$$

where $a = \lfloor \alpha/2 \rfloor$. If α is odd we have the extra non-local mode $c = \frac{1}{2}(\gamma_\alpha + i\tilde{\gamma}_{N-\alpha+1})$. We now define $\tilde{K}$ as complex conjugation in the basis of these fermionic modes. Equivalently:

$$\tilde{K}\ \overset{(\sim)}{\gamma}_n\ \tilde{K} = (-1)^{n+1}\ \overset{(\sim)}{\gamma}_n \tag{B.10}$$

One can ascertain that in this gauge we have $P_L\tilde{K}P_L\tilde{K} = 1$, i.e. $\beta = 0$ (the other gauge would correspond to changing $(-1)^{n+1} \to (-1)^n$). Comparing Eq. (B.10) to the action of T, i.e. $T\gamma_n T = \gamma_n$ and $T\tilde{\gamma}_n T = -\tilde{\gamma}_n$, we see that

$$U_L = \prod_{1\leq \text{even } n\leq \alpha} \gamma_n \qquad U_R = \prod_{0\leq \text{odd } n<\alpha} \tilde{\gamma}_{N-n} \tag{B.11}$$

The above explicit symmetry fractionalizations allow us to read off the invariants a, b, c, as summarized in Table. (B.1). As an example, consider $\alpha = 3$ such that $U_L = \gamma_2$. Then $U_L\overline{U}_L = \gamma_2(-\gamma_2) = -1$, hence $b = 1$.

From our earlier discussion (and characterization) of how the symmetry fractionalization of T depends on the choice of basis, we can also directly obtain the values for the gauge choice $P_R\tilde{K}P_R\tilde{K} = 1$ (i.e. $\beta = 1$ if $a = 1$). When b or c depend on this choice, we show it in parentheses, where value in round (square) brackets corresponds to $\beta = 0$ ($\beta = 1$). Note that one can also directly calculate it in the basis where $P_R\tilde{K}P_R\tilde{K} = 1$ by redefining $\tilde{K} \to P_L P_R \tilde{K}$, in which case the sign in Eq. (B.10) changes from $(-1)^{n+1}$ to $(-1)^n$. For example, U_L is now given by the product of *odd* Majorana modes instead of even ones.

This information is represented in the main text in Table (3.1). There we have inserted an extra column specifying the symmetry fractionalization of PT, which can be derived from that of P and T as mentioned before. Note that changing the gauge choice is equivalent to swapping the $T \leftrightarrow PT$ and 'left' $\leftrightarrow$ 'right' in Table (3.1). This allows one to directly see which values are gauge-independent.

C. Symmetry-enriched quantum criticality

C.1. Symmetry fluxes and their charges

C.1.1. Symmetry properties of unique symmetry fluxes

For any $g \in G$ and $h \in C(g)$, we define $\chi_g(h)$ through $U^h \mathcal{S}^g U^{h\dagger} = \chi_g(h)\mathcal{S}^g$ (presuming we have chosen the endpoint operator $\mathcal{O}^g$ such that $C(g)$ acts nicely on it; otherwise we have to use the inner product, as discussed in the main text). From this definition, it directly follows that $\chi_g(hk) = \chi_g(h)\chi_g(k)$, i.e., $\chi_g : C(g) \to U(1)$ is a one-dimensional representation. Other useful properties—which hold for bosonic systems which are gapped or described by a CFT—are $\chi_g(h) = \chi_h(g)^{-1}$ and $\chi_g(g) = 1$. In the gapped case, these can be derived from the concept of symmetry fractionalization. More generally, these can be argued based on modular invariance of the partition function. Note that $\chi_g(g) = 1$ need not be true for fermionic systems: the Kitaev chain is a paradigmatic example where the symmetry flux of P is charged under itself!

C.1.2. From abelian charges to cocycles

Here we show how specifying the above charge χ_g for any $g \in G$ is equivalent to specifying a projective representation of G if G is abelian.

Due to the structure theorem, we have $G \cong \mathbb{Z}_{r_1} \times \cdots \mathbb{Z}_{r_n}$ (for convenience we take G to be finite). Let g_1, ..., g_n be a set of generators. We now define a central extension of G, which is a group $\tilde{G}$ generated by the symbols $\hat{g}_1$, ..., $\hat{g}_n$, and complex phases. To define the relations between these generating elements, it is useful to introduce the shorthand $[a, b] \equiv aba^{-1}b^{-1}$. The relations of $\tilde{G}$ are then $\hat{g}_j^{r_j} \equiv 1$ and $[\hat{g}_j, \hat{g}_k] \equiv \chi_{g_k}(g_j)$. A priori, it is not trivial that this definition is consistent, since there are non-trivial relationships between commutators. In particular: $[a, b] = [b, a]^{-1}$ and $[a, bc] = [a, b][b, [a, c]][a, c]$ and $[g, g^{-1}] = 1$. However, the properties of χ_g mentioned in the previous subsection indeed show that the consistency relations are satisfied.

We have thus defined a central extension $U(1) \to \hat{G} \to G$. This short exact sequence simply means that $G \cong \tilde{G}/U(1)$, as one can readily verify. This is equivalent to defining a projective representation of G. The latter is often characterized in terms of a cocycle $\omega(g, h)$. The standard way of obtaining this from the extension, is by first defining a section $s : G \to \hat{G}$, i.e., an embedding of the original group into the extended one. It is sufficient to define this on the products of the generating elements: $s(g_1^{k_1} \cdots g_n^{k_n}) \equiv \hat{g}_1^{k_1} \cdots \hat{g}_n^{k_n}$. The cocycle is then determined via $\omega(g, h) = s(g)s(h)s(gh)^{-1}$.

C.1.3. Gapped symmetries

In this subsection, we focus on symmetries which act only on gapped degrees of freedom.

Symmetry flux from symmetry fractionalization: string order parameter

For gapped symmetries, there is the notion of symmetry fractionalization [16, 17]. This says that if one acts with the symmetry operator on a finite but large region, it effectively only acts non-trivially near the edges: $U_m^g U_{m+1}^g \cdots U_{n-1}^g = U_L^g U_R^g$. These obey a *projective* representation $U_R^g U_R^h = e^{i\omega(g,h)} U_R^{gh}$; here $\omega(\cdot, \cdot)$ characterizes the so-called second group

cohomology class. These fractional symmetries, U_L^g and U_R^g, might have non-trivial symmetries properties which force their expectation value to be zero. A string order parameter is then usually defined by finding an operator $\mathcal{O}^g$ that cancels these symmetry properties such that $\langle \mathcal{O}_m^g U_L^g \rangle \neq 0$ and $\langle U_R^g \mathcal{O}_n^g \rangle \neq 0$. The resulting string order parameter is then $\mathcal{O}_m^g U_m^g U_{m+1}^g \cdots U_{n-1}^g \mathcal{O}_n^g$ which has long-range order *by construction*. Note that this exactly satisfies the condition for the symmetry flux of g as defined in subsection 4.2.1.

Uniqueness of symmetry flux

Suppose one has a second operator $\tilde{\mathcal{O}}$ that satisfies the same properties. In particular, $\langle \tilde{\mathcal{O}}_m^g U_L^g \rangle \neq 0$ and $\langle U_R^g \tilde{\mathcal{O}}_n^g \rangle \neq 0$. From this, we can then directly observe that its symmetry flux is *linearly dependent* with the other one. More precisely, using the inner product of Eq. (4.6) (using that $\Delta_g = 0$):

$$\langle \tilde{\mathcal{S}}^g | \mathcal{S}^g \rangle_{\text{sym}} = \lim_{|n-m|\to\infty} \langle \tilde{\mathcal{O}}_m^g U_m^g \cdots U_{n-1}^g \mathcal{O}_n^g \rangle \tag{C.1}$$

$$= \lim_{|n-m|\to\infty} \langle \tilde{\mathcal{O}}_m^g U_L^g \rangle \langle U_R^g \mathcal{O}_n^g \rangle \neq 0. \tag{C.2}$$

Charges from the cocycle

Having shown the uniqueness of the symmetry flux of $g \in G$, we can now consider on its symmetry properties. For any $h \in C(g)$ (i.e., the elements of commuting with g), we can consider $U^h \mathcal{S}^g \left(U^h\right)^\dagger = \chi_g(h) \mathcal{S}^g$ with $\chi_g(h) \in U(1)$. As noted before, the function $\chi_g : C(g) \to U(1) : h \mapsto \chi_g(h)$ is a one-dimensional representation of the stabilizer of g. We now show that $\chi_g(h) = e^{-i(\omega(h,g)+\omega(hg,h^{-1}))}$. By definition of $\mathcal{O}^g$, it has the opposite symmetry property of U_R^g (indeed, otherwise $\mathcal{O}^g U_R^g$ could not have a nonzero expectation value), hence $U^h U_R^g U^{h\dagger} = \chi_g^*(h) U_R^g$. The left-hand side equals $U_R^h U_R^g U_R^{h\dagger} = e^{i\omega(h,g)} U_R^{hg} U_R^{h^{-1}} = e^{i(\omega(h,g)+\omega(hg,h^{-1}))} U_R^g$. QED.

Note that in subsection C.1.2 we proved that this relationship can be inverted if G is abelian.

C.2. Duality mapping $(I_x, I_y, I_z) \leftrightarrow (1, \mathbf{Hal}, 0)$

One can define the following unitary mapping (ignoring boundary conditions):

$$X_{2n+1} = (-1)^n \tilde{Z}_1 \cdots \tilde{Z}_{2n-1} \tilde{Z}_{2n} \tag{C.3}$$

$$Y_{2n+1} = (-1)^n \tilde{Z}_1 \cdots \tilde{Z}_{2n-1} \tilde{Y}_{2n} \tilde{Y}_{2n+1} \tag{C.4}$$

$$Z_{2n+1} = -\tilde{X}_{2n} \tilde{Y}_{2n+1} \tag{C.5}$$

$$X_{2n+2} = (-1)^n \tilde{Z}_1 \cdots \tilde{Z}_{2n-1} \tilde{Z}_{2n} \tilde{X}_{2n+1} \tilde{X}_{2n+2} \tag{C.6}$$

$$Y_{2n+2} = (-1)^{n+1} \tilde{Z}_1 \cdots \tilde{Z}_{2n-1} \tilde{Z}_{2n} \tilde{Z}_{2n+1} \tag{C.7}$$

$$Z_{2n+2} = \tilde{Y}_{2n+1} \tilde{X}_{2n+2}. \tag{C.8}$$

One can check that as thus defined, the operators satisfy the relevant algebra: operators on different sites commute, and on the same site they form a representation of the Pauli algebra.

From the above correspondences, one can derive:

$$X_{2n} X_{2n+1} = \tilde{Y}_{2n-1} \tilde{Y}_{2n} \tag{C.9}$$

$$Y_{2n} Y_{2n+1} = \tilde{Y}_{2n} \tilde{Y}_{2n+1} \tag{C.10}$$

$$X_{2n+1} X_{2n+2} = \tilde{X}_{2n+1} \tilde{X}_{2n+2} \tag{C.11}$$

$$Y_{2n+1} Y_{2n+2} = \tilde{X}_{2n} \tilde{X}_{2n+1}. \tag{C.12}$$

This directly implies that $H_x \leftrightarrow H_1$ and $H_y \leftrightarrow H_{\text{Hal}}$.

Similarly, one can check:

$$Z_{2n}Z_{2n+1} = -\tilde{Y}_{2n-1}\tilde{Y}_{2n+1} \tag{C.13}$$

$$Z_{2n+1}Z_{2n+2} = -\tilde{X}_{2n}\tilde{X}_{2n+2} \tag{C.14}$$

$$-Y_{2n}Y_{2n+2} = \tilde{Z}_{2n}\tilde{Z}_{2n+1} \tag{C.15}$$

$$-X_{2n+1}X_{2n+3} = \tilde{Z}_{2n+1}\tilde{Z}_{2n+2}. \tag{C.16}$$

Hence, $H_z \leftrightarrow H_0$. (Caveat: depending on which direction of the mapping one takes, H_0 has XX couplings on even/odd sites. However, since all five other Hamiltonians are inversion symmetric (when inverting along bonds *between* two-site unit cells), we can always concatenate with spatial inversion to obtain the desired variant.)

C.3. The bait-and-switch lemma

Consider two G-enriched Ising CFTs, which we refer to as the A and B systems. Suppose that each has the same charge for their σ operator. We now prove that if we stack the A-system which has been perturbed into its *gapped* symmetry-preserving phase on top of the *critical* B-system, then we can *smoothly* connect this to the B-system in its *gapped* symmetry-preserving phase stacked on top of the *critical* A-system. Conceptually, this says that all (non-symmetry-breaking) G-enriched Ising CFTs with the same charges for local operators can be realized by stacking gapped SPT phases on top of a reference Ising CFT. (Note that in the presence of symmetry-breaking, one can apply this lemma to the remaining symmetry group.) This lemma can be seen as a generalization of Corollary 1 in Appendix A (subsection A.4.3).

It is convenient to use the representation of the Ising CFT as a ϕ^4 theory. In particular, for a decoupled stack of the above two critical Ising CFTs, the Lagrangian would be

$$\mathcal{L}_0 = \sum_{i=A,B} \left((\partial\phi_i)^2 - \phi_i^4 - m_c^2\phi_i^2 \right). \tag{C.17}$$

The parameter m_c is taken such that we are at the Ising fixed point. (This is roughly $m_c^2 \approx 0.5$ according to Ref. [287], but its precise value is not important to the argument.) We now show that the situation where (only) the A system is gapped, i.e. $\mathcal{L} = \mathcal{L}_0 - m^2\phi_A^2$, can be smoothly connected to where (only) the B system is gapped, i.e. $\mathcal{L} = \mathcal{L}_0 - m^2\phi_B^2$, preserving both the Ising universality class and the G symmetry throughout.

Since by assumption the ϕ_A and ϕ_B fields have the same charges under each element of G, we can consider the following symmetric coupling (where $\theta \in [0, \pi/2]$ is a free parameter):

$$\mathcal{L} = \mathcal{L}_0 - m^2(\underbrace{(\cos\theta)\phi_A + (\sin\theta)\phi_B}_{\equiv\varphi_1})^2 + f(m,\theta)(\underbrace{-(\sin\theta)\phi_A + (\cos\theta)\phi_B}_{\equiv\varphi_2})^2. \tag{C.18}$$

For $\theta = 0$ (taking $f(m, 0) = 0$), the A d.o.f. are indeed gapped out and decoupled from the critical B d.o.f., whereas for $\theta = \pi/2$ the roles are reversed. We now show how to define $f(m, \theta)$ to keep the system Ising critical for intermediate values of θ.

If we express the Lagrangian in terms of the new fields φ_1 and φ_2 which were defined in Eq. (C.18), we obtain

$$\mathcal{L} = \sum_{i=1,2} \left((\partial\varphi_i)^2 - \left(\frac{3 + \cos(4\theta)}{4} \right) \varphi_i^4 - m_c^2\varphi_i^2 \right) - m^2\varphi_1^2 + f(m,\theta)\varphi_2^2 - V, \tag{C.19}$$

where the coupling V arises due to the quartic term,

$$V = \frac{3}{2}\left(1-\cos(4\theta)\right)\varphi_1^2\varphi_2^2 + \sin(4\theta)\left(\varphi_1\varphi_2^3 - \varphi_1^3\varphi_2\right). \tag{C.20}$$

If we work in the limit of large m^2, then φ_1 will be pinned to $\varphi_1 = 0$, such that

$$\mathcal{L} = (\partial\varphi_2)^2 - \left(\frac{3+\cos(4\theta)}{4}\right)\varphi_2^4 - \left(m_c^2 + \frac{3}{2}(1-\cos(4\theta))\langle\varphi_1^2\rangle_{m,\theta} - f(m,\theta)\right)\varphi_2^2. \tag{C.21}$$

Here $\langle\varphi_1^2\rangle_{m,\theta}$ depends on the UV (lattice) scale a. (Note that there is no effective coupling through $\langle\varphi_1\rangle$ or $\langle\varphi_1^3\rangle$ since symmetry forces this to be zero.) The Lagrangian in Eq. (C.21) is at the Ising critical point if we enforce the ratio

$$m_c^2 = \frac{m_c^2 + \frac{3}{2}(1-\cos(4\theta))\langle\varphi_1^2\rangle_{m,\theta} - f(m,\theta)}{\frac{3+\cos(4\theta)}{4}} \quad \Rightarrow \quad f(m,\theta) \equiv \sin^2(2\theta)\left(\frac{m_c^2}{2} + \langle\varphi_1^2\rangle_{m,\theta}\right). \tag{C.22}$$

Note that when integrating out φ_1, higher-order corrections can be generated; these can be included, leading to a slight shift in $f(m,\theta)$. The main conceptual point is that we can reach (or better yet, stay on) criticality by tuning a single parameter.

C.4. SU(2) symmetry at the self-dual radius

At the self-dual radius of the compact boson CFT (i.e., $K = 1/2$, or $r_c = 1/\sqrt{2}$), we have an emergent $SU(2)\times SU(2)$ symmetry, generated by the following operators with dimensions $(1,0)$ and $(0,1)$, respectively:

$$\begin{array}{lll} J^x = \cos(\theta+\varphi) & J^y = \sin(\theta+\varphi) & J^z = \frac{1}{2}i\partial_z\left(\theta+\varphi\right) \\ \bar{J}^x = \cos(\theta-\varphi) & \bar{J}^y = \sin(\theta-\varphi) & \bar{J}^z = \frac{1}{2}i\partial_{\bar{z}}\left(\theta-\varphi\right). \end{array} \tag{C.23}$$

For clarity, we are using a convention such that $\theta+\varphi$ is holomorphic and $\theta-\varphi$ is antiholomorphic at $K = 1/2$. We can define a change of variables which corresponds to a rotation generated by J^x, such that $\tilde{J}^x \equiv J^x$ but $\tilde{J}^z \equiv J^y$ and $\tilde{J}^y \equiv -J^z$ (and similarly for the anti-holomorphic sector). Note that this transformation is a symmetry *only* at the self-dual radius (i.e., at that point the theory is identical in these new variables)! We thus find $\partial_x\tilde{\theta} = -2\cos\theta\sin\varphi$, $\partial_x\tilde{\varphi} = -2\sin\theta\cos\varphi$, $\cos\tilde{\theta}\cos\tilde{\varphi} = \cos\theta\cos\varphi$, and $\sin\tilde{\theta}\sin\tilde{\varphi} = \sin\theta\sin\varphi$.

C.5. Relation to the literature

"Quantum Criticality in Topological Insulators and Superconductors: Emergence of Strongly Coupled Majoranas and Supersymmetry"

In this subsection, we discuss a model appearing in Ref. [165], reinterpreting certain aspects in terms of symmetry-enriched quantum criticality. For that reason, we closely follow the notation used in that paper. To start, let us consider a model which does not directly appear in Ref. [165], but which will aid our analysis:

$$H = \sum_{n\geq 1}\left(J_{n \bmod 2}\ \chi_{2n-1}\chi_{2n}\chi_{2n+1}\chi_{2n+2} - \frac{g}{2}\,i\chi_{4n-1}\chi_{4n+1} + \frac{g}{2}\,i\chi_{4n}\chi_{4n+2}\right). \tag{C.24}$$

The Hamiltonian is pictorially represented in Fig. C.1. It has an anti-unitary symmetry T_- defined by $(\chi_{2n-1},\chi_{2n}) \overset{T_-}{\mapsto} (\chi_{2n},-\chi_{2n-1})$, satisfying $T_-^2 = -1$. If we set $J_0 = J_1 = 0$ (but $g \neq 0$), then in Fig. C.1 we directly see that we are in a topological phase with two

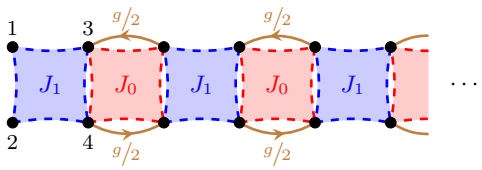

Figure C.1.: **A strongly-interacting Majorana model in the DIII class.** A sketch of Eq. (C.24).

zero-energy Majorana edge modes at a *single* edge, χ_1 and χ_2, which T_- prevents us from gapping out. This is the only non-trivial class in DIII. Oppositely, if we make J_0 and J_1 positive and large, then the ground state wants to occupy vertical bonds, spontaneously breaking T_-.

Note that—similar to the SSH model—the above model is only non-trivial if we fix our convention of the physical unit cells to be $(1234)(5678)\cdots$, i.e. the blue boxes in Fig. C.1.

Deriving an effective (almost-)spin model (as $J_0 \to +\infty$)

Note that the J_0 term is an integral of motion. In fact, it is already minimized in the above phase, so we can adiabatically ramp up the term J_0 such that $J_0 \gg \max\{|J_1|, |g|\}$. We can then work in the subspace $\mathcal{H}_0$ where for all n, we have $\chi_{4n-1}\chi_{4n}\chi_{4n+1}\chi_{4n+2} = -1$. In this subspace, we can define the following *bosonic* operators:

$$\sigma^z_n := i\chi_{4n-1}\chi_{4n} = i\chi_{4n+1}\chi_{4n+2}, \tag{C.25}$$
$$\sigma^x_n := i\chi_{4n-1}\chi_{4n+1} = -i\chi_{4n}\chi_{4n+2}. \tag{C.26}$$

In this sector, we then obtain

$$H_{\text{eff}} = \sum_{n\geq 1} \left(J_1 \chi_{4n-3}\chi_{4n-2}\chi_{4n-1}\chi_{4n} - g\, i\chi_{4n-1}\chi_{4n+1}\right) \tag{C.27}$$
$$= -J_1\, \sigma^z_1\, i\chi_1\chi_2 - \sum_{n\geq 1} \left(J_1 \sigma^z_n \sigma^z_{n+1} + g\sigma^x_n\right). \tag{C.28}$$

The model in Eq. (C.28) is the one appearing Ref. [165] (Eq. (1) of that work). The anti-unitary symmetries acts the following way on the bosonic operators: $(\sigma^x_n, \sigma^y_n, \sigma^z_n) \overset{T_-}{\mapsto} (\sigma^x_n, \sigma^y_n, -\sigma^z_n)$. In other words, for the spin variables, we can write $T_{-,\text{eff}} = (\prod \sigma^x_n)\, K$. Note that this implies $T^2_{-,\text{eff}} = +1$.

We see that the anti-unitary symmetry in H_{eff} is spontaneously broken for $|J_1| > |g|$, whereas for $|J_1| < |g|$ we have two protected Majorana modes (per edge).

Symmetry fluxes

Let us first obtain the symmetry flux for fermionic parity symmetry $P = \prod_n P_n$ where $P_n = \gamma_{4n-3}\gamma_{4n-2}\gamma_{4n-1}\gamma_{4n}$ is the fermionic parity per unit cell (i.e., per blue box in Fig. C.1). Since we work in the limit where $J_0 \to +\infty$, we have that *the product of red boxes* has long-range order. We conclude that the symmetry flux of P is $\mathcal{S}^P_n = \cdots P_{n-2}P_{n-1}(i\gamma_{4n-3}\gamma_{4n-2})$ (note that the i is there to ensure that $\left\langle \left(\mathcal{S}^P_n\right)^2 \right\rangle > 0$). We observe that $T_-\mathcal{S}^P T_- = -\mathcal{S}^P$, i.e., the symmetry flux of P is odd under T. This gives us a discrete label which is moreover topologically non-trivial.

By the reciprocal nature of charges of symmetry fluxes, we expect that the symmetry flux of T should be odd under P. However, in this work we have not studied the notion of symmetry fluxes for anti-unitary symmetries. Nevertheless, a closely related statement

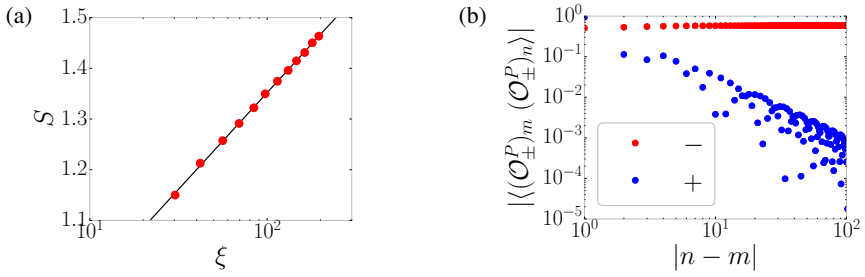

Figure C.2.: **Spinful fermions with triplet-pairing.** We study the model of Ref. [46] as shown in Eq. (C.29) (or Eq. (C.30)) with $U = -0.9$. (a) Confirmation that the bulk (which has central charge $c = 2$ for $U = 0$) has flown to central charge $c = 1$. The black line is a fit $S \sim \frac{c_{\text{fit}}}{6} \ln \xi$ with $c_{\text{fit}} \approx 0.994$. (b) Correlation function for $\mathcal{O}^P_\pm$ (where $T\mathcal{O}^P_\pm T = \pm\mathcal{O}^P_\pm$). We find that the T-odd string operator has long-range order; this is thus the unique symmetry flux of P.

is that we expect that $P\mu P = -\mu$. To make this precise, we can consider a lattice $\mathbb{Z}_2$ symmetry which we can relate to the unitary $\mathbb{Z}_2$ symmetry of the Ising CFT. This is of course $\prod_n \sigma^x_n$, or in the original fermionic model, the fermionic parity symmetry of a single leg, $P_{\text{odd}} = \prod_n (\chi_{4n-1}\chi_{4n+1})$. Indeed, for $J_0 \to +\infty$, one can derive that $P_{\text{odd}} = \prod_n \sigma^x_n$ (at least without boundaries). Similar to P, the symmetry flux of P_{odd} has an extra Majorana mode: $\mathcal{S}^{P_{\text{odd}}} = \cdots (P_{\text{odd}})_{n-2}(P_{\text{odd}})_{n-1}\chi_{4n-1}$. Hence, we conclude that the symmetry flux of P_{odd} is odd under fermionic parity symmetry. Equivalently, the symmetry flux of $\prod_n \sigma^x_n$ is $\cdots \sigma^x_{n-2}\sigma^x_{n-1}\chi_{4n-1}$; we thus conclude that $P\mu P = -\mu$.

If we do not enforce the lattice $\mathbb{Z}_2$ symmetry $\prod_n \sigma^x_n$, then it becomes subtle to claim that $P\mu P = -\mu$ is well-defined. However, in this particular case, we expect that due to T_- symmetry being enforced, this invariant remains well-defined even in the absence of explicit $\prod_n \sigma^x_n$ symmetry; the methods developed in this paper do not allow us to prove this.

Edge modes

Since μ is charged under P, we know that by the general arguments in Section 4.3, the Ising CFT will have a degeneracy with open boundaries. This is in fact easy to see in Eq. (C.24) and Eq. (C.28). In both cases, we see that $i\chi_1\chi_2$ and $\chi_1\sigma^x_2\sigma^x_3\cdots$ are symmetries of the Hamiltonian, whereas they mutually anticommute. The half-infinite geometry thus has a twofold degeneracy labeled by the occupation $i\chi_1\chi_2 = \pm 1$. Remarkably, this degeneracy is protected by the bulk CFT being enriched non-trivially by P and T_-. Even with generic symmetry-preserving perturbations, the system will have a global twofold degeneracy whose splitting is exponentially small in system size.

"Gapless symmetry-protected topological phase of fermions in one dimension"

Let us recall the model in Eq. (4.20) of the main text:

$$H = -\sum_{n,\sigma}\left(c^\dagger_{n,\sigma}c_{n+1,\sigma} + h.c.\right) + U\sum_n \left(-c^\dagger_{n,\uparrow}c_{n,\downarrow}c_{n+1,\uparrow}c^\dagger_{n+1,\downarrow} + h.c. + n_{i,\uparrow}n_{i+1,\downarrow} + n_{i,\downarrow}n_{i+1,\uparrow}\right). \tag{C.29}$$

If we relabel the indices as $2j-1 \equiv (j,\uparrow)$ and $2j \equiv (j,\downarrow)$, then one can straightforwardly apply the Jordan-Wigner transformation to obtain the spin-1/2 chain $H =$

$\frac{1}{2}\sum_i (X_{i-1}Z_iX_{i+1} + Y_{i-1}Z_iY_{i+1}) + UH_{\text{pert}}$ with

$$H_{\text{pert}} = \sum_i \left(S^+_{2i-1}S^-_{2i}S^-_{2i+1}S^+_{2i+2} + h.c. + n_{2i-1}n_{2i+2} + n_{2i}n_{2i+1}\right), \tag{C.30}$$

where $S^\pm = (X_i \pm iY_i)/2$ and $n_i = (1+Z_i)/2$. In this bosonic language, we have the symmetries $P = \prod_i P_i$ (where $P_i = Z_{2i-1}Z_{2i}$) and $T = \prod_j e^{i\frac{\pi}{4}\left(S^x_{2j-1}S^y_{2j} - S^y_{2j-1}S^x_{2j}\right)}K$. Note that $T^2 = P$.

We will consider the two string operators $(\mathcal{O}^P_\pm)_i \equiv \cdots Z_{2i-3}Z_{2i-2}\,(Z_{2i-1} \pm Z_{2i})$. Note that $T\mathcal{O}^P_\pm T^{-1} = \pm\mathcal{O}^P_\pm$. If $U = 0$, the bulk is a $c = 2$ CFT and both operators have the same scaling dimension $\Delta = 1/2$. For $U \neq 0$, the bulk gaps out the spin sector (of the original spinful fermions), stabilizing a $c = 1$ CFT. We confirm this in Fig. C.2(a) for $U = -0.9$. Moreover, we find that $\mathcal{O}^P_+$ remains critical, whereas $\mathcal{O}^P_-$ now has long-range order; this is shown in Fig. C.2(b). We conclude that the system has flown to a $c = 1$ CFT which is non-trivially enriched by P and T; in particular, the (unique) symmetry-flux of P is odd under T.

D. Numerical aspects for DMRG study of Kitaev-Heisenberg model

D.1. Symmetry breaking: 1D vs 2D

From Monte-Carlo studies [288] it is known that the ground state of the Heisenberg antiferromagnet (AFM) on the honeycomb lattice displays symmetry breaking Néel order. However, when we place the Heisenberg AFM on an infinitely long cylinder of finite circumference, it is in principle a 1D system and the presence of a continuous symmetry in fact forbids spontaneous symmetry breaking [230]. Instead we numerically find a gapped state which preserves both spin rotation and translation symmetry. This is analogous to the results for stacking an even number of coupled spin-$\frac{1}{2}$ Heisenberg chains [289]. The transition from 1D to 2D can be understood by noting that this symmetry-preserving state is effectively Néel-like within a correlation length ξ, the latter growing with circumference. Similarly to how one determines spontaneous symmetry breaking from finite size scaling in the context of exact diagonalization, one can conclude that the 2D limit achieves Néel order by scaling with respect to circumference.

The presence of a gap implies this symmetry-preserving state is stable under $SU(2)$-breaking perturbations. For example, for $L_{\text{circ}} = 6$ it extends over $-0.2\pi \leq \alpha \leq 0.43\pi$, with a symmetry-breaking (Néel) phase arising for larger α until we hit the spin liquid. The stability of this symmetry-preserving state under Kitaev perturbations is presumably related to the fact that the Néel order which arises in the 2D limit would have a very small spin gap. This is different for XXZ-type perturbations, which induce Néel order for relatively small anisotropies as shown in Fig. D.1 (with $\Delta = 1.1$), where our state is numerically converged (for large χ) and the physics quickly becomes independent of circumference.

The DMRG simulations use a parameter χ which gives an upper bound on the entanglement. By limiting χ we can find a variational state with $\xi < L_{\text{circ}}$. Locally this state then looks two-dimensional and hence it can exhibit spontaneous symmetry breaking even for the $SU(2)$-symmetric Heisenberg model, as confirmed in Fig. D.1. As we increase χ, eventually ξ becomes of the order of L_{circ}, signaling the cross-over from 2D to 1D physics, and the symmetry of the state is restored. For $L_{\text{circ}} = 12$, the necessary ξ is already out of reach, explaining the effective Néel order we see in Fig. 6.1 in Chapter 6. Similarly, in the zigzag phase there is an extended region with a gapped symmetry-restored ground state. This is in keeping with the sublattice transformation, which maps the zigzag to the Néel phase (in particular $\alpha = \frac{3}{4}\pi$ maps onto $\alpha = 0$).

D.2. Entanglement scaling of the gapless Kitaev spin liquid

Matrix-product states (MPS) cannot capture algebraic ground state correlations. However, increasing the bond dimension gives an increasingly accurate estimate of the wave function. In Ref. [133], it was shown that the entanglement entropy S scales logarithmically with the correlation length ξ. In the MPS formalism, this is known as finite-entanglement scaling with $S(\chi) = \frac{c}{6} \ln \xi(\chi)$, where χ is the bond dimension of the MPS and c is the central charge [231, 232].

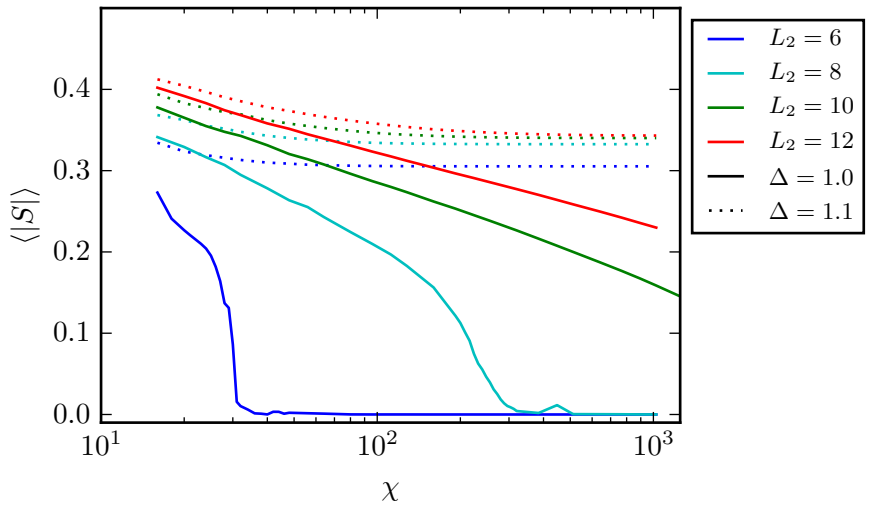

Figure D.1.: The absolute on-site magnetization for the pure Heisenberg AFM (solid) and for the AFM XXZ model with $\Delta = 1.1$ anisotropy (dashed) for different circumferences ($L_2 \equiv L_{\text{circ}}$).

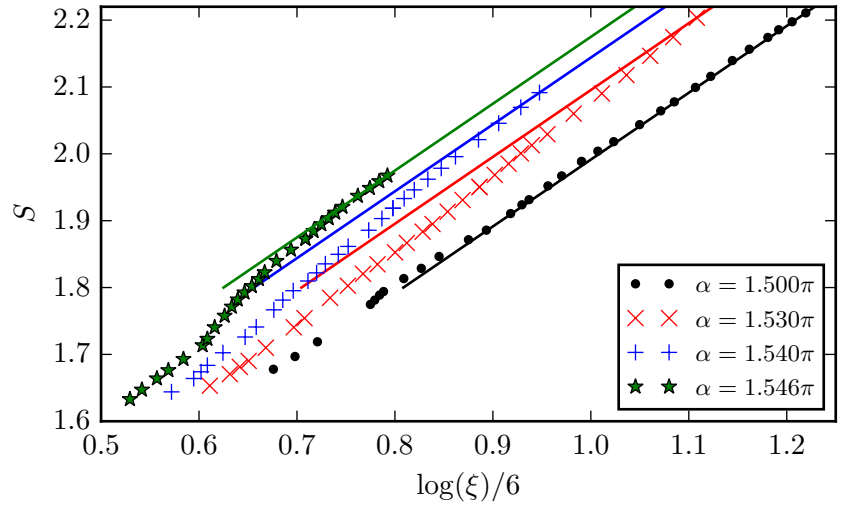

Figure D.2.: Entanglement entropy S and logarithm of correlation length ξ for different bond dimensions. The lines correspond to a central charge of $c = 1$.

	ED	iPEPS	DMRG			
			$L_{\text{circ}} = 6$		$L_{\text{circ}} = 12$	
			gapped	gapless	gapped	gapless
AF/KSL	0.488	0.487	0.484	0.494	0.485	0.487
KSL/ZZ	0.510	0.513	0.523	0.513	0.514	0.512
FM/KSL	1.399	1.432	1.405	1.44	1.421	1.428
KSL/ST	1.577	1.557	1.573	1.548	1.562	1.558

Table D.1.: Transition points α/π for different circumferences sectors compared to exact diagonalization (ED)[212] and infinite Projected Entangled Pair States (iPEPS)[226].

Figure D.2 shows S and $\ln \xi$ for various MPS bond dimensions χ of up to 1024. The lines serve as a guide to the eye corresponding to a slope with $c = 1$. We observe a good match of the scaling for the pure Kitaev spin liquid at $\alpha = 3/2\pi$. This reflects the fact that the KSL can be mapped to a free fermion problem with two Majorana cones in the first Brillouin zone, each contributing $1/2$ to the central charge. The gapless nature persists within the whole KSL phase and the scaling suggests $c = 1$.

D.3. Ground sectors of the Kitaev spin liquid on the cylinder

Similar to the plaquette operators $W_p = \prod_{j \in \hexagon} \sigma_j^{\gamma_j}$ we define a loop operator around the cylinder as

$$W_l = \prod_{j \in loop} \sigma_j^{\gamma_j} \ , \tag{D.1}$$

where $\gamma_i = \{x, y, z\}$ corresponds to the bond that is not part of the loop at site i. Following Ref. [95], W_l can be expressed in terms of $\mathbb{Z}_2$ gauge field variables u_{jk},

$$\tilde{W}_l = \prod_{(j,k) \in loop} u_{jk} \ . \tag{D.2}$$

For our choice of lattice periodicity, both loop operators are related by a minus sign. Thus, $\tilde{W}_l \to +1$ (periodic boundary condition of the fermions) translates to $W_l \to -1$, which corresponds to the gapless sector if the cylinder is chosen such that cuts in reciprocal space go through the nodes of the Majorana cones. The second sector (antiperiodic boundary condition of the fermions) is always gapped and has a lower ground state energy than the gapless sector.

Regarding the computation of the ground state, we can now make use of the loop operator and initialize DMRG with a state $|\psi\rangle$ that has $\langle\psi|W_l|\psi\rangle = \pm 1$ depending on the desired sector. Table D.1 contains the phase transitions for the gapped and the gapless sector and compares it to exact diagonalization (ED) and infinite Projected Entangled Pair States (iPEPS). As the gapped sector has a lower energy, its stability is enhanced and widens the KSL phase. This effect is more pronounced for a small circumference $L_{\text{circ}} = 6$.

D.4. Dynamics within the zigzag phase

In Fig. D.3(a) we show $\mathcal{S}(\boldsymbol{k} = \boldsymbol{0}, \omega)$ for the same choices of α as in Fig. 6.4, but now with a sharper ω-resolution (corresponding to $T = 40$) which is possible due to a smaller circumference ($L_{\text{circ}} = 6$). The finer features are most likely discretization effects due to the finite circumference, but the main points are that the broadness in ω-space persists

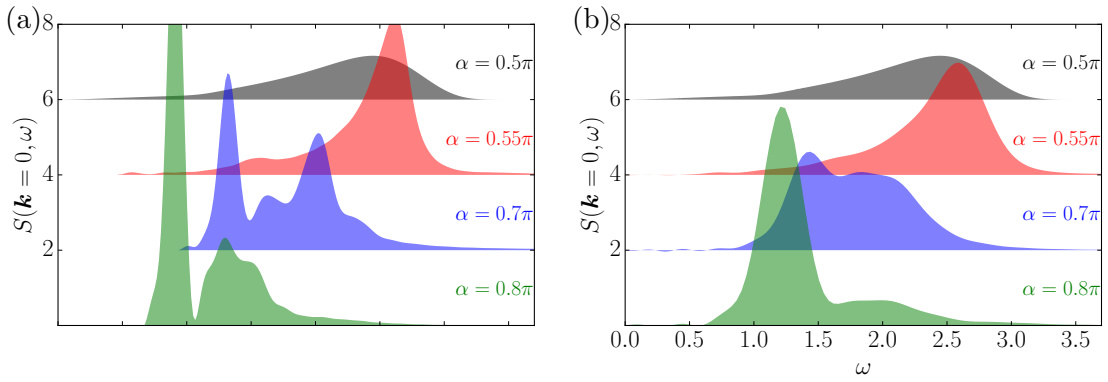

Figure D.3.: Complementing Fig. 6.4: $\mathcal{S}(\boldsymbol{k}=\mathbf{0},\omega)$ for $\alpha = 0.5\pi$ (2D analytic result) and $\alpha = 0.55\pi, 0.7\pi, 0.8\pi$. (a) $L_{\text{circ}} = 6$ and $\sigma_\omega \approx 0.06$. (b) $L_{\text{circ}} = 12$ and $\sigma_\omega \approx 0.12$.

despite a finer resolution, and that the high-energy feature gets squeezed downward as we get further away from the nearby spin liquid. Note that the latter is a meaningful statement and not just due to an overall α-dependent scaling of the Hamiltonian since the minima of the spin bands (as shown in the first row of Fig. 6.4) do *not* come down in energy (all at approximately $\omega = 0.4$).

In Fig. D.3(b) we have the same set-up but now for a system twice as wide where we time-evolve half as long. Interestingly, the spectra are quite smooth—smoother than need be based on the broadening—which suggests finite-size effects are small. In fact, we can explicitly confirm this. For $L_{\text{circ}} = 12$, all three different directions of the symmetry broken zigzag phase fit, which despite being equivalent in the two-dimensional limit are in principle not equivalent on the cylinder. The data we show is for the ground state where the zigzag pattern winds along the circumference. We have checked that if we start from a different symmetry broken direction, the difference of the spectra is negligible.

E. Effective Hamiltonians to arbitrary order

For completeness, we reproduce the general perturbative scheme that allows to obtain a well-defined effective Hamiltonian to any order (this is used in Chapter 7). We consider a Hamiltonian of the form $H = H_0 + \lambda V$. Let $\mathcal{H}_0$ be the Hilbert space associated with the degenerate eigenvalue E_0 of H_0. Moreover, let P_0 be the projector onto $\mathcal{H}_0$, and $Q_0 = 1 - P_0$. Note that we can decompose the total Hilbert space as $\mathcal{H} = \mathcal{H}_0 \oplus \mathcal{H}_0^\perp$.

Suppose that for $0 \leq \lambda \leq \lambda_c$, we can decompose the Hilbert space into $\mathcal{H} = \mathcal{H}_\lambda \oplus \mathcal{H}_\lambda^\perp$ in such a way that

1. $(\mathcal{H}_\lambda)\,|_{\lambda=0} = \mathcal{H}_0$;
2. $\mathcal{H}_\lambda$ is a smooth function of $\lambda \in [0, \lambda_c]$;
3. the Hamiltonian respects the decomposition.

Physically speaking, this formalizes the idea that we want the the energy levels of the sector we are interested to stay separated from the remaining levels; otherwise the idea of an effective Hamiltonian is misguided.

If those conditions hold, the work by Kato [260] and Takashi [261] showed that for the same range $0 \leq \lambda \leq \lambda_c$, one can explicitly construct a smooth unitary mapping $\Gamma_\lambda : \mathcal{H}_0 \to \mathcal{H}$ which maps the unperturbed eigenstates into the perturbed ones. Hence, the desired effective Hamiltonian on $\mathcal{H}_0$ is then simply $H_{\text{eff}} := \Gamma_\lambda^\dagger H \Gamma_\lambda$.

To perturbatively express Γ_λ as a function of the known quantities H_0, λ and V_0, it is useful to define a few other quantities. Firstly, let $P_\lambda : \mathcal{H} \to \mathcal{H}_\lambda$ be the projector onto $\mathcal{H}_\lambda$; we will derive a perturbative expression for this object as well. Secondly, define

$$S^0 := -P_0, \tag{E.1}$$

$$S^k := \tilde{G}_0(E_0)^k := \left(Q_0 \frac{1}{E_0 - H_0} Q_0\right)^k \quad (k \neq 0). \tag{E.2}$$

Note that S^k is expressed in terms of *known* quantities.

One can then derive [260, 261] that

$$P_\lambda P_0 = \sum_{n=0}^{\infty} \lambda^n \sum_{\substack{k_1+k_2+\cdots+k_n=n,\\ k_i \geq 0}} S^{k_1} V S^{k_2} V \cdots S^{k_n} V P_0. \tag{E.3}$$

Moreover, it can be shown that the following function then has the desired properties:

$$\Gamma_\lambda := P_\lambda P_0 \left(P_0 + \sum_{n=1}^{\infty} \frac{(2n-1)!!}{(2n)!!} [P_0 - P_0 P_\lambda P_0]^n\right). \tag{E.4}$$

It can be proven that Γ_λ as thus defined indeed satisfies $\Gamma_\lambda^\dagger \Gamma_\lambda = P_0$.

In terms of the above quantities, we thus have that

$$H_{\text{eff}} := \Gamma_\lambda^\dagger H \Gamma_\lambda = E_0 P_0 + \lambda\, \Gamma_\lambda^\dagger V \Gamma_\lambda - \Gamma_\lambda^\dagger S^{-1} \Gamma_\lambda\,. \tag{E.5}$$

The result in Eq. (E.5), namely that $\Gamma_\lambda^\dagger H_0 \Gamma_\lambda = E_0 P_0 - \Gamma_\lambda^\dagger S^{-1} \Gamma_\lambda$, is a direct consequence of $H_0 = H_0 P_0 + H_0 Q_0 = E_0 P_0 + (E_0 Q_0 - S^{-1}) = E_0 - S^{-1}$ and the fact that $\Gamma_\lambda^\dagger \Gamma_\lambda = P_0$.

F. Avoided quasiparticle decay

F.1. The interacting single-particle Green's function and spectral function

F.1.1. The general formula

We will first calculate $G(E) = \langle\psi|(E-\hat{H})^{-1}|\psi\rangle$ for the model in Eqs. (8.2) and (8.3). If we think of $E-\hat{H}$ as a matrix (with indices labeled by $|\psi\rangle$ and $|\varphi_\alpha\rangle$), then $G(E)$ is the top left element of its inverse. This is easily calculated. Schematically, first write

$$E-\hat{H} = \begin{pmatrix} A & B \\ C & D \end{pmatrix} \text{ with } A = E-E_b, \quad D_{\alpha\beta} = (E-E_\alpha)\,\delta(\alpha-\beta) \quad \text{and } B_\alpha = C_\alpha = -\gamma. \tag{F.1}$$

Since D is diagonal, one can apply the well-known result that

$$\det(E-\hat{H}) = \det(A-BD^{-1}C)\det D = \left(E-E_b-\gamma^2\int \mathrm{d}\alpha \frac{1}{E-E_\alpha}\right)\det D. \tag{F.2}$$

Finally, by Cramer's rule, we can express

$$G(E) = \langle\psi|(E-\hat{H})^{-1}|\psi\rangle = \frac{\det D}{\det(E-\hat{H})} = \frac{1}{E-E_b-\gamma^2 g(E)}, \tag{F.3}$$

where we have introduced the Cauchy principal value $g(E) := \int_0^\infty \frac{\nu(\varepsilon)}{E-\varepsilon}\mathrm{d}\varepsilon$, as in the main text.

Note that

$$g(E-i\eta) = \int_0^\infty \nu(\varepsilon)\frac{E-\varepsilon+i\eta}{(E-\varepsilon)^2+\eta^2}\mathrm{d}\varepsilon, \text{ hence } \frac{1}{\pi}\mathrm{Im}\, g(E-i0^+) = \int_0^\infty \nu(\varepsilon)\,\delta(E-\varepsilon) = \nu(E). \tag{F.4}$$

In other words, $g(E-i0^+) = g(E) + i\pi\nu(E)$.

We can now calculate $\mathcal{A}(E) = \frac{1}{\pi}\mathrm{Im}G(E-i0^+)$ as follows,

$$\mathcal{A}(E) = \frac{1}{\pi}\mathrm{Im}\left(\frac{1}{E-E_b-\gamma^2 g(E-i0^+)-i0^+}\right) \tag{F.5}$$

$$= \frac{1}{\pi}\mathrm{Im}\left(\frac{1}{E-E_b-\gamma^2 g(E)-i\pi\gamma^2\nu(E)-i0^+}\right) \tag{F.6}$$

$$= \begin{cases} \frac{\gamma^2\nu(E)}{(E-E_b-\gamma^2 g(E))^2+(\pi\gamma^2\nu(E))^2} & \text{if } \nu(E)\neq 0, \\ \delta(E-E_b-\gamma^2 g(E)) & \text{if } \nu(E)=0. \end{cases} \tag{F.7}$$

F.1.2. Examples

For the left column of Fig. 8.2(a), we consider the DOS

$$\nu(E) = \begin{cases} 0 & \text{if } E<0, \\ \nu_0/\sqrt{E} & \text{if } E>0, \end{cases} \tag{F.8}$$

which is what one expects for the two-particle continuum of a one-dimensional gapped model. A straight-forward calculation gives

$$g(E) = \nu_0 \int_0^\infty \frac{\mathrm{d}\varepsilon}{\sqrt{\varepsilon}(E-\varepsilon)} = \begin{cases} -\frac{\pi\nu_0}{\sqrt{-E}} & \text{if } E < 0, \\ 0 & \text{if } E > 0. \end{cases} \tag{F.9}$$

We can now plug this into Eq. (F.7). We set $\nu_0 = 1$. In the top left panel of Fig. 8.2(a) we take $\gamma = 0.2$, whereas in the bottom left panel, $\gamma = 0.7$. We consider the hypothetical scenario where the onset of the continuum is at $\omega_{\min} = 2 - \cos(k)$, where k can physically be thought of as (total) momentum. Moreover, we take the bare level to be flat, $\omega_b = 2$. In terms of our earlier variable, where the DOS has its onset at $E = 0$, we can thus say that $E_b = \omega_b - \omega_{\min} = \cos(k)$.

For the right column of Fig. 8.2(a), we consider the DOS

$$\nu(E) = \begin{cases} 0 & \text{if } E < 0 \text{ or } E_m < E, \\ \nu_0\sqrt{E(E_m - E)} & \text{if } 0 \le E \le E_m, \end{cases} \tag{F.10}$$

which is what one expects for the two-particle continuum of a three-dimensional gapped model. This has a square-root onset at $E = 0$ and a square-root termination at $E = E_m$. We obtain

$$g(E) = \begin{cases} \pi\nu_0 \left(E - E_m/2\right) & \text{if } 0 < E < E_m, \\ \pi\nu_0 \left(E - E_m/2 - E\sqrt{1 - E_m/E}\right) & \text{otherwise.} \end{cases} \tag{F.11}$$

Given our earlier results, we know that there will not *always* be an isolated state below the continuum. Instead, there is a threshold value $\gamma_{\mathrm{th}} = \sqrt{E_b/|g(0^-)|} = \sqrt{2E_b/(\pi\nu_0 E_m)}$. If $E_b > 0$, an isolated state exists below the continuum if and only if $|\gamma| > \gamma_{\mathrm{th}}$.

We again consider $\nu_0 = 1$, $\omega_{\min} = 2 - \cos(k)$ and $\omega_b = 2$, but now we also have to choose an upper threshold energy: $\omega_{\max} = 5 + \cos(k)$. The top right panel of Fig. 8.2(a) has $\gamma = 0.2$, whereas the bottom right panel has $\gamma = 0.5$. We note that the minimum interacting strength for which there is a state below the continuum for *all* values of k is $\gamma = \sqrt{\frac{2}{\pi\nu_0}} \times \sqrt{1/(2 + 3\sec(k))}\big|_{k=0} = \sqrt{2/5\pi} \approx 0.357$.

Finally, with regards to Fig. 8.2(a), we mention that we also plot the real part of complex poles when they exist. We see that their location nicely agrees with where the intensity of $\mathcal{A}(E)$ is largest. Moreover, the data in Fig. 8.2(a) has been convoluted with a gaussian with $\sigma = 0.025$ (in units shown). This is to give the delta-function outside the continuum a visible width.

F.2. Convergence of DMRG for spectral function of TLHAF

Here we investigate the convergence of the spectral function shown in Section 8.2 for triangular-lattice Heisenberg antiferrogmagnet in Eq. (8.9). We will consider both $\delta = 0.1$ and $\delta = 0.05$, the latter being the value discussed in Section 8.2.

F.2.1. Convergence in bond dimension

Fig. F.1 shows the spectral function obtained with DMRG for a cylinder with circumference $L_{\mathrm{circ}} = 6$ where we have set the anisotropy parameter $\delta = 0.1$ (to wit, $\delta = 0$ is the isotropic TLHAF). We observe that whilst the lowest-energy mode (near the zone center, Γ) is still converging, the mid- and high-energy regions of the single-magnon branch display convergence.

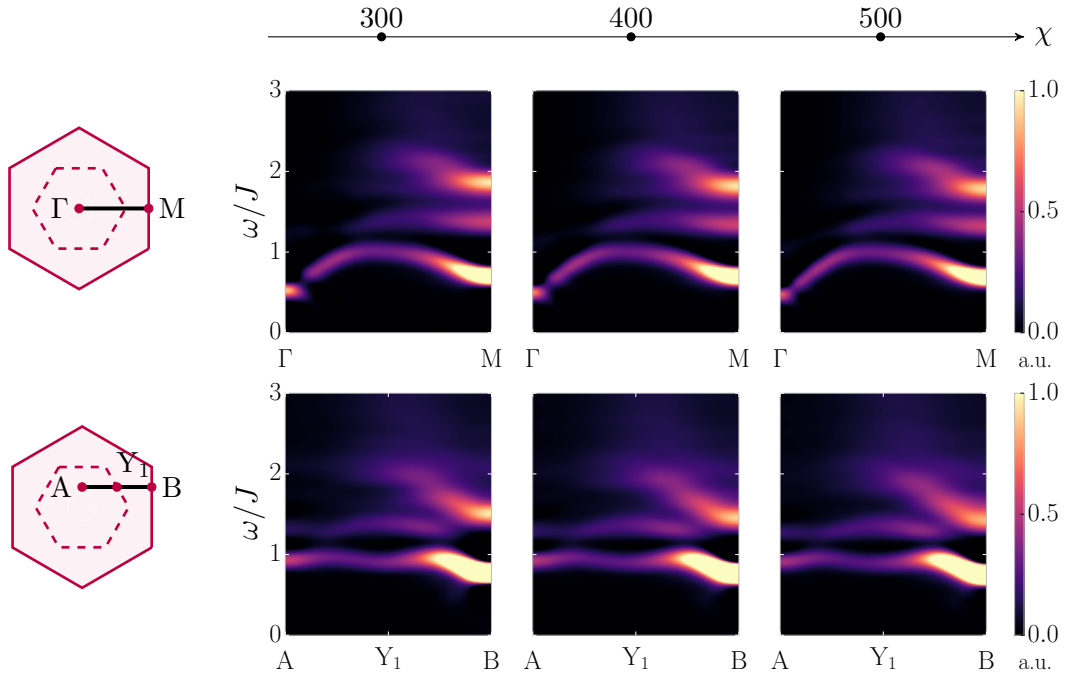

Figure F.1.: Comparing the out-of-plane spectral functions for the TLHAF with anisotropy parameter $\delta = 0.1$ for three different bond dimensions χ.

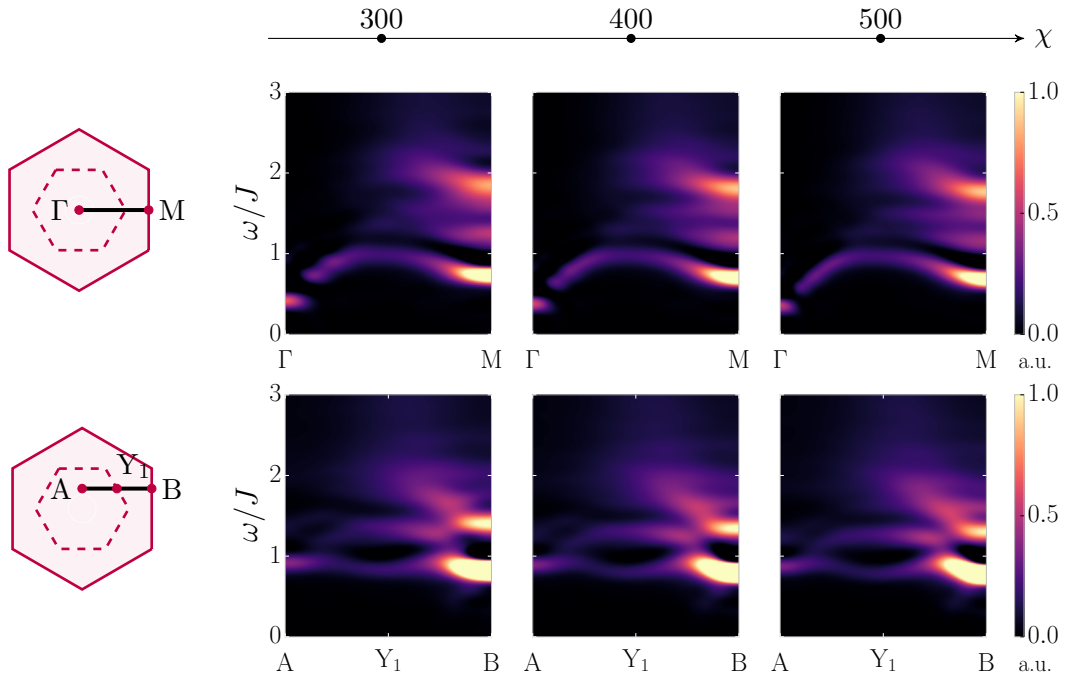

Figure F.2.: Comparing the out-of-plane spectral functions for the TLHAF with anisotropy parameter $\delta = 0.05$ for three different bond dimensions χ.

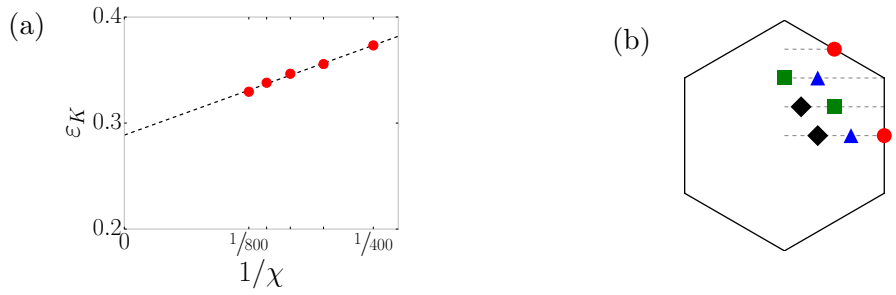

Figure F.3.: (a) Determining the energy of the near-Goldstone mode at the zone corner for anisotropy parameter $\delta = 0.05$. Extrapolating $\chi \to \infty$, we find $\varepsilon_K \approx 0.3J$. (b) Four pairs of points (accessible for $L_{\text{circ}} = 6$) which are symmetry-equivalent in the two-dimensional limit, but which are not equivalent on the cylinder. Comparing the dispersion at these points gives an independent probe of finite-circumference effects.

Fig. F.2 shows the analogous data for the anisotropy parameter $\delta = 0.05$—the case studied in the main text. We similarly observe convergence for the mid- and high-energy magnon dispersion.

As discussed in the main text, to conclude that magnon decay is absent, we mainly require the dispersion at such higher energies, supplemented with the value of the gap at the quasi-Goldstone mode at the zone corner, i.e. ε_K. To determine the latter, we need $\chi > 500$, as we saw in Fig. F.1 and Fig. F.2. Fortunately, this is possible by time-evolving for a shorter period of time, which effectively broadens the spectral function. Such broadening usually makes it harder to pinpoint the location of the magnon dispersion, as the broadened lineshape merges with other features. However, at the lowest energies, the band is well-separated from such other features, and one can reliably extract its center from short-time data. This way we obtain values for ε_K up to $\chi = 800$, as shown in Fig. F.3(a); these points allow one to roughly extrapolate $\varepsilon_K \approx 0.3J$ as $\chi \to \infty$.

F.2.2. Convergence in cylinder circumference

Given that the ground state order is 120°, circumferences which are not multiples of three would usually frustrate the ground state order—making it useless for the purpose of checking convergence. However, one can work in a local/rotating frame. More precisely, considering the Hamiltonian on the infinite lattice, one can rotate the spin by 120° degrees on the three sublattices; in these new variables, the $SU(2)$ symmetry of the Hamiltonian is no longer explicit, and one of the ground states looks like a ferromagnetic state. The beauty of this approach is that the Hamiltonian turns out to still be translation-invariant in these new variables, and hence one can sensibly put it on cylinders with circumferences that are *not* a multiple of three *without* frustrating the ground state order.

Hence, this allows us to compare the spectral functions for circumferences $L_{\text{circ}} = 4, 5, 6$, giving a sense of convergence in this parameter. Note that the momentum slices we can access depend on the circumference (since it determines the quantization conditions on the momentum along the circumference); we can always access the momentum slice $\Gamma - M$, and for L_{circ} even, we can access the $C - M - C'$ slice, as shown in Fig. F.4, which shows the results for the anisotropy $\delta = 0.1$.

Remarkably, in Fig. F.4, we observe that the *single*-magnon dispersion is close to being converged in circumference, aside from the variations at the lowest energies. The multi-magnon continuum does show variations. For our purposes, it is important to emphasize that we do not use the properties of this continuum in our argument: we consistently

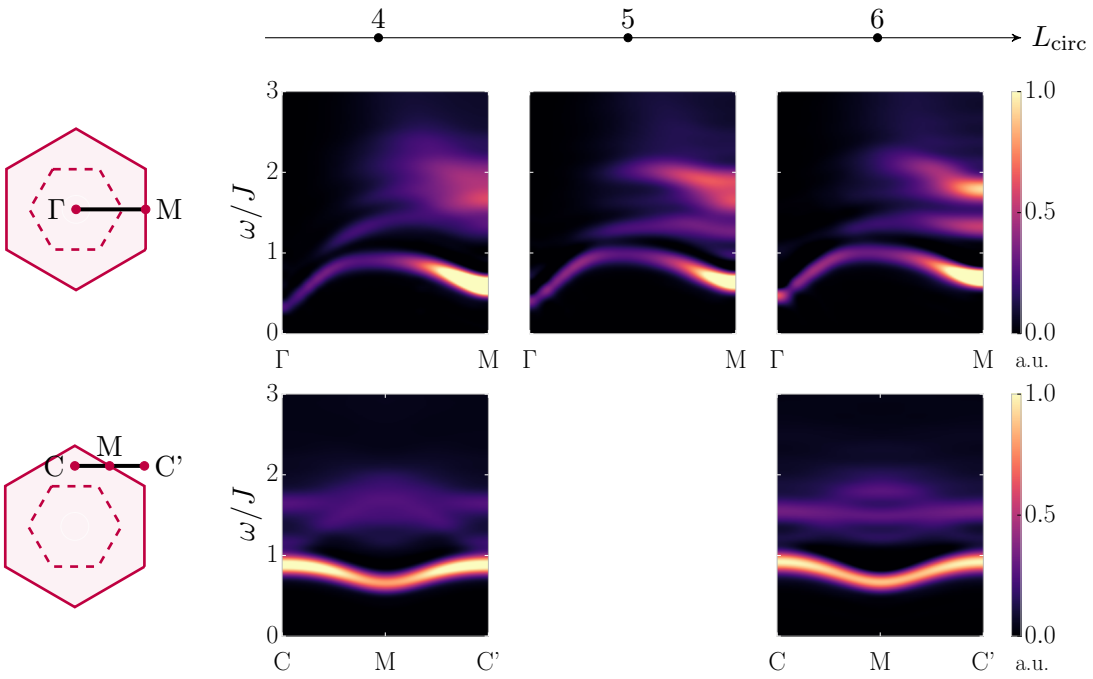

Figure F.4.: Comparing the out-of-plane spectral functions for the TLHAF with anisotropy parameter $\delta = 0.1$ for three different cylinder circumferences L_{circ}.

determine the continuum from taking combinations of the (converged) single-magnon dispersion (as discussed in the main text and in section F.2.1). Given that the single-magnon dispersion shows convergence in both bond dimension and system size, this is a reasonable way of figuring out where the continuum will be in the two-dimensional limit.

Fig. F.5 shows the analogous result for $\delta = 0.05$, which is the value of anisotropy discussed in the main text. We see that the single-magnon dispersion looks similar in all pictures, but at the same time, some variation is still noticeable. However, the bottom row (along the $C-M-C$) slice is more stable, hence this panel should give us a good estimate for the two-dimensional limit. We can use this as an independent measure of determining that the $L_{\mathrm{circ}} = 6$ is close to the two-dimensional limit: M appears in both the top and bottom rows, and whereas for $L_{\mathrm{circ}} = 4$ these two values disagree (indeed, despite both M points being symmetry-equivalent in the two-dimensional limit, they are *not* equivalent on the cylindrical geometry, which does not obey the six-fold rotation symmetry of the triangular lattice), for $L_{\mathrm{circ}} = 6$, these two values closely agree.

Another way of probing that the $L_{\mathrm{circ}} = 6$ is close to the two-dimensional limit as far as the single-magnon dispersion is concerned, is by comparing integrated weights. For example, for the top slice shown in Fig. F.5, one can compare the weight in the multi-magnon sector at M compared to the weight in the single-magnon sector at that same point. For the circumferences $L_{\mathrm{circ}} = 4, 5, 6$, we find, respectively, the ratios 1.3, 2.6, and 2.6. This indicates that for the larger circumferences that we can probe, the multi-magnon sector is decoupled from the single-magnon band. This is reassuring, since as we have observed already, there are clear variations within the continuum.

Finally, fixing $L_{\mathrm{circ}} = 6$, there is an independent check we can perform regarding finite-circumference effects. As mentioned above, there are various points in the two-dimensional Brillouin zone which are symmetry-equivalent in the two-dimensional geometry, but which are no longer symmetry-equivalent on the cylindrical geometry. Fig. F.3(b) shows such points: there are four pair of points (each denoted by a symbol) where the single-magnon energies must agree in the two-dimensional limit by symmetry arguments. Comparing the

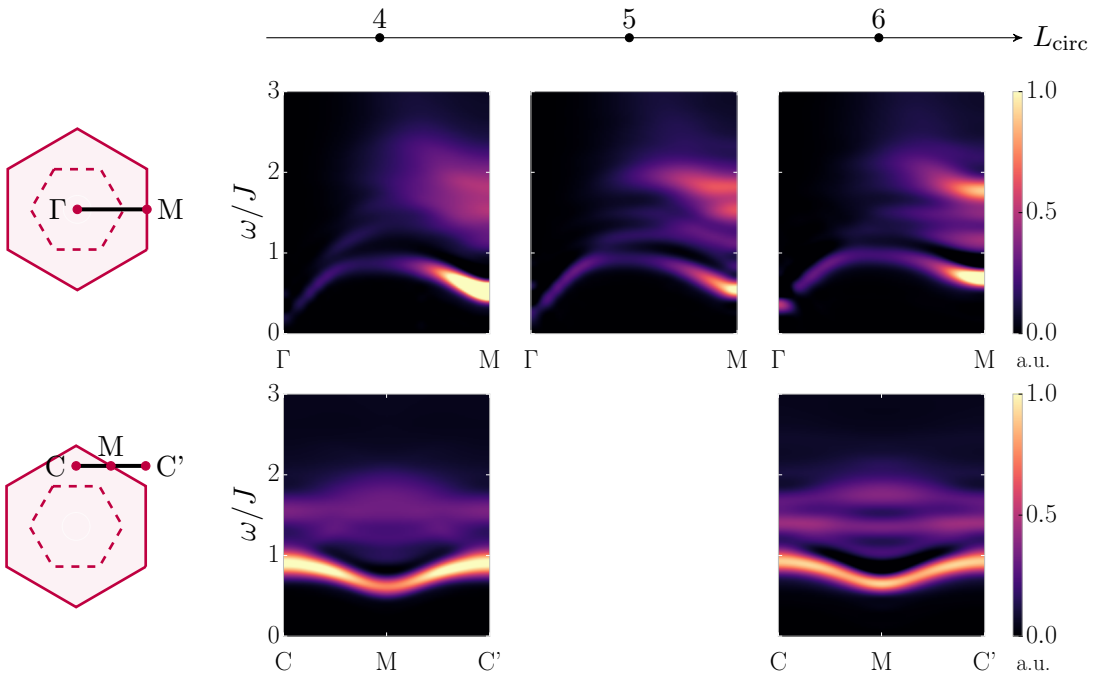

Figure F.5.: Comparing the out-of-plane spectral functions for the TLHAF with anisotropy parameter $\delta = 0.05$ for three different cylinder circumferences L_{circ}.

numerically obtained dispersions, we find that they differ by 3.1% (black diamonds), 4.8% (green squares), 5.7% (red dots) and 7.7% (blue triangles). Given that there would be no reason that these points would have similar energies aside from convergence toward the two-dimensional limit, we see these numbers as a reliable indication that we are close to said limit.

F.3. Density of states for two-roton continuum in superfluid helium

Let us consider the dispersion relevant to the roton minimum appearing in, for example, superfluid helium,

$$\varepsilon_{\boldsymbol{k}} = \Delta + \frac{1}{2m}(|\boldsymbol{k}| - K)^2. \tag{F.12}$$

We restrict ourselves to dimension $D \geq 3$, such that for the two-particle density of states, we can write

$$\rho_2(\boldsymbol{k}, \varepsilon) \propto \int \delta(\varepsilon_{\boldsymbol{q}} + \varepsilon_{\boldsymbol{k}-\boldsymbol{q}} - \varepsilon)\, \mathrm{d}^D\boldsymbol{q} \propto \int \left(\frac{1}{|\partial_\theta \varepsilon_{\boldsymbol{k}-\boldsymbol{q}}|} \sin\theta \right)\Big|_{\varepsilon_{\boldsymbol{q}}+\varepsilon_{\boldsymbol{k}-\boldsymbol{q}}=\varepsilon} q^{D-1}\mathrm{d}q. \tag{F.13}$$

Since $|\boldsymbol{k} - \boldsymbol{q}| = \sqrt{k^2 + q^2 - 2kq\cos\theta}$, we have that

$$\partial_\theta \varepsilon_{\boldsymbol{k}-\boldsymbol{q}} = {}^1\!/_m \times (|\boldsymbol{k} - \boldsymbol{q}| - K) \times \frac{1}{2|\boldsymbol{k} - \boldsymbol{q}|} \times 2kq\sin\theta. \tag{F.14}$$

We are interested in $0 < k < 2K$, where the threshold is near $\varepsilon \approx 2\Delta$, which forces the decay products to be very close to the roton minimum, i.e $q \approx K$ and $|\boldsymbol{k} - \boldsymbol{q}| \approx K$. Hence,

near the threshold we have

$$\rho_2(\boldsymbol{k},\varepsilon) \propto m \int \left(\frac{|\boldsymbol{k}-\boldsymbol{q}|}{||\boldsymbol{k}-\boldsymbol{q}|-K|}\right)\Bigg|_{\varepsilon_{\boldsymbol{q}}+\varepsilon_{\boldsymbol{k}-\boldsymbol{q}}=\varepsilon} \frac{q^{D-2}}{k}\,\mathrm{d}q \tag{F.15}$$

$$\approx \frac{mK^{D-1}}{k} \int \left(\frac{1}{\sqrt{2m\left(\varepsilon_{\boldsymbol{k}-\boldsymbol{q}}-\Delta\right)}}\right)\Bigg|_{\varepsilon_{\boldsymbol{q}}+\varepsilon_{\boldsymbol{k}-\boldsymbol{q}}=\varepsilon} \mathrm{d}q \tag{F.16}$$

$$= \frac{mK^{D-1}}{k} \int_{K-\sqrt{2m(\varepsilon-2\Delta)}}^{K+\sqrt{2m(\varepsilon-2\Delta)}} \frac{1}{\sqrt{2m(\varepsilon-2\Delta)-(q-K)^2}}\mathrm{d}q \tag{F.17}$$

$$= \frac{mK^{D-1}}{k} \int_{-1}^{1} \frac{1}{\sqrt{1-x^2}}\mathrm{d}x \quad \left(\text{where } x := \frac{q-K}{\sqrt{2m(\varepsilon-2\Delta)}}\right) \tag{F.18}$$

$$\propto \begin{cases} 0 & \text{if } \delta < 0 \\ \frac{mK^{D-1}}{k} & \text{if } \delta > 0 \end{cases} \qquad \text{where } \varepsilon \approx 2\Delta + \delta. \tag{F.19}$$

We repeat that the above derivation is for $0 < k < 2K$. We conclude that in this regime, there is a jump discontinuity at the onset.

Bibliography

[1] P. W. Anderson, Science **177**, 393 (1972).

[2] P. W. Anderson, Phys. Rev. **130**, 439 (1963).

[3] G. A. et al., Physics Letters B **716**, 1 (2012).

[4] G. Baym, C. Pethick, and D. Pines, Nature **224**, 673 (1969).

[5] D. Page, M. Prakash, J. M. Lattimer, and A. W. Steiner, Phys. Rev. Lett. **106**, 081101 (2011).

[6] N. Ashcroft and N. Mermin, *Solid State Physics* (Cengage Learning, 1976).

[7] P. Nozières and D. Pines, *Theory Of Quantum Liquids*, Frontiers in Physics (CRC Press, 1999).

[8] P. Hořava, Phys. Rev. Lett. **95**, 016405 (2005).

[9] X. Wen, *Quantum Field Theory of Many-body Systems: From the Origin of Sound to an Origin of Light and Electrons*, Oxford graduate texts (Oxford University Press, 2004).

[10] M. Z. Hasan and C. L. Kane, Rev. Mod. Phys. **82**, 3045 (2010).

[11] J. K. Asbóth, L. Oroszlány, and A. Pályi, *A Short Course on Topological Insulators* (Springer International Publishing, 2016).

[12] S. R. White, Phys. Rev. Lett. **69**, 2863 (1992).

[13] S. Paeckel, T. Köhler, A. Swoboda, S. R. Manmana, U. Schollwöck, and C. Hubig, arXiv e-prints , arXiv:1901.05824 (2019), arXiv:1901.05824 [cond-mat.str-el] .

[14] T. Giamarchi and O. U. Press, *Quantum Physics in One Dimension*, International Series of Monogr (Clarendon Press, 2004).

[15] M. B. Hastings and T. Koma, Communications in Mathematical Physics **265**, 781 (2006).

[16] L. Fidkowski and A. Kitaev, Phys. Rev. B **83**, 075103 (2011).

[17] A. M. Turner, F. Pollmann, and E. Berg, Phys. Rev. B **83**, 075102 (2011).

[18] X. Chen, Z.-C. Gu, and X.-G. Wen, Phys. Rev. B **83**, 035107 (2011).

[19] Schuch, N. and Pérez-García, D. and Cirac, J. I., Phys. Rev. B **84**, 165139 (2011).

[20] Y. Fuji, F. Pollmann, and M. Oshikawa, Phys. Rev. Lett. **114**, 177204 (2015).

[21] F. D. M. Haldane, Rev. Mod. Phys. **89**, 040502 (2017).

[22] F. D. M. Haldane, Phys. Lett. A **93**, 464 (1983).

[23] T. Kennedy and H. Tasaki, Comm. Math. Phys. **147**, 431 (1992).

[24] F. Pollmann, A. M. Turner, E. Berg, and M. Oshikawa, Phys. Rev. B **81**, 064439 (2010).

[25] I. Affleck, T. Kennedy, E. H. Lieb, and H. Tasaki, Comm. Math. Phys. **115**, 477 (1988).

[26] T. Kennedy, Journal of Physics: Condensed Matter **2**, 5737 (1990).

[27] M. Suzuki, Progress of Theoretical Physics **46**, 1337 (1971).

[28] W. P. Su, J. R. Schrieffer, and A. J. Heeger, Phys. Rev. Lett. **42**, 1698 (1979).

[29] K. Totsuka and M. Suzuki, Journal of Physics: Condensed Matter **7**, 6079 (1995).

[30] A. Kitaev, Physics-Uspekhi **44**, 131 (2001).

[31] R. Raussendorf and H. J. Briegel, Phys. Rev. Lett. **86**, 5188 (2001).

[32] L. Fidkowski and A. Kitaev, Phys. Rev. B **81**, 134509 (2010).

[33] J. McGreevy, *Whence QFT?* (University of California San Diego, 2014) lecture notes.

[34] P. Jordan and E. Wigner, Zeitschrift für Physik **47**, 631 (1928).

[35] A. Rosch, Phys. Rev. B **86**, 125120 (2012).

[36] S. Moudgalya and F. Pollmann, Phys. Rev. B **91**, 155128 (2015).

[37] P. Di Francesco, P. Mathieu, and D. Senechal, *Conformal Field Theory*, Graduate Texts in Contemporary Physics (Springer-Verlag, New York, 1997).

[38] S. Sachdev and J. Ye, Phys. Rev. Lett. **69**, 2411 (1992).

[39] A. V. Chubukov, S. Sachdev, and J. Ye, Phys. Rev. B **49**, 11919 (1994).

[40] S. Sachdev, *Quantum Phase Transitions* (Cambridge University Press, 2001).

[41] J. P. Kestner, B. Wang, J. D. Sau, and S. Das Sarma, Phys. Rev. B **83**, 174409 (2011).

[42] M. Cheng and H.-H. Tu, Phys. Rev. B **84**, 094503 (2011).

[43] L. Fidkowski, R. M. Lutchyn, C. Nayak, and M. P. A. Fisher, Phys. Rev. B **84**, 195436 (2011).

[44] J. D. Sau, B. I. Halperin, K. Flensberg, and S. Das Sarma, Phys. Rev. B **84**, 144509 (2011).

[45] C. V. Kraus, M. Dalmonte, M. A. Baranov, A. M. Läuchli, and P. Zoller, Phys. Rev. Lett. **111**, 173004 (2013).

[46] A. Keselman and E. Berg, Phys. Rev. B **91**, 235309 (2015).

[47] F. Iemini, L. Mazza, D. Rossini, R. Fazio, and S. Diehl, Phys. Rev. Lett. **115**, 156402 (2015).

[48] N. Lang and H. P. Büchler, Phys. Rev. B **92**, 041118 (2015).

[49] N. Kainaris and S. T. Carr, Phys. Rev. B **92**, 035139 (2015).

[50] A. Montorsi, F. Dolcini, R. C. Iotti, and F. Rossi, Phys. Rev. B **95**, 245108 (2017).

[51] J. Ruhman and E. Altman, Phys. Rev. B **96**, 085133 (2017).

[52] T. Scaffidi, D. E. Parker, and R. Vasseur, Phys. Rev. X **7**, 041048 (2017).

[53] N. Kainaris, R. A. Santos, D. B. Gutman, and S. T. Carr, Fortschritte der Physik **65**, 1600054 (2017).

[54] H.-C. Jiang, Z.-X. Li, A. Seidel, and D.-H. Lee, Science Bulletin **63**, 753 (2018).

[55] R.-X. Zhang and C.-X. Liu, Phys. Rev. Lett. **120**, 156802 (2018).

[56] R. Verresen, N. G. Jones, and F. Pollmann, Phys. Rev. Lett. **120**, 057001 (2018).

[57] D. E. Parker, T. Scaffidi, and R. Vasseur, Phys. Rev. B **97**, 165114 (2018).

[58] A. Keselman, E. Berg, and P. Azaria, Phys. Rev. B **98**, 214501 (2018).

[59] E. Lieb, T. Schultz, and D. Mattis, Ann. Phys. (N. Y.) **16**, 407 (1961).

[60] I. Affleck and E. H. Lieb, Letters in Mathematical Physics **12**, 57 (1986).

[61] M. Oshikawa, Phys. Rev. Lett. **84**, 1535 (2000).

[62] S. C. Furuya and M. Oshikawa, Phys. Rev. Lett. **118**, 021601 (2017).

[63] Y. Yao, C.-T. Hsieh, and M. Oshikawa, arXiv e-prints , arXiv:1805.06885 (2018), arXiv:1805.06885 [cond-mat.str-el] .

[64] X. Wan, A. M. Turner, A. Vishwanath, and S. Y. Savrasov, Phys. Rev. B **83**, 205101 (2011).

[65] S. Matsuura, P.-Y. Chang, A. P. Schnyder, and S. Ryu, New Journal of Physics **15**, 065001 (2013).

[66] I. A. Zaliznyak and S.-H. Lee, in *Modern Techniques for Characterizing Magnetic Materials*, edited by Y. Zhu (Springer US, Boston, MA, 2005) pp. 3–64.

[67] I. A. Zaliznyak and J. M. Tranquada, in *Strongly Correlated Systems: Experimental Techniques*, edited by A. Avella and F. Mancini (Springer Berlin Heidelberg, Berlin, Heidelberg, 2015) pp. 205–235.

[68] J. Goldstone, Il Nuovo Cimento (1955-1965) **19**, 154 (1961).

[69] J. Goldstone, A. Salam, and S. Weinberg, Phys. Rev. **127**, 965 (1962).

[70] S. A. Bludman and A. Klein, Phys. Rev. **131**, 2364 (1963).

[71] H. Nielsen and S. Chadha, Nuclear Physics B **105**, 445 (1976).

[72] I. Tamm, Zeitschrift für Physik **60**, 345 (1930).

[73] J. Frenkel, *Wave Mechanics: Elementary Theory*, International Series of Monographs on Physics; ed. by R.H. Fowler and P. Kapitza No. Vol. 1 (Clarendon Press, 1932).

[74] L. P. Pitaevskii, Journal of Experimental and Theoretical Physics **9**, 830 (1959).

[75] A. L. Chernyshev and M. E. Zhitomirsky, Phys. Rev. B **79**, 144416 (2009).

[76] M. E. Zhitomirsky and A. L. Chernyshev, Rev. Mod. Phys. **85**, 219 (2013).

[77] S. Ito, N. Kurita, H. Tanaka, S. Ohira-Kawamura, K. Nakajima, S. Itoh, K. Kuwahara, and K. Kakurai, Nature Communications **8**, 235 (2017).

[78] A. D. B. Woods and R. A. Cowley, Reports on Progress in Physics **36**, 1135 (1973).

[79] R. J. Donnelly, J. A. Donnelly, and R. N. Hills, Journal of Low Temperature Physics **44**, 471 (1981).

[80] H. R. Glyde, M. R. Gibbs, W. G. Stirling, and M. A. Adams, EPL (Europhysics Letters) **43**, 422 (1998).

[81] M. R. Gibbs, K. H. Andersen, W. G. Stirling, and H. Schober, Journal of Physics: Condensed Matter **11**, 603 (1999).

[82] R. T. Azuah, S. O. Diallo, M. A. Adams, O. Kirichek, and H. R. Glyde, Phys. Rev. B **88**, 024510 (2013).

[83] H. R. Glyde, Reports on Progress in Physics **81**, 014501 (2018).

[84] L. Landau, Phys. Rev. **60**, 356 (1941).

[85] H. M. Rønnow, D. F. McMorrow, R. Coldea, A. Harrison, I. D. Youngson, T. G. Perring, G. Aeppli, O. Syljuåsen, K. Lefmann, and C. Rischel, Phys. Rev. Lett. **87**, 037202 (2001).

[86] N. B. Christensen, H. M. Rønnow, D. F. McMorrow, A. Harrison, T. G. Perring, M. Enderle, R. Coldea, L. P. Regnault, and G. Aeppli, Proceedings of the National Academy of Science **104**, 15264 (2007).

[87] B. Dalla Piazza, M. Mourigal, N. B. Christensen, G. J. Nilsen, P. Tregenna-Piggott, T. G. Perring, M. Enderle, D. F. McMorrow, D. A. Ivanov, and H. M. Rønnow, Nature Physics **11**, 62 (2015).

[88] A. W. Sandvik and R. R. P. Singh, Phys. Rev. Lett. **86**, 528 (2001).

[89] H. Shao, Y. Q. Qin, S. Capponi, S. Chesi, Z. Y. Meng, and A. W. Sandvik, Phys. Rev. X **7**, 041072 (2017).

[90] R. R. P. Singh and M. P. Gelfand, Phys. Rev. B **52**, R15695 (1995).

[91] W. Zheng, J. Oitmaa, and C. J. Hamer, Phys. Rev. B **71**, 184440 (2005).

[92] A. Lüscher and A. M. Läuchli, Phys. Rev. B **79**, 195102 (2009).

[93] M. Powalski, G. S. Uhrig, and K. P. Schmidt, Phys. Rev. Lett. **115**, 207202 (2015).

[94] M. Powalski, K. P. Schmidt, and G. S. Uhrig, SciPost Phys. **4**, 001 (2018).

[95] A. Kitaev, Annals of Physics **321**, 2 (2006).

[96] T. Suzuki, T. Yamada, Y. Yamaji, and S.-i. Suga, Phys. Rev. B **92**, 184411 (2015).

[97] A. Banerjee, C. A. Bridges, J.-Q. Yan, A. A. Aczel, L. Li, M. B. Stone, G. E. Granroth, M. D. Lumsden, Y. Yiu, J. Knolle, S. Bhattacharjee, D. L. Kovrizhin, R. Moessner, D. A. Tennant, D. G. Mandrus, and S. E. Nagler, Nat Mater **15**, 733 (2016).

[98] J. Knolle, D. L. Kovrizhin, J. T. Chalker, and R. Moessner, Phys. Rev. Lett. **112**, 207203 (2014).

[99] J. S. Bell, Physics Physique Fizika **1**, 195 (1964).

[100] W. Kohn, Rev. Mod. Phys. **71**, 1253 (1999).

[101] P. Fulde, Nature Physics **12**, 106 (2016).

[102] M. B. Hastings, Journal of Statistical Mechanics: Theory and Experiment **2007**, P08024 (2007).

[103] R. Baxter, *Exactly Solved Models in Statistical Mechanics*, Dover Books on Physics (Dover Publications, 2013).

[104] M. Fannes, B. Nachtergaele, and R. F. Werner, Communications in Mathematical Physics **144**, 443 (1992).

[105] V. Murg, F. Verstraete, and J. I. Cirac, Phys. Rev. A **75**, 033605 (2007).

[106] S. R. White, Phys. Rev. B **48**, 10345 (1993).

[107] U. Schollwöck, Annals of Physics **326**, 96 (2011).

[108] M. P. Zaletel, R. S. K. Mong, C. Karrasch, J. E. Moore, and F. Pollmann, Phys. Rev. B **91**, 165112 (2015).

[109] A. P. Schnyder, S. Ryu, A. Furusaki, and A. W. W. Ludwig, Phys. Rev. B **78**, 195125 (2008).

[110] A. Kitaev, AIP Conference Proceedings **1134**, 22 (2009).

[111] S. Ryu, A. P. Schnyder, A. Furusaki, and A. W. W. Ludwig, New Journal of Physics **12**, 065010 (2010).

[112] L. Fu, Phys. Rev. Lett. **106**, 106802 (2011).

[113] T. Neupert and F. Schindler, "Topological crystalline insulators," in *Topological Matter: Lectures from the Topological Matter School 2017*, edited by D. Bercioux, J. Cayssol, M. G. Vergniory, and M. Reyes Calvo (Springer International Publishing, Cham, 2018) pp. 31–61.

[114] A. Altland and M. R. Zirnbauer, Phys. Rev. B **55**, 1142 (1997).

[115] L. Fu, C. L. Kane, and E. J. Mele, Phys. Rev. Lett. **98**, 106803 (2007).

[116] W. DeGottardi, M. Thakurathi, S. Vishveshwara, and D. Sen, Phys. Rev. B **88**, 165111 (2013).

[117] O. Motrunich, K. Damle, and D. A. Huse, Phys. Rev. B **63**, 224204 (2001).

[118] S. Das and I. I. Satija, ArXiv e-prints (2014), arXiv:1409.6139 [cond-mat.mes-hall] .

[119] I. Mandal, EPL (Europhysics Letters) **110**, 67005 (2015).

[120] C. L. Kane and E. J. Mele, Phys. Rev. Lett. **95**, 146802 (2005).

[121] P. De Gennes, *Superconductivity Of Metals And Alloys* (CRC Press, 2018).

[122] R. Verresen, R. Moessner, and F. Pollmann, Phys. Rev. B **96**, 165124 (2017).

[123] M. Nielsen and I. Chuang, *Quantum Computation and Quantum Information: 10th Anniversary Edition* (Cambridge University Press, 2010).

[124] D. Vodola, L. Lepori, E. Ercolessi, A. V. Gorshkov, and G. Pupillo, Phys. Rev. Lett. **113**, 156402 (2014).

[125] O. Viyuela, D. Vodola, G. Pupillo, and M. A. Martin-Delgado, Phys. Rev. B **94**, 125121 (2016).

[126] N. G. Jones and R. Verresen, Journal of Statistical Physics **175**, 1164 (2019).

[127] C. W. J. Beenakker, Rev. Mod. Phys. **69**, 731 (1997).

[128] P. W. Brouwer, C. Mudry, B. D. Simons, and A. Altland, Phys. Rev. Lett. **81**, 862 (1998).

[129] I. C. Fulga, F. Hassler, A. R. Akhmerov, and C. W. J. Beenakker, Phys. Rev. B **83**, 155429 (2011).

[130] A. B. Zamolodchikov, JETP Lett. **43**, 730 (1986).

[131] G. Refael and J. E. Moore, Phys. Rev. Lett. **93**, 260602 (2004).

[132] N. Laflorencie, Phys. Rev. B **72**, 140408 (2005).

[133] P. Calabrese and J. Cardy, J. Stat. Mech. **2004**, P06002 (2004).

[134] W. Son, L. Amico, R. Fazio, A. Hamma, S. Pascazio, and V. Vedral, EPL (Europhysics Letters) **95**, 50001 (2011).

[135] J. Keating and F. Mezzadri, Communications in Mathematical Physics **252**, 543 (2004).

[136] P. Smacchia, L. Amico, P. Facchi, R. Fazio, G. Florio, S. Pascazio, and V. Vedral, Phys. Rev. A **84**, 022304 (2011).

[137] Y. Niu, S. B. Chung, C.-H. Hsu, I. Mandal, S. Raghu, and S. Chakravarty, Phys. Rev. B **85**, 035110 (2012).

[138] V. Lahtinen and E. Ardonne, Phys. Rev. Lett. **115**, 237203 (2015).

[139] F. Anfuso and A. Rosch, Phys. Rev. B **75**, 144420 (2007).

[140] A. Kopp and S. Chakravarty, Nature Physics **1**, 53 (2005).

[141] B. Zeng, X. Chen, D. Zhou, and X. Wen, *Quantum Information Meets Quantum Matter: From Quantum Entanglement to Topological Phases of Many-Body Systems*, Quantum Science and Technology (Springer New York, 2019).

[142] P. Fendley, Journal of Physics A: Mathematical and Theoretical **49**, 30LT01 (2016).

[143] N. Bultinck, D. J. Williamson, J. Haegeman, and F. Verstraete, Phys. Rev. B **95**, 075108 (2017).

[144] T. Morimoto, H. Ueda, T. Momoi, and A. Furusaki, Phys. Rev. B **90**, 235111 (2014).

[145] C. Yang and S. Zhang, Modern Physics Letters B **04**, 759 (1990).

[146] S. R. Manmana, A. M. Essin, R. M. Noack, and V. Gurarie, Phys. Rev. B **86**, 205119 (2012).

[147] F. Verstraete, J. I. Cirac, J. I. Latorre, E. Rico, and M. M. Wolf, Phys. Rev. Lett. **94**, 140601 (2005).

[148] Y.-Z. You, Z. Bi, A. Rasmussen, M. Cheng, and C. Xu, New Journal of Physics **17**, 075010 (2015).

[149] Y.-Z. You and C. Xu, Phys. Rev. B **90**, 245120 (2014).

[150] T. Ohta, S. Tanaka, I. Danshita, and K. Totsuka, Phys. Rev. B **93**, 165423 (2016).

[151] F. Pollmann and A. M. Turner, Phys. Rev. B **86**, 125441 (2012).

[152] D. Gross, J. Eisert, N. Schuch, and D. Perez-Garcia, Phys. Rev. A **76**, 052315 (2007).

[153] D. V. Else, I. Schwarz, S. D. Bartlett, and A. C. Doherty, Phys. Rev. Lett. **108**, 240505 (2012).

[154] R. Raussendorf and T.-C. Wei, Annual Review of Condensed Matter Physics **3**, 239 (2012).

[155] H. A. Kramers and G. H. Wannier, Phys. Rev. **60**, 252 (1941).

[156] Z.-C. Gu and X.-G. Wen, Phys. Rev. B **80**, 155131 (2009).

[157] W. Chen, K. Hida, and B. C. Sanctuary, Phys. Rev. B **67**, 104401 (2003).

[158] C. Vafa and E. Witten, Journal of Geometry and Physics **15**, 189 (1995).

[159] M. R. Douglas, arXiv e-prints , hep-th/9807235 (1998), arXiv:hep-th/9807235 [hep-th] .

[160] E. Sharpe, Phys. Rev. D **68**, 126003 (2003).

[161] D. V. Else, S. D. Bartlett, and A. C. Doherty, Phys. Rev. B **88**, 085114 (2013).

[162] G. Watts, Nuclear Physics B **596**, 513 (2001).

[163] J. L. Cardy, Nuclear Physics B **275**, 200 (1986).

[164] D. E. Parker, R. Vasseur, and T. Scaffidi, arXiv e-prints , arXiv:1808.07485 (2018), arXiv:1808.07485 [cond-mat.str-el] .

[165] T. Grover and A. Vishwanath, arXiv e-prints , arXiv:1206.1332 (2012), arXiv:1206.1332 [cond-mat.str-el] .

[166] P. Ruelle and O. Verhoeven, Nuclear Physics B **535**, 650 (1998).

[167] J. A. Kjäll, M. P. Zaletel, R. S. K. Mong, J. H. Bardarson, and F. Pollmann, Phys. Rev. B **87**, 235106 (2013).

[168] M. Yamanaka, Y. Hatsugai, and M. Kohmoto, Phys. Rev. B **48**, 9555 (1993).

[169] S. Ejima, T. Yamaguchi, F. H. L. Essler, F. Lange, Y. Ohta, and H. Fehske, SciPost Phys. **5**, 59 (2018).

[170] J. L. Cardy, Nuclear Physics B **324**, 581 (1989).

[171] R. Blumenhagen and E. Plauschinn, *Introduction to Conformal Field Theory: With Applications to String Theory*, Lecture Notes in Physics (Springer Berlin Heidelberg, 2009).

[172] K. Hida, Phys. Rev. B **45**, 2207 (1992).

[173] P. Ginsparg, in *Les Houches, Session XLIX, 1988, Fields, Strings and Critical Phenomena*, edited by E. Brezin and J. Zinn-Justin (Elsevier, 1990).

[174] I. Affleck, in *Les Houches, Session XLIX, 1988, Fields, Strings and Critical Phenomena*, edited by E. Brezin and J. Zinn-Justin (Elsevier, 1990).

[175] X. Chen, Y.-M. Lu, and A. Vishwanath, Nature Communications **5**, 3507 (2014).

[176] J. Knolle, "Results for the structure factor," in *Dynamics of a Quantum Spin Liquid* (Springer International Publishing, Cham, 2016) pp. 59–65.

[177] G. Jackeli and G. Khaliullin, Phys. Rev. Lett. **102**, 017205 (2009).

[178] J. Chaloupka, G. Jackeli, and G. Khaliullin, Phys. Rev. Lett. **110**, 097204 (2013).

[179] K. W. Plumb, J. P. Clancy, L. J. Sandilands, V. V. Shankar, Y. F. Hu, K. S. Burch, H.-Y. Kee, and Y.-J. Kim, Phys. Rev. B **90**, 041112 (2014).

[180] A. Banerjee, J. Yan, J. Knolle, C. A. Bridges, M. B. Stone, M. D. Lumsden, D. G. Mandrus, D. A. Tennant, R. Moessner, and S. E. Nagler, Science **356**, 1055 (2017).

[181] T. C. Hsu, Phys. Rev. B **41**, 11379 (1990).

[182] C.-M. Ho, V. N. Muthukumar, M. Ogata, and P. W. Anderson, Phys. Rev. Lett. **86**, 1626 (2001).

[183] O. F. Syljuåsen and P. A. Lee, Phys. Rev. Lett. **88**, 207207 (2002).

[184] F. Ferrari and F. Becca, Phys. Rev. B **98**, 100405 (2018).

[185] G. H. Wannier, Phys. Rev. **79**, 357 (1950).

[186] D. A. Huse and V. Elser, Phys. Rev. Lett. **60**, 2531 (1988).

[187] B. Bernu, C. Lhuillier, and L. Pierre, Phys. Rev. Lett. **69**, 2590 (1992).

[188] W. Zheng, J. O. Fjærestad, R. R. P. Singh, R. H. McKenzie, and R. Coldea, Phys. Rev. B **74**, 224420 (2006).

[189] O. A. Starykh, A. V. Chubukov, and A. G. Abanov, Phys. Rev. B **74**, 180403 (2006).

[190] A. L. Chernyshev and M. E. Zhitomirsky, Phys. Rev. Lett. **97**, 207202 (2006).

[191] M. Mourigal, W. T. Fuhrman, A. L. Chernyshev, and M. E. Zhitomirsky, Phys. Rev. B **88**, 094407 (2013).

[192] E. Stoudenmire and S. R. White, Annual Review of Condensed Matter Physics **3**, 111 (2012).

[193] S. R. White and I. Affleck, Phys. Rev. B **77**, 134437 (2008).

[194] S. R. White, Phys. Rev. Lett. **77**, 3633 (1996).

[195] F. Pollmann, in *Topological Aspects of Condensed Matter Physics*, edited by C. Chamon, M. O. Goerbig, R. Moessner, and L. F. Cugliandolo (Oxford University Press, 2017).

[196] G. Vidal, Phys. Rev. Lett. **98**, 070201 (2007).

[197] J. Haegeman, J. I. Cirac, T. J. Osborne, I. Pižorn, H. Verschelde, and F. Verstraete, Phys. Rev. Lett. **107**, 070601 (2011).

[198] P. Calabrese and J. Cardy, Journal of Statistical Mechanics: Theory and Experiment **2005**, P04010 (2005).

[199] H. Kim and D. A. Huse, Phys. Rev. Lett. **111**, 127205 (2013).

[200] A. Nahum, J. Ruhman, S. Vijay, and J. Haah, Phys. Rev. X **7**, 031016 (2017).

[201] V. Alba and P. Calabrese, SciPost Phys. **4**, 17 (2018).

[202] M. Žnidarič, T. c. v. Prosen, and P. Prelovšek, Phys. Rev. B **77**, 064426 (2008).

[203] J. H. Bardarson, F. Pollmann, and J. E. Moore, Phys. Rev. Lett. **109**, 017202 (2012).

[204] P. Calabrese and J. Cardy, Journal of Statistical Mechanics: Theory and Experiment **2016**, 064003 (2016).

[205] M. Collura and P. Calabrese, Journal of Physics A: Mathematical and Theoretical **46**, 175001 (2013).

[206] S. He, T. Numasawa, T. Takayanagi, and K. Watanabe, Phys. Rev. D **90**, 041701 (2014).

[207] P. Caputa and M. M. Rams, Journal of Physics A: Mathematical and Theoretical **50**, 055002 (2017).

[208] Y. Kusuki and T. Takayanagi, Journal of High Energy Physics **2018**, 115 (2018).

[209] J. Chaloupka, G. Jackeli, and G. Khaliullin, Phys. Rev. Lett. **105**, 027204 (2010).

[210] J. Knolle, G.-W. Chern, D. L. Kovrizhin, R. Moessner, and N. B. Perkins, Phys. Rev. Lett. **113**, 187201 (2014).

[211] X.-Y. Song, Y.-Z. You, and L. Balents, Phys. Rev. Lett. **117**, 037209 (2016).

[212] D. Gotfryd, J. Rusnačko, K. Wohlfeld, G. Jackeli, J. c. v. Chaloupka, and A. M. Oleś, Phys. Rev. B **95**, 024426 (2017).

[213] R. D. Johnson, S. C. Williams, A. A. Haghighirad, J. Singleton, V. Zapf, P. Manuel, I. I. Mazin, Y. Li, H. O. Jeschke, R. Valenti, and R. Coldea, Phys. Rev. B **92**, 235119 (2015).

[214] H.-S. Kim and H.-Y. Kee, Phys. Rev. B **93**, 155143 (2016).

[215] L. J. Sandilands, Y. Tian, A. A. Reijnders, H.-S. Kim, K. W. Plumb, Y.-J. Kim, H.-Y. Kee, and K. S. Burch, Phys. Rev. B **93**, 075144 (2016).

[216] L. J. Sandilands, C. H. Sohn, H. J. Park, S. Y. Kim, K. W. Kim, J. A. Sears, Y.-J. Kim, and T. W. Noh, Phys. Rev. B **94**, 195156 (2016).

[217] J. Chaloupka and G. Khaliullin, Phys. Rev. B **94**, 064435 (2016).

[218] F. Lang, P. J. Baker, A. A. Haghighirad, Y. Li, D. Prabhakaran, R. Valenti, and S. J. Blundell, Phys. Rev. B **94**, 020407 (2016).

[219] G. B. Halász, N. B. Perkins, and J. van den Brink, Phys. Rev. Lett. **117**, 127203 (2016).

[220] A. Koitzsch, C. Habenicht, E. Müller, M. Knupfer, B. Büchner, H. C. Kandpal, J. van den Brink, D. Nowak, A. Isaeva, and T. Doert, Phys. Rev. Lett. **117**, 126403 (2016).

[221] Y. Kubota, H. Tanaka, T. Ono, Y. Narumi, and K. Kindo, Phys. Rev. B **91**, 094422 (2015).

[222] A. U. B. Wolter, L. T. Corredor, L. Janssen, K. Nenkov, S. Schönecker, S.-H. Do, K.-Y. Choi, R. Albrecht, J. Hunger, T. Doert, M. Vojta, and B. Büchner, Phys. Rev. B **96**, 041405 (2017).

[223] J. Zheng, K. Ran, T. Li, J. Wang, P. Wang, B. Liu, Z.-X. Liu, B. Normand, J. Wen, and W. Yu, Phys. Rev. Lett. **119**, 227208 (2017).

[224] S.-H. Baek, S.-H. Do, K.-Y. Choi, Y. S. Kwon, A. U. B. Wolter, S. Nishimoto, J. van den Brink, and B. Büchner, Phys. Rev. Lett. **119**, 037201 (2017).

[225] J. A. Sears, Y. Zhao, Z. Xu, J. W. Lynn, and Y.-J. Kim, Phys. Rev. B **95**, 180411 (2017).

[226] J. Osorio Iregui, P. Corboz, and M. Troyer, Phys. Rev. B **90**, 195102 (2014).

[227] H.-C. Jiang, Z.-C. Gu, X.-L. Qi, and S. Trebst, Phys. Rev. B **83**, 245104 (2011).

[228] E. Sela, H.-C. Jiang, M. H. Gerlach, and S. Trebst, Phys. Rev. B **90**, 035113 (2014).

[229] K. Shinjo, S. Sota, and T. Tohyama, Phys. Rev. B **91**, 054401 (2015).

[230] S. Coleman, Communications in Mathematical Physics **31**, 259 (1973).

[231] L. Tagliacozzo, T. R. de Oliveira, S. Iblisdir, and J. I. Latorre, Phys. Rev. B **78**, 024410 (2008).

[232] F. Pollmann, S. Mukerjee, A. M. Turner, and J. E. Moore, Phys. Rev. Lett. **102**, 255701 (2009).

[233] Y.-C. He, M. P. Zaletel, M. Oshikawa, and F. Pollmann, Phys. Rev. X **7**, 031020 (2017).

[234] J. Knolle, (2016), unpublished data.

[235] Z. Weihong, J. Oitmaa, and C. J. Hamer, Phys. Rev. B **44**, 11869 (1991).

[236] R. Yadav, N. A. Bogdanov, V. M. Katukuri, S. Nishimoto, J. van den Brink, and L. Hozoi, Scientific Reports **6**, 37925 (2016).

[237] W. Wang, Z.-Y. Dong, S.-L. Yu, and J.-X. Li, Phys. Rev. B **96**, 115103 (2017).

[238] S. M. Winter, K. Riedl, P. A. Maksimov, A. L. Chernyshev, A. Honecker, and R. Valentí, Nature Communications **8**, 1152 (2017).

[239] W. Heisenberg, Zeitschrift für Physik **49**, 619 (1928).

[240] L. Hulthén, Proc. Roy. Acad. Sci. Amsterdam **39**, 190 (1936).

[241] P. W. Anderson, Phys. Rev. **86**, 694 (1952).

[242] A. B. Harris, D. Kumar, B. I. Halperin, and P. C. Hohenberg, Phys. Rev. B **3**, 961 (1971).

[243] F. Keffer, H. Kaplan, and Y. Yafet, American Journal of Physics **21**, 250 (1953).

[244] R. R. P. Singh, Phys. Rev. B **39**, 9760 (1989).

[245] M. P. Gelfand, Solid State Communications **98**, 11 (1996).

[246] P. W. Anderson, Science **235**, 1196 (1987).

[247] T. M. Rice, Zeitschrift für Physik B Condensed Matter **67**, 141 (1987).

[248] S. Chakravarty, B. I. Halperin, and D. R. Nelson, Phys. Rev. Lett. **60**, 1057 (1988).

[249] R. Kubo, Phys. Rev. **87**, 568 (1952).

[250] S. Stringari, Phys. Rev. B **49**, 6710 (1994).

[251] T. Oguchi, Phys. Rev. **117**, 117 (1960).

[252] Z. Weihong, J. Oitmaa, and C. J. Hamer, Phys. Rev. B **43**, 8321 (1991).

[253] C. J. Hamer, Z. Weihong, and P. Arndt, Phys. Rev. B **46**, 6276 (1992).

[254] Z. Weihong and C. J. Hamer, Phys. Rev. B **47**, 7961 (1993).

[255] A. V. Syromyatnikov, Journal of Physics: Condensed Matter **22**, 216003 (2010).

[256] G. S. Uhrig and K. Majumdar, The European Physical Journal B **86**, 282 (2013).

[257] N. S. Headings, S. M. Hayden, R. Coldea, and T. G. Perring, Phys. Rev. Lett. **105**, 247001 (2010).

[258] J. Oitmaa, private communications (2018).

[259] N. D. Mermin and H. Wagner, Phys. Rev. Lett. **17**, 1133 (1966).

[260] T. Kato, Progress of Theoretical Physics **4**, 514 (1949).

[261] M. Takahashi, Journal of Physics C: Solid State Physics **10**, 1289 (1977).

[262] S. Dusuel, M. Kamfor, K. P. Schmidt, R. Thomale, and J. Vidal, Phys. Rev. B **81**, 064412 (2010).

[263] G. Baskaran, Z. Zou, and P. Anderson, Solid State Communications **63**, 973 (1987).

[264] G. Baskaran and P. W. Anderson, Phys. Rev. B **37**, 580 (1988).

[265] M. B. Stone, I. A. Zaliznyak, T. Hong, C. L. Broholm, and D. H. Reich, Nature **440**, 187 (2006).

[266] T. Masuda, A. Zheludev, H. Manaka, L.-P. Regnault, J.-H. Chung, and Y. Qiu, Phys. Rev. Lett. **96**, 047210 (2006).

[267] J. Oh, M. D. Le, J. Jeong, J.-h. Lee, H. Woo, W.-Y. Song, T. G. Perring, W. J. L. Buyers, S.-W. Cheong, and J.-G. Park, Phys. Rev. Lett. **111**, 257202 (2013).

[268] N. J. Robinson, F. H. L. Essler, I. Cabrera, and R. Coldea, Phys. Rev. B **90**, 174406 (2014).

[269] T. Hong, Y. Qiu, M. Matsumoto, D. A. Tennant, K. Coester, K. P. Schmidt, F. F. Awwadi, M. M. Turnbull, H. Agrawal, and A. L. Chernyshev, Nature Communications **8**, 15148 (2017).

[270] B. Gaveau and L. S. Schulman, Journal of Physics A: Mathematical and General **28**, 7359 (1995).

[271] S. Zimering, Journal of Mathematical Physics **10**, 181 (1969).

[272] M. E. Zhitomirsky, Phys. Rev. B **73**, 100404 (2006).

[273] Y. Kojima, M. Watanabe, N. Kurita, H. Tanaka, A. Matsuo, K. Kindo, and M. Avdeev, Phys. Rev. B **98**, 174406 (2018).

[274] K. W. Plumb, K. Hwang, Y. Qiu, L. W. Harriger, G. E. Granroth, A. I. Kolesnikov, G. J. Shu, F. C. Chou, C. Rüegg, Y. B. Kim, and Y.-J. Kim, Nature Physics **12**, 224 (2016).

[275] F. D. M. Haldane, arXiv e-prints , arXiv:1401.0529 (2014), arXiv:1401.0529 [cond-mat.str-el] .

[276] B. Yan and C. Felser, Annual Review of Condensed Matter Physics **8**, 337 (2017).

[277] L. Zhang and F. Wang, Phys. Rev. Lett. **118**, 087201 (2017).

[278] C. Ding, L. Zhang, and W. Guo, Phys. Rev. Lett. **120**, 235701 (2018).

[279] L. Weber, F. Parisen Toldin, and S. Wessel, Phys. Rev. B **98**, 140403 (2018).

[280] J. I. Cirac and G. Sierra, Phys. Rev. B **81**, 104431 (2010).

[281] G. Vidal, Physical Review Letters **99**, 220405 (2007).

[282] J. C. Bridgeman and D. J. Williamson, Phys. Rev. B **96**, 125104 (2017).

[283] S. Singh, N. A. McMahon, and G. K. Brennen, Phys. Rev. B **99**, 195139 (2019).

[284] P. A. McClarty and J. G. Rau, arXiv e-prints , arXiv:1904.02160 (2019), arXiv:1904.02160 [cond-mat.str-el] .

[285] E. Fradkin, *Field Theories of Condensed Matter Physics*, 2nd ed. (Cambridge University Press, 2013).

[286] E. Gibney and D. Castelvecchi, Nature **538**, 18 (2016).

[287] N. Anand, V. X. Genest, E. Katz, Z. U. Khandker, and M. T. Walters, Journal of High Energy Physics **2017**, 56 (2017).

[288] J. D. Reger, J. A. Riera, and A. P. Young, J. Phys.: Condens. Matter **1**, 1855 (1989).

[289] S. R. White, R. M. Noack, and D. J. Scalapino, Phys. Rev. Lett. **73**, 886 (1994).

Acknowledgments

I am indebted to my supervisors Frank Pollmann and Roderich Moessner. They have taught me so much and showed me unwavering support for pursuing my interests. A continuous source of inspiration for me is their uncanny physical intuition, which I actively deconstruct in the hope of having it rub off on me. Also in terms of content, I am grateful to Frank for infecting me with his love for one-dimensional systems, and to Roderich for raising the very question of quasiparticle properties away from the low-energy regime—it is thus immediately clear that this thesis would be nowhere without them. Their influence even seeps through the very exposition (or so I hope), since I consider both as role models for their clarity. In other respects, however, I sometimes feel as if I have only just started my PhD—fascinated and mystified—such as when observing Frank's wizardry in coding or Roderich's ability to impart knowledge in such a concise yet deep way that it is best mulled over in private. Also beyond physics, I have found their value systems to be an inspiring and reliable guideline. I hope to have them as mentors and collaborators for many more years to come.

The work in this thesis would not have been possible without my other collaborators—nor would it have been nearly as fun. First and foremost, there is Nick Jones, a dear friend with whom our nearly daily chats about physics (spanning across four years) have always been in the spirit of following one's passion. In this last year, Nick and I have had the good fortunate of welcoming Ryan Thorngren into this team. The week we spent in Bristol deriving the $1/L^{14}$ finite-size splitting leaves me no doubt that many more amusing endeavors will follow. I also have fond memories of my very first project, in collaboration with Matthias Gohlke. And despite those works not being discussed in this thesis, I want to thank my other collaborators, Pablo Sala, Tibor Rakovszky, Michael Knap and Ashvin Vishwanath.

Throughout my PhD, I have been wonderfully supported by the Sonderforschungsbereich 1143 "Korrelierter Magnetismus: Von Frustration zu Topologie" under the leadership of Matthias Vojta and with a large team, including Carsten Timm and Tatjana Schoffer. In addition to my home bases at MPI-PKS and the Technical University of Munich, I would also like to acknowledge the Grad Fellow Program program at the Kavli Institute for Theoretical Physics which gracefully supported me for half a year. Another indispensable type of support was provided by Hubert Scherrer-Paulus and the entire IT crowd at MPI-PKS.

I thank Nick, Konstantinos, Markus and Tibor for proofreading parts of this thesis.

Of course, my time at MPI-PKS, TUM and KITP was made all the more enjoyable by the lovely company of Jan, Sid, Talía, Omar, Younes, Cécile, Giuseppe, Johannes, Tibor, Pablo, Kevin, Alex, Ella, Julian, Markus, Dave, Dominic, Adam, Andrew, Gautam, and many others! I fear I cannot adequately express my heartfelt love for my flatmates, Henrik, Nico and András for an unforgettable time in Munich. A special shout-out is also in line for my dear friend Simon. Lastly, then, I want to thank—for unconditionally putting up with me—my sister and brothers, Karen, Rolf, Nils, and the world's cutest nephews, Ravi, Arto, Nero, and my parents.

List of Publications

1. Ruben Verresen, Roderich Moessner, Frank Pollmann, "Avoided quasiparticle decay from strong quantum interactions", *Nature Physics* **15**, 750–753 (2019)

2. Nick G. Jones, Ruben Verresen, "Asymptotic correlations in gapped and critical topological phases of 1D quantum systems", *Journal of Statistical Physics* **175**, 1164 (2019)

3. Ruben Verresen, Frank Pollmann, Roderich Moessner, "Quantum dynamics of the square-lattice Heisenberg model, *Physical Review B* **98**, 155102 (2018)

4. Ruben Verresen, Nick G. Jones, Frank Pollmann, "Topology and edge modes in quantum critical chains", *Physical Review Letters* **120**, 057001 (2018)

5. Ruben Verresen, Roderich Moessner, Frank Pollmann, "One-dimensional symmetry protected topological phases and their transitions", *Physical Review B (Editors' Suggestion)* **96**, 165124 (2017)

6. Matthias Gohlke, Ruben Verresen, Roderich Moessner, Frank Pollmann, "Dynamics of the Kitaev-Heisenberg model", *Physical Review Letters* **119**, 157203 (2017)

Publications 1 and 3–6 resulted from the work presented in this thesis. For Publication 6, Matthias Gohlke focused on the ground state study, whereas I focused on the spectral function calculations.

Pre-prints

P1. Ruben Verresen, Ryan Thorngren, Nick G. Jones, Frank Pollmann, "Gapless topological phases and symmetry-enriched quantum criticality", arXiv:1905.06969

P2. Pablo Sala, Tibor Rakovszky, Ruben Verresen, Michael Knap, Frank Pollmann, "Ergodicity-breaking arising from Hilbert space fragmentation in dipole-conserving Hamiltonians", arXiv:1904.04266

P3. Ruben Verresen, Ashvin Vishwanath, Frank Pollmann, "Stable Luttinger liquids and emergent $U(1)$ symmetry in constrained quantum chains", arXiv:1903.09179

Pre-print P1 resulted from the work presented in this thesis.

Versicherung

Diese Arbeit wurde am Max-Planck-Institut für Physik komplexer Systeme in Dresden unter der wissenschaftlichen Betreuung von Prof. Dr. Roderich Moessner und Prof. Dr. Frank Pollmann durchgeführt. Hiermit versichere ich, dass ich die vorliegende Arbeit ohne unzulässige Hilfe Dritter und ohne Benutzung anderer als der angegebenen Hilfsmittel angefertigt habe; die aus fremden Quellen direkt oder indirekt übernommenen Gedanken sind als solche kenntlich gemacht. Die Arbeit wurde bisher weder im Inland noch im Ausland in gleicher oder ähnlicher Form einer anderen Prüfungsbehörde vorgelegt. Darüber hinaus erkenne ich die Promotionsordnung des Bereichs Mathematik und Naturwissenschaften der Technischen Universität Dresden vom 23. Februar 2011 an.

Ruben Verresen

Dresden, 04.07.2019